Functional surface coatings and novel materials derived from hydroxypropyl cellulose

TECHNISCHE UNIVERSITÄT DARMSTADT

vom Fachbereich Chemie

der Technischen Universität Darmstadt

zur Erlangung des Grades

Doctor rerum naturalium

(Dr. rer. nat.)

Dissertation

von

Maximilian Nau

Erstgutachter: Prof. Dr. Markus Biesalski

Zweitgutachterin: Prof. Dr. Annette Andrieu-Brunsen

Darmstadt 2019

Tag der Einreichung: 05.11.2019

Tag der mündlichen Prüfung: 19.12.2019

Nau, Maximilian: Functional surface coatings and novel materials derived from hydroxypropyl cellulose

Darmstadt,Technische Universität Darmstadt,
Jahr der Veröffentlichung der Dissertation auf TUprints: 2020
URN: urn:nbn:de:tuda-tuprints-113451
Tag der mündlichen Prüfung: 19.12.2019

This thesis is the result of work carried out from July 2015 through February 2019 at the Technische Universität Darmstadt in the Department of Macromolecular Chemistry and Paper chemistry at the Ernst-Berl-Institute for Technical and Macromolecular Chemistry under the supervision of Prof. Dr. Markus Biesalski.

Part of this work has been published in:

Peer-reviewed articles:

Maximilian Nau, David Seelinger, Markus Biesalski

"Functional surface coatings from tailor-made long-chain hydroxypropyl cellulose ester nanoparticles", *Cellulose*, **2018**, 25 (10), 5769-5780

Maximilian Nau, David Seelinger, Markus Biesalski

"Independent Two Way Switching of the Wetting Behavior of Cellulose-Derived Nanoparticle Surface Coatings by Light and by Temperature", *Adv. Mater. Interfaces* **2019**, 6, 1900378

Maximilian Nau, Simon Trosien, David Seelinger, Anna K. Boehm, Markus Biesalski

"Spatially resolved crosslinking of hydroxypropyl cellulose esters for the generation of functional surface-attached organogels", *Front. Chem*., **2019**, 7, 367

Peer-reviewed articles (in cooperation):

Caterina Czibula, Gundula Teichert, Maximilian Nau, Mathias Hobisch, Chonnipa Palasingh, Markus Biesalski, Stefan Spirk, Christian Teichert and Tiina Nypelö

"Design of friction, morphology, wetting and protein affinity by cellulose blend thin film composition", *Front. Chem.*, **2019**, 7, 239

Maximilian Nau and Nicole Herzog, Johannes Schmidt, Tobias Meckel, Annette Andrieu-Brunsen and Markus Biesalski

"Janus-Type Hybrid Paper Membranes" *Adv. Mater. Interfaces* **2019**, 6, 1900892

Patent applications:

DE 102018111495.8 „Thermoresponsiven Papierbeschichtungen auf Basis von Cellulosederivaten“

DE 102018124255.7 "Verfahren zur Erzeugung von chemischen anisotropen Papierbeschichtungen"

Oral presentations:

„New Functional Hydroxypropyl Cellulose Based Materials“ EDSSC, **2016**, Stockholm (Sweden)

„Stimulus-responsive surface coatings and films from hydroxypropyl cellulose“ European Cellulose Materials Doctoral Students Conference, **2017**, Graz (Austria)

„Funktionale Papierbeschichtungen“ Zellcheming Bezirksgruppentreffen, **2017**, Mayen (Germany)

„Spielereien mit Wasser, Licht und Cellulose oder: Cellulosederivate als funktionale Polymere“ Zellcheming Science Flash, **2018**, Frankfurt am Main (Germany)

Table of Contents

Glossary

AFM	Atomic force microscopy
AGU	Anhydroglucose unit
AIBN	2,2′-Azobis(2-methylpropionitrile)
BP	Benzophenone
BPA	Bisphenol A
BSA	Bovine serum albumin
c	Concentration
CA	Cellulose acetate
CAB	Cellulose acetate butyrate
CAP	Cellulose acetate propionate
CE	Cellulose ester
CMC	Carboxymethylcellulose
CTA	Cellulose tri acetate
CLSM	Confocal fluorescence scanning microscopy
DASA	Donor–acceptor Stenhouse adducts
DCC	*N,N*′-Dicyclohexylcarbodiimide
DEABP	4,4′-Bis(diethylamino)benzophenone
DMAc	Dimethylacetamide
DMAP	4-Dimethylaminopyridine
DMF	Dimethylformamide
DMSO	Dimethyl sulfoxide
DS	Degree of substitution
DSC	Differential scanning calorimetry
EDC	1-Ethyl-3-(3-dimethylaminopropyl)carbodiimide
E_λ	Absorption/extinction
EtOH	Ethanol
EU	European Union
EVOH	Ethylene vinyl alcohol
GAC	Glycidyltrimethylammonium chloride

HEC	Hydroxyethyl cellulose
HPC	Hydroxypropyl cellulose
IPDEA	*N,N*-Diisopropylethylamine
λ	Wavelength
λ_{max}	Wavelength at absorption maximum
LCST	lower critical solution temperature
MC	Merocyanine
MeOH	Methanol
MS	Molar substitution
NC	Nitrocellulose
NHS	*N*-Hydroxysuccinimide
NMR	Nuclear Magnetic Resonance
PE	Polyethylene
PLA	Poly lactic acid
PMT	Photomultiplier tube
PP	4-Pyrollidinopyridine
POS	Point of sale
PVA	Polyvinyl alcohol
QCM	Quartz crystal microbalance
S_0	Electronic ground state
S_{1-X}	Exited singlet state
SEC	Size Exclusion Chromatography
SP	Spiropyran
SPR	Surface plasmon resonance
SVHC	Substance of very high concern
t	Time
T	Temperature
TAPPI	Technical Association of the Pulp and Paper Industry
TBAF	Tetra-n-butylammonium fluoride
TEA	Triethylamine
TEMPO	(2,2,6,6-Tetramethylpiperidin-1-yl)oxyl

TEOS	Tetraethyl orthosilicate
TFAA	Trifluoroacetic anhydride
THF	Tetrahydrofuran
T_g	Glass transition temperature
T_m	Melting point
TMSC	Trimethylsilyl cellulose
TsCl	4-Toluenesulfonyl chloride
UV	Ultraviolet

Danksagung

Hiermit bedanke ich mich zunächst bei allen, die mich in den vergangenen Jahren bei meiner Promotion unterstützt und begleitet haben, auch wenn sie hier nicht explizit genannt sind.

Besonderer Dank gilt meinem Doktorvater *Prof. Dr. Markus Biesalski* für die Möglichkeit, seiner Arbeitsgruppe beizutreten und die Chance, an einem so spannenden Thema zu forschen. Ich bedanke mich speziell für die großen Freiräume, die mir zur Verfügung gestellt wurden und für das mir entgegengebrachte Vertrauen. Die vielen Gespräche und Anregungen, gerne auch mal kritischer Art, haben erheblich zum Gelingen der vorliegenden Arbeit beigetragen. Zudem möchte ich mich dafür bedanken, dass ich an einer Reihe von spannenden und herausfordernden Kooperationsprojekten teilnehmen konnte. Ferner gilt mein Dank *Prof. Dr. Annette Andrieu-Brunsen* und ihrer Arbeitsgruppe für die spannende Zusammenarbeit und tollen Projekte.

Des Weiteren möchte ich mich bei *allen ehemaligen und noch aktiven Mitgliedern des Arbeitskreises* für die schöne Zeit bedanken, sei es für die Unterstützung bei zahlreichen Fragestellungen, die tolle Stimmung oder die unzähligen gemeinsamen Erinnerungen. Es war nie langweilig mit euch und was kann man sich mehr wünschen?

Speziell möchte ich noch *Kornelia Golla*, *Vanessa Schmidt* und *Bärbel Webert* für die kontinuierliche Unterstützung im administrativen Bereich danken. Ferner danke ich *Martina Ewald* sowie *Heike Herbert* für ihre unermüdliche Hilfe bei technischen oder analytischen Fragestellungen.

Ebenso möchte ich mich an dieser Stelle bei meinen Praktikanten und Bachelor-Studenten, *David Seelinger*, *Jenny Cejmer*, *Carsten Biebesheimer*, *Philipp Kukla*, *Anna Boehm*, *Daniel Thomasberger*, *Dominik Richter* und *Benjamin Duttine* bedanken.

Meinen Eltern *Hubertus* und *Renate* und meiner Partnerin *Isabella* spreche ich meinen größten Dank aus, ohne eure unermüdliche Unterstützung und euren Rückhalt wäre diese Arbeit nicht möglich gewesen und ich bin dankbar, euch in meinem Leben zu wissen.

1. Introduction

On the 25th of September 2015 the United Nations General Assembly adopted resolution 70/1, titled “Transforming our world: the 2030 Agenda for Sustainable Development”, also known as “2030 Agenda”. Within this resolution 17 sustainable development goals (SDGs) are formulated with the purpose to guide humanity towards a more equal and sustainable future, as the successor of the Millennium Development Goals. Following the famous statement from former UN Secretary General Ban Ki-Moon “There is no Plan B because there is no planet B.”.[1-2]

Without going into too much detail, these goals are targeting social, political, and industrial development. Regarding the latter, pollution of soil and water (Goals 3, 6, and 14), and development of sustainable products and production chains (Goal 12) are core-aspects of the 2030 Agenda and deeply intertwined with the prospect of a brighter future for mankind.

Fossil carbon sources are a limited supply and will, given the current consumption rate, run out before the end of the 21st century, some estimates going as low as 40 years. Since the polymer and plastics industry relies almost completely on crude oil and gas as raw materials this presents a major challenge. In recent years, production of bio based plastics as sustainable, both biodegradable and non-biodegradable, has increased rapidly with annual growth-rates between 20 and 100 %. As of 2017 they account for around 2.05 Mt (~1%) of the 320 Mt large worlds annual plastic production.[3] Furthermore, plastic pollution of land and water, has been strongly in focus of the public eye, be it classical plastic waste – as for instance in the Great Pacific garbage patch – or be it micro plastics that are detected more and more in soil, water, aquatic life, and humans. Seeing that around one fifth of the global protein consumption is based on fish and seafood, it becomes painfully clear that this large-scale-issues have to be addressed as soon as possible.[4]

Since the 1970s, but especially within the last decade, great efforts have been made to reduce the output of non-biodegradable and unsustainable plastics into the environment. These can be roughly categorized in two groups of approaches, reduction and substitution.

The former aims at the elimination of “unnecessary” plastic waste, by removal (i.e. ban) of one-way products like shopping bags, cutlery, and drinking cups from the market. This, of course, is only effective to a certain degree and relies heavily on wide-range compliance, not only by end-users, but also by a broad spectrum of governments with largely varying interests.

The second general approach is targeting not elimination, but rather the substitution of existing products with biodegradable and sustainable alternatives. This strategy has up until now only been partially successful. On the one hand a range of products from flexible packaging to (semi-) disposable houseware is already on the market, primarily comprised of poly lactic acid (PLA) and starch based polymers. On the other hand, “biodegradable” infers to most customers, that these products can be added to compost at home and will be decomposed in a reasonable amount of time, this unfortunately is not the case with a lot of the materials in use and causes problems on the end-user recycling side.[5]

Unfortunately, no all-encompassing solution for the aforementioned challenges that lie in the future of sustainable production and economy will be presented within this work. Nevertheless, novel approaches to create (highly) functional materials and surface coatings from bio-based polymers, especially cellulose-derivatives, will be presented.

1.1. Polysaccharide based coatings on paper substrates

In this chapter some established applications of polysaccharides (PS) and PS-derivatives as paper and cardboard coatings will be presented, with the aim to provide a scope of the current range of uses. Furthermore, some promising research level application will be discussed.

Looking into paper coatings, especially in the areas of packaging and printing it becomes apparent, that the 100 % bio based source material is typically coated with a wide range of unsustainable, fossil resource based materials. These coatings serve a broad range of purposes, from barrier against gases, water vapor, mineral oil, grease, water, aroma, and electromagnetic radiation, over improvement of printability and thermal printing, to release coatings used in labeling applications. As it stands in most areas there are currently no competitive bio based alternatives that are used on a larger scale, nevertheless there is a range of applications where polysaccharide based coatings have found use and a plethora of lab scale systems in almost all aforementioned areas of interest.

The research into PS based coatings has increased immensely over the last three decades, as can be seen in Figure 1-1 which depicts the "Web of Science" metrics for the search "polysaccharide+coating".[6] Since almost all state-of-the-art barrier materials impede recyclability and biodegradation in a major fashion it comes with no surprise that most of the present polysaccharide coating research is focused on generating the barrier properties lined out earlier in this chapter, with the goal to discover more sustainable alternatives. Due to the size of the body of work published in the last 30 years the reader is pointed towards the review articles by Park, Tharanathan, and Cazón, which cover a broad range of polysaccharide based films with focus on their respective barrier properties.[7-9] Despite this, the work directed towards PS coatings **on paper**, is a subset of this publications. Mayor players in this area are starch, alginate, and more recently chitosan.

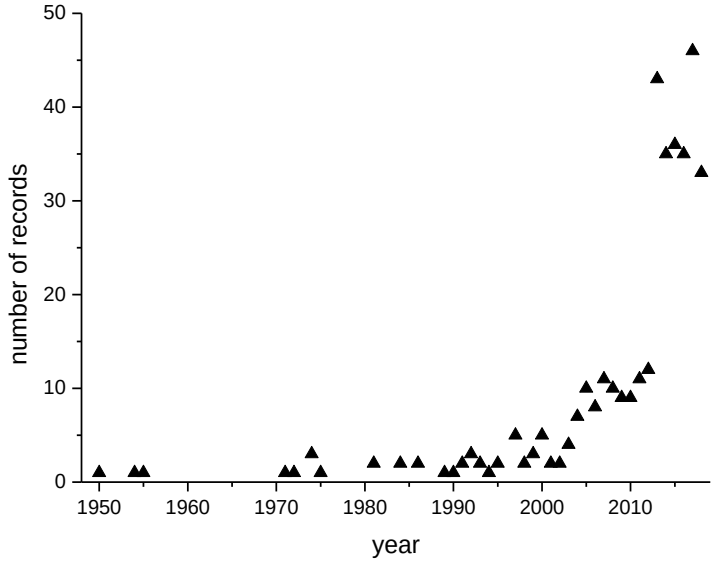

Figure 1-1: Results for the search term "polysaccharide+coating" (including quotation marks) on "Web of Science". The metrics demonstrate in a facile manner how the research interest in polysaccharide coatings has grown rapidly in the last two decades and that is does not appear to slow down in any way.[6]

The most prominent example of a polysaccharide that **is** used on a large scale for coatings in the paper industry is starch: in fact starch is the third most common component (by weight)

used in the paper industry as a whole.[10] Next to surface coatings, including sizing, (cationic) starch is used in waste water treatment to reduce unwanted release of pigments, filler, and fibers, furthermore it is employed in flocculation and as an additive to improve sheet formation and operate as internal sizing agent. The use of cationic starch has been dominating these fields since the efficiency is far greater compared to native starch and the synthesis is carried out via etherification e.g. with glycidyltrimethylammonium chloride, a low cost commodity chemical (Figure 1-2).[11-12] Beyond these applications in the sheet formation process starch is furthermore used as glue, e.g. in corrugated cardboard.[13] In the area of surface application surface sizing is a process with the aim to modulate wetting and penetration behavior, e.g. to increase ink-jet printability. In regards to surface coating, starch is primarily utilized as a co-binder, to increase surface coverage, and smoothness of the coating. Furthermore, the presence of starch in topcoats decreases coating color immobilization times thus leading to a better localization of the color.[14] While starch is fully established in the paper industry, it is not the best starting point for sustainable materials since the origin of starch, mainly corn, is essential to provide food for humans and livestock. Up until now this problem is rather theoretical, but if one would plan to substitute for example the worldwide polyethylene (PE) production with starch based products the ramifications would be all too real.

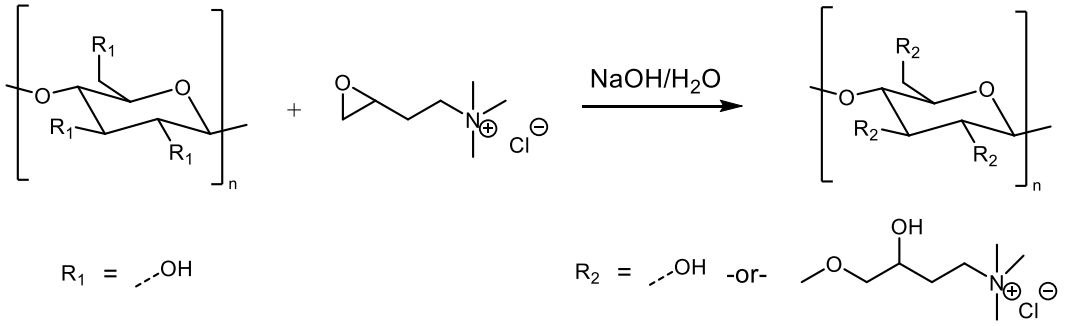

Figure 1-2: Synthesis of cationic starch via the "wet" process. The etherification is carried out in a basic aqueous environment with glycidyltrimethylammonium chloride as example, alternatively the corresponding 3-chloro-2-hydroxy compound can be utilized, so form the epoxide in situ. As further development the "dry" process has gained increasing attention since the 1990s, which utilized only limited amount of moisture to reduce side reactions and facilitate high degrees of substitution.

Interestingly enough, besides all the auxiliary uses of the starch, the performance of starch as primary component in top coatings is typically subpar. This is due to the poor mechanical properties, i.e. cracking, brittleness, etc., which can be achieved. The tensile strength and film formation of starch coatings can be drastically improved by the addition of methyl cellulose, which leads to smooth and (semi)flexible coating with good optical properties. Nevertheless, the very limited barrier against water vapor and negligible barrier against O_2 and water remain unimproved.[15-16] A facile opportunity to improve the intrinsic properties of starch lies in acetylation, which has been employed successfully. Acetylated starch coatings provide roughly a 75% increase in water vapor barrier compared to uncoated paper (0 % r.h. to 33 % r.h.), but as soon as the humidity is increased on both sides of the barrier (62 % r.h. to 90 % r.h.), the barrier benefit breaks down to 15 % due to swelling and disruption of the hydrogen bonds.[17] Similarly acetylated starch coatings show some limited barrier against O_2 and CO_2 permeation, comparable to cellulose acetate, which is breaking down quickly once the coatings begins to swell.[18] This parallel to cellulose acetate is mirrored in the behavior towards liquid water, while some swelling does occur, the coating does not dissolve and does only absorb limited amounts of water.[19]

Properties comparable to starch are displayed by alginate coatings, which are produced from seaweeds in large amounts. They exhibit similar water vapor barrier to starch coatings, perform worse than chitosan in this area, but achieve Kit-test (TAPPI T 559) values over 11 which opens an interesting opportunity as grease barrier.[20] This grease resistance is increased even further through blending with starch or chitosan, which has been explained by synergetic/complementary effects, in the sense that the individual grease resistances are adding up in the polymer blend.[21-22]

Chitosan, which is prepared by de-acetylation of chitin, Figure 1-3, is known as wet end additive in papermaking to increase wet web strength during sheet formation.[23] This effect can be attributed to the cationic nature of chitosan, which also mediates good adhesion to paper when used in coatings. Studies on the barrier properties of chitosan have been numerous and are covering barriers against, water vapor, oxygen, CO_2, and as an antimicrobial surface.[24-26] Chitosan, especially in combination with lactic acid, can provide antimicrobial properties regardless of hydration state, the barrier properties however degrade rapidly with increased moisture content.[27-28] The good oxygen barrier for example breaks down as soon as the polymer is swollen, since the crystalline domains providing the barrier effect are broken down by the ingress of water between the polymer chains. Another factor, which has impeded the broad application of Chitosan is the pricing. While pharmaceutical grade products can cost as much as 1000 $/kg, the technical grade is current sold for around 10-20 $/kg, which is far more expensive, than current petrochemical based polymers for these barrier applications.[29-30] Nevertheless, chitosan is a, if not the, most promising bio polymer for the generation of oxygen barriers, once the price drops, since commercial O_2 barriers like EVOH are moisture sensitive in a similar manner.

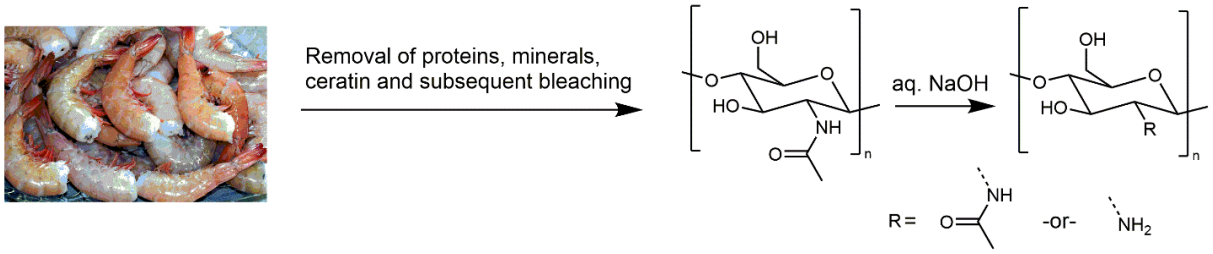

Figure 1-3: Shellfish, in this example shrimp, is the typical starting point the industrial scale synthesis of chitosan. More precisely the waste from the food industry, i.e. the shells, is the material of interest as it contains the desired chitin. After several chemical cleaning steps, typically involving subsequent alkali, acid, solvent, and bleach treatments, the crude chitin is isolated, which can already be used in some applications. To afford chitosan, the chitin is deacetylated with aqueous NaOH in separate reaction, where the degree of deacetylation and molecular weight can be adjusted. (The picture on the left is licensed under CC0, i.e. public domain, free for all uses).[31]

This leaves the group of coatings based on polysaccharide composites, where the research has been focused on composites constituted of a polymeric component and small molecules like waxes, acids, or surfactants, and materials composed from a polymer and inorganic layered silicates (nano clay).

Often, small molecule components are introduced to address the shortcomings of the intrinsic polysaccharide properties. For example, chitosan coatings have been successfully combined with carnauba wax and bees wax to decrease the strong effect of moisture on the oxygen barrier and also increase the resistance against grease.[32-33] In the case of chitosan coatings, this still leaves poor mechanical properties – e.g. low tensile strength – which lead to brittle coatings. One strategy to address this is the addition of plasticizers, like lipids or glycerin.

Unfortunately, the incorporation of plasticizers, by design, disturbs the formation of large crystal domains, which are for the best part responsible for good oxygen barrier, hence it comes as no surprise, that with the use of plasticizers, the oxygen barrier decreases rapidly.[34] Intriguing properties of coatings from the hydroxypropyl methyl- and methyl- cellulose ethers and a mixture of palmitic and stearic acid have been reported by Kester. These highly hygroscopic cellulose ethers together with the fatty acids form a water vapor barrier with permeability just 5-8 times higher than PVC and PE. This behavior is explained by partial phase separation and crystallization of the acids via hydrogen bond formation. Most remarkably these coatings hold their properties even when tested under high humidity (65 % r.h. to 97 % r.h.), making them superficially stand out in comparison to most other polysaccharide based coatings.[7, 35]

The research regarding composites of polysaccharides and layered silicates could easily fill a whole chapter, when looking at biopolymers and nano clay in general even a book. Thus the following will only be a brief overview and the reader is referred to the review articles by Grewal, Pavlidou, and Alateyah as starting point for a more comprehensive and detailed coverage. [36-38] The basic operating principle on nano clay composites relies effectively on diffusion path elongation by the incorporation of mineral particles. The minerals are made up of 1 nm thick clay sheets, that are naturally occurring due to a sandwich-like structure build by two tetrahedric silica sheets and one octahedric sheet of alumina. These sheets exhibit typical lateral sizes between 0.1 and 1 μm, leading to aspect ratios as high as 1000. When a given coating is combined with these nano clays – ideally – a brickwork-like structure is formed, which forces any diffusing compound, like oxygen, water, etc. to follow a highly elongated path, as displayed in Figure 1-4. The path length elongation is proportional to the aspect ratio and volume fraction of the nano clay in the barrier coating. An impressive example for this is presented by Laufer, who prepared a multilayered system from montmorillonite clay, chitosan and carrageenan, which improved the barrier of a PET-film against oxygen by a factor of 30, by applying just 55 nm of coating.[39] Generally the reported improvement factor by incorporation of nano clay is located more in the range of 2 to 10, which is still impressive and explains the large body of work that has been produced in the last two decades. While this in a technology with great possibilities, there are some limitations and challenges during the application of nano clay in polysaccharide coatings. The primary obstacle lies in the need for exfoliation of the clay sheets from larger aggregates, this is the basic prerequisite to generate the elongated diffusion path. To achieve this, the ionic interactions – which are mediated by cations between the clay layers – have to be overcome. There are numerous methods described to achieve exfoliation, involving exchange of the sodium ions with organic cations, ultrasonic treatment and a range of dispersion methods. A second challenge is that the silicates have to align in a roughly layered manner in the polymer matrix, which again can be modulated by addition of surfactants and melt dispersion methods. Lastly most of the produced nano composites exhibit poor tensile strength, which in turn has been addressed with plasticizers, once again impeding the barrier properties.

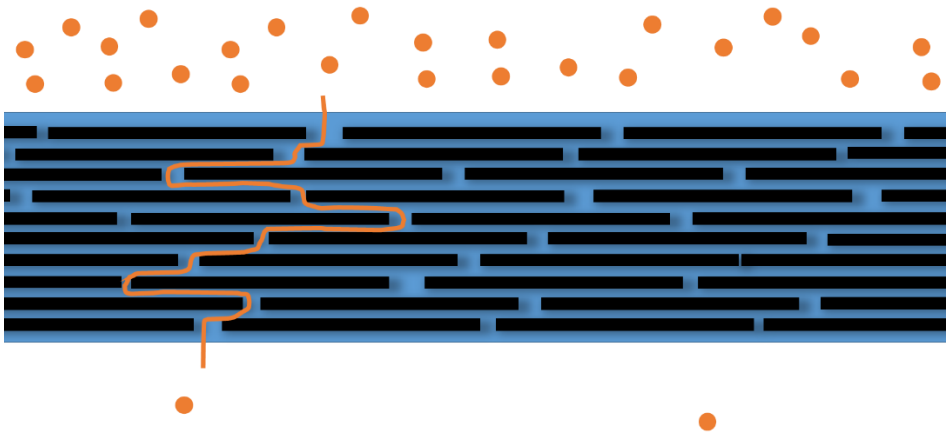

Figure 1-4: A simplified representation of the effect that nano clay (black) has on the diffusion of oxygen (orange) through a polymer film (blue). While the diffusion rate of the gas through the polymer matrix is essentially unchanged, the effective diffusion path can be elongated to yield diffusion characteristics similar to a much thicker polymer layer. Note that this assumes no interaction between the diffusing molecules and the clay, and that this representation is not to scale.

To sum this chapter up, polysaccharides in combination with paper are currently used in a broad range of fields, while industry-wise limited to the use of process additive and sizing agent, the research literature focuses mainly on barrier properties. One topic that is currently rather limited is the investigation into high-performance, or functional coatings derived from polysaccharides.

1.2. Cellulose derivatives and their suitability for surface coatings

One typical use and a big contributor to the unintentional environmental release of polymers are surface coatings. There are in essence two major uses for polymers in these coatings, the first is as secondary component in paint formulations, where they act for example as a binder for particle based systems, modulator for viscosity, charge, water retention, and also as stabilizer to inhibit aggregation. The other large scale use of polymers in coatings is as functional barrier layer or semipermeable membranes. In these applications the polymer itself blocks the passage of specific substances, e.g. gases, water, water vapor, or hydrocarbons. A general overview of cellulose derivatives, grouped by production method and solubility is displayed in Figure 1-5.

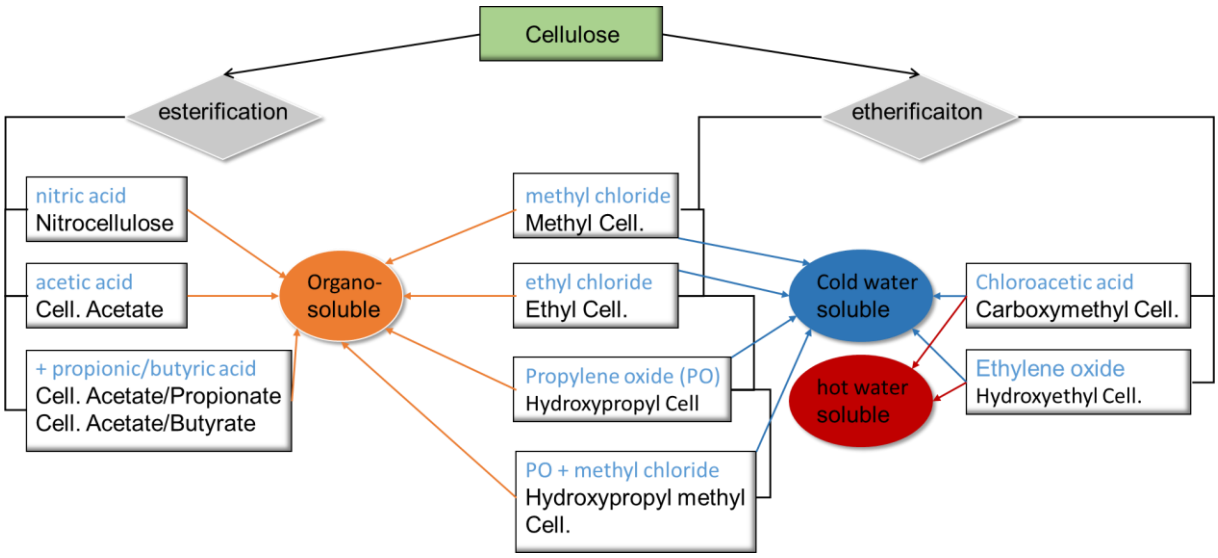

Figure 1-5: Overview about common cellulose derivatives, which are produced on an industrial scale. The derivatives are divided by method of production (esterification/etherification) and grouped by solubility. While this overview demonstrates the broad range of cellulose based materials, that are already in use, it is by no means complete and should not be regarded as such.[40]

Since more than 70 years, cellulose esters (CEs) play an important role as sustainable materials, used in a wide range of industries and markets, from coating additive to filtration membrane.[41] Note: to describe cellulose derivatives, the degree of substitution (DS) is the parameter of choice as it provides the number of substituted hydroxyl groups per anhydroglucose unit (AGU, Figure 1-6), which is a value between 0 (no modification) to 3 (complete substitution).

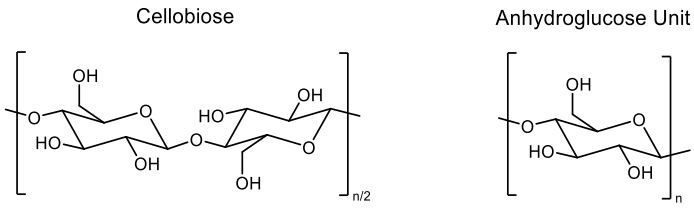

Figure 1-6: The formal repeating unit of cellulose is cellobiose, which consist of two β1→4 linked D-glucose subunits which are rotated 180° to one another. Rather than using this formally correct cellobiose, it is established practice to refer molecular properties like degree of polymerization (DP, denoted "n" in the figure above) and the degree of substitution to the anhydroglucose unit (AGU).

The CEs used, and in fact the only ones that are produced on a large industrial scale at this point in time are nitrocellulose (NC) and cellulose esters with acetic, propionic, and butyric acid (CA, CAP, CAB). All industrial processes to produce cellulose esters are initially heterogeneous, leading to challenges further discussed in chapter 1.2. The procedures to produce these inorganic and organic esters of cellulose are somewhat similar. To synthesize nitrocellulose (NC), cellulose (typically from cotton) is placed in a mixture of nitric and sulfuric acid. These acid mixture generates nitronium ions, which are highly reactive and capable of reaction with the rather unreactive cellulose alcohol groups.[42] Comparatively, the general procedure for the preparation of organic CEs utilizes the so called acetic acid/anhydride process. In this approach, cellulose is suspended in a mixture of acetic acid, the desired acid anhydride, i.e. acetic acid, propionic acid, and/or butyric acid anhydride, and a catalytic amount of sulfuric acid. It is theorized, that the sulfuric acid forms a mixed anhydride with the present acyl compound, which generates highly reactive acyl cations – similar to the nitronium ions in the nitrocellulose process – that are susceptible to nucleophilic attack by the alcohol moieties of the cellulose to form the desired product. In the case of the cellulose acetate synthesis, the reaction is also carried out in dichloromethane to reduce the amount of catalyst needed and improve reaction control.[43]

Applications for nitrocellulose range from the use as main propellant in smokeless gunpowder, over lacquers which are used in surface coatings due to their exceptional film forming properties, and finally in celluloid, which is despite its high inflammability still in use in some niche markets, for example in ping-pong balls.[44] In addition NC has found widespread use in life science applications – e.g. northern- and western blots, and lateral flow assays – due to the high affinity to bind proteins nonspecifically.

Cellulose ester with organic acids are utilized in an even wider area of applications. Within the organic CEs, cellulose acetate (CA) is dominating commercially. The market size, based on one source, was between 4.82 and 8.76 billion $ in 2017 with an expected annual growth rate between 3.6 and 6 % until 2023. While over 80 % of the global production volume of CA are utilized in cigarette filters, CA finds also use as fibers in the textile industry, as extruded foil for labeling and tapes and in extrusion molding, to create everyday items like shirt buttons or hair combs. Whereas CA is used in dominantly as structural material in applications where mechanical toughness is required, CAP and CAB are primarily used in coating formulations and printing inks, e.g. as binder, viscosity modulator, film forming agent, pigment orientation aid, curing additive, and to control color.[41, 45-48]

Regarding esters of cellulose with aliphatic acids larger than butyric acid, commonly referred to as long chain or fatty acid cellulose esters, the application has been limited to research level in the past. The main reason for this is the trend of reactivity, which greatly diminishes with increasing acid hydrocarbon chain length from acetic acid to butyric acid anhydride in the aforementioned industrial process.[49-51]

To produce long chain cellulose esters a wide range of techniques have been investigated on the laboratory and even pilot scale, but an industrial scale production is not yet established. The following passage is intended to give a brief overview over some of these approaches but is not a comprehensive review, since this topic alone is worth its own book. Fortunately, this has been covered by Heinze, Liebert, and Koschella, in “Esterification of Polysaccharides” to which the reader is referred for further study.[43]

Since the limited reactivity of longer chain acid anhydrides towards cellulose is getting to low to produce substantial degrees of substitution, alternative routes of esterification have to be applied. Looking at the reactivity of acyl compounds in esterifications, the reactivity increases with decreased mesomeric stabilization of the C=O double bond and thus a higher affinity of the leaving group to get cleaved of during the nucleophilic attack by the alcohol.[52] This is already exploited in the acetic acid/anhydride process by the *in-situ* activation of the acid anhydride with sulfuric acid via formation of the mixed anhydride of sulfuric and acetic acid. This process does, however, not provide suitable activation for longer chain acids, which lead to the study of alternative ways of (*in situ*) activation (Figure 1-7).

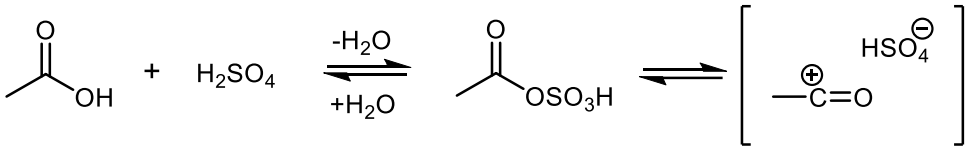

Figure 1-7: Proposed reaction scheme for the formation of highly reactive acetyl sulfuric acid. The carbocation is an exceptional electrophile, and thus highly susceptible towards a nucleophilic attack, since the leaving group (see Figure 3-1), formally HSO_4^-, is already dissociated.[43]

One large group of methods is using an “impeller” approach. The sulfuric acid catalyst used in the classic anhydride process is herein substituted by a range of more efficient catalysts, such as *N*-bromosuccinimide or the anhydrides of chloroacetic and trifluoroacetic acid. These compounds form highly reactive intermediates with the long chain acids and provide excellent leaving groups for succeeding reaction with the cellulose. After this reaction the “impeller”-compound is regenerated and will act as catalyst over and over in the same manner, therefore the name “impeller”.[53-56]

The second group of approaches involves the use of bases, either catalytic or as scavenger. This is an important pathway, since the aforementioned acidic approach is always accompanied by degradation of the cellulose. While in an industrial setting, this is rather convenient side-effect to adjust chain-length and thus the viscosity of the product, it inherently adds a second, non-independent variable. A system utilizing basic catalysis – or basic reaction conditions in general – can, while not eliminate, greatly decrease this side reaction, depending on the base used. Typical bases for this purpose are pyridine and trimethylamine, sometimes in combination with *N,N*'-Dicyclohexylcarbodiimide (DCC) and 4-dimethylaminopyridine (DMAP) or 4-pyrollidinopyridine (PP) following the Steglich esterification route [57-58] Furthermore, instead of acid anhydrides, acid chlorides can also be used in combination with pyridine as catalyst/scavenger and solvent at once in a Schotten-Baumann-type reaction to form fatty acid cellulose esters. While this method yields high degrees of substitution even with stearic acid in short (<1 h) reaction times, the price of this is payed during a multistep workup, involving several extraction steps with a number of organic solvents. Of course, the use of rather large amounts of the toxic pyridine and the problematic workup impede large scale production in this way.[59-61]

The third and last group utilizes transesterification to produce long chain acids of cellulose. First work in this area dates back to 1921, where Wittka and Grün used ethyl stearate and ethyl laureate to produce the respective cellulose esters. The reaction conditions reported were rather violent – 5-6h at 270 °C under H_2-atmosphere – nevertheless they achieved, at least with ethyl stearate, high degrees of substitution, but were struggling with different esters and polymer degradation.[62] The general idea has been revisited several times in the last

century and underwent stepwise improvement. For starters, the addition of alkaline compounds (sodium- or potassium hydroxide) yielded better results under much milder reaction conditions, furthermore the introduction of microwave assisted synthesis and combination with an impeller yielded better reaction control.[56, 63] The, as of yet, last iteration step was the introduction of vinyl esters, which was most interestingly disclosed already in 1969, but has only recently garnered a broad scientific interest. This method relies on the isomerization of the leaving group after the reaction. Vinyl alcohol isomerizes to the thermodynamic stable tautomer acetaldehyde. This inhibits the reverse reaction and thus increases the conversion rate and makes it possible to achieve good esterification even with mild bases such as K_2CO_3.[64-66]

Most of the aforementioned methods for cellulose esterification have been employed in heterogeneous and homogeneous conversions, respectively. To illustrate the differences and respective challenges, the acetylation of cellulose will be used as example. During the heterogeneous process, cellulose is, typically after alkaline activation, suspended in the reaction mixture and the reaction is starting. In the beginning, the suspended cellulose is esterified from the surface to the inner part of the material starting with the alcohol functions on the material's surface that are exposed to the reactants. In the course of this conversion the substitution patterns on the cellulose chains are not random, since parts of the polymer that are partially esterified become more soluble, thus more reactive, and are therefore preferably acetylated.[67] Because of this, if the acetylation would be stopped once an overall DS of 2.5 (typical for industrial grade CA) is reached, one would be left with the product as a mixture of random substitution patterns and with poorly defined properties. To circumvent this, the acetylation is run until a DS of 3 is achieved, during which the reaction becomes homogeneous. This cellulose tri acetate (CTA) is also commonly referred to as *primary acetate* since it is the result of the first reaction step. While this product is well defined in regards to the substitution pattern, the *primary acetate* exhibits poor solubility, limited thermoplasticity, and often insufficient mechanical properties (brittleness). Therefore this intermediate product is partly hydrolyzed in a consecutive step to yield the widely used *secondary acetate* with a degree of substitution of approximately 2.5.[68-69] This illustrates both, the strengths and weaknesses of an (initially) heterogenic process. On the one hand, without much, if any, complicated preparation a completely esterified cellulose derivative can be synthesized and DP can be adjusted via process parameters. On the other hand, this step has to be run to completion to yield a defined product, and a second reaction is necessary. In fact this is done to somewhat extreme levels, where the readily water soluble CA with a DS of 0.6-0.9 is produced via hydrolysis of *primary acetate* (DS 3). This poor atomic efficiency and the necessity for longer chain acid esters to use rather aggressive chemistry (like the Schotten-Baumann-synthesis), represent serious challenges in research and application of more sophisticated cellulose derivatives.

These challenges have been addressed through various solvent systems for cellulose, which can be classified as depicted in Figure 1-8. Dissolution of the cellulose enables quantitative and tailored conversion, trough good control of the distribution of the substituents and degree of substitution.[70] Although considerable work has been done using these solvent systems, each of them comes with specific limitations. Specifically, the majority rely on solvents with high boiling points (e.g., DMAc/LiCl, DMF/N_2O_2, and DMSO/TBAF), which can pose a challenge in workup, whereas others are water based (e.g. cuprammonium hydroxide (Cuam)

and cupriethylenediamine hydroxide (Cuen)) or contain ammonia and thus limit the available chemistry considerably.[71-75]

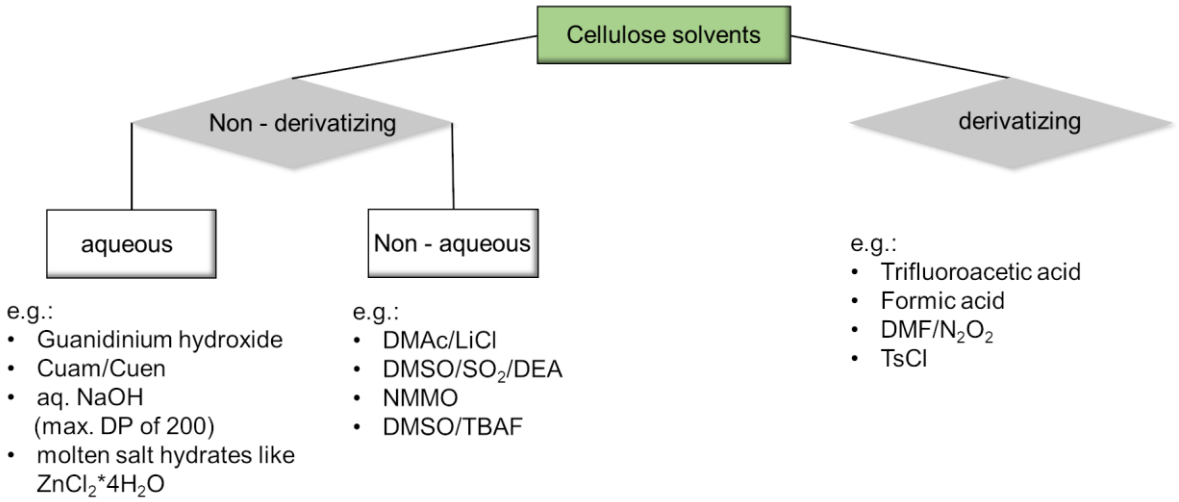

Figure 1-8: Classification of cellulose solvent systems based on the solvent method (i.e. with or without covalent modification of the cellulose) and the presence of water. The systems listed are the most prominent examples, nevertheless a plethora of different variations, with i.e. different salts, counter ions, etc. is reported.[71]

1.3. Hydroxypropyl Cellulose

Given the various cellulose derivatives with different properties that are readily available and produced on an industrial scale, it becomes an obvious choice to use one of them as a bio based building block for further functionalization while avoiding the drawbacks of either of the aforementioned strategies. This approach opens up the possibility of using accessible cellulose derivatives with high intrinsic solubility in common organic solvents, like the examples provided in Figure 1-5. When screening the available cellulose esters, ethers, and combinations thereof, with further functionalization in mind, some benchmarks have to be established. The most relevant parameters are: solubility in common organic solvents, remaining reactive functions, production volume, and price. Based on this, partially esterified celluloses present two distinct challenges. First of all, the reactive domains are partially occupied by the ester groups that are essential for the solubility, furthermore the solubility of short chain CE´s changes drastically with the degree of substitution. For low DS values (<1) they are soluble in water, while they become soluble in 2-methoxy-ethanol, acetone, and finally in chloroform and dichloromethane with increasing DS. Note, that each of these solubilities is mutually exclusive, which infers that during homogeneous modification one will most certainly run into solubility issues.[43, 76] Because of this commercial CEs have been disregarded as starting points for further conversion in this work.

A good alternative to CEs can be found in cellulose ethers, which are similar to CEs in regards to production volume and marked size (6.41 bn $ in 2017) and therefore comparatively available, while exhibiting promising intrinsic solution properties.[77] During the evaluation of cellulose ethers, we have to visit three groups: alkyl-, hydroxyalkyl-, and carboxymethyl celluloses. The well-established carboxymethylcellulose (CMC), which is used widely in food and drug preparation, is completely insoluble in organic solvents, although some literature points towards water-based modification, the available chemistry would be too limited and thus CMC was discarded in the selection process.[78] There are three notable cellulose alkyl-ethers, namely methyl, ethyl, and ethyl methyl cellulose. Methyl cellulose is soluble in organic

solvents at high degrees of substitution (exceeding DS 2) and at lower DS only cold water can dissolve this polymer, since it exhibits a lower critical solution temperature (LCST). Comparatively, ethyl and ethyl methyl cellulose are also – depending on the respective DS – soluble in common organic solvents like acetone, alcohols, toluene, and THF. While this appears promising, the required ethyl content is also quiet high (about 46 %), which corresponds to a DS of 2.44.[79] This is leaving at best half a reactive function per AGU for further modification, on average. Finally, hydroxyalkyl ethers, i.e. hydroxyethyl and hydroxypropyl cellulose remain for consideration. Both of these retain all three reactive moieties per AGU since every etherification of an alcohol with an epoxide in turn generates a new alcohol function. Nevertheless, hydroxyethyl cellulose is only soluble in a limited amount of solvents (e.g. DMF, DMAc, and DMSO) which would in turn limit the amount of possible modifications.[80] Consequently, hydroxypropyl cellulose (HPC) remains as building block.

HPC exhibits good solubility in a wide range of polar organic solvents (e.g. THF, Chloroform, Acetone, Pyridine, MeOH, EtOH, DMF, DMSO, ethyl acetate) and still provides three alcohol functionalities per anhydroglucose unit. Furthermore, it is readily available because of its widespread industrial use in concrete and food manufacturing.[81] The combination of these two aspects makes HPC, within the scope of this work, a very promising bio-based starting point for the synthesis of functional polymers.

HPC is synthesized from cellulose, which is treated with sodium hydroxide solution (optionally in the presence of a dispersant like hexane or toluene) to form the more reactive alkali cellulose, this aqueous dispersion then undergoes etherification with propylene oxide. During workup, the crude product is washed with hot water, this treatment utilizes the LCST of HPC and provides a facile method to remove undesired impurities(Figure 1-9).[82] Since it is possible for propylene oxide to react with already formed hydroxypropyl groups on the cellulose chain, the degree of substitution is insufficient to describe the actual degree of modification. Because of this predicament, the molar substitution (MS) ratio, i.e. the number of propylene oxide groups added per AGU during reaction, was introduced as facile measure. While the cellulose involved in the HPC synthesis is, of course, renewable by nature, the propylene oxide (PO) asks for further investigation. PO is synthesized from propylene, via different processes. The oldest route is involving two steps, first propylene is converted to the corresponding chlorohydrin and in a second step dehydrochlorinated PO is produced. Due to a range of (unwanted) side reactions, direct oxidation of propylene, the second approach, has risen massively in importance during the last decades. One of the two dominant propylene oxidation methods without byproducts is the cumene hydroperoxide process, where the oxidizing agent can be regenerated and reused. The “even greener” hydrogen peroxide propylene oxide process uses solely H_2O_2 as oxidizing agent, which is mediated via transition-metal-catalysis, with the only “byproduct” being water. This route leads to the next step up, the sustainability of propylene production.[83] As of today propylene – at least on an industrial scale – currently only produced from fossil resources, nevertheless a range of promising photocatalytic and enzymatic processes to synthesize propylene from biomass have been reported in recent years.[84-87] These processes are currently not pursued on an industrial scale, simply since they are too expensive in contrast to the, at least at the moment, still comparatively cheap fossil resource based processes.

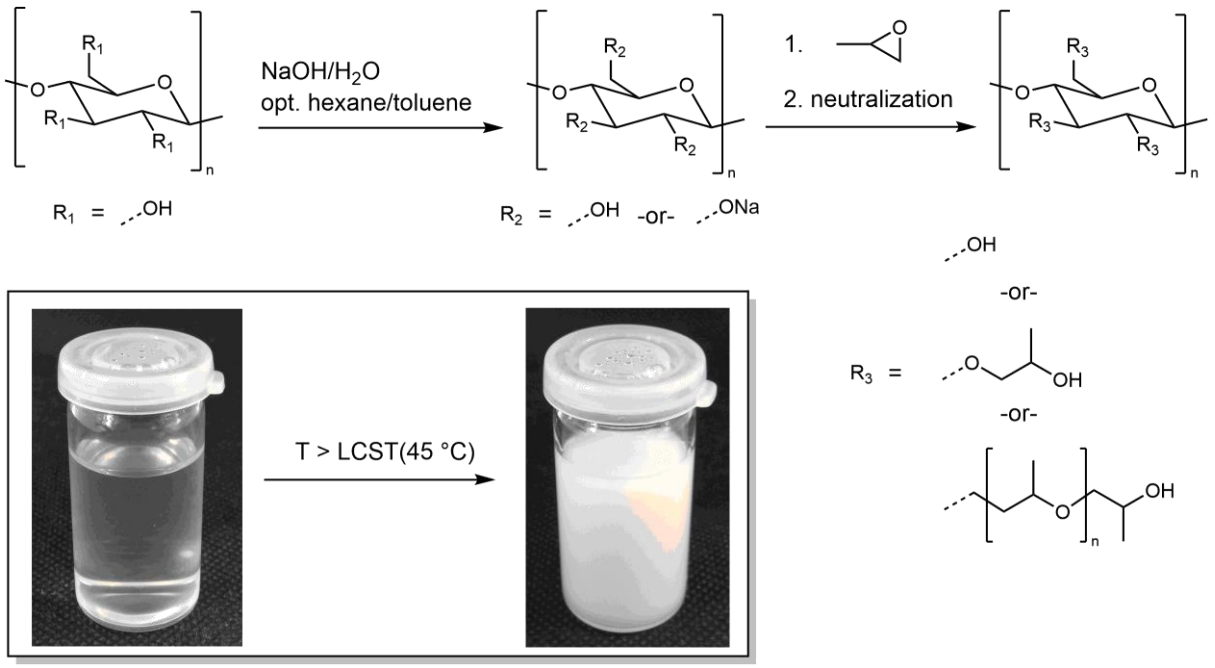

Figure 1-9: Synthesis of HPC, starting from cellulose. The cellulose is converted to alkali cellulose using NaOH and subsequently etherified with propylene oxide to yield the crude product. The phase transition induced by exceeding the LCST, which is exploited during workup is illustrated on the lower left in a model demonstration.

HPC and some of its esters have already been investigated in a range of different fields in the past, with a focus on their mesophasic behavior and thermal properties. The research into the mesophasic properties of HPC derivatives, for instance the studies performed by Steinmeier, Tu, Ishizaki, Hou, Tseng, Huang, Fangmin or Yamagshi, was and is driven primarily by the desire to understand and control the liquid-crystalline phases which are present in HPC esters with short-chain acyl groups (up to the heptanoic acid derivative).[88-96] The researchers used a range of protocols utilizing the given acid chloride without further additive, either in pyridine, acetone, THF/pyridine, or without solvent (effectively leading to heterogeneous conditions). Another system, used by Khan, to yield amino-acid esters of HPC involved standard EDC-coupling, known from peptide synthesis protocols.[95] The choices, at least based on the published data, appear arbitrary without concern for reaction kinetics, possible chain degradation or even inhomogeneous substitution patterns. This is not meant to criticize the approaches taken, all studies mentioned provided interesting insights into the mesophasic properties of HPC derivatives, they simply employed one protocol that worked and produced the desired material.

Nevertheless, this points towards a general lack in research of the fundamental understanding of HPC esterification, core questions in the topic, like optimal solvent, optimal catalyst, reactivity of different acids, and kinetics have not been addressed systematically in the research literature. Regarding long chain fatty acid HPC esters, the body of work in the scientific literature is rather small, the organic synthetic routes utilized pyridine as solvent, DMAc as catalyst and tosyl chloride for *in situ* activation.[97-98] Chen et al. used a mixture of stearic and palmitic acid with an excess of 9 equivalents per AGU and achieved full esterification (determined via mass gain) after 50 hours of reaction time, but gave no indication of respective degrees of substitution. Their primary research target was the investigation of these HPC esters as thermal storage material, and again not the actual chemistry to produce the material. At the time of this writing the only other research covering

HPC fatty acid esters is using an enzyme-mediated approach to achieve esterification of HPC with lauric acid, which yielded ester contents of 14- 15 %, since no MS for the used HPC is given, an assumed best case (i.e. lowest water soluble MS) gives a corresponding DS of roughly 0.8 after 184 h (8 days). The lauric acid equivalents were not precisely determined (since the MS was unknown) but fall in the range between 8 and 20 equiv. and there was no correlation found between lauric acid equiv. and achieved DS.[99]

Furthermore, there appear to be no follow up-studies conducted on either of the presented investigations and there is currently no work utilizing HPC fatty acid derivatives in coatings of any kind in the literature pointing towards an untapped field of high potential research.

1.4. Stimulus responsive coatings (on paper)

Due to the broad nature of the field, only a small portion of stimulus responsive materials will be covered in this chapter. The main focus is aimed towards photo and temperature responsive materials, which change in optical properties and wetting behavior, respectively.

Photo responsive materials contain domains, which absorb electromagnetic radiation, often in or near the visible spectrum, and in turn undergo a distinct alteration of their chemical and/or physical properties. Due to the ability to trigger reactions, the release of drugs or chemicals, or molecular conformation, especially in polymers, they received widespread attention in recent years.[100-104] A typical reaction to cause drug release or alter solubility-properties is the photocleavage of aryl-groups like pyrenyl-, coumarinyl-, or nitrobenzyl esters.[105-107] The irradiation of pyrenly- and nitrobenzyl-esters promote the hydrolysis of the esters, while nitrobenzyl-esters undergo a intramolecular rearrangement. This kind of reaction is especially useful since it works without the presence of additional reactants. Another family of photo responsive that can be "activated" in the absence of specific additional reactants contains photo isomerizable groups. These moieties undergo isomerization once irradiated, typical representatives which undergo E/Z isomerization, include azobenzene, stilbenes, and – more recently – hemithioindigo (Figure 1-10 a, b, and c).[108-109] This switched state is, in contrast to the photo-cleavage described before, reversible via irradiation at higher wavelength and/or via thermal back switching into the thermodynamically stable initial state. Furthermore, and this holds true for most photo responsive chemicals, the wavelength of light needed for activation can be tuned via chemical modification of the active domains, i.e. by altering the size of the conjugated electron system and electron densities.[110]

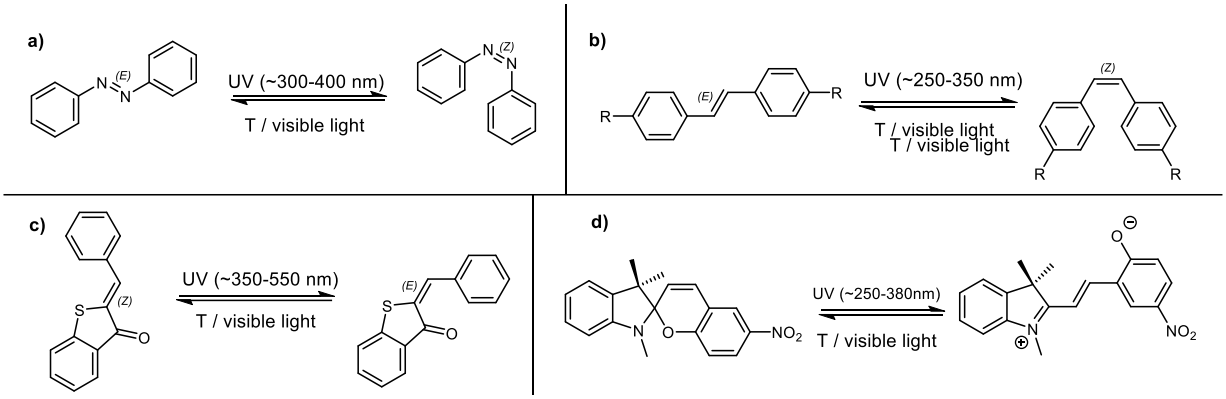

Figure 1-10: a) azobenzene, b) stilbene, and c) hemithioindigo undergo reversible E/Z-isomerization when illuminated with mid- to long wavelength UV-light and can be switched back thermally or by the absorbtion of higher wavelength, visible light. d) spiropyran undergoes a more complex mechanism, involving cleavage and formation of covalent bonds, and the transition from an uncharged to a charged species.

There are also species that undergo different isomerization processes, for example the well-studied spiropyran (SP-form), which isomerizes into merocyanine (MC-form), displayed in Figure 1-10.[111] The photochemical conversion of SP-form to MC-form starts by of the C-O bond at the spiro-carbon, followed by a change in conformation from the twisted spiro-conformation to a thermodynamically more stable planar conformation.[112-113] This leaves the pH-dependently charged, deep violet colored MC-form, which can be switched back by visible light or via increased temperatures. Spiropyran containing polymers have been reported by Li et al. as a facile UV-sensor, that was able to resolve UV doses between 0 and 2000 J/cm² through the photochromatic reaction.[114] A more recently discovered photo responsive

compound, or rather a group of compounds, are donor acceptor Stenhouse adducts (DASAs), which were introduced by Helmy et al.[115] In 1832, Döbereiner synthesized furfural as side product during efforts to produce formic acid. This research was picked up three decades later, when namesake John Stenhouse started to investigate the as of yet unknown properties of furfural. The work was initially focused on the production of furfural, which found that it could be produced by steam distillation of a mixture of sulfuric acid in most plant matter. Further investigation lead to the formation of a deep purple substance when “furfurol” was treated with aniline and hydrochloric acid.[116-117] Subsequently, a range of similar compounds, called Stenhouse salts, was produced in the followings decades by the use of different secondary and primary amines.[118-119] During this period it was speculated, that furfural would undergo a ring opening reaction, which was supported by an analysis of thermal decomposition products of the Stenhouse salts in 1942.[120] It was only in 1977 when Lewis was finally able to prove the constitution of the product via NMR analysis, which led to investigations into the switching of Stenhouse salts. It was discovered that the back-switching was faster at elevated temperatures and the conformational change was proven by Lewis in 1985.[121-122] At this point in time the synthesis was quiet rigid and inflexible, subsequently the research interest on the topic was underwhelming, since the “interesting” questions seemed to be answered. This – kind of – changed when Safar introduced a new approach to produce compounds similar to Stenhouse salts through the reaction of furfural and Meldrum’s-acid, which activates the furan ring towards nucleophilic attack by withdrawing electrons from the heterocycle.[123] The corresponding compounds to this developments are displayed in Figure 1-11.

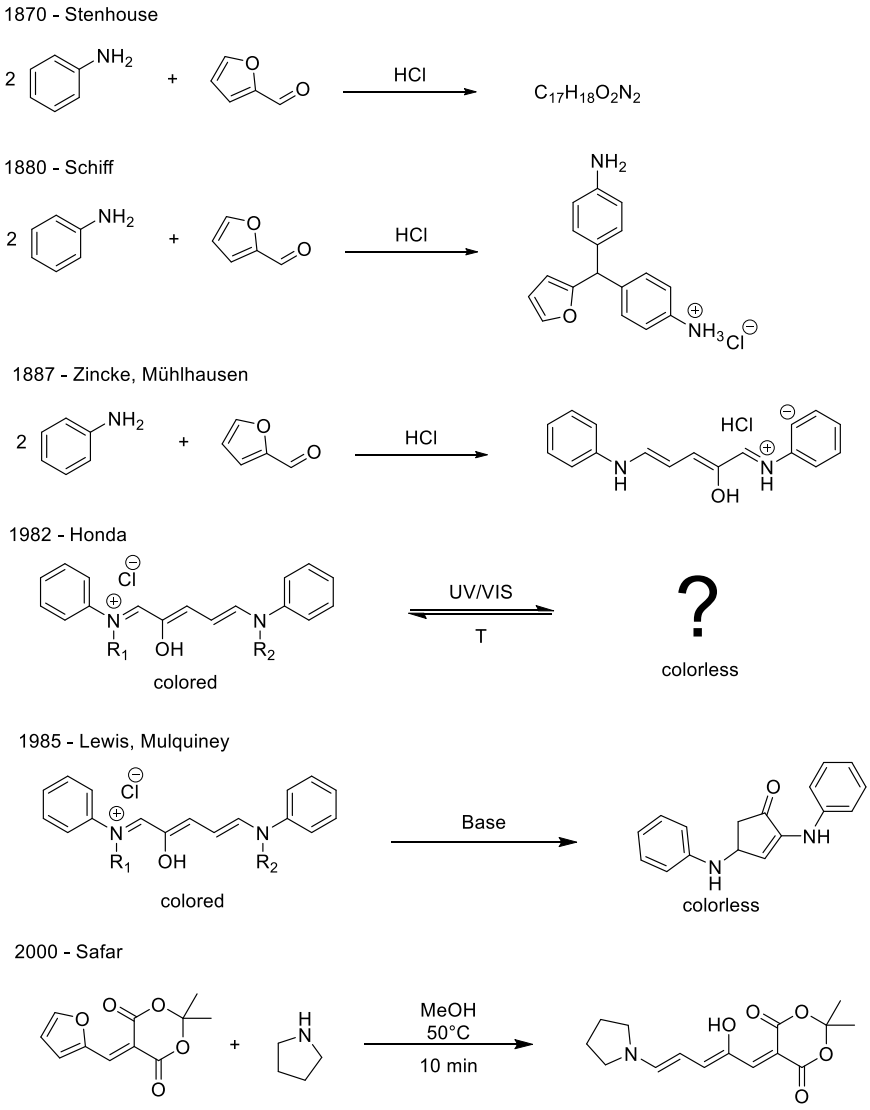

Figure 1-11: Research milestones that subsequently lead to the discovery of DASAs and laid the foundation for the current rise of research interest into the subject.

The work of Safar opened up the range of usable amines which was exploited by Helmy, who coined the term donor acceptor Stenhouse adduct and demonstrated the versatility of the system in 2014, displayed in Figure 1-12.[124] This article (currently cited over 120 times) kick-started recent research with over 70 publications on DASAs in the last three years alone. In addition to the Meldrum's-acid furfural derivative they introduced barbituric acid furfural derivate, that in turn opened up the N-R groups of the barbituric acid moieties as variable section, which further increased the possible modifications. Using these tools, it was possible to implement different aromatic amines, which enabled researchers to adjust the absorption maximum of DASAs between 580 and 670 nm.[125] These second generation DASAs are also less susceptible to thermal degradation, which gives the opportunity to switch them back faster at higher temperatures. The switching process of DASAs is, similarly to spiropyranes, strongly dependent of the chemical surroundings, in polar protic solvents – e.g. methanol – the DASA can be switch from the open (colored) form to the cyclic form, but since the cyclic form is highly polar, it becomes stabilized trough hydrogen bonds to solvent molecules, the opposite behavior can be observed in non-polar solvents like toluene.[115, 126] The mechanism of DASA photo switching has been studied in detail, the irradiation promotes an Z/E isomerization in the unsaturated chain of the DASA, effectively leading to the formation of a

4 π electron system, similar to the intermediate state found in Piancatelli rearrangements, which can undergo a thermal cyclization.[127] DASAs further have been investigated as a way to change surface polarity, wetting behavior, drug delivery aid, and even as sensor for chemical weapons.[128-131] This illustrates the versatility of these materials, that are – at their core – build on the ubiquitous and sustainably sourced furfural.

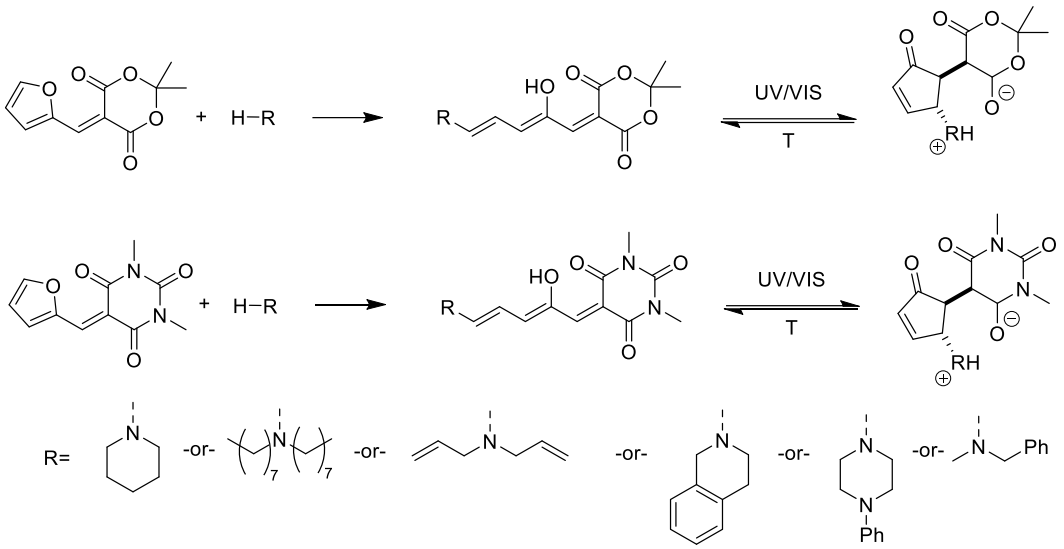

Figure 1-12: Initial demonstration of the flexibility of donor acceptor Stenhouse adducts by Helmy in 2014. The range of amines used has currently been expanded to several dozen different materials, including phenyl-amines compounds which allow tuning of the absorption wavelength.[115]

The industrial application of stimulus responsive materials is limited to a few applications, but where they are used, the application depends critically on their properties. One example of these applications are moisture sensors, for instance in electronics, that indicate water ingress which is important in the case of warranty claims. Another big group of paper based coatings are thermally reactive coatings, that change their optical properties when exposed to heat and thus facilitate inkless printing. These materials are employed on a global scale in thermal printing systems, which range from point of sale (POS), i.e. cash registers at stores, over labeling up to graphical applications. Conventional thermal paper coatings contain a leuco-dye, typically a triarylmethane with varying substituents at the aryl moieties, and either an alcohol, ether, amine, or lactone function (-X) present at the central methyl group.[132] The coating contains also a phase-separated acid – typically a phenol – which is initially present in the form of small crystallites.[133] As both components are initially separated no reaction is taking place, during thermal activation the phenol is molten and mixes with the leuco-dye.[134] Subsequently, the phenol protonates one of the aryl substituents and promotes the cleavage of the methane-X bond that leaves the central carbon atom as carbonium ion, as displayed in Figure 1-13 a. This carbonium ion is thus stabilized through the aryl groups which leads to change in absorption, thus generating the impression of color when illuminated.[132]

Along with these essential compounds, sensitizers are added to promote the mixing process of the molten phases as well as stabilizers to retain the color over longer periods. In recent years, bisphenol A (BPA), which was dominantly used as phenolic component in these coatings, has attracted a lot of negative attention and was classified as substance of very high concern (SVHC) due to its effect as endocrine disruptor.[135] As of today, it is unclear to what extent BPA has other adverse effects on the human body, nevertheless due to the indications, that BPA might exhibit a risk to human health, the EFSA has started re-evaluation the compound

and consumers have become aware of possible concerns.[136] Consequently BPA will be effectively banned for paper-based products that are sold in the EU after the 2nd January 2020.[137] Therefore, the paper industry has been putting a lot of effort into the development of alternative methods to create thermal papers. One approach is simply a substitution of BPA with another, less potentially harmful, phenolic compound like bisphenol S. While this approach is addressing the issue, there are still reactive chemicals, with potentially harmful properties in the coatings, which are handled by millions of people on a daily basis. Another approach, that eliminated the need for reactive leuco-dye/developer systems was presented and commercialized by the Papierfabrik August Koehler SE under the name Blue4est™. These coatings do not generate color, instead an initially highly opaque coating is applied to a colored base paper. Since the opacity is achieved by air-filled micro/nano thermoplastic capsules made from thermoplastic polymers like poly styrene, once heated, the capsules collapse which destroys diffraction centers and in turn makes the base paper locally visible, both methods are illustrated in Figure 1-13 b.[138] Due to the purely physical process, there is no need for stabilization or sensitization, and no reactive chemicals come into contact with the consumer. This goes to show, that sometimes it is necessary to walk on drastically new paths to address challenges at their core. Nevertheless, currently those systems still rely on polymers produced from fossil resources, leaving them essentially only marginally more sustainable than their reaction based counterpart.

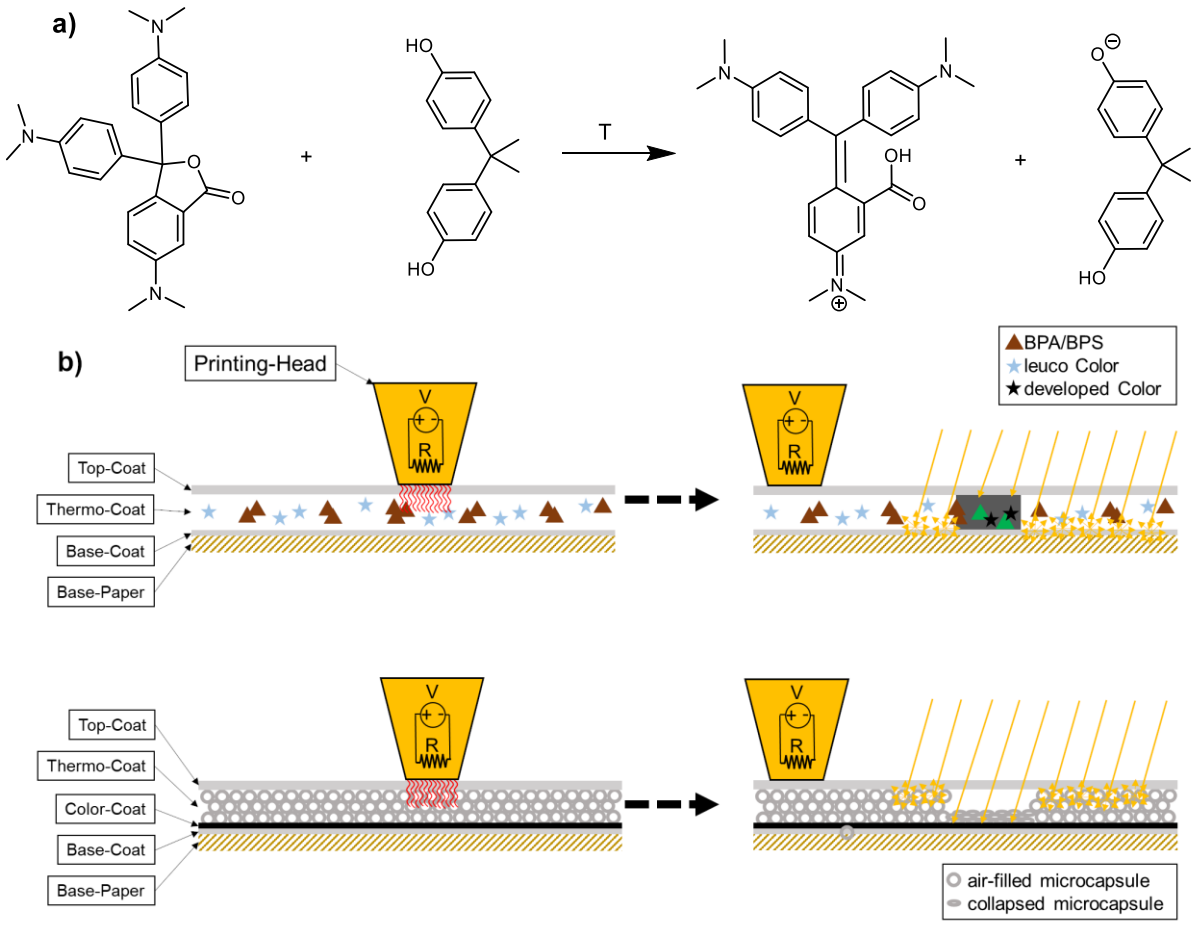

Figure 1-13: a) Example of a thermally induced halochromic reaction (Crystal violet lactone – a typical leuco-dye – with BPA) that is started trough melting and subsequent mixing of the components and forms the resonance stabilized, charged and colored species. b) Comparison of the conventional, reaction based, thermal paper (top) and more recent, scattering based systems, that work on the thermal destruction of scattering interfaces via the collapse of air-filled capsules.

With all those challenges presented in this chapter we were, at the beginning of this work, interested in one question. What if we, instead of chasings a “greener” solution to address an existing challenge, investigate the possible scope of a fixed starting material, and then look for problems to solve. This inverted approach aims at generating a fundamental understanding of structure property relationships, scope of accessible modifications and potential reveal of completely unexpected properties of the material of interest, which in this case was hydroxypropyl cellulose.

2. Goals and Strategy

2.1. Goals

The goal of this thesis is to investigate the utility of hydroxypropyl cellulose as building block and sustainable starting material to generate functional polymers and surface coatings thereof. Consequently, the work aims to address the following fundamental questions:

- How is it possible to produce esters of HPC with long chain carboxylic acids? How do solvent, reaction additive and acid chain length effect the reaction and what are optimal conditions, with respect to reproducibility and control of the DS?

- How do these reaction systems compare to other well investigated polysaccharide fatty acid esterifications? Is it possible to analyze the DS of HPC fatty acid esters via fast and inexpensive methods and still obtain reliable results?

- How are the structure-property relations effected by the derivatization, will new thermal phase transitions be generated? How do different degrees of substitution influence these properties?

- Can one form small particles from HPC ester and is it possible to generate nano structured surface coatings from HPC-derivatives? Is there a change in wetting behavior and can this in fact be controlled?

- Can functional moieties, such as photo cross linkable groups, unsaturated side-chain, or photo responsive compounds be incorporated into HPC and how do they effect the material properties?

- Finally, is it possible to tailor polymer networks with adjustable net point density and polarity and can these materials be of practical use i.e. in detection of analytes in microfluidic systems?

Based around these questions this thesis aims to uncover fundamental structure property relationships of HPC derivatives, to establish a better understanding of the reaction behavior of HPC in homogenous conditions, and yields first possible applications of functionalized HPC derivatives, as visualized in a schematic illustration Figure 2-1.

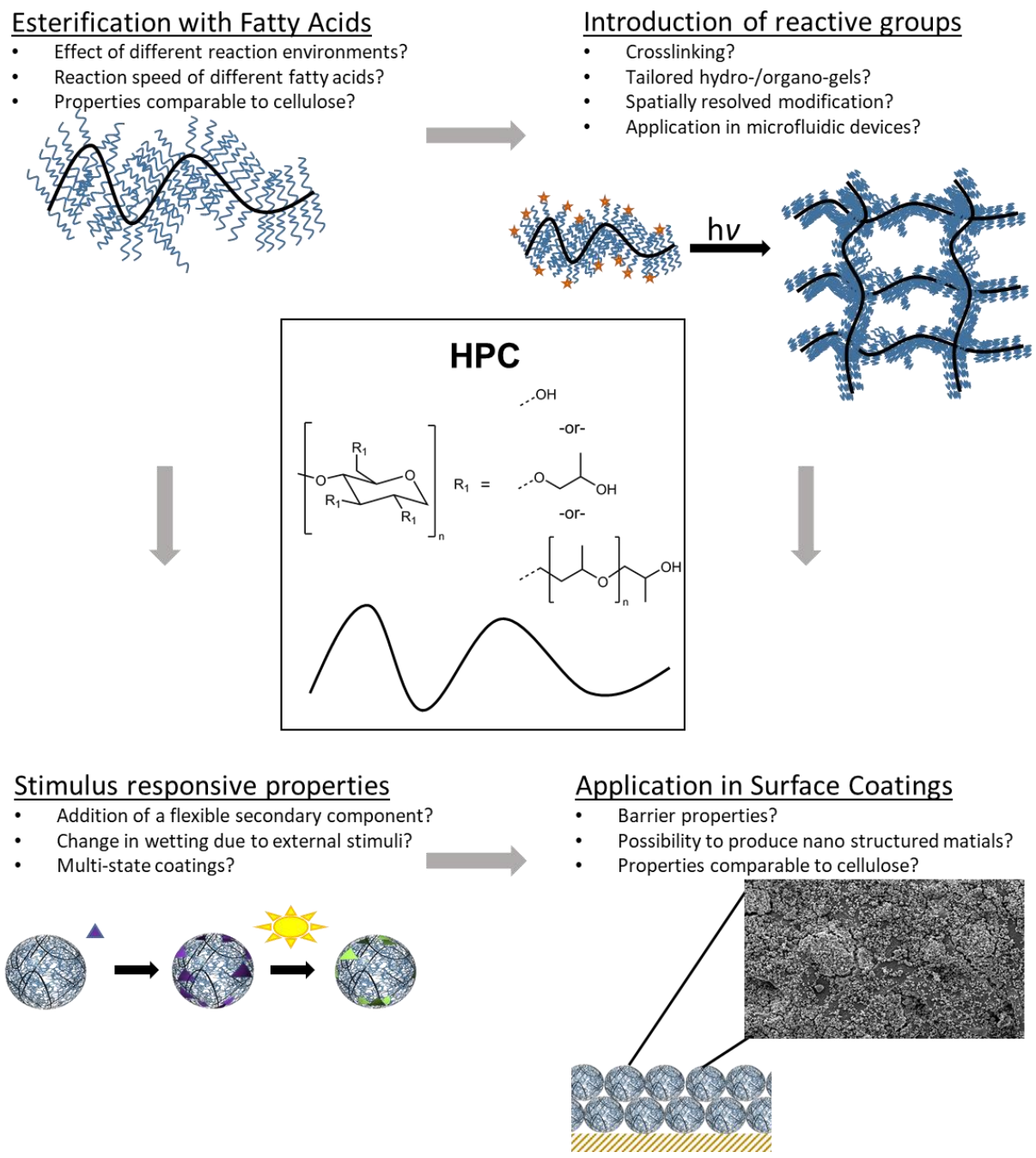

Figure 2-1: Representation of the different target areas of this work and their interdependencies. To establish HPC as a facile bio based platform chemical, this work revisits the chemical modification of HPC with fatty acids and reactive moieties. The application of HPC based materials to surfaces to provide tunable interfacial properties is the next consequential step. Furthermore, the scope of possible applications is broadened through the targeted generation of HPC-based gels, either as organo-, or hydro-gel and finally the possibility to incorporate stimulus responsive domains, and their resulting properties are investigated.

2.2. Strategy

2.2.1. Polymer analogous conversion of HPC

As pointed out in section 1.2, the literature in regards to HPC fatty acid esters is still limited in scope, hence HPC derivatives will be synthesized in a systematic fashion, including completely novel co-esters with different acids. To facilitate this in an efficient manner, first of all the optimum reaction conditions for fast conversion and minimal polymer degradation will be established. During this investigations stearic acid will be used as model reactant, since it is the most unreactive representative of the fatty acid chlorides.[139] The choice is made because an unreactive compound will give better resolution on the effects of accelerating/decelerating reaction conditions. After baseline optimal conditions are established, fatty acid esterification of HPC with lauric, myristic, palmitic, and stearic acid will be investigated to determine the respective reaction kinetics and solution properties. Based on this data, a toolbox for targeted synthesis of specific degrees of substitution, ranging from 0.5 to 3, for all respective derivatives will be composed. Subsequently these different materials will be investigated with the aim to correlate the chemical structure of the polymers to their properties and develop a better understanding of the underlying relationships. These polymers will be analyzed by standard analytical methods, like NMR, SEC, and DSC as necessary and specialized methods if interesting properties, like tunable surface properties, are suspected. A summary of this strategy, the produced polymers, and the workflow within this part of the thesis can be found in Figure 2-2 and Figure 2-3, respectively.

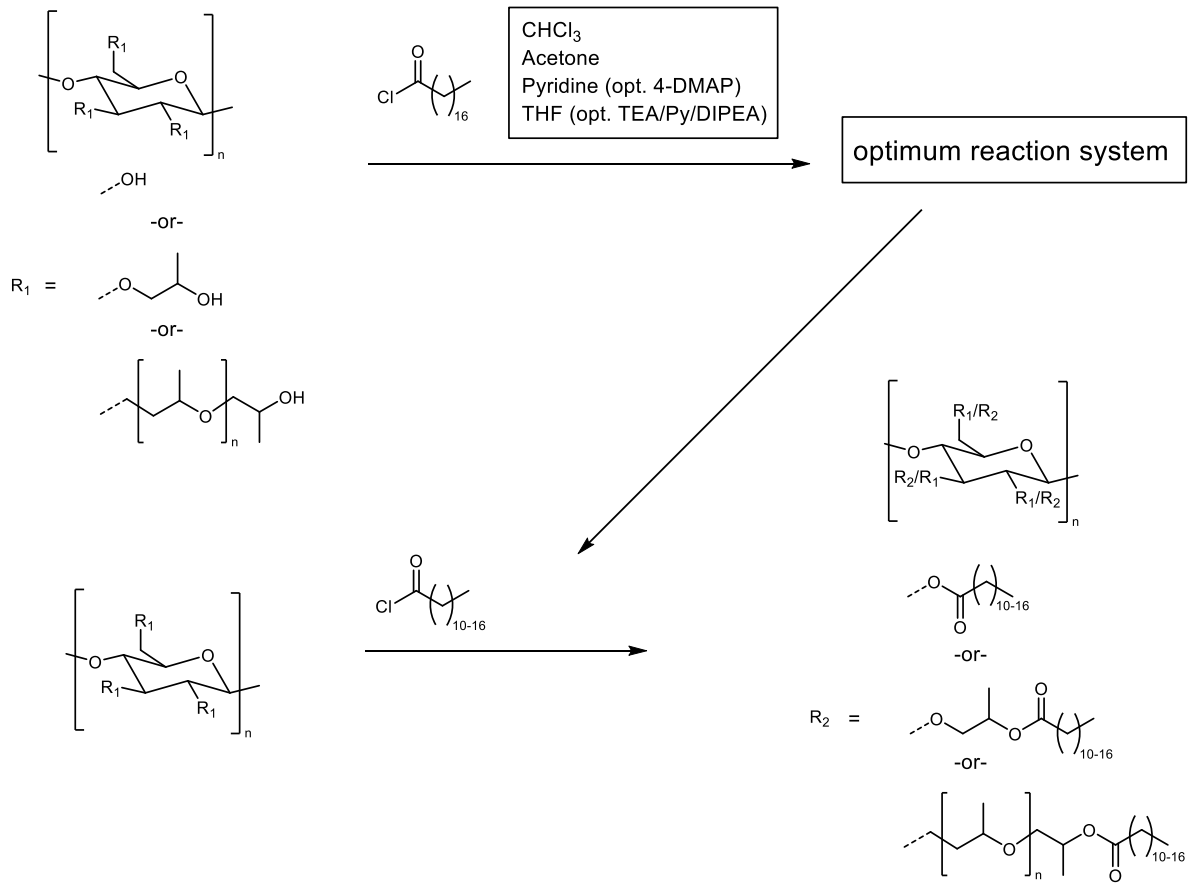

Figure 2-2: Representation of the initial workflow to determine the optimal reaction system for the esterification of HPC with different fatty acid chlorides. This forms the foundation for the systematic production of specific DS values for each derivative, as lined out in Figure 2-3.

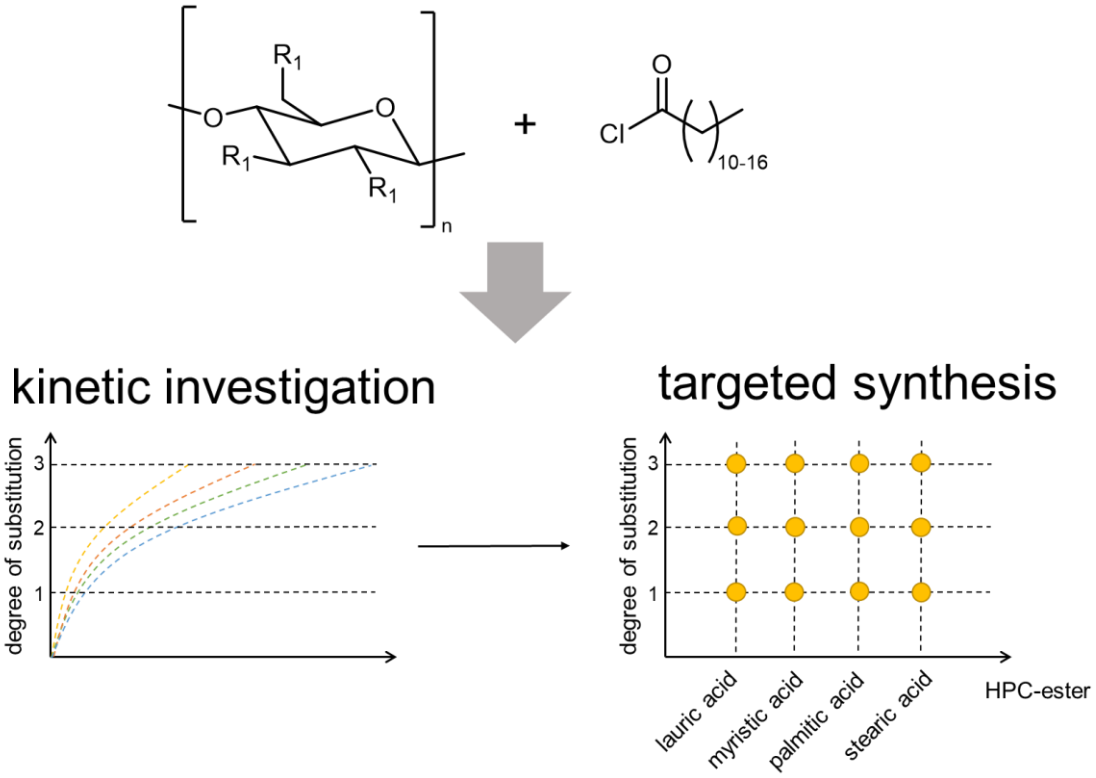

Figure 2-3: Based on an optimized reaction system, it will be possible to determine the respective reaction kinetics of HPC and the different fatty acid chlorides of interest. Consequently, it will be possible to produce a "grid" of different DS-values for each derivative for further investigation of their respective thermal, chemical, and macromolecular properties and thus increase the understanding of underlying mechanism. The R_1 placeholder corresponds to Figure 2-2.

2.2.2. Preparation of photo cross linkable HPC derivatives

Based around the results obtained from 2.2.1, functional groups with an initial focus on light-responsive moieties will be introduced. For this purpose, photo reactive groups will be incorporated to produce starting materials for the generation of tailored networks. This will be achieved through different strategies, in a first effort well known benzophenone (BP) functions will be introduced by esterification of HPC with acid chloride derivatives of benzophenone, namely 4-carboxy benzophenone and 10-((4-benzoylbenzoyl)oxy)decanoic acid, Figure 2-4. [140-141]

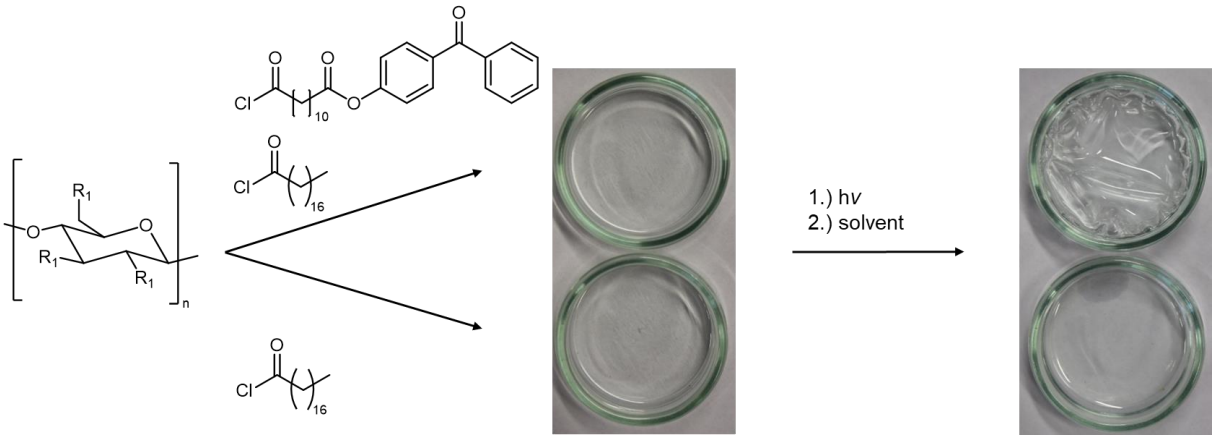

Figure 2-4: Strategy to generate photo crosslinkable HPC derivatives, with the core aim to establish feasibility of a known crosslinking system (BP-derivatization) in the HPC-system. In comparative experiments between BP-modified systems and systems that do not contain BP moieties, the crosslinking-performance will be examined qualitatively. The R_1 placeholder corresponds to Figure 2-2.

Once this crosslinking system is successfully implemented, more flexible approaches, based on the incorporation of unsaturated side chains will be investigated. To facilitate this, unsaturated HPC derivatives based on the results of 2.1 with the optional incorporation of fatty acids as co-substituents will be prepared to yield hydrophobic and hydrophilic materials. This will give the building blocks necessary to produce hydro- and organo gels respectively. The swelling behavior of these gels, both in bulk and attached to model surfaces, will be investigated with the aim to understand the relation between crosslinking conditions and the afforded network structures. Furthermore, photo lithographic techniques – both, with masks and with a x/y-laser system – will be utilized to determine the abilities in tailoring structures in surface attached networks as shown in Figure 2-5.

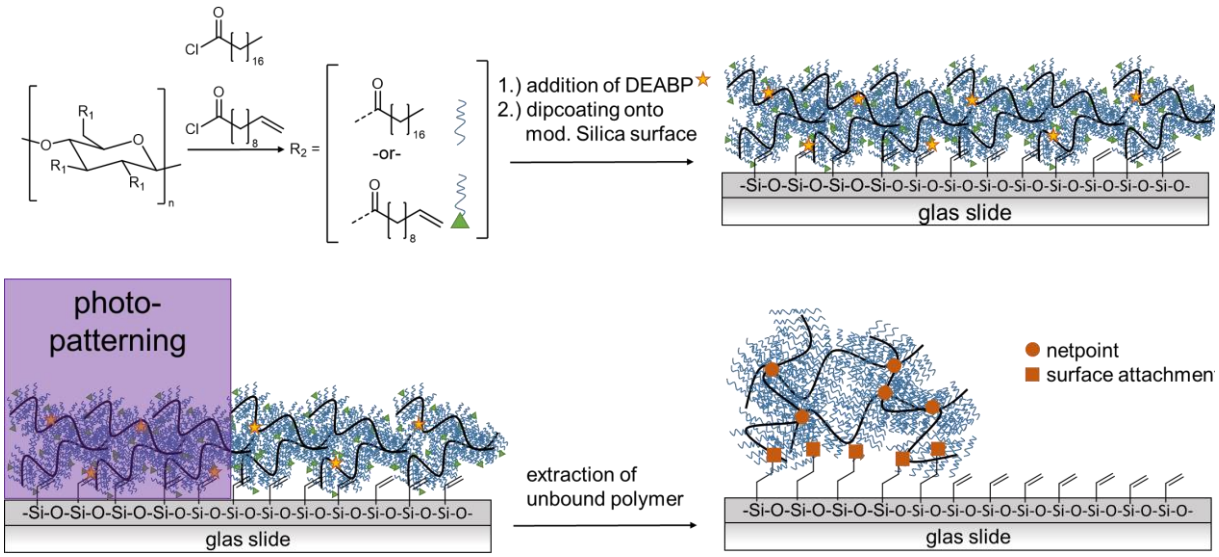

Figure 2-5: Schematic representation of a more flexible approach to photo crosslink, based on the incorporation of unsaturated side-chain into the HPC substitution pattern. These polymers can present several advantages above materials that intrinsically contain photo sensitive groups, like higher stability for storage and the ability to use a broad range of radical generating species, e.g. different photo reactive materials (e.g. BP derivatives, coumarin derivatives, DMPA, camphorquinone) or thermal radical starters like 2,2′-azobis(2-methylpropionitrile) (AIBN). Through this feature, the amount of initiator in a system like this can easily be altered, without the need to carry out different polymer analogous conversions. Finally, the afforded materials con be photo- attached and cross-linked simultaneously to surfaces exposing unsaturated moieties via a multistep-process consisting of coating, photo patterning, and removal of unbound polymer. The R_1 and R_2 placeholder correspond to Figure 2-2.

2.2.3. Preparation and study of nanostructured surface coatings

As pointed out in section 1.3 stearic acid esters of cellulose can be transferred into nano-scale particles to create super hydrophobic surface coatings. Since these systems have some drawbacks, e.g. challenging reaction system to produce the material and limited tolerance towards water in the NP dispersion, we will develop nano dispersions from HPC stearic acid esters. Furthermore, the possibility of transferring these to a water based system will be investigated (Figure 2-6).

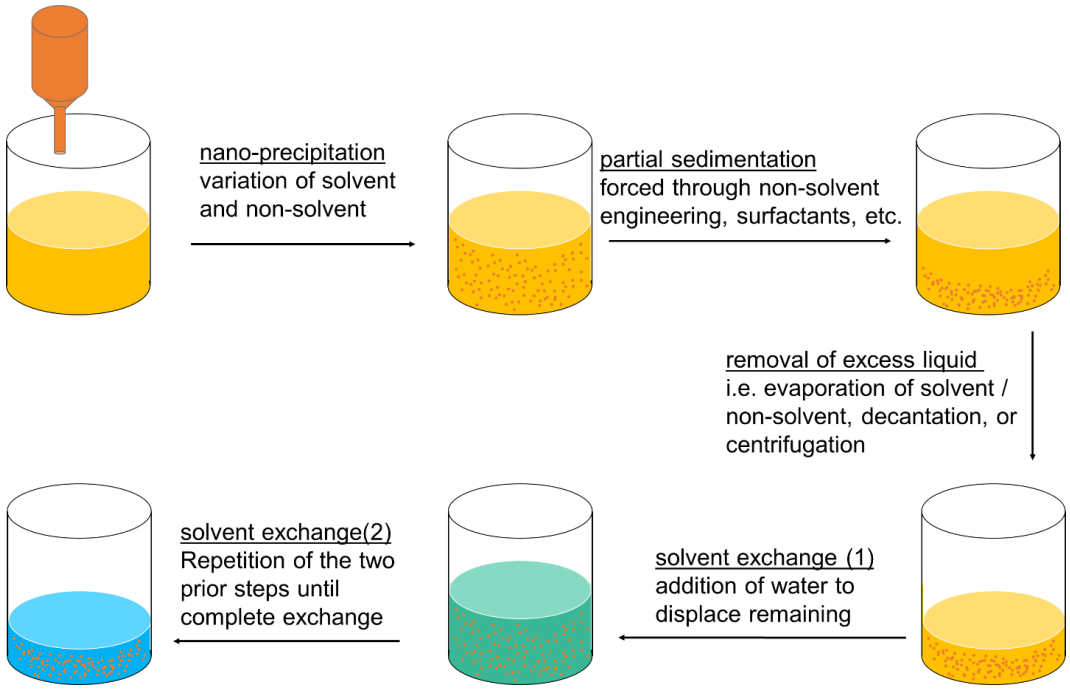

Figure 2-6: Depiction of the major steps involved in the production of water-borne nano particle dispersions. The process begins with the dissolution of the material of interest (i.e. HPC stearic acid ester or commercial thermoplastic cellulose esters) in a solvent that is miscible with a given non-solvent. After the precipitation process, the nano dispersion will be concentrated, and the remaining organic solvent / non-solvent will be exchanged with water in an effort to yield water based coatings for potential applications.

Once this stage is reached, coatings of these particles on model substrates, like glass slides or polymer films, and on paper substrates will be prepared and the effect of the coatings as towards the wettability and the optical properties will be evaluated. Subsequently, the change of the aforementioned properties in response to localized thermal manipulation will be studied in an effort to understand possible applications of HPC stearic acid ester nano particles in sustainable thermo responsive coatings, Figure 2-7. Based on the known high refractivity of nanostructured coating, there will also be complementary investigation of commercial thermoplastic cellulose esters with the goal to possibly design a thermo-optical surface coating, i.e. one that changes its opacity if exposed to heat. The latter may become useful for possible commercial applications.

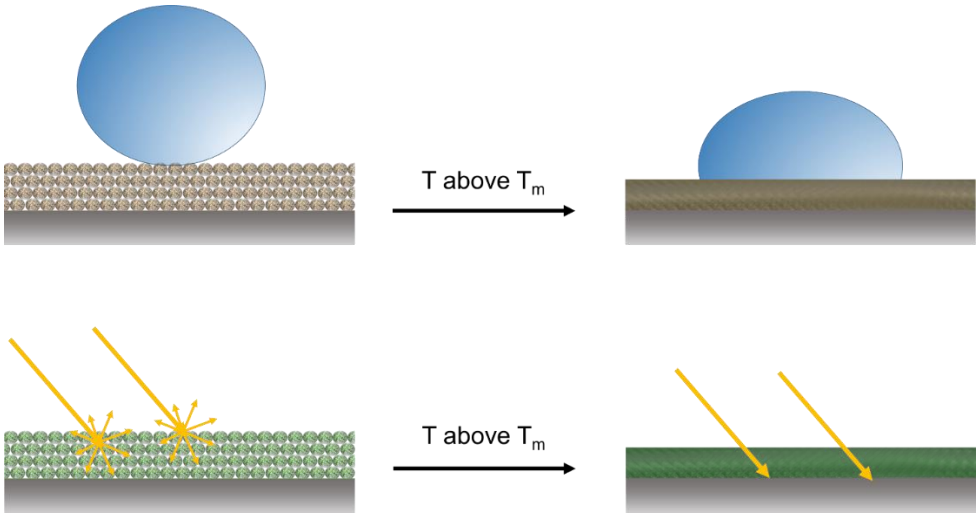

Figure 2-7: Schematic illustration of the strategy to produce surfaces with nano particles prepared as depicted in Figure 2-6. The surfaces will be investigated with regards to their wetting behavior (top) and their optical properties with respect to visible light (bottom). Of special interest is the question if thermally induced changes in the surface morphology (i.e. melting of the coatings) can be used to alter these respective properties in a controlled fashion.

2.2.4. Generation of photo responsive coatings

Starting with the results obtained in 2.2.3, the generated nanostructured surface coatings will be modified by the incorporation of photo responsive groups. For this purpose, donor acceptor Stenhouse adducts (DASAs, see section 1.4 for details) are identified as compound of choice, because they exhibit fast switching behavior, a strong change in polarity. In addition, the flexible synthesis will allow an easy modification to cover a broad range of N-alkyl substituents (Figure 2-8 a and b).

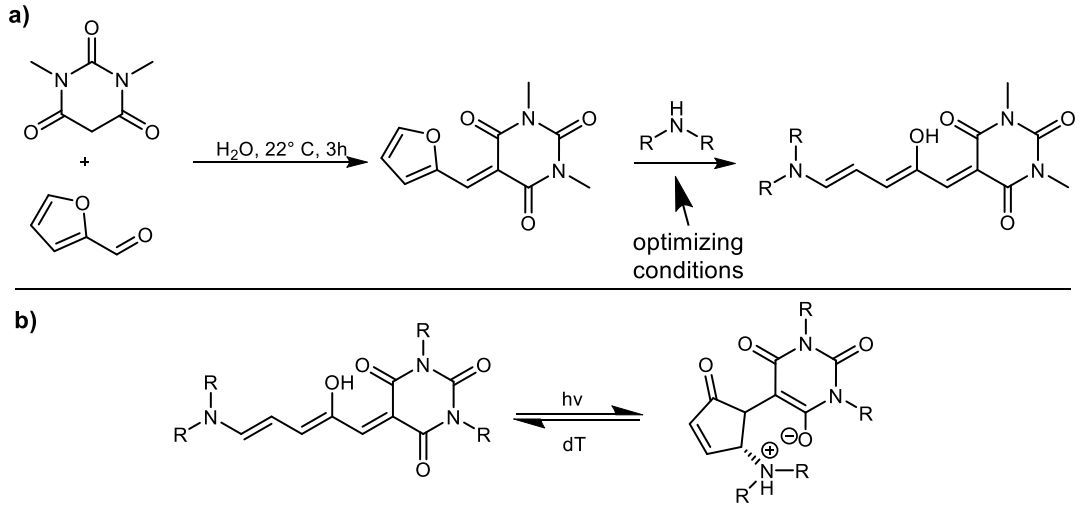

Figure 2-8: **a)** Scheme of the synthetic route to produce differently *N*-substituted DASAs with the aim to optimize the interaction with the nano particle surface to preserve the initial hydrophobic properties and expose the switchable domain within the molecule towards the surrounding environment. Model-reactants will be used to establish optimized reaction conditions, i.e. fastest conversion with highest yields. **b)** Switching mechanism an example DASA, the details of this reaction are covered in section 3.3.

Since the formation of nano particles depends strongly on the solution behavior of the polymers, which is in turn heavily dependent on the polymer chemistry, the direct incorporation of photo responsive groups into the polymer chains would appear to be a non-

trivial endeavor, posing a comparatively large risk of failure and will therefore not be pursued. An alternative, and far more flexible route presents itself by physisorption of DASAs to the prior established nano particle systems. As synthesis of a range of DASAs with varying N-alkyl substituents can be achieved relatively fast due to the facile one-step synthesis, the DASAs will be engineered to assemble themselves on the surface via Van der Waals interactions in a manner that exposes the polarity chancing domain away from the particle surface towards the surrounding medium. To achieve this, amine substituents on nucleophilic attacking secondary amine will be varied from short to long alkyl chains. Subsequently the different new DASAs will be screened for their performance as photo responsible polarity switch (as illustrated in Figure 2-9) in an effort to produce a surface coating that can be triggered to switch from super hydrophobic to hydrophilic. These coatings will be studied in detail to optimize switching speed and identify optimum DASA composition and concentration.

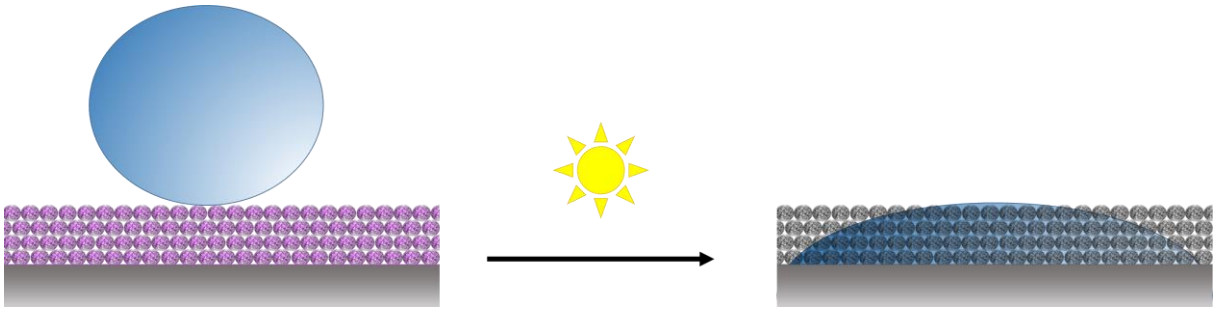

Figure 2-9: Schematic representation of the stimulus response within the targeted surface coating: the initially hydrophobic DASAs should still retain the hydrophobic properties inferred by the nano particle coating. Through illumination with visible light the DASAs are planned to switch into their uncolored, hydrophilic state, which breaks the hydrophobic barrier and thus lead to imbibition of the water into the coating.

3. Methods

In this work several different scientific methods were employed in an effort to increase the understanding of the formation and possible fields of application of hydroxypropyl cellulose derivatives. The work progresses from the synthesis and analysis of HPC esters via typical esterification reactions, over the generation of nanoscale materials, to photo crosslinking, surface coating and thorough surface analysis. The core-methods employed to this respect in this thesis will be described in the following section, starting with the HPC derivatization (section 3.1), followed by nano precipitation techniques, the synthesis of DASAs and coatings thereof (section 3.2, 3.3, and 3.4), and finally the core characterization methods employed to investigate the produced materials and coatings (section 3.5 and 3.6) will be outlined. Note, the theory behind characterization methods like e.g. standard NMR, SEC, and IR-spectroscopy will not be covered here and the reader is referred to respective textbooks.

3.1. Synthesis and Analysis of HPC Esters

Polymer analogous conversion of polysaccharides in general has been covered in section 1.1 in detail, so this section is going to focus on the specifics of esterification of hydroxypropyl cellulose. Due to the good solubility of HPC in common organic solvents, the esterification is typically carried out under homogeneous conditions, this leads ideally to homogeneous modification along the polymer chain throughout the whole range of degrees of substitution. A typical esterification procedure for short chain acid chlorides, which was adopted to fatty acid chlorides is a straight-forward endeavor, HPC is dissolved in the solvent of choice, the acid chloride is added, and the reaction takes place. The mechanism of esterification always starts with a nucleophilic attack of a free electron pair of the alcohol function on the electron poor acyl carbon. Subsequently the leaving group (or electron withdrawing group) of the acyl-compound is eliminated and the intermediate oxonium ion formed from the alcohol is deprotonated, which forms the final ester, as shown in Figure 3-1.

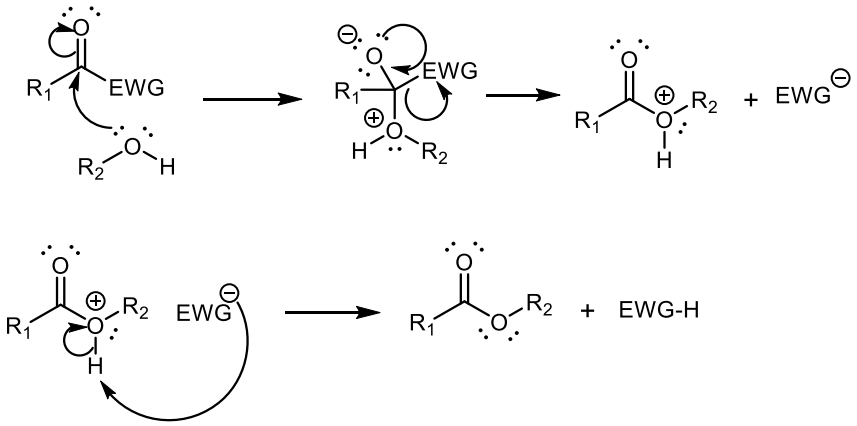

Figure 3-1: General reaction scheme for the esterification of carboxylic acid (derivatives) with an alcohol. The electron withdrawing group (EWG), also called leaving group, is the main variable between different approaches, as well as methods to scavenge the protonated EWG on the product side to shift the reaction equilibrium.

The main variable between different esterification systems is the leaving group. Since the hydroxyl function of the carboxylic acid is a hard nucleophile (in terms of its electronic makeup) it is naturally a poor leaving group. Therefore, the substitution of the leaving group with other moieties, either in prior reaction or *in situ*, is a dominating route to improve the reactivity of carboxylic acid. A facile method to activate carboxylic acids prior to the esterification is the conversion to acyl chlorides with a range of chlorination agents like

phosphorous pentachloride, oxalyl chloride, or thionyl chloride. An elegant feat of the latter two is, that all by-products of the reactions are gaseous, what drives the reaction to the product side. Nevertheless, this makes careful management of the gases released from the reaction mixture necessary. When these acid chlorides are employed in esterification the addition of amine bases like TEA, IPDEA, or pyridine can further improve conversion rate by scavenging the produced hydrochloric acid. Furthermore, activation agents like tri fluoro acetic acid anhydride (TFAA), and EDC/NHS are employed to activate the acid by producing a mixed (TFAA) or labile (EDC/NHS) ester, which has an electron-rich, well stabilized leaving group.

In particular, esterification reaction kinetics of HPC polymers have not been studied in detail until now, hence a system to determine the reaction behavior had to be established. In theory, it is as simple as monitoring the DS while the reaction progresses to determine the function of d[DS]/d[t]. In practice, this poses several challenges because the solubility of HPC esters in different solvents changes drastically even with small changes in DS, which makes it necessary to engineer appropriate precipitation and purification procedures to separate the product in the sampled aliquots from remaining reactants. In regards to this another factor is that the remaining acid chloride has still to be quenched at a precise point in time, e.g. by addition of methanol. Consequently, the precipitation agent has to mix with the quenching agent, the quenched acyl chloride, as well as the reaction solvent, but has to be a non-solvent towards the formed HPC ester. To approach this purely scientific, would necessitate to prepare the exact HPC esters prior to the kinetic analysis, which in turn is only possible based on kinetic data. Since this leads to a circular problem, the decision was made to engineer an appropriate precipitation system for every sample in an empiric fashion, based on the assumption, that with increasing DS of longer acids, the product would precipitate in more and more polar solvents. At low DS-values typically polar solvents like petrol ether are employed for the workup, while at higher DS values, a change to alcohols like isopropanol is made. The solvent used for re-precipitation has to be changed accordingly. To obtain kinetic data of HPC a reliable, fast, and labor-effective method for the analysis has to be established. In order to analyze the DS of HPC derivatives, the degree of hydroxypropylation, i.e. the amount of propylene oxide added per AGU – commonly referred to as molar substitution value (MS) – has to be known in the first place. The MS has been determined in literature via ^{1}H-NMR without further pretreatment. To verify this procedure for this thesis, the MS value was calculated, as a known reference, based on the information given by the supplier. The manufacturer has determined a 71.6 % content of hydroxypropoxy groups, which translates to an MS of 5.45 based on equation (3-1).

$$\mathrm{MS}_{\mathrm{supplier}} = \left[\frac{162}{100\ \% - \%hydroxypropoxy} - 162\right]\frac{1}{75} \tag{3-1}$$

Note, the method for MS determination described in the literature, which was applied based on the Figure 3-2 and equation (3-1), leads to a MS of 3.2 ± 0.3 which significantly differs from the expected value. The following part of this section, up to section 3.2, is adopted from the publication covered in section 4.1.

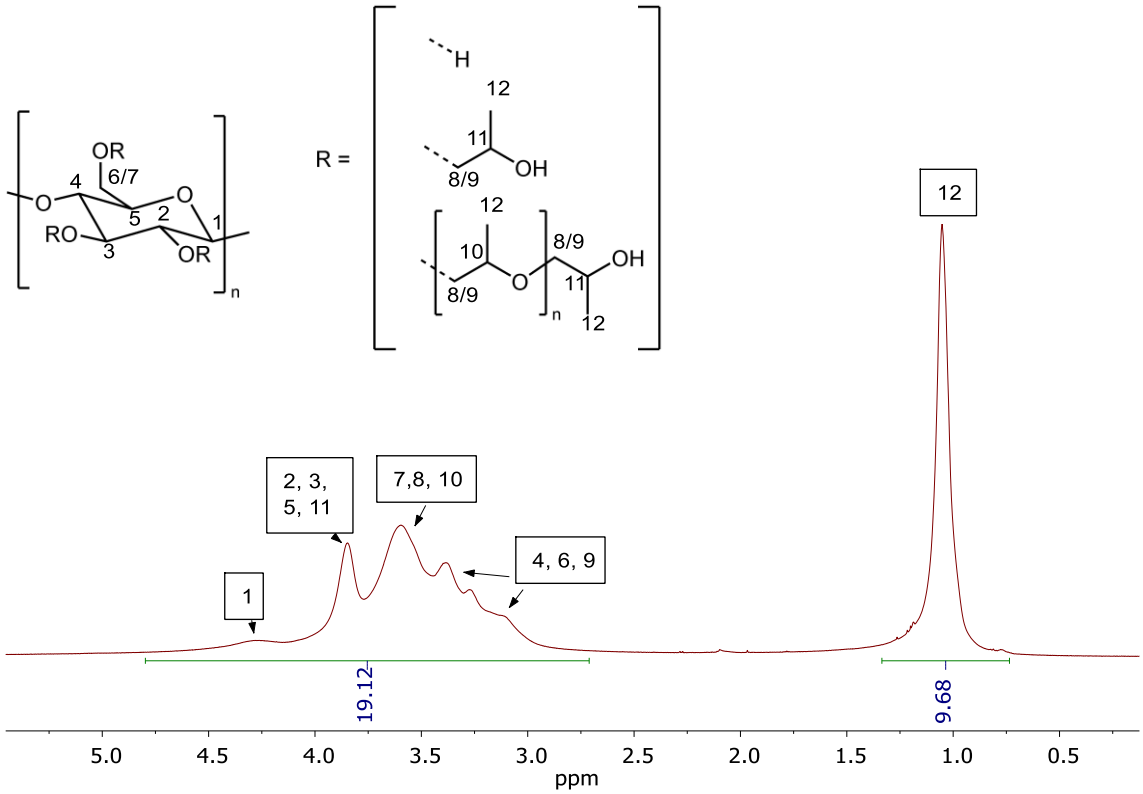

Figure 3-2: ^{1}H-NMR spectrum of HPC. Native HPC was dried under vacuum and then dissolved in $CDCl_3$. The signals can be grouped in two major areas: (i) the protons of the terminal methyl groups within the hydroxypropyl moieties (0.7 - 1.4 ppm) and (ii) the remaining protons of the cellulose backbone and methylene and methine groups within the hydroxypropyl moieties (2.6 - 4.8 ppm).

$$\mathrm{MS}_{\mathrm{NMR\ native}} = \frac{10}{3\left[\frac{\int(2.65-4.8\ \mathrm{ppm})}{\int(0.7-1.4\ \mathrm{ppm})}-1\right]} \tag{3-2}$$

The same ^{1}H-NMR experiment with native HPC using another sample of the same dried material led to an apparent MS of 2.8 ± 0.3, indicating the poor reliability of the previously acquired data. Interference with the measurement by the alcoholic protons due to supramolecular interactions was considered likely. Therefore, an exchange of the alcohol protons for deuterons via the dissolution of dried HPC in D_2O and subsequent lyophilization was performed, leading to the ^{1}H-NMR spectrum shown in Figure 3-3. Based on equation (3-3), the newly calculated MS was found to be 5.48 ± 0.80.

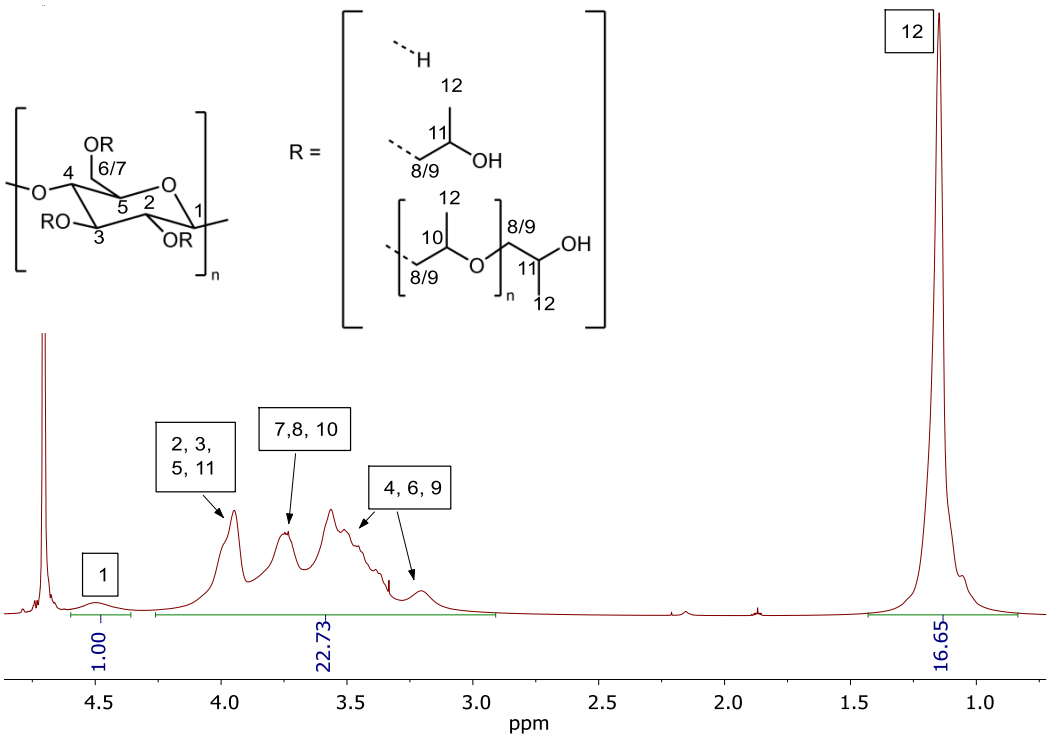

Figure 3-3: ^{1}H-NMR spectrum of HPC after the alcohol protons were exchanged with deuterons. HPC was dissolved in D_2O, lyophilized to remove the proton-enriched D_2O and then dissolved again in D_2O. The signals form three groups: (i) the protons of the terminal methyl groups within the hydroxypropyl moieties (0.7 - 1.4 ppm), (ii) the remaining protons of the cellulose backbone (without the anomeric protons at position 1) and methylene and methine groups within the hydroxypropyl moieties (2.85 - 4.25 ppm), and (iii) the anomeric proton at position 1 (4.5 ppm). The spectrum was acquired without water suppression.

$$\mathrm{MS}_{\mathrm{NMR\ native(deuterated)}} = \frac{2\int(0.7-1.4\ \mathrm{ppm})}{\int(2.85-4.25\ \mathrm{ppm})-\int(0.7-1.4\ \mathrm{ppm})} \tag{3-3}$$

As a complementary and independent method, analysis of fully propionated HPC was also conducted, and based on the assignment shown in Figure 3-3 and equation (3-4), an MS of 5.57 ± 0.42 was calculated. The calculation was based on the assumption that the DS is 3 because complete propionation is achieved by an established method for realizing total esterification. The MS values determined by both, this method and by the analysis of deuterated HPC were consistent with the value supplied by the HPC manufacturer, showing that the method for determining the MS using native HPC without proton exchange is not suitable.

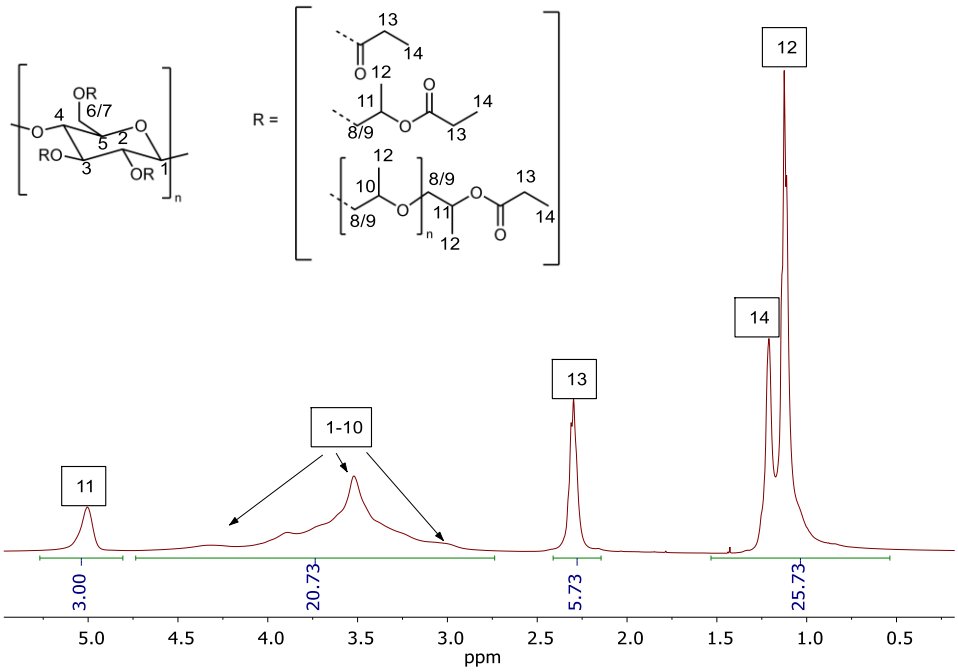

Figure 3-4: ^{1}H-NMR spectrum of HPC after full propionation recorded in $CDCl_3$. The signals form four groups: (i) the protons of the terminal methyl groups within the hydroxypropyl moieties and the propionic esters (0.5 - 1.5 ppm), (ii) the methylene protons of the ester groups (2.3 ppm), (iii) the remaining protons of the cellulose backbone and methylene and methine groups within the hydroxypropyl moieties (2.75 - 4.70 ppm), and (iv) the proton at position 11 (5 ppm).

$$\mathrm{MS}_{\mathrm{NMR\ per\ propionated}} = \frac{\int(0.5\text{–}1.5\ \mathrm{ppm}) - 3\int(5\ \mathrm{ppm})}{3} \tag{3-4}$$

To verify these data, elemental analysis (EA) was performed on both the native (dried) HPC (equation (3-5)) and the fully propionated HPC (equation (3-6)). The MS values from the NMR and EA data are compared in Table 3-1. Regarding the MS, it can be concluded that the proposed methods yielded results that were highly comparable to the standard method used by the supplier. This was an interesting outcome, as our methods use a very limited amount of lab equipment and synthetic conversion compared to the chromium trioxide distillation and several titrations used in the USP method.

$$\mathrm{MS}_{\mathrm{EA\ native\ HPC}} = \left[5\frac{C(mol\%)}{O(mol\%)} - 6\right] \Big/ \left[3 - \frac{C(mol\%)}{O(mol\%)}\right] \tag{3-5}$$

$$\mathrm{MS}_{\mathrm{EA\ fully\ propionated\ HPC}} = \left[8\frac{C(mol\%)}{O(mol\%)} - 15\right] \Big/ \left[3 - \frac{C(mol\%)}{O(mol\%)}\right] \tag{3-6}$$

Table 3-1: MS values of HPC determined via different methods. All values were within the same range. Since these are basically 4 methods with two independent samples, the data are considered reliable. The values match the one given by the supplier.

	MS determined via ^{1}H-NMR	MS determined via CNH-EA
native HPC (dried)	5.48 ± 0.80 (deuterated)	5.48 ± 0.06
fully propionated HPC	5.57 ± 0.42	5.51 ± 0.11

Since ^{1}H-NMR is preferable as standard method for analyzing DS values because of its fast measurement, low cost, and ease of sample preparation, a comparison of the DS values of HPC stearic acid esters obtained by ^{1}H-NMR and EA (calculated with equation (3-7), where n was the number of carbon atoms in the fatty acid) was conducted. The result of this investigation validate ^{1}H-NMR as a facile method for analysis of the kinetics of HPC esterification reactions and are depicted in Figure 3-5.

$$DS = \frac{\left[[5 + MS]\frac{C(mol\%)}{O(mol\%)} - 3MS - 6\right]}{\left[n - \frac{C(mol\%)}{O(mol\%)}\right]} \tag{3-7}$$

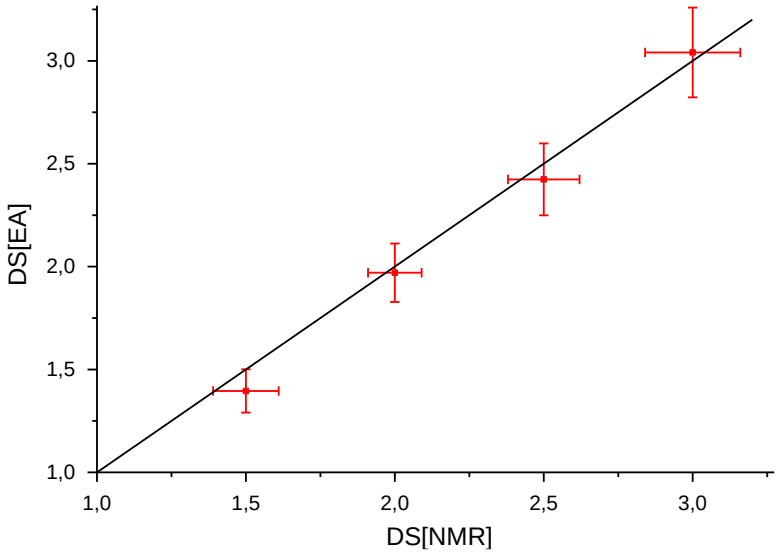

Figure 3-5: Correlation between DS values of HPC stearic acid esters obtained via ^{1}H-NMR and EA. The black diagonal indicates a perfect correlation. The actual data show that within the margin of error, there is a good correlation between the values determined with both methods.

3.2. Generation of polymeric nano particles

There are two general routes to form polymer (nano) particles. One approach is to polymerize monomers via suspension or emulsion polymerization. During these processes the monomers are initially dispersed, either mechanical (suspension) or as an emulsion and then polymerized in place, these methods are used generally to improve control during the conversion or to produce a microencapsulated system. Since this is no option, if the material of interest is already a pre-formed macromolecule, another route has to be used during this work. The procedure is based on the formation of nano scale particles from polymers via phase separation, which is typically achieved using dialysis, emulsion-evaporation, and nano precipitation, respectively. Dialysis was employed by Hornig for the preparation of different short chain CE based nano particles, this was achieved by the dissolution of the CEs in DMAc, and dialysis of this solutions against water, Figure 3-6 b.[142] While this method provided monodisperse nano particle suspensions with particle sizes ranging from 100-300 nm, it is time and labor intensive since it is limited by diffusion. For the emulsion-evaporation method, the polymer is dissolved in an organic solvent, that is immiscible with a non-solvent for the polymer and then emulsified via mechanical force – i.e. stirring or ultrasonic agitation – and the aid of protective colloids like polyvinyl alcohol (PVA). Subsequently, the emulsion is heated to remove the solvent which leaves polymeric particles. An example for this method utilizing CEs is presented by Wondraczek, where CEs were dissolved in dichloro methane, and this solution was emulsified in an aqueous PVA solution via sonication, Figure 3-6 a.[143] In this work it was only possible to adjust the particle size between 200 and 260 nm, via modification of the sonication parameters. In addition, evaporation of the solvent necessitates elevated temperatures, which for polymers with low glass transition temperatures or melting points – e.g. for fatty acids derivatives of HPC – leads to the formation of aggregates.

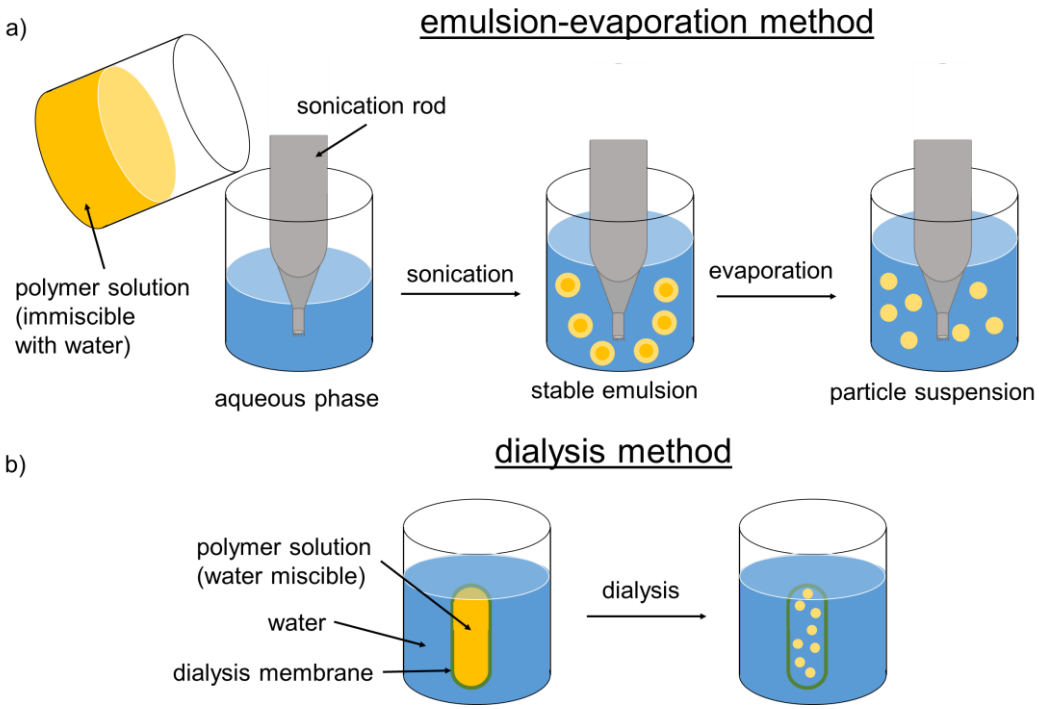

Figure 3-6: The emulsion- evaporation method a) employed to produce nano particles, this approach is based on the formation of a stable emulsion of a water immiscible polymer solution and subsequent evaporation of the solvent. The dialysis method b) follows the complementary route through use of a solution based on a water miscible solvent, which is slowly exchanged for water, leading to the formation of nano particles once the polymer becomes insoluble.

This leaves precipitation as a potential option to produce nano particles. In principle, there are two approaches to nano precipitation, the first is the addition of a diluted polymer solution to a non-solvent that is miscible with the employed solvent. The other approach is inverted precipitation, where the non-solvent is added to the polymer solution. Typically for CE nano precipitation, in either method, volatile organic solvents like THF and Acetone are employed and the non-solvent component is water based, with the optional addition of protective colloids to aid particle separation. During precipitation, the solvent is replaced by non-solvent molecules through diffusion, which leads to the formation of spheroid particles. The remaining solvent may then be separated under reduced pressure without the need for elevated temperatures. To obtain isolated particles, the initial polymer concentration has to be below the critical overlap concentration (c*), since the polymer chain interaction would otherwise lead to large scale aggregation during this diffusion driven process, which is desired e.g. during workup after chemical modifications. For polymers c* is defined as the concentration of a given polymer, in a specific solvent at a defined temperature, above which the volume of individual chains starts to overlap which leads to an entanglement of the macromolecules. The behavior of polymers in solution below, at, and above c* is illustrated in Figure 3-7 schematically.

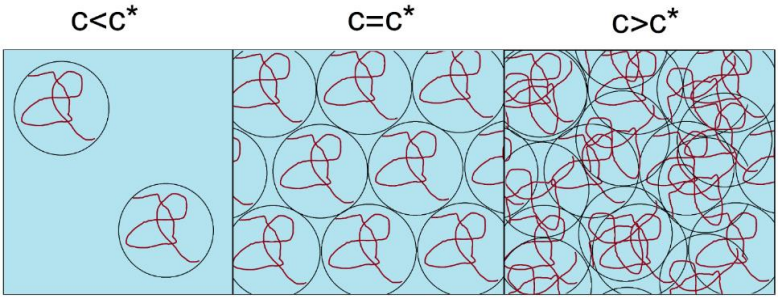

Figure 3-7: Representation of the interactions of polymers in solution below (left), at (center), and above the critical overlap concentration. Once the concentration is above c*, the polymer chains start to interact with each other, leading to a sharp change in viscosity and precipitation behavior.

While the direct precipitation method has been widely reported to be suitable for various polymers, in the case of cellulose derivatives this process is in generally accompanied by the formation of larger aggregates, if aqueous systems are being employed.[142] The reason for this behavior is as of today not fully understood. It is speculated, that local gelation encapsulates pockets of polymer solution, which in turn solidifies as a whole via the aforementioned diffusion process. Nevertheless, these unwanted aggregation diminishes the yields, requires additional workup steps, and reduces over all control about the particle formation and geometric structure. Controversially, during inverted precipitation the latter aggregation is not found, likely due to the fact that local peaks in non-solvent concentration are eliminated. In general, the particle size can be adjusted by the polymer concentration, and while direct precipitation leads to smaller particles, the inverse method leads to narrower particle size distributions, respectively. Without regard for the employed method, one underlying challenge in preparation of polymer nano particles is the highly diluted state (typically well below 1 % by weight) of the final product, which necessitates additional steps to increase the concentration. During processes that aim to increase the concentration of nano particle dispersions and the curing of the particles, the stabilizing mechanisms that prevent the agglomeration of the isolated particles play an essential role. Two major mechanisms that are effecting the stability of polymer particles in dispersions are steric and electrostatic stabilization. Steric stabilization takes place when the surface of the particles is partially

solved or swollen. When particles now approach each other the local concentration of partially dissolved polymer increases, which leads to a higher osmotic pressure in this area. This increased osmotic pressure causes solvent from the surrounding medium to diffuse into the space between the particles, which subsequently separates the particles and prevents agglomeration. Because the extent of this effect depends on the state of the polymer exposed on the particle surface and the solvent interaction, it is influenced highly by the solvent composition and temperature. Of course this effect only can contribute substantially if the polymer is partially dissolved by interaction with the surrounding medium. Nevertheless, even systems where the polymer is completely insoluble can be stable (e.g. polyolefin nano particles in water). This is due to the second mechanism, i.e. electrostatic stabilization. The most basic explanation of colloidal stabilization is given by the DLVO-theory. This approach combines attractive (Van der Waals) and repulsive (electrostatic) forces, which leads to a relation of distance between the particles and total potential energy as displayed in Figure 3-8.[144] The electrostatic repulsion is the result of surface charges, that are acquired by particles in aqueous systems. These surface charges bind corresponding counter ions permanently, and thus form an electrical double layer, commonly referred to as Helmholtz layer. Since all particles of the same kind share the same surface polarity, they repulse each other according to the laws of electrostatics. When this repulsive force is combined with the attractive Van der Waals forces between the colloids, a local energy minimum is formed, which leads to separation of the particles. As evident in Figure 3-8 the potential barrier between this local minimum and the absolute minimum – at zero distance – is not infinite, which is the cause for agglomeration.

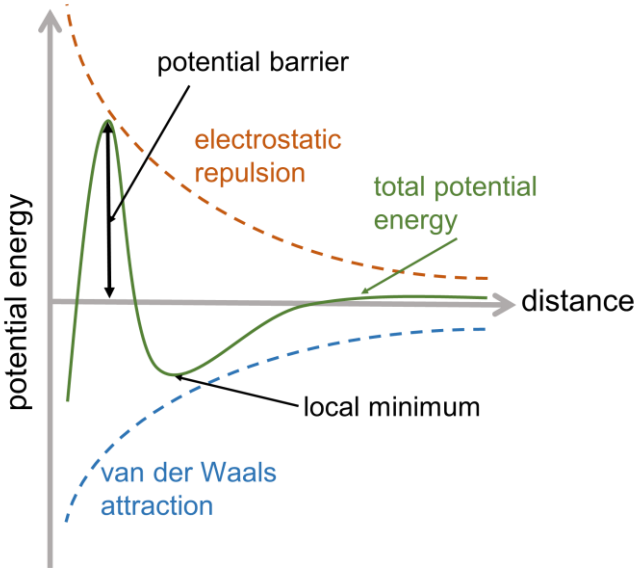

Figure 3-8: The DLVO-theory combines both, electrostatic repulsion and van der Waals attraction to yield an approximation for the total potential energy between two particles in relation to their difference. The combined potential exhibits both, a local and an absolute minimum, which are responsible for stabilization at relative low distance and for the agglomeration (domination of attraction) respectively.

The quantity of this potential barrier is determined by the surface charge of the particles, which in turn is determined by the surrounding medium. This explains the possibility of agglomeration when the medium is changed or modified, as a result of particles overcoming this barrier even by Brownian motion. Furthermore, attempts to increase concentration by i.e. centrifugation can supply enough energy to overcome this barrier and thus lead to complete aggregation, which has to be considered. The particle size distributions can be determined

either by electron microscopy and image analysis or by dynamic laser light scattering, which analyze time-dependent fluctuations of the scattering to determine the diffusion coefficient and from this, the particle size. These methods are not discussed in detail due to their well-established nature.

3.3. Synthesis of Donor Acceptor Stenhouse Adducts (DASAs)

While the history of DASAs has been covered in section 1.4, this section will give a detailed overview about the state of the current research. The DASAs introduced by Helmy (Figure 3-9) are produced via a two-step reaction.[124] Initially, furan-2-carbaldehyde **1** is converted with electron poor malonic acid derivatives like Meldrums acid **2** or *N,N*'-dimethyl barbituric acid **3** to yield the respective precursors **4** and **5** via a Knoevenagel condensation. In this stage it is possible to influence the switching kinetics and absorption maxima of the final product by the use of different malonic acid derivatives. In the second step, the condensation product is converted with a secondary amine to form the DASA **6**. While it is possible to produce a wide range of different *N*-Substituted barbituric acid derivative for alterations in the first step, the second reaction introduces the real versatility of DASAs. Already in the first publication Helmy presented over 30 different DASAs based on this approach, including sterically challenging and electron depleted amines like the ones shown in Figure 1-11 and Figure 1-12. In addition, the second generation DASAs based on Meldrums acid and aromatic amines show a great variability in absorption wavelength and the thermally driven rotation is slower by factor of 10.[125]

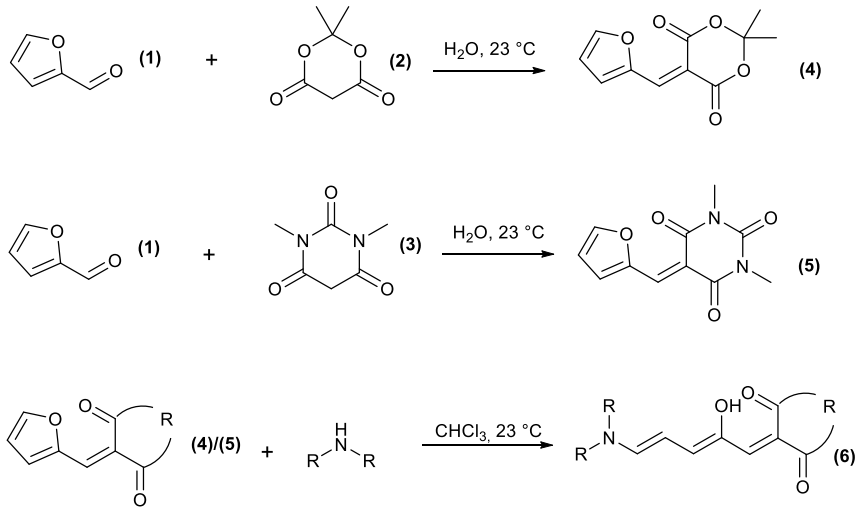

Figure 3-9: General synthetic route for the production of donor acceptor Stenhouse adducts, as presented by Helmy et al., the versatile two step reaction is carried out at ambient temperature and without the need for a special atmosphere or expensive reactants/catalysis.

Since DASAs are T-type photochromic molecules, the switching from the triene form to the cyclopentone form is achieved by illumination and the reaction back to the triene state is induced thermally as displayed in Figure 3-10. The fast reaction induced by the light for both, first and second generation DASAs has been studied by Lerch and confirmed to be a two-step process.[145] Firstly in the fast actinic step – taking place in fs- to ns-time domain – light induces a E/Z isomerization of the C2-C3 bond to form **7**. This is followed by a thermally driven, comparatively slow (ms-scale), rotation along the C3-C4 bond. Afterwards, a 4π-electrocyclization and proton transfer takes place, leading to the zwitter ionic form **8**.

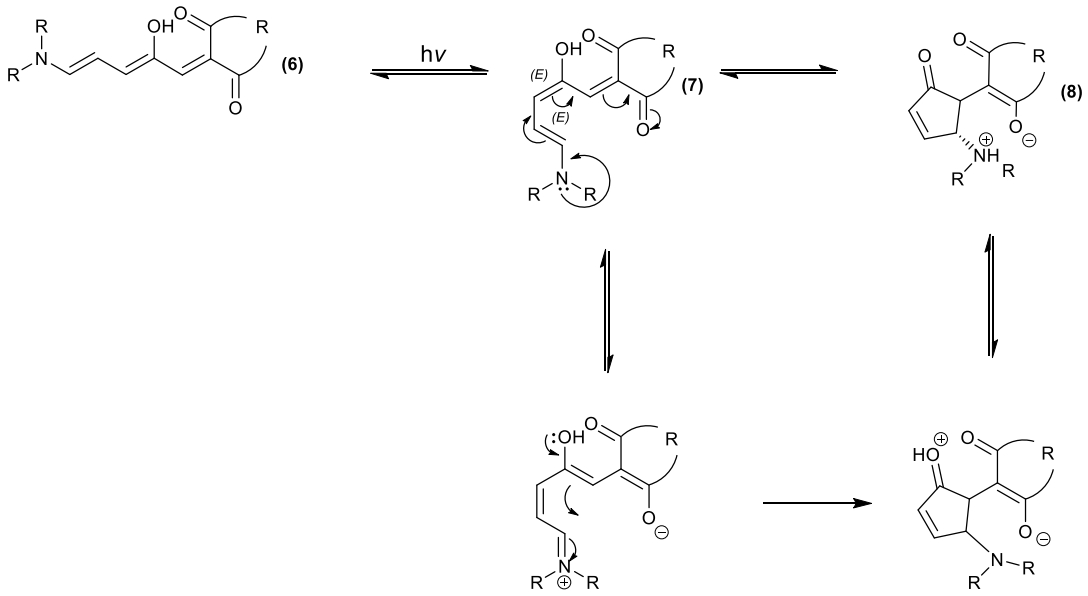

Figure 3-10: The switching mechanism of DASAs is divided into two different steps, light induces the fast actinic E/Z isomerization, followed by a thermally driven rotation along the C3-C4 bond and finally a 4π-electrocyclization. The switching back is an entirely thermally driven process.

Despite the fast reaction of small secondary amines with the furfural adducts and complete conversion in THF within a couple of hours, in this thesis longer chain alkyl substituted amines have been found to react rather slow in THF. Subsequently the effect of different solvents is of interest to investigate if the conversion rate can be improved by the choice of solvent. Since the DASAs absorb visible light, it is possible to monitor the conversion in real time via UV-Vis spectroscopy to determine the solvent that yields the highest reaction rate and the reaction order with respect to both reactants. In a first step, the solvent specific absorption maxima for the product have to be determined. According to the Lambert-Beer law (equation (3-8)) the absorption/extinction (E_λ) of light is equal to the product of the optical path length (L), the concentration (c) and the molar attenuation coefficient at this specific wavelength (ε_λ). The latter can be determined via measuring the absorption at different known concentrations and linear regression of the data, illustrated in Figure 3-11, to facilitate determination of unknown concentrations.

$$E_\lambda = \varepsilon_\lambda * c * L \tag{3-8}$$

Note: The Lambert-Beer law is only applicable if a number of criteria – e.g. homogeneous interaction medium and independent attenuators – are met, fortunately a deviation from the law becomes self-evident if a change in concentration does not correlate linearly to a change in absorption. Subsequently, the reaction rates (r, equation (3-9)) are determined through the increase of the product concentration via in situ UV-Vis spectroscopy of several reactions with known reactant concentrations, which is possible since for a basic bi-molecular reaction like the DASA formation, the product formation is equal to the consumed reactant. From this data the reaction rate constant (k) can be calculated. The last unknown kinetic parameters at this point are the partial reaction orders (x and y), i.e. the exponents of the concentrations effecting the reaction rate.

$$r = k * [A]^x * [B]^y \tag{3-9}$$

Those are determined via measuring of reaction rate at different reactant concentrations and calculation of the exponents according to equations (3-10) and (3-11), where r_{11} denominates the reaction rate determined for equal concentrations of reactants, r_{21} means a twice increased concentration of reactant A and r_{12} a twofold increased concentration of reactant B.

$$x = log_2\left(\frac{r_{21}}{r_{11}}\right) \tag{3-10}$$

$$y = log_2\left(\frac{r_{12}}{r_{11}}\right) \tag{3-11}$$

The solubility of the reactants in the given solvents, combined with the kinetic data enables one to calculate relative reaction rates as the product of reaction rate constant (k) and reactant concentrations to the power of the partial reaction orders. For example, a second order bimolecular reaction will show a 4-fold increased conversion rate when the reactant concentrations are doubled. The latter provides all necessary information for efficient decision on which solvent-system is to be used ideally.

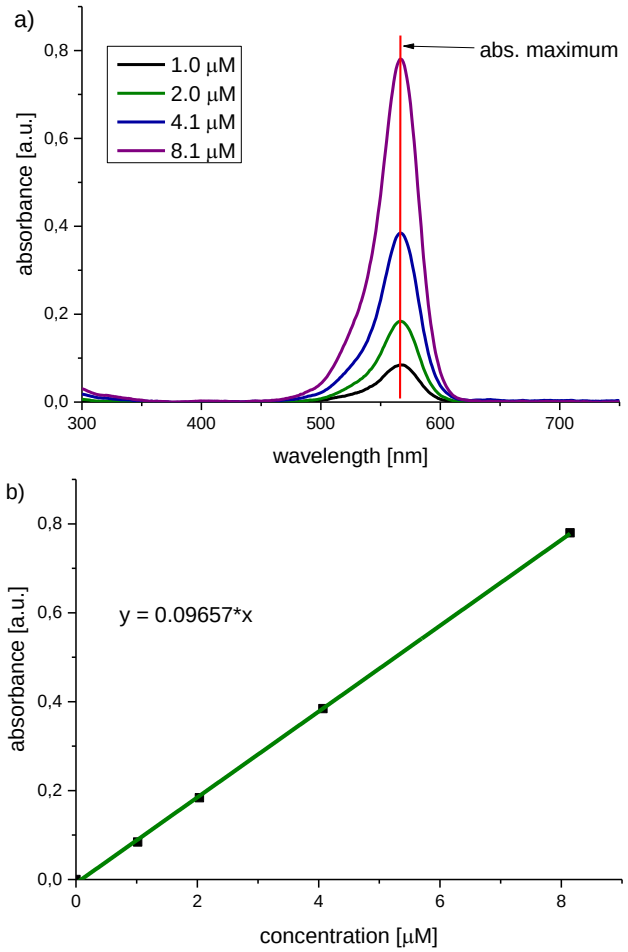

Figure 3-11: a) UV-Vis spectra of 5-((2Z,4E)-5-(diethylamino)-2-hydroxypenta-2,4-dien-1-ylidene)-1,3-dimethyl-pyrimidine-2,4,6(1H,3H,5H)-trione (DASA synthesized using *N,N'*-dimethyl barbituric acid and diethylamine) in $CHCl_3$ in different concentrations, λ_{max} = 566 nm. b) Determination of absorption coefficient based on the plot of the maxima provided by a).

3.4. Coating methods for paper and model substrates

In general, a broad range of different coating methods can be used to apply colloidal or dissolved coatings onto surfaces. In this section common techniques used for the coating of paper and shed light in their respective advantages and disadvantages will be discussed. Furthermore, the basic principles behind dip-coating, which were employed to create model surfaces, will be presented. The following section is based primarily on the book sections “Paper and Board, 7. Coating of Paper and Board” and “Taschenbuch der Papiertechnik, 12. Streichen von Papieren”, respectively. [146-147]

While uncoated papers play an important role in packaging, tissue, or even high voltage transformers, a broad range of desirable surface properties can be introduced trough the addition of coatings. In almost all cases these coatings are applied as aqueous dispersion, referred to as coating colors, with solid contents typically ranging from 15 to 70 % by weight. Conventional paper coating colors are composed of pigments, binders and process additives like viscosity modulators and defoaming agents. The composition of the color depends on the surface properties that the coating aims to achieve, the coating method, and base paper. Furthermore, a paper with expensive coating components, like a coating that is intended to provide barrier properties against oxygen (e.g. ethylene vinyl alcohol, EVOH), will typically be coated in several steps. First a base coat containing clay and/or calcium carbonate as pigment is applied with a direct application method (details below) to close and level the paper. This surface provides the basis for subsequent coating with functional components – in this example EVOH – to provide the desired properties while using minimal amounts of expensive materials. Looking into coating techniques, there are two main approaches when it comes to the actual application of the color onto the substrate. The first approach deposits an excess amount of color on the paper and meters it by a secondary process through removal of excess material, this approach is also called the direct method, Figure 3-12 a. While this strategy is typically used for base coatings, to yield an even surface as lined out earlier, the second approach is applying a predetermined amount of color per surface area, which is the reason why it is referred to as indirect approach, Figure 3-12 b. Indirect methods are used primarily if well-defined and highly homogeneous coating weights are desired and the for expensive coating colors, to minimize waste.

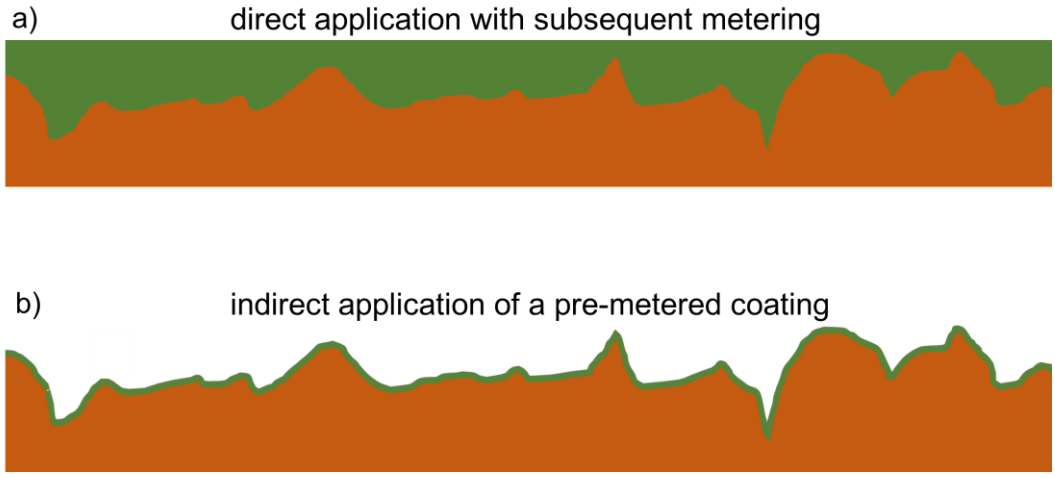

Figure 3-12: Schematic illustration of a rough paper coated using a) a direct application method, e.g. blade coating and b) an indirect method like roll-transfer coating.

The direct methods differ primarily in the way in which the paint is initially applied, the two main methods are application from a roll (not to be confused with the indirect film press) and jet application. Roll application (Figure 3-13 a) transfers the color in a nip between the color carrying roll and the roll backed paper web, this limits the maximum operating speed through fluid dynamics in the nip gap and increased water penetration through nip load. These drawbacks are eliminated via jet application (Figure 3-13 b), where a thin continuous jet of color is applied in a contact free system, which also bears the benefit, that the amount of color that is initially applied can be reduced in comparison to roll application. Whatever method is used for primary application in these direct methods, the final amount of coating is metered by subsequent scraping off of excess color with a blade (smoother finish) or a metering rod (better coverage).

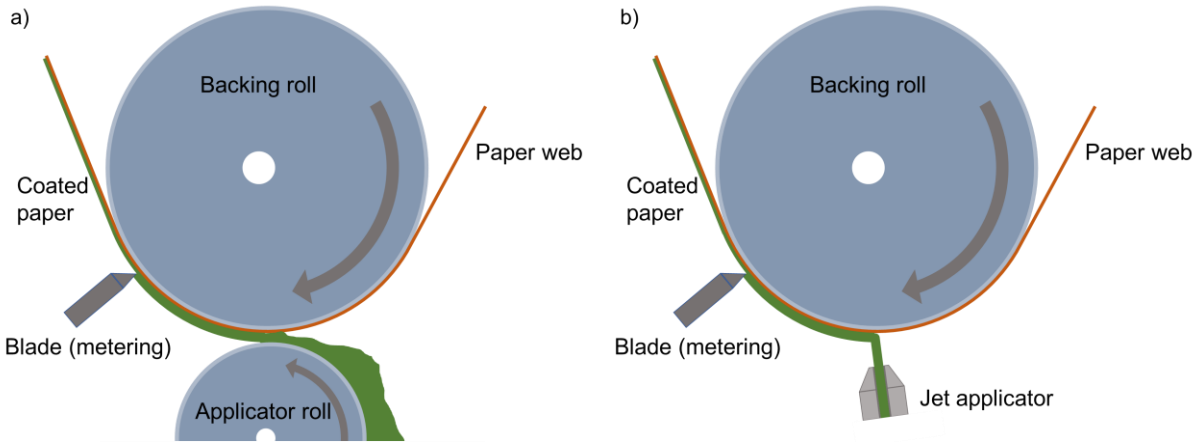

Figure 3-13: Direct application of a coating color to a paper web via a) roller application and b) jet application, followed by subsequent metering with a blade to yield a smooth surface on the coated paper.

In comparison the indirect method is using a roll on which the coating metered with rods prior to the application on the paper web, Figure 3-14. This film pressing process, which is similar to the operation of a size press, has the distinct advantage, that both sides of the web can be coated simultaneously and that, in comparison to the direct methods, lower coat weights can be achieved. Furthermore, the amount of coating applied per unit area is largely independent of the substrate topology which leads to homogeneous coating distributions. Nevertheless, at higher speeds this method tends to produce a mist of coating color during the transfer process which can impede surface quality.

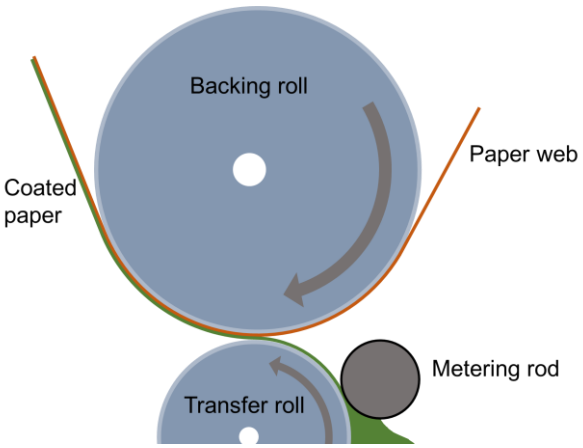

Figure 3-14: Indirect application of a pre-metered coating to a paper web though the use of a transfer roll, on which the film-thickness is metered by an either smooth or structured (depending on the application) metering rod.

There are however two more methods, which have been emerging recently, that don't quite fit in the two aforementioned categories, namely curtain and spray coating. While curtain coating is known since the 19th century, it only gained substantial traction on a larger scale in the last 25 years with an increased demand in specialty papers. In a curtain coater, the color is applied as a free falling liquid film – the curtain – which is produced from a slit nozzle that is placed above the moving web, as shown in Figure 3-15. The film is metered trough the nozzle size, via the gravitational forces working during the vertical fall and also by the speed of the fiber web. This leads to exceptional coverage and homogeneity of the coating, which enables the use of a minimum amount of expensive specialty coating color. Furthermore, due to the contact free nature of this method, it is much less prone to web breaks, which is of great importance to reduce waste and increase efficiency. Finally, there is spray coating as newest arising method for paper coating. During this process the color is atomized in a nozzle and transferred in a contact free manner, similar to curtain coating. While this process is able to precisely dose coatings, there are some limitations. To overcome mottling and infer complete coverage, the droplets have to disperse and coalesce, once on the paper surface. This allows only relatively low viscosity colors, with comparatively low solid contents and the base paper must exhibit low water absorption. Due to this limitations spray coating is only used sparsely on a larger scale.[148]

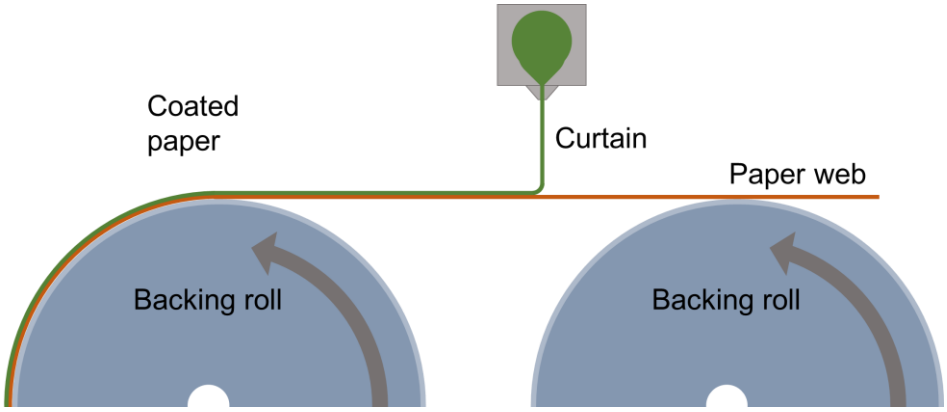

Figure 3-15: General operation of a curtain coater, the metering is performed through the gap in the nozzle, the length of the fall and the velocity of the web. The final coatings excel in homogeneity of coat thickness, but the setup and maintenance of a well running curtain can be rather challenging.

On the lab scale, the dominating technique to produce paper coatings is called film application. This utilized an automatic film applicator which draws a frame with a defined gap or a spiral rod across the surface which meter the coat height similarly to direct blade coating used on an industrial scale, as seen in Figure 3-16 a. The final coat weight corresponds to the height of the gap or the geometry of the spiral rod. Typically, the wet layer height is 30 to 40 % lower than the theoretical value due to sheering of the wet layer in the metering gap. While the technique is well established, it shows similar limitations towards the coating thickness as blade metered coating, and coating thicknesses below 5 g/m² – at least on paper webs without a basecoat – are typically accompanied by mottling and uncoated areas. Because of these drawbacks, a method following the indirect, pre-metered approach is also realized on the lab scale through the use of a multi-roll system, which is displayed in Figure 3-16 b. Furthermore, spray coating (mostly handheld) is often utilized to deposit coatings when small coat weights and homogeneous coating distribution are desired and volatile components are involved. This method is highly versatile and can be used with organic solvents as well as water borne coatings. Furthermore, the coat weight can easily be

adjusted by subsequent coating steps without risk of surface destruction due to the contactless nature of this process.

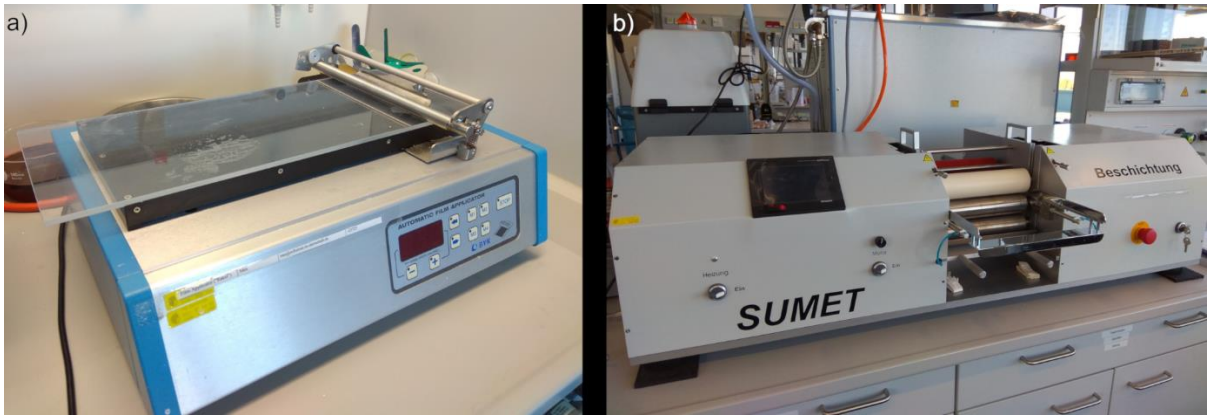

Figure 3-16: Lab-scale coating devices for realization of a) direct application followed by metering with a rod and b) application of a pre-metered coating utilizing a multi-roller system to obtain highly controlled films.

Beyond the methods for paper coating, a method that has found widespread attention in the creation of coatings from sol-gel processes is dip-coating. The process is on the first glance rather trivial: A dip-coating solution is prepared, which in the most basic system consists of partially polymerized siloxanes, and subsequently the substrate is dipped vertically into the solution and – with a controlled rate – pulled out again. But there is in fact nothing trivial about dip-coating, even for this basic system, there are a range of different processes involved in the method. The first important step is the formation of a gel phase in the coating solution, which is in this case achieved through pre-condensation, subsequently the transferred amount of coating is determined by the viscosity, degree of polymerization, gel content, withdrawal rate, ambient atmosphere, pretreatment of the substrate, and sol-gel interactions. For brevities sake the reader is referred to the following references as starting point for further studies. [149-150] The brief conclusion here is, that dip coating needs to be carried out with considerations to all the above mentioned factors in a well-defined environment to guarantee reproducibility and facilitate precise control over the achieved surface properties. With regards to siloxane based coatings, this method is a facile way to produce coatings with a defined surface chemistry – e.g. through the incorporation of allyltriethoxysilane – which is one of the reasons for its recent popularity.

3.5. Analysis of surfaces and coatings

This part of the section will cover water contact angle (CA) analysis, note that CA analysis can be carried out using different liquid phases, or even gases in inverted setups. When a droplet of water is placed on a surface the outer border of the contact area is formed by a line where the three phases – liquid, solid, and gaseous – are in contact, hence the name 3-phase contact line. When the system is in an equilibrium state, the angle between the liquid-sold and liquid-gas interface (contact angle, θ) is determined by the interfacial free energies at the three interfaces (γ_{SL}, γ_{SG}, and γ_{LG}) and the surface structure, Figure 3-17. For an ideal flat surface the relation between contact angle and the surface tensions follow Youngs equation (equation 3-12).[151]

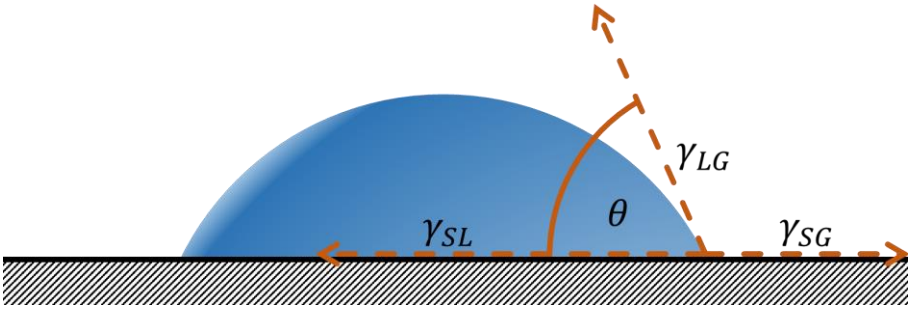

Figure 3-17: Determination of the contact angle and the relevant energies involved according to Young. This model does not take into account surface roughness and does in fact assume a molecular perfect planer surface.

$$\cos\theta = \frac{\gamma_{SG} - \gamma_{SL}}{\gamma_{LG}} \tag{3-12}$$

Unfortunately, atomically smooth surfaces are not the typical makeup of samples in the real world, hence a range of different approaches to account for rough surface topologies have been developed. The two prevalent models to describe wetting on rough surfaces are the Wenzel and the Cassie-Baxter model, Figure 3-18. Following Wenzels model (equation 3-13) introduces a roughness factor (r) to Youngs equation, to accommodate for deviations of a non-ideal surface from the ideal model. This assumes penetration of the water into the valley of a textured surface, which is hence commonly referred to as Wenzel state.[152] If the droplet is however not wetting the valleys of the rough surface, the Cassie-Baxter model (equation 3-14) applies. This model factors in the fraction of the surface below the droplet that is actually wetted, i.e. in contact with the water (f). [153-154]

$$\cos\theta^* = r * \cos\theta \tag{3-13}$$

$$\cos\theta^* = r * f * \cos\theta + f - 1 \tag{3-14}$$

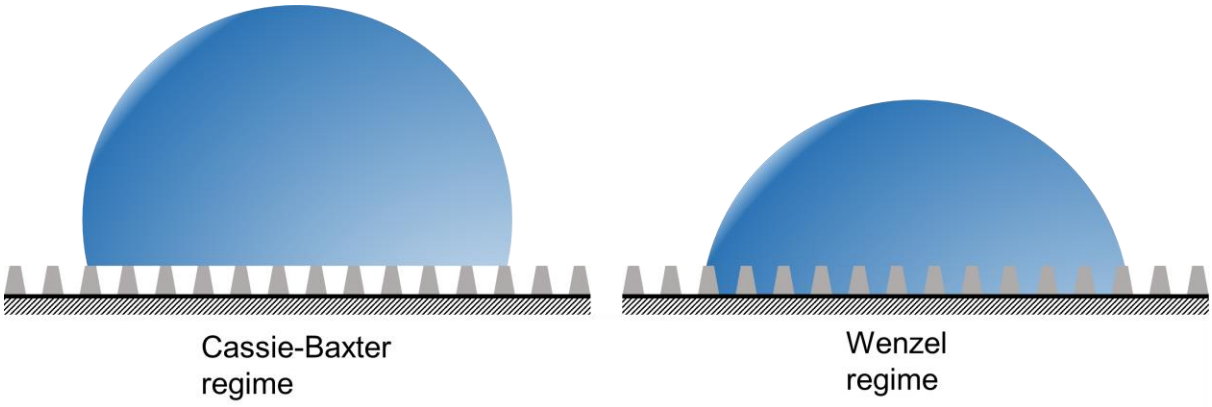

Figure 3-18: The Cassie-Baxter model (left) and Wenzel model (right) both take into account surface roughness when trying to describe the contact angle theoretically, while the more complex Cassie-Baxter model does in fact take into account only partial wetting below the droplet, the Wenzel model assumes complete wetting below the droplet. The equations describing both regimes become interchangeable once the wetted surface fraction (f) becomes 1, leading to the conclusion, that the Wenzel model is in fact a special case of the Cassie-Baxter model.

Whether the wetting is in a Wenzel or in a Cassie-Baxter state, can be determined through the contact angle hysteresis, i.e. the difference of the advancing and receding contact angle. A high CA hysteresis indicates, that the droplet is in a Wenzel state. In contrast a low CA hysteresis points towards Cassie-Baxter like behavior, which can be explained by the reduced contact area, which in turn reduced the amount of pinning and accompanying stick-slip phenomena. [155-156] Note that this model is in perfect agreement with Wenzels model since for complete wetting of the valleys, f becomes 1 and both equations will be equivalent. And in fact a transition between the Cassie-Baxter and Wenzel state is regularly used to produce a stimulus induced change in wetting, the transition is in general however irreversible.

3.6. Principles of confocal fluorescence scanning microscopy (CLSM)

The aim of this section is to convey the basic operating principles of a CLSM. A decent understanding of this advanced imaging technique requires basic concepts of fluorescence, wide field fluorescence microscopy, and scanning microscopy techniques, which will be explained briefly. This section is based on chapter 1 through 3, and 11 of the textbook "Molecular Fluorescence: Principles and Applications" from Bernard Valeur. [157]

For the analysis via fluorescence microscopy, samples have to contain fluorophores that are either natural occurring (like for example lignin) or are introduced on purpose to label components of interest. These fluorophores are illuminated with a controlled/defined spectrum of light, that covers wavelengths which have to overlap with the excitation spectrum of the fluorophore. This excitation promotes the molecules from the stable electronic ground state (S_0) into an exited singlet state ($S_{1\text{-}X}$). Due to the timeframe of this process – in the range of 10^{-15} seconds – the exited singlet state is most likely the one with the highest molecule orbital overlap to the ground state, since molecular vibration or movement to accommodate for electronic change occur three orders of magnitude slower (10^{-12} s range). This is called the Franck-Condon principle and the state resulting of this vertical transition is referred to as Franck-Condon state, Figure 3-19. If a singlet state above S_1 (i.e. S_2) is reached, the system relaxes partially through internal conversion until S_1 is reached and if vibrational energy level above the lowest level of S_1 is present, the molecule will dissipate this additions energy through vibration until the vibrational state 0 of S_1 is reached. Because the energy gap between S_1 and S_0 is larger than the gap between subsequent higher energy states, the transition from S_1 to S_0 can be achieved by other relaxation mechanism than internal conversion, i.e. spontaneous emission of photons (fluorescence) and intersystem crossing to triplet states that relax trough phosphorescence (delayed emission of photons), Figure 3-20.

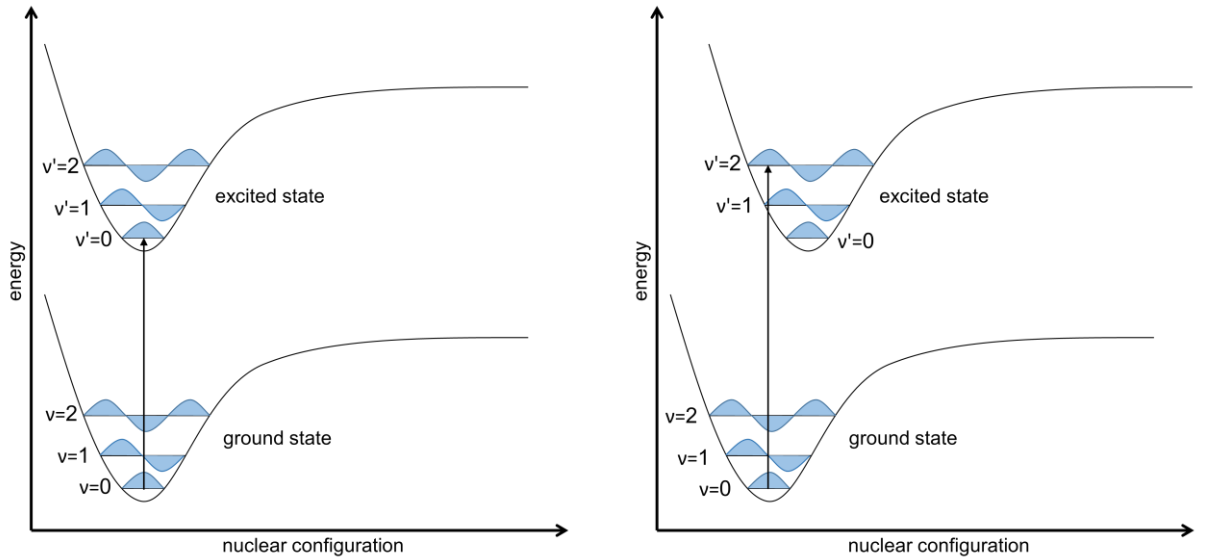

Figure 3-19: Illustration of the Franck-Condon principle. It states, that a vertical transition with minimal change in nuclear configuration (vertical arrow) is the preferred. In practice this means, that a transition to higher vibration level (i.e. v' = 2, right) in the exited state might be favored, even if the energy needed is higher than a transition to v` = 0. This is based on the fast nature of electronic transitions, compared to changes in nuclear configuration. This figure is redrawn from chapter 2.4 in the textbook by Bernard Valeur.[157]

When fluorescence occurs, it could be expected, that the emitted photons would be of the same wavelength as the photons absorbed during the excitation process. Nevertheless, since electrons can be exited to higher states then the lowest S_1 state (absorbing lower wavelength

photons) and also de-excite to a vibrational higher S_0 state (emitting lower energy, higher wavelength photons), the emission spectrum is red-shifted. This phenomenon is referred to as “Stokes shift” named after George Gabriel Stokes. The partial overlap of the emission and absorption spectra, which is oftentimes present, appears to violate this.

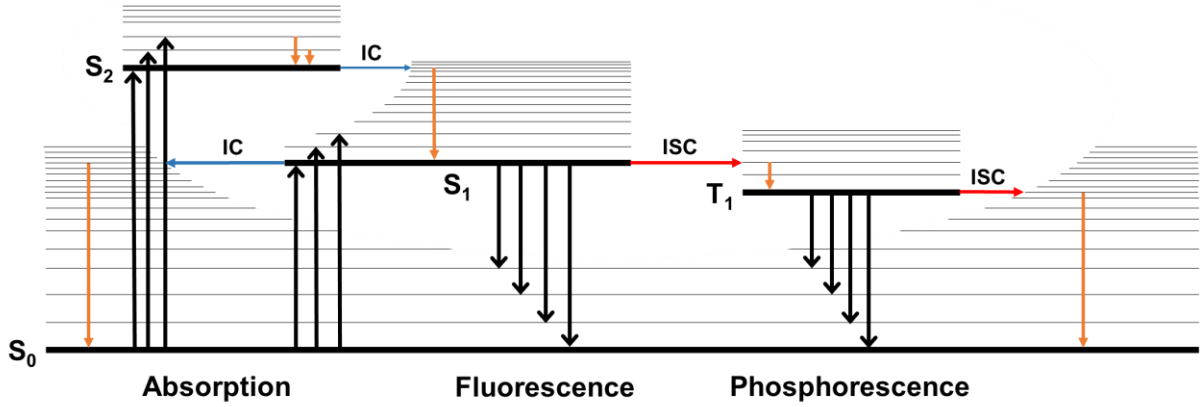

Figure 3-20: Perrin-Jablonski diagram, to the left, the absorption of high energy photons and subsequent promotion of electrons from the ground state S_0 to different vibrational levels of the excited states S_1 and S_2 is illustrated. Through vibrational relaxation (orange), and internal conversion (IC, blue) the electrons can reach the lowest vibrational level of S_1 and subsequently relax via fluorescence. Alternative relaxations Pathways include inter system crossing (ISC, red) to a triplet state and subsequent fluorescence or relaxation without emission of photons. This figure is redrawn from chapter 3.1 in the textbook by Bernard Valeur.[157]

In fluorescence microscopes the excitation is accomplished by light sources ranging from gas arc lamps, over LEDs combined with excitation filters, to lasers (Figure 3-21). A portion of this light is absorbed by the fluorophores and promotes them into an excited state, which leads to the subsequent emission of higher wavelength light through fluorescence. This light is then isolated from the remaining excitation light by a dichroitic mirror acting as beam splitter before it is diverted through a secondary emission filter into the occular for viewing by eye or into a tubular lens combined with a camera. The purpose of the secondary filter is to isolate precisely the wavelengths of interest and eliminate all residual excitation light to further improve imaging quality and yield a bright fluorescent image against a dark background. While this wide field microscopy setup is broadly implemented it comes with a big intrinsic challenge. Not only light from the focal is observed plane but also from areas that are out of focus. This leads to so called out-of-focus blur, which diminishes image quality and makes observation of three dimensional samples challenging. In this case, structures of interest may be obscured, and relative sample concentrations cannot precisely be determined, since the features may be overlaying each other.

While these drawbacks can be compensated partially by deconvolution and other post-processing like focus stacking, confocal laser scanning microscopy (CLSM) was introduced commercially in the 1980s to address this challenge on a fundamental level. CLSM enables the user to scan the isolated focal plane, by blocking all photons emitted from fluorophores that are not located in the focal plane (Figure 3-21, right). As of today CLSMs are highly sophisticated devices, easily costing several 100k $, nevertheless the basic function relies on fundamental optical principles. Note, CLSM is a scanning technique, in contrast to wide field microscopy, where an image is projected. This infers, that at any given moment in time only distinct spots of the sample are observed. The light utilized by CLSMs is produced from a laser and “cleaned up” optically to produce a small, evenly illuminated area in the sample. The

light is then guided through a x/y servo controlled mirror array into the objective and onto the sample, where it excites fluorophores in a given spot that can be moved via the mirror array. The fluorophores that are excited in this spot subsequently emit fluorescent photons, that are – in a manner similar to the wide field setup – separated from the excitation photons by a dichroitic mirror and a subsequent emission filter. Now the key component of the CLSM comes into play, a pinhole (which is acting as an optical aperture) blocks all emitted photons that do not originate from the focal plane. This is also one major drawback of CLSM, compared to wide field microscopy, since only a small portion of the emitted light is collect, overall higher amounts of energy have to be deposited into the samples, which in turn increases the risk of photobleaching und phototoxicity (the latter only applies to living samples, e.g. cells). The isolated photons are then detected by a "device" that converts photons into an electrical signal.

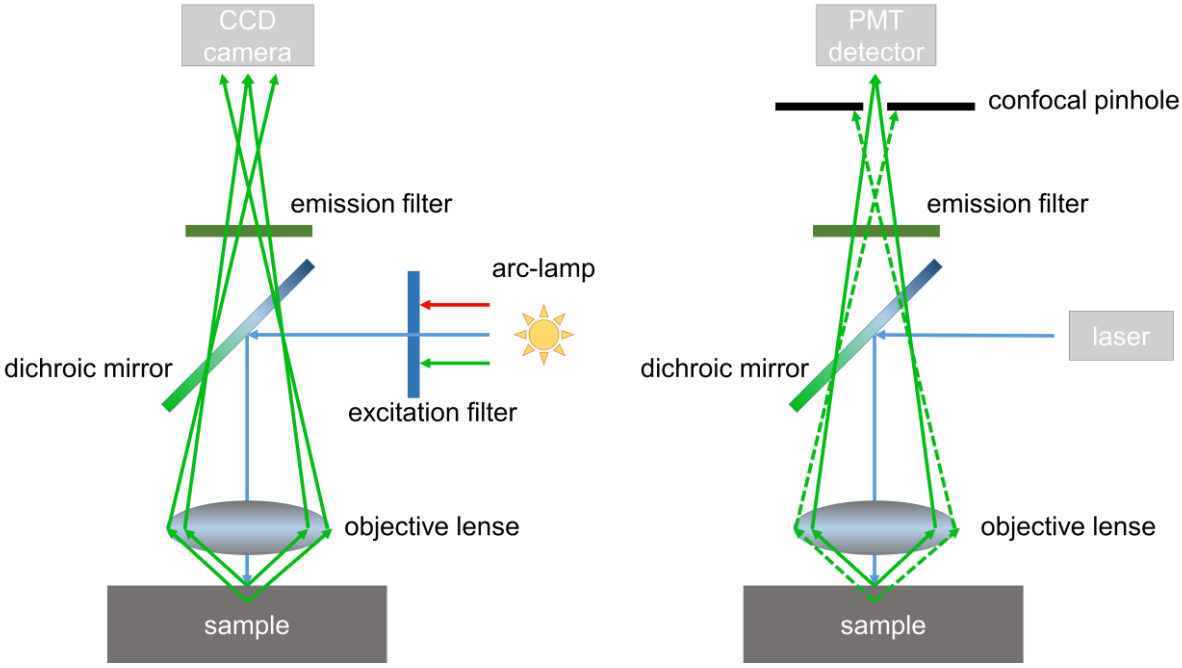

Figure 3-21: Side-by-side comparison between a wide field fluorescence microscope setup (left) and a confocal microscope (right). The main difference in the optical setup lies in the presence of the confocal pinhole, which is essentially an aperture that blocks all photons, which emerge from planes that are not in focus. Additionally, the CLSM is not projecting an image, but rather scans the sample spot wise and composes the image in software, similar to the function of a SEM. This figure is based on a schematic from chapter 11 in the textbook by Bernard Valeur.[157]

The most widely used implementation of this is a photomultiplier tube (PMT), which is rather robust, but needs comparatively high photon counts for good signal to noise ratios, alternatively photodiodes (PIPN-configuration) or hybrid detectors are employed, which are more susceptible to damage by excess illumination but can provide better signal to noise ratios at low photon counts. The data generated by this is correlated with the known location and size of the laser spot and assembled into an image a dedicated computer. Through the advent of piezo electrical motors, it is possible to precisely and repeatable control the z-position of the sample in the sub micrometer range, this allows vertical (optical) slicing of the samples, given they are sufficiently translucent for light, without the need to prepare cross sections. To give an idea of the optical limitations, this means that a typical lab-formed paper sample can be scanned in z-positions up to 30 μm deep into the highly scattering material until the effect diminishes image quality. For optical translucent samples, like clear polymers,

several 100 μm are however easy to achieve. This feature is especially interesting for analysis of coatings and material distribution.

4. Cumulative Part

4.1. Functional surface coatings from tailor-made long-chain hydroxypropyl cellulose ester nanoparticles

The content of this chapter has been published in:

Maximilian Nau, David Seelinger, Markus Biesalski, "Functional surface coatings from tailor-made long-chain hydroxypropyl cellulose ester nanoparticles", *Cellulose*, **2018**, 25 (10), 5769-5780 published by Springer Nature, © 2018, reprinted with permission.

During the first phase of this work we were focused on gaining a more detailed understanding of the esterification of hydroxypropyl cellulose with fatty acids. This curiosity was based on our interest in the investigation of HPC as bio-based building block for the production of functional polymers. The choice fell on HPC as starting material as compared to, e.g. cellulose, this compound is intrinsically soluble in a wide range of organic solvents, which in turn opens up a broad spectrum of possible modification. Initial investigations were focused on fatty acid esterification, because only a small amount of work was present in the literature, hence we choose this reaction type as a facile way to gain insight into the reaction behavior of HPC and produce first functional materials. For this purpose, we compared range of different reaction conditions, with the finding that neat, dry THF provided the best results (DS 3 after 6h @ 83 °C) in terms of control, toxicity and workup, while the reaction with 4-dimethylaminopyridine (4-DMAP) under Schotten-Baumann conditions provided the fastest overall conversion (DS 3 after 3h@ 110°C). Subsequently, we analyzed reaction kinetics for the derivatization with lauric, myristic, palmitic, and stearic acid chloride, Figure 4-1 a, with the interesting finding, that the reactions became faster with increasing fatty acid chain length. Those results opposed the expected trend, since for reactions with low molecular weight alcohols, the reactivity of acid chlorides diminished with increasing chain length. We suspected the opening of the polymer coil during the conversion as reason for this behavior, which would mean that the apparent difference in reactivity stems from a difference in the reactivity of the partially modified HPC during conversion. To investigate further, we prepared half-way converted (DS 1.5) HPC with lauric and stearic acid chloride, respectively. These two HPC derivatives were now both converted with stearic acid chlorides under identical conditions and the kinetics of both reactions were monitored, Figure 4-1 b. We found that the lauric acid HPC ester reacted considerably slower at first, but then started to accelerate with increasing stearoyl content, which infers that the reaction speed is in fact controlled via the accessibility/reactivity of the alcohol moieties presented by polymer. Subsequently, we investigated thermal behavior of HPC-fatty acid esters with different fatty acids and degrees of substitution, which led to a range of polymers with tunable melting and glass transitions points from -40°C to 39°C. In a first proof of principle, we finally produced nano-particle dispersions from the HPC stearic acid ester DS3 and prepared surfaces from these materials. The generated coatings provided super hydrophobic static contact angles (154±3°, sessile drop method), which could be thermally switched to become "just" hydrophobic with a CA of 111±4°, Figure 4-1 c and d. Worthy of note is that these particles could be transferred to an aqueous dispersion, which provides an advantage over comparable systems based on other polysaccharide derivatives.

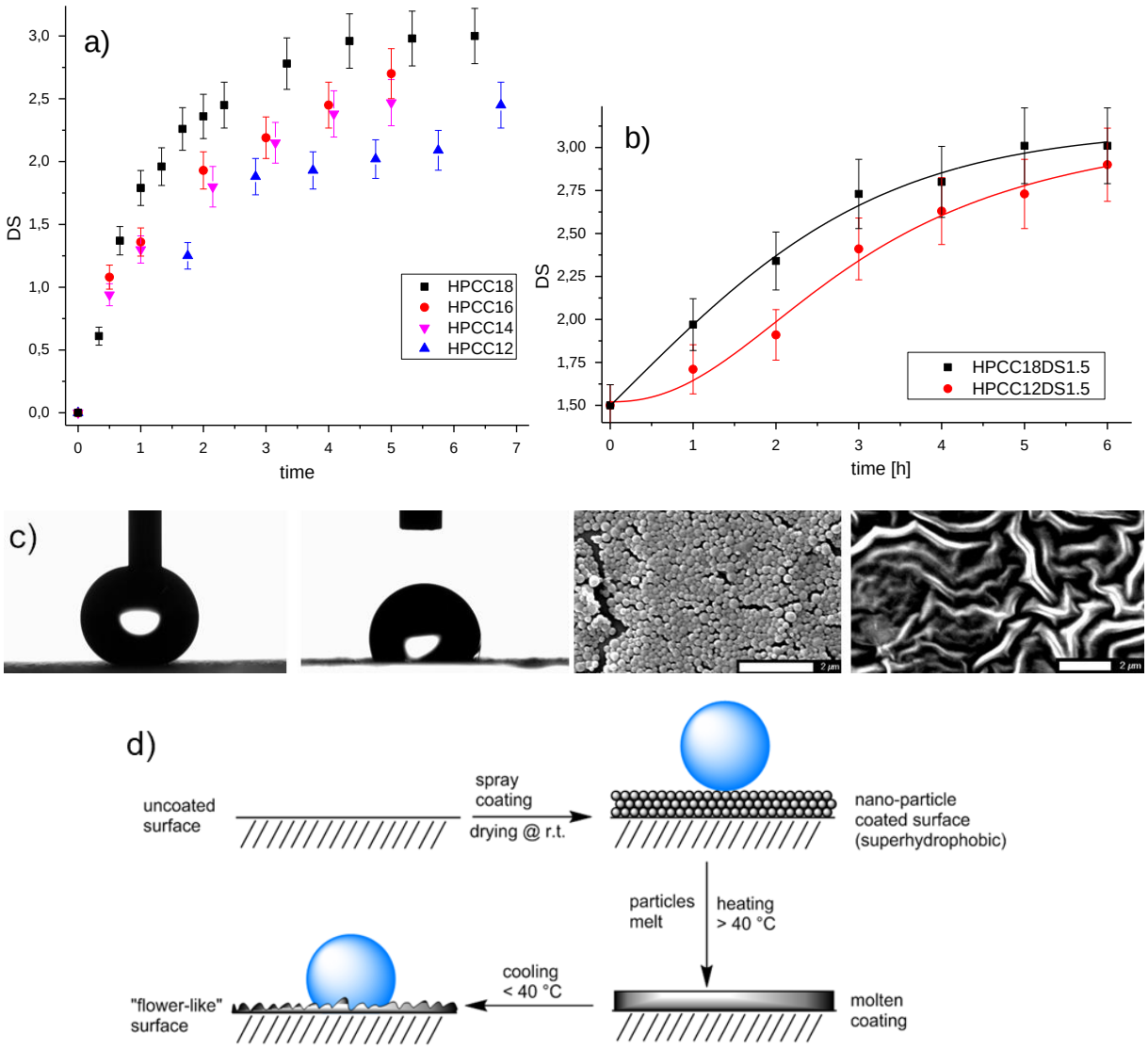

Figure 4-1: a) Kinetic analysis of the esterification of HPC in THF with different fatty acid chlorides. The kinetics approximately follow typical first-order kinetics. Surprisingly, lauric acid chloride shows the slowest reaction rate, even though the reactivity increases with decreasing chain length. This trend continues for the other fatty acid chlorides, with stearic acid chloride displaying the highest reaction rate. b) Kinetic analysis of the reactions between HPCC18DS1.5 and stearic acid chloride and between HPCC12DS1.5 and stearic acid chloride. The reaction of HPCC12DS1.5 initially shows a lower rate but then speeds up, leading to kinetics similar to the reaction of its C18 homologue. This observation indicates that the different and "inverse" overall reaction rates of HPC with stearic acid chloride and lauric acid chloride are the result of a difference in reactivity of the partially esterified HPC derivatives. c) Left: CA measurement of an HPCC18DS3-NP-coated glass slide. The surface is highly hydrophobic, which prevents the droplet from being released from the needle. Center left: Measurement of the same surface after the morphology is changed by heating. Center right: SEM image of a glass slide coated with HPCC18DS3-NP´s Right: SEM image of a "flat" HPCC18DS3 surface obtained after heating an NP coating above 40 °C. d) Visualization of the steps involved in preparing the surfaces depicted in c). Furthermore, the different wetting states on the nanoparticle surface (Cassie state) and the "flat" surface (Wenzel state) are illustrated.

Cellulose (2018) 25:5769–5780
https://doi.org/10.1007/s10570-018-1981-2

ORIGINAL PAPER

Functional surface coatings from tailor-made long-chain hydroxypropyl cellulose ester nanoparticles

Maximilian Nau · David Seelinger · Markus Biesalski

Received: 8 March 2018 / Accepted: 8 August 2018 / Published online: 10 August 2018

Abstract Hydroxypropyl cellulose (HPC)-esters were prepared by a homogeneous reaction of HPC with fatty acid chlorides. The effects of different solvent systems and reaction additives were evaluated, and plain, dried THF was established as best system in terms of toxicity, targeted synthesis of desired degree of substitution (DS), chain degradation and ease of workup. Moreover, pyridine/4-dimethylaminopyridine (4-DMAP) was found to be the fastest system overall. The reaction kinetics with different fatty acids—lauric, myristic, palmitic and stearic acid—were characterized and comprehensively compared. The DS could be adjusted precisely, giving control over the glass transition temperature (T_g)/melting point (T_m) of the HPC-esters, yielding a toolbox to tailor HPC-ester. In a next step, nanoparticles are formed from HPC stearic acid ester and used to generate superhydrophobic surface coatings, thereby demonstrating one of the interesting potential uses of this sustainable material.

Electronic supplementary material The online version of this article (https://doi.org/10.1007/s10570-018-1981-2) contains supplementary material, which is available to authorized users.

M. Nau · D. Seelinger · M. Biesalski (✉)
Ernst-Berl-Institut für Technische und Makrokolekulare Chemie, Technische Universität Darmstadt, Alarich-Weiss-Str. 8, 64287 Darmstadt, Germany
e-mail: biesalski@tu-darmstadt.de

Graphical abstract

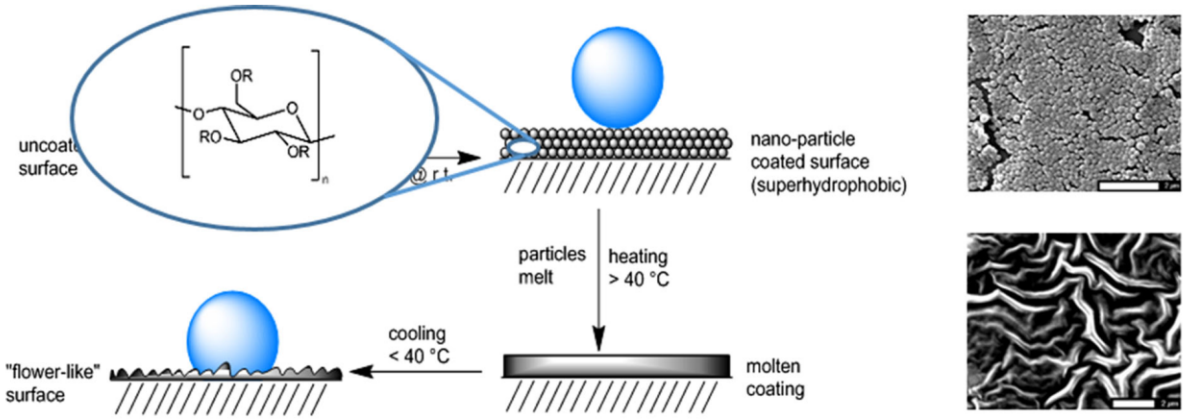

Keywords Hydroxypropyl cellulose · Sustainable thermoplastics · Bio based polymer · Kinetic investigation · Surface coating

Introduction

Cellulose modification, a well-known and widely investigated method for adding value to our planet's most abundant biopolymer, has introduced a plethora of bio-based products to the industrial world. Among the best known ways of modifying cellulose is esterification to provide products such as cellulose acetate, acetate/propionate and acetate/butyrate, which are produced mainly via the acetic acid/anhydride process (Malm et al. 1957; Malm and Tanghe 1955). Within the process of cellulose acetate synthesis, cellulose is converted to cellulose triacetate (CTA) via an initial heterogeneous reaction that accelerates during the conversion because partial esterification renders the cellulose soluble, thereby leading to high conversion through homogeneous reaction conditions. Since CTA exhibits poor dissolution and mechanical properties, this intermediate product is partly hydrolyzed in a second step to yield the widely used cellulose acetate with a degree of substitution (DS) of approximately 2.5, commonly referred to as *secondary acetate*. Such a reaction sequence is necessary because of the initially heterogeneous reaction (Malm et al. 1957; Malm and Tanghe 1955). The reactivity of the alcohol functionalities along the cellulose chains in a non-dissolved state is greatly restricted due to limited accessibility of groups not exposed on the material's surface to reactants (Meller 1953). Thus, for numerous specialty cellulose applications, various solvent systems for cellulose have been established to enable quantitative and tailored conversion and to obtain control of the distribution of the substituents (Heinze and Glasser 1998). Although considerable work has been done using these solvent systems, each of them presents distinct challenges. Specifically, the majority rely on solvents with high boiling points (e.g., DMAc/LiCl, DMF/N_2O_2, and DMSO/TBAF), which can pose a challenge in workup, whereas others are water based (e.g., cuprammonium hydroxide and cupriethylenediamine hydroxide) or contain ammonia and thus limit the available chemistry (Heinze and Koschella 2005; Launer and Wilson 1950; Ostlund et al. 2009; Philipp 1993; Sihtola et al. 1957). To circumvent these limitations, various readily soluble cellulose derivatives can be utilized as a cellulose-derived building block for further functionalization. This approach opens up the possibility of using accessible cellulose derivatives with high intrinsic solubility in common organic solvents. Consequently, we consider hydroxypropyl cellulose (HPC) a very promising bio-based polymer. HPC exhibits good solubility in a wide range of polar organic solvents and still provides 3 alcohol functionalities per anhydroglucose unit (AGU). Furthermore, it is readily available because of its widespread industrial use in concrete and food manufacturing (Wüstenberg 2014). HPC and its esters have already been investigated widely in the past, with a focus on their mesophasic behavior and thermal

properties (Hou et al. 2001; Ishizaki et al. 2015; Khan et al. 2008; Situ et al. 2015; Steinmeier and Zugenmaier 1988; Tseng et al. 1982; Tu et al. 2012; Yamagishi et al. 1994). In the literature, most studies used short-chain aliphatic esters; however, the longer fatty acid esters have been the subject of some limited work that has primarily focused on their thermal and crystallization behavior. Synthetic routes for the preparation of HPC fatty acid esters used pyridine and DMAc as solvents, which exhibit unfavorable characteristics such as high toxicity and high boiling points (Chen et al. 2017; Lee et al. 1997). Furthermore, for complete grafting, an excess of 3 eq. acid per alcohol functionality (i.e., 9 eq. per AGU) and equivalent amounts of tosyl chloride were utilized. Another interesting approach uses an enzyme-mediated esterification of HPC with lauric acid, which yielded ester contents of less than 15%, roughly corresponding to a degree of substitution (DS) < 1 (Sereti et al. 2001).

Although remarkable effort has been devoted to HPC modification, the behavior of the esterification reaction is still not fully understood: The selection of solvent in prior work appears to be a rather arbitrary choice between acetone, pyridine and THF, catalysts and scavengers such as tosyl chloride and triethylamine (TEA) were added according to standard procedures, but whether these agents have an influence on the achieved esterification, i.e., on the reaction kinetics, was not studied in detail. This lack of experimental evidence also applies to the employed solvent systems. However, only with a thorough understanding of such reaction kinetics, as well as possible limitations that may occur, and may be associated to various reaction conditions as well as to the molecular structure of the macromolecule itself, we will be capable to fully understand the structure–property relation. Therefore, in this work, we present a systematic and in-depth study of the effects of the aforementioned components on the esterification kinetics of HPC with fatty acids (C12, C14, C16 and C18) to obtain a fundamental understanding of this particular reaction. By this, we are closing the knowledge gap left by many other groups addressing similar reactions. The reaction conditions are optimized, including the choice of solvent, catalyst and scavenger. We reaffirm reliable and reproducible methods for characterizing the desired products. Furthermore, the underlying kinetics are examined, and the obtained products with varying DS are characterized. Primary aim of this particular part of the work was to establish a comprehensive set of data for reproducible synthesis condition of a range of different HPC fatty acid esters with tailored DS values. In the present literature such information is scarce to date. In a second part of our work, inspired by previous studies on cellulose-ester, we transfer HPC-ester into hydrophobic, nanoscale particles through nanoprecipitation. We evaluate the particle structure and we utilize and investigate these materials as coatings on planar surfaces.

Experimental section

Materials

Hydroxypropyl cellulose (Alfa Aesar, Mw 100.000 g/mol), stearic acid (Merck, 97%), sodium hydroxide (Grüssing, 99%), thionyl chloride (Sigma-Aldrich, 97%), toluene (Sigma Aldrich, 99.9%), $CDCl_3$ (Sigma Aldrich, 99.8%), methanol (Brenntag, technical grade), *n*-hexane (Brenntag, technical grade), isopropanol (Brenntag, technical grade), 4-dimethylaminopyridine (Sigma-Aldrich, 99%), propionic acid chloride (Acros Organics, 98%), $CaCl_2$ (Grüssing, 99%), molecular sieve (Roth, 3 Å), deuterium oxide (Sigma-Aldrich, 99.8%), triethylamine (Roth, 99%), diisopropylethylamine (Fluka, 99%), lauric acid chloride (Acros Organics, 98%), myristic acid chloride (Aldrich, 97%) and palmitic acid chloride (Merck, 98%) were used as received. THF (Roth, 98%), pyridine (Fisher, 99%) and chloroform (Roth, 99%) were dried according to standard procedures.

Methods

Synthesis of stearic acid chloride

Stearic acid (284.4 g, 1 mol) was placed in a 1000 mL round-bottom flask equipped with a KPG stirrer with a 75 mm blade, a reflux condenser and 3 gas-washing bottles. The first gas-washing bottle was connected inversely as a protective measure, the second was filled with distilled water to collect the bulk of the released HCl, and the third was filled with 5 M NaOH. Thionyl chloride (131 g, 1.1 mol, 1.1 eq.) dissolved in 200 mL of toluene was added and the reaction was heated to 75 °C until no more gas was released, which

indicated complete conversion. The reaction mixture was then fractionated by distillation, everything up to 180 °C under normal pressure was collected as residual reactants and decomposition by-products. For the next part of the distillation, the Liebig condenser was replaced by an ether bridge, and the product flask was cooled in liquid nitrogen. A vacuum of 0.5 mbar was applied, and the immersed flask was heated to 198 °C. Distilled stearic acid chloride was collected as a clear liquid with a melting point at 21–22 °C. The product was stored under nitrogen, and NMR analysis was conducted in $CDCl_3$ dried over molecular sieve (3 Å).

Synthesis of HPC fatty acid ester—general procedure

Dried HPC was dissolved in a given solvent at a concentration of 5 wt%; this concentration is chosen because viscosity increases greatly beyond this point. The dissolution can take up to several hours. In a typical reaction, 10 mmol AGU equivalents (4.855 g ≡ 103 mL of 5 wt% solution) of HPC was placed in a 250 mL round-bottom flask equipped with an egg-shaped magnetic stirring bar and a reflux condenser. A heating bath was preheated to 83 °C to investigate the reaction kinetics. Typically, 6 eq. of a given fatty acid chloride was dissolved in 20 mL of solvent. Note that the addition of undiluted acid chloride led to the precipitation of HPC, thus causing inhomogeneous reaction conditions. The fatty acid chloride solution was then added to the HPC solution, and the flask was placed in the preheated bath. It is imperative that the level of the heating oil used for the bath was below the reaction mixture level and that the reaction was vigorously stirred. If not done correctly, evaporation of the solvent causes the formation of a polymer layer on the inner surface of the reaction vessel, leading to inhomogeneous conversion. If additives were used, they were added at this time. During workup, different precipitation methods had to be employed because the solubility of HPC fatty acids changes with the DS. For DS < 1.3, the reaction was quenched by adding 3 vol% MeOH, and then the resulting polymer was precipitated in four parts (∼ 1000 mL) of *n*-hexane. The resulting polymer was isolated by decanting, redissolved in 200 mL of THF and reprecipitated in 1000 mL of *n*-hexane; this procedure was repeated at least three times. For 1.3 < DS < 2.5, the HPC-esters can be directly precipitated in 1000 mL of isopropanol. The resulting polymer was isolated by decanting, redissolved in 200 mL THF and reprecipitated in 1000 mL of isopropanol; this procedure was repeated at least three times. For DS > 2.5, the polymer was precipitated in 1000 mL of a mixture of isopropanol and MeOH (4:1 by volume). The resulting polymer was isolated by decanting, redissolved in 200 mL THF and reprecipitated in 1000 mL of the same mixture as before; this procedure was repeated at least 3 times. The resulting polymers were dried under vacuum at 40 °C and 1 mbar for 48 h. Analysis is described in detail within the results-section.

Synthesis of fully propionated HPC

HPC (0.486 g, 1 mmol AGU equivalents) was dissolved in 10 mL of dried pyridine in a 50 mL round-bottom flask. 4-Dimethylaminopyridine (4-DMAP) (36 mg, 0.3 mmol) and propionic acid chloride (555 mg, 6 mmol) were added while stirring. The reaction mixture was then heated up to 60 °C for 24 h. The product was precipitated in water. The resulting polymer was isolated by decanting, redissolved in THF and reprecipitated in water; this procedure was repeated three times. The resulting polymers were dried under vacuum at 40 °C and 1 mbar for 48 h. Analysis is described in detail within the results-section.

Nanoprecipitation of HPCC18DS3

A solution of 1 wt% HPCC18DS3 in THF was added dropwise to a fivefold volume of a stirred isopropanol-water mixture (9:1 by volume) at room temperature. Stirring had to be conducted with a bar stirrer rotating in range of 200 rpm (depending on vessel geometry). Note that too fast stirring led to aggregation of the polymers. After the addition of the polymer solution, stirring was continued for 30 min, and 0.5 wt% (calculated based on the HPCC18DS3 mass) $CaCl_2$ was added as a 5% solution in water. The system then started to form two layers over the course of approximately one h, with the particles accumulating in the lower part of the vessel. The upper part of the system became completely transparent. This up-concentration process continued for approximately 2 weeks, until a particle concentration of ∼ 10% was reached in the remaining precipitation solution.

Characterization methods

^{1}H-NMR spectra were recorded using 300 MHz Avance III NMR and 500 MHz Avance DRX spectrometers from Bruker. All deuterated solvents were acquired from Sigma Aldrich.

CHN elemental analysis (EA) was performed using a VarioEL III CHN from Elementar.

Size exclusion chromatography (SEC) analysis was conducted using a PSS-Agilent 1200 with an SDV column set from PSS (SDV 103, SDV 105 and SDV 106) at 30 °C using THF as the mobile phase with a flow rate of 1 mL/min and polystyrene (from Polymer Standard Service, Mainz) as internal standard.

Differential scanning calorimetry (DSC) analysis was conducted under nitrogen using a Mettler Toledo DSC with a heating/cooling rate of 10 K/min. If not mentioned otherwise, the analysis was based on the second heating cycle.

Dynamic light scattering (DLS) was performed using a Nanophox from Sympatec. The analysis was carried out in water with particle concentrations corresponding to count rates between 150 and 300 kcps.

Scanning electron microscopy (SEM) samples were sputtered with 10 nm Pt80/Pd20 in an argon plasma. The samples were analyzed using a Philips XL30 SEM equipped with a field effect gun. Acceleration voltages between 5 and 15 keV were used.

Contact angles (CA) were acquired with a Data-Physics Contact Angle System OCA 35. Each measurement used 4 µL of Millipore water. The measurements were carried out in a normal climate room with 50% relative humidity and 23 °C.

Errors for ^{1}H-NMR analysis were calculated via Gaussian error propagation with an assumed integral error of 5%. Errors for EA, DSC, DLS, SEM (size distribution) and CA were based on the standard deviation of multiple measurements.

Results and discussion

To simplify the following sections, we introduce a custom nomenclature for the HPC-esters: HPCCxDSy, where x indicates the number of carbon atoms in the corresponding acid and y indicates the DS; i.e., fully propionated HPC would be denoted HPCC3DS3.

Characterization of HPC and HPC-esters—optimized synthesis protocols

Any emerging application where HPC-esters may potentially be interesting candidates as biogenic polymers require a fundamental knowledge upon the structure–property relation of these macromolecules. As such, a control over molecular parameters, such as molar mass and chemical structure, in particular DS of the ester side-groups, are of utmost importance. Thus, a first step in our fundamental approach was to understand the behavior of HPC towards esterification. Reliable methods for determining the DS have been reported in the literature, such as ^{1}H-NMR, but since some challenges with the ^{1}H-NMR analysis of unmodified HPC were encountered, CNH-EA has additionally been utilized as a complementary method (Chen et al. 2017; Huang et al. 2007; Richardson et al. 2003). Note, during the process of HPC synthesis,

Table 1 Synthesis of HPC stearic acid esters from HPC and stearic acid chloride under different reaction conditions. Each reaction used 6 eq. of stearic acid chloride per mol AGU

#	DS_{NMR}	Solvent	Temp. (°C)	Reaction time (h)	Additive
1	1.9 ± 0.2	$CHCl_3$	83	3	
2	1.4 ± 0.1	Acetone	83	3	
3	1.8 ± 0.1	Pyridine	110	3	
4	3.1 ± 0.2	Pyridine	110	3	4-DMAP[a]
5	2.3 ± 0.2	THF	83	3	
6	2.0 ± 0.1	THF	83	3	TEA[b]
7	2.2 ± 0.2	THF	83	3	Pyridin[b]
8	1.7 ± 0.2	THF	83	3	DIPEA[b]
9	2.98 ± 0.1	THF	83	6	

[a]0.3 eq

[b]6 eq

cellulose can react with more than three eq. of propylene oxide per AGU; therefore, the parameter molar DS with propylene oxide (MS) is commonly used to describe HPC (Ho et al. 1972). Detailed description of MS and DS determination will not be outlined here, but can be found in the supplemental information.

Within the margin of error, the results obtained were very similar for elemental analysis and ^{1}H-NMR, thereby verifying ^{1}H-NMR as a valid standard analytical technique for this system. To establish optimized reaction conditions, solvent and additives were subsequently screened. For this task, different literature known systems were used under comparable conditions. The esterification with stearic acid chloride was chosen as a model reaction because it was presumably the slowest reaction among the esterifications with various fatty acids, as this behavior had been previously observed for the low-molecular-weight esterification of fatty acids (Liu et al. 2006). Therefore, this model thus should yield the best resolution in terms of acceleration/deceleration of the reaction because of the lower reaction rates. As solvents, acetone, THF, pyridine and chloroform were used. The investigated additives, which are commonly used for this type of reaction, were TEA, diisopropylethylamine (DIPEA), pyridine and 4-DMAP. HPCC18-esters were prepared according to the standard protocol given in the experimental section. After completion of the reaction, the DS of the polymers was analyzed by ^{1}H-NMR. The DS values along with the corresponding reaction conditions are displayed in Table 1.

The results obtained by changing only the solvents showed that among them, THF (#5) provided the fastest conversion, i.e., the highest DS (compared to #1–3). For the latter reason, THF was chosen as solvent for further additive screening. This finding was due to several factors: First, HPC was highly soluble in THF (the polymer dissolves readily within 10–15 min). In acetone, the HPC used did not yield a clear solution, whereas in $CHCl_3$ and pyridine, the dissolution process took 1–2 h. Regarding the use of reaction additives, pyridine combined with 4-DMAP (#4) afforded the highest reaction rate. Notably, however, this system was not further investigated because of the highly carcinogenic byproduct formed in this reaction (Levin 1997). When additives were used in THF (#6–8), the reactions consistently yielded lower DS values. Under normal esterification conditions, the reaction would be expected to follow a general base-catalyzed mechanism; however, the exact mode by which the base acts—either serving as acid scavenger or undergoing an intermediate substitution of the acyl compound—depends on the combination of acid chloride and alcohol (Hubbard and Brittain 1998). The unexpected behavior in the reaction here can be explained by the formation of the stearyl ketene dimer, as depicted in Scheme 1, which exhibits lower reactivity than the corresponding acid chloride—specifically, it is stable in aqueous solution for weeks. The synthesis of ketene dimers in aprotic solvents using a tertiary amine such as TEA as a reactant is well documented in the literature (Zhang et al. 2013). The initial step of ketene formation does not normally occur in this kind of esterification since it is slower than the esterification reaction. However, because of the low reactivity of the HPC alcohol functionalities, it was suspected to become an important factor in this system. In a reference experiment conducted in the same fashion but without HPC, stearyl ketene dimer was isolated from the reaction mixture, thus indicating that the aforementioned process occurs (^{1}H-NMR spectrum can be found in Figure SI 5).

Considering the results shown in Table 1, further experimental work was done under the "optimal"

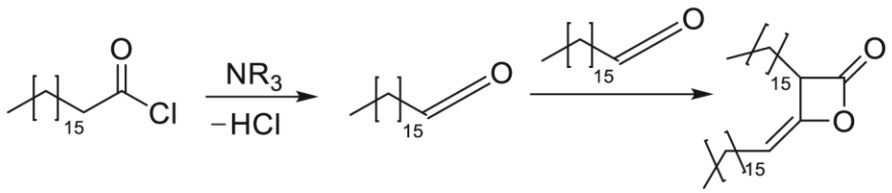

Scheme 1 Reaction steps involved in formation of stearyl ketene dimer. First, the stearic acid undergoes a base-catalyzed elimination of HCl, forming reactive ketene compounds. In the second step, these ketenes form dimers. Details regarding the mechanism of this reaction can be found in Zhang et al. (2013)

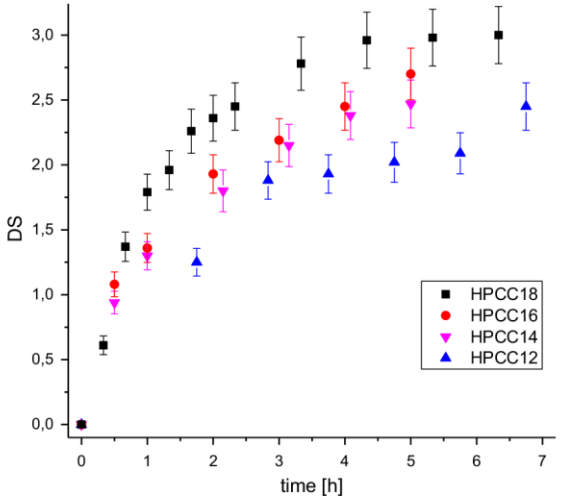

Fig. 1 Kinetic analysis of the esterification of HPC in THF with different fatty acid chlorides. The kinetics approximately followed typical first-order kinetics. Surprisingly, lauric acid chloride shows the slowest reaction rate, even though the reactivity increases with decreasing chain length. This trend continued for the other fatty acid chlorides, with stearic acid chloride displaying the highest reaction rate

conditions, i.e., pre-dried HPC dissolved in dry THF with no additives and T_{bath} = 83 °C.

Preparation of HPC fatty acid esters and analysis of the reaction kinetics

Next, to understand the reaction kinetics in more detail, we conducted a number of reactions using the previously determined optimum conditions. As a variable, the reaction times were altered between 30 min and 7 h. As another variable, the length of the fatty acid chain was considered, and in the first set of experiments, C12, C14, C16, and C18 fatty acid chlorides were used. The reaction kinetics for HPC fatty acid esterification using these 4 fatty acid chlorides are displayed in Fig. 1. The data indicate that the reactions were, in good approximation, following a simple first-order exponential function.

The results described above suggest that in general, the chemical reactivity and accessibility of the individual OH-groups present within the HPC at different positions may not significantly impact the esterification kinetics. However, once a significant number of ester bonds are formed, the accessibility of the free OH-groups may become dependent on the polymer macro-conformation as well. The second hypothesis was further underpinned by the finding that longer chain fatty acids reacted faster. The reactivity of carboxylic acids of linear alkanes decreases as the chain length increases. For the esterification of low-molecular-weight alcohols, this effect leads to higher reaction speeds (Liu et al. 2006). Thus, the expected behavior was a decrease in reaction speed with increasing chain length on the acid side. As mentioned before, the reactions becoming faster indicates that the larger C18 chains of the stearic acid ester groups induced a chain expansion. In particular, with increasing DS, the macromolecule was stretched along the main chain of the polysaccharide because of excluded volume effects. Comparable findings for cellulose stearic acid esters have been reported by Geißler et al., however, they only investigated the behaviour of cellulose stearate with DS 3 in neat THF (Geissler 2017; Geissler et al. 2013). The HPC fatty acids esters were suspected of forming rigid, brush-like structures in solution, which could explain these "upside-down" kinetics. In principle, scattering and/or combined viscosity/scattering techniques may be used to determine the actual polymer conformations. Since the macro-conformation of polymers is highly influenced by temperature, solvent as well as the presence of small molecules. As such, this kind of analysis is by no means trivial: Measurements need to be performed at reflux temperature under variable reaction conditions, obtaining accurate data for the polymer conformation

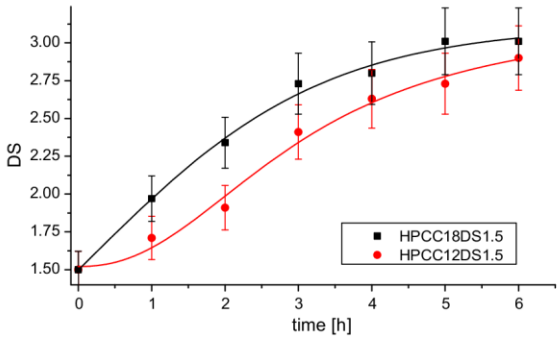

Fig. 2 Kinetic analysis of the reactions between HPCC18DS1.5 and stearic acid chloride and between HPCC12DS1.5 and stearic acid chloride. The reaction of HPCC12DS1.5 initially shows a lower rate but then speeds up, leading to kinetics similar to the reaction of its C18 homologue. This observation indicates that the different and "inverse" overall reaction rates of HPC with stearic acid chloride and lauric acid chloride were the result of a difference in reactivity of the partially esterified HPC derivatives

in situ. Nevertheless, to shed more light on the particular above mentioned hypothesis, we followed an indirect approach. Two additional kinetic measurements were performed using HPCC12DS1.5 and HPCC18DS1.5 as starting materials. Both polymers were reacted with 4.5 eq. of steric acid chloride under identical conditions. The evolution of the DS is depicted in Fig. 2. If the chain conformations were unaffected by the initial modification, then the reactions should exhibit identical kinetics. As it can be inferred from Fig. 2, this was clearly not the case, and the reaction using HPCC12DS1.5 as starting material was considerably slower than the reaction using HPCC18DS1.5. Furthermore, HPCC12DS1.5 was obviously not following a first-order exponential function, as it showed a significant delay-phase during the beginning of the reaction (0–2 h) and then accelerated to show the expected kinetics, reaching a final DS of almost 3, similar to the other sample with HPCC18DS1.5 used as starting material. Together with molar mass analytics (see below), these findings thus indicate that accessibility of the OH-groups is an important parameter, and it depends on the type of fatty acid used in the esterification step.

Table 2 T_g and T_m of selected HPC-esters, HPC lauric acid esters begin to show a transition at a DS of 1.5 with a T_g starts to appear at − 40 °C. with an increase in DS, that transition turns into a melting point at − 34 °C. For stearic acid esters the same tendency is apparent, mixed esters show a rather drastic change in thermal behaviour with only small changes in the DS

Polymer	DS_{NMR}	T_g	T_m
HPC-C12	1	n.a.	n.a.
HPC-C12	1.5	− 40 °C	n.a.
HPC-C12	2	− 38 °C	n.a.
HPC-C12	2.5	− 37 °C	− 34 °C
HPC-C12	3	n.a.	− 32 °C
HPC-C18	1	n.a.	n.a.
HPC-C18	1.5	4 °C	n.a.
HPC-C18	2	6 °C	27 °C
HPC-C18	2.5	n.a.	29 °C
HPC-C18	3	n.a.	39 °C
HPC-C18/C12	1.5/0.5	− 28 °C	n.a.
HPC-C18/C12	1.5/0.8	− 28 °C	− 11 °C
HPC-C18/C12	1.5/1.2	n.a.	− 1 °C
HPC-C18/C12	1.5/1.3	n.a.	5 °C
HPC-C18/C12	1.5/1.5	n.a.	16 °C

Thermal properties

The most remarkable feature of the prepared HPC-esters was the wide range of glass transition temperatures (T_g) and melting points (T_m) that could be achieved by adjusting the DS, a selection of which is displayed in Table 2. Our data match as well as complement (with respect to HPCC12) the study of Chen et al. (2017) on HPCC16/C18 esters, which was, to the best of our knowledge, the only work that very recently explored the thermal properties of HPC fatty acid esters. Compared to the literature data for cellulose fatty acid esters, the T_m values of HPC-esters were 15 K (C18)–19 K (C12) lower (Sealey et al. 1996). The mixed esters produced within the kinetic analysis displayed a melting transition that shifted with increasing DS of stearic acid, this combined with the thermal behavior of the myristic and palmitic acid esters yields the ability to tailor the melting point between − 34 and 39 °C via adjustment of fatty acid length and DS. Detailed DSC can be found in Figure SI 6 a–c.

Molar mass analysis

For strongly acidic reaction conditions, random chain fragmentation of HPC has been reported for HPC-esters prepared in acetone. This fragmentation is inferred from a strong decrease in the molar mass of

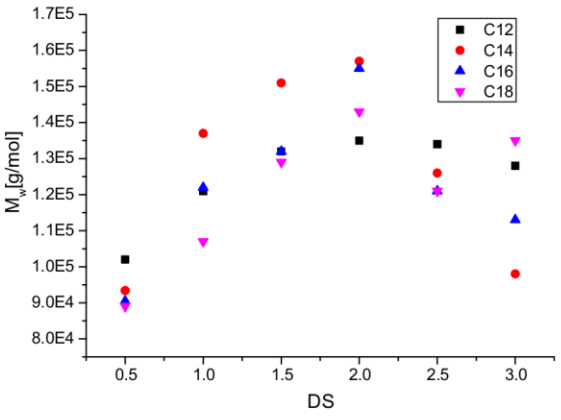

Fig. 3 Change in molecular mass (GPC) correlated with the DS for different HPC fatty acid esters. The apparent molar masses increased up until a DS of 2 and then began to decrease again

the polymer during esterification (Daruwalla and Nabar 1956; Hou et al. 2000). To investigate the possibility of polymer degradation with our macromolecules, HPC-esters prepared with their respective fatty acids were analyzed via SEC. Figure 3 shows the weight average molar mass as a function of the respective DS values for different HPC-esters. The apparent molar masses generally increased as the DS of the different fatty acids increased until a maximum at DS of 2 was reached. If DS $>$ 2 are considered, the apparent molar mass decreased; however, the polydispersity (M_w/M_n) did not increase, which would be the case if the polymer had degraded. This behavior again points to the change in polymer conformation, if sufficiently high substitution level has been reached; i.e., the polymer forms a straighter backbone, thus leading to hydrodynamic behavior that was completely different from that of the polystyrene standard used.

Most remarkably, we did not observe the random chain degradation associated with acidic cellulose hydrolysis, as indicated by the measurements of only monomodal mass distributions. This result could be attributed to the poor solubility of the formed hydrochloric acid in refluxing dry THF, as during the conversion, substantial amounts of gaseous HCl were released from the reaction mixture.

Nanoprecipitation of HPC-ester

Because HPC-esters with modular DSs were available by adjusting the esterification conditions, we turned our attention towards using these polymers as biogenic coating materials, alternative to fossil-based polymeric coatings. In particular, HPC-ester with high DS values should result in very hydrophobic coatings, which are of great interest in numerous applications. Recently, Geißler et al. have shown that cellulose C18 ester with a DS of 3 can be engineered into small particles by nanoprecipitation (Geissler et al. 2013). Such particles can be applied to various surfaces, including paper, to endow these materials with superhydrophobic properties. Inspired by this work, we were interested to learn whether similar approaches are possible with HPC-esters prepared here. Accordingly, we applied similar nanoprecipitation protocols to HPCC18DS3. A morphology analysis by microscopy means (details see below) showed that the prepared particles were very similar to those initially shown by Zhang et al. (2013). In contrast to the study by this group, and to produce more long-term stable particles, a different solvent system had to be used. The newly engineered isopropanol/water precipitation system for HPCC18DS3 has the distinct advantage that complete solvent exchange to water was easily possible while retaining the colloidal nature of the system. Note, for most applications, a water-based formulation of the coating material is of great interest. For size and structural characterization of the nanoparticles, DLS and SEM (Fig. 4, right) were used. The values for size and size distribution obtained from both methods matched sufficiently: SEM analysis provided a size of 177 $\pm$ 21 nm, whereas DLS yielded 186 $\pm$ 18 nm (Figure SI 7). The precipitation system used here is not suitable for other HPC fatty acid esters, as a solubility behavior can differ

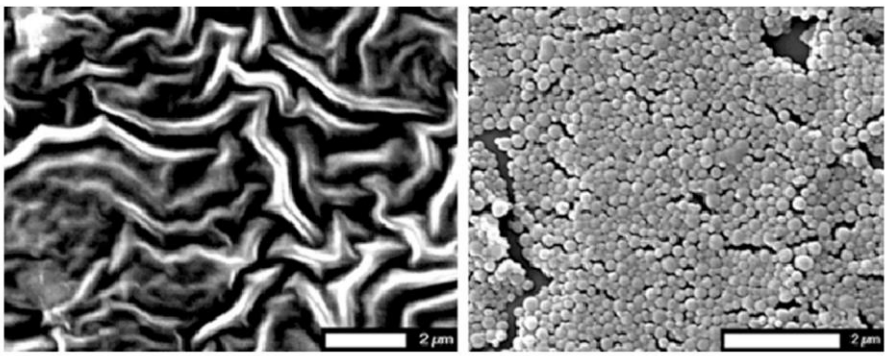

Fig. 4 Left: Morphology of a "flat" HPCC18DS3 surface obtained after heating an NP coating above 40 °C. These structures resemble the crystalline domains observed on short side-chain HPC-esters by Tu et al. who described these as "flower-like" Right: Determination of the size distribution of HPCC18DS3NP via graphical image analysis using SEM imaging

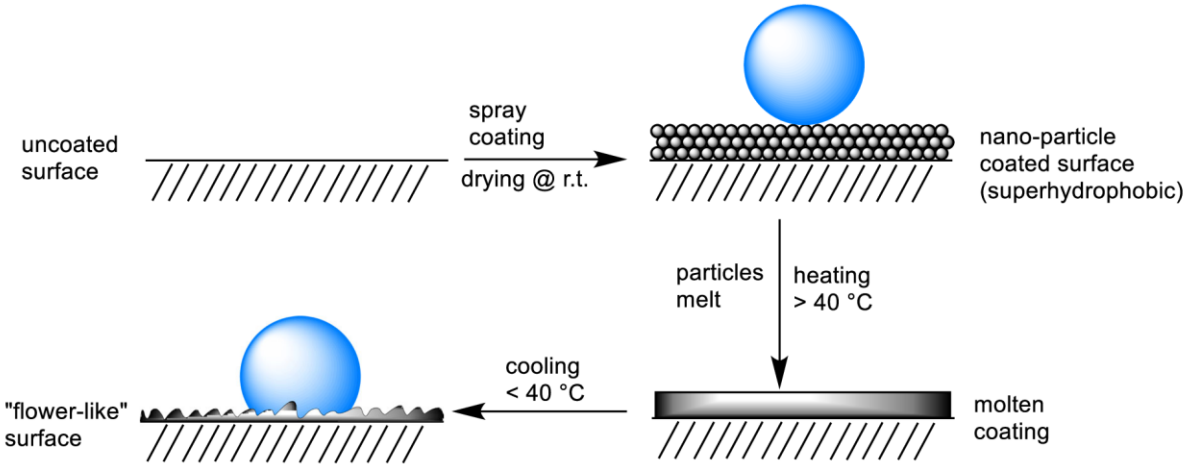

Fig. 5 Visualization of the steps involved in preparing the surfaces depicted in Fig. 4. Furthermore, the different wetting states on the nanoparticle surface (Cassie state) and the "flower-like" surface (Wenzel state) are shown

accordingly. Hence, we did not extend these particular studies to other than HPCC18-esters.

After preparation of the particles model substrates were prepared by spray coating an NP dispersion in isopropanol onto silicon wafer and yielded a coating of approximately 1.5 g/m^2. The coatings were dried under standard climate conditions. When heated above 40 °C, the particles melted and formed a macroscopically flat and transparent surface; this process is shown in Fig. 5. SEM revealed a "flower-like" planar surface morphology (Fig. 4, left), which was comparable to the surface morphologies of short side-chain HPC-esters observed by Tu, et al. They attributed this characteristic to the formation of crystal domains in the films during the curing process, while studying their materials on planar solid substrates (Tu et al. 2012).

Next, we were interested in understanding the surface-wetting of water on the HPCC18DS3 film. The measurements were conducted in dynamic mode: A small droplet (~ 4 µL) was dispensed onto the surface and then retracted into the syringe. Investigating the wetting behavior of the HPCC18DS3-NPs versus "flat" HPCC18DS3 surfaces by static CA analysis showed that the CA was 154° ± 3° when the material was applied in form of NPs and 111° ± 4°

Fig. 6 Left: CA measurement of an HPCC18DS3-NP-coated glass slide. The surface was highly hydrophobic, which prevented the droplet from being released from the needle. Right: Measurement of the same surface after the morphology was changed by heating, as illustrated in Fig. 5

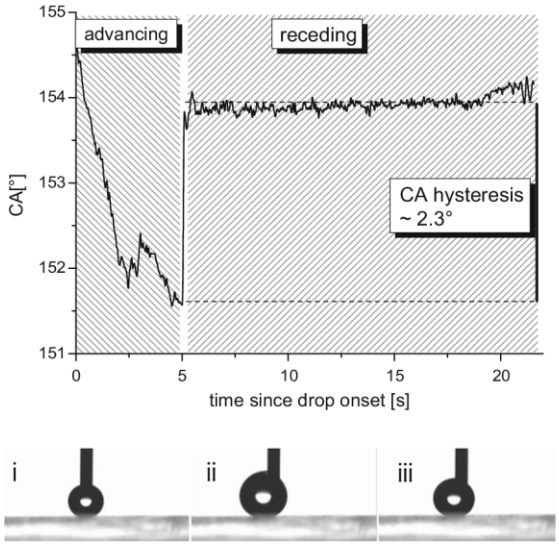

Fig. 7 Dynamic CA measurement on a microscope slide coated with approximately 0.3 g/m^2 HPCC18DS3-NPs. The droplet was touching the surface at t = 0 s (i) and was further dispensed until t = 5 s (ii), which yields the advancing CA of 151.7°. At t = 5 s, the droplet was retracted until the droplet lost contact with the surface at t = 22 s (iii), which gives the receding CA. On the lower part, images of the actual measurement are displayed

after heating to obtain the "flat" polymer, as shown in Fig. 6.

This result was due to a change in wetting from the Cassie-Baxter state to the Wenzel state, as indicated by the small CA hysteresis of 2.4° acquired via dynamic CA analysis, i.e., the difference between the advancing and receding CAs, for the NP surfaces (Fig. 7). Thus, a superhydrophobic, stimuli-responsive surface was formed from this bio-based material. Compared to similar systems the novelty of our system is two-sided. On the one hand the solvent used during synthesis (THF) can be removed during workup with greatly reduced effort, compared to pyridine which was used on comparable work performed with cellulose. On the other hand, the HPCC18DS3-NPs can be simply applied from water, in comparison other NP formulation commonly used, which are often applied from organic solvents. Coating from aqueous formulations are of great advantage with respect to technical requirements during film preparation and drying, as such, most of today's coating processes use water-based coatings.

Conclusions

HPC was characterized using several complementary methods, which provided reliable data regarding the MS values. Moreover, ^{1}H-NMR spectroscopy was established as a reliable and fast standard analytical technique to determine the DS values of a wide range of HPC fatty acid esters. The fast and low-cost synthesis of HPC fatty acid esters was performed in different reaction systems, with pure dried THF identified as the most suitable system for our purposes and pyridine/DMAP as the fastest reaction system. A range of HPC fatty acid esters with lauric, myristic, palmitic and stearic acid were synthesized, and the kinetics of these reactions were studied in detail. During the analysis of the reaction kinetics, the lauric acid esterification of HPC was found to be remarkably slower than the equivalent reaction with stearic acid, which was contrary to the results obtained from low-molecular-weight esterifications with fatty acids. This finding led to the hypothesis that with the longer chains of stearic acid, the polymer coils of HPC unwind to a greater degree than with the short lauric acid chains, thereby making more reaction sites sterically available. Subsequent comparative kinetics using partially esterified HPC as starting material indicated that compared to lauric acid, esterification of HPC with stearic acid indeed increases its reactivity. As such accessibility of the OH-groups becomes a critical parameter, which determines the possibility for a reproducible control over DS values with various HPC-esters. The thermal properties of the obtained products were within the expected margins and were comparable to those of the cellulose esters of fatty acids, but the melting points were between 15 and 19 K lower for the DS = 3 derivatives. The data also match the values for highly substituted the palmitic and stearic acid esters of HPC recently reported in the literature by others. Molar mass analysis showed that no significant polymer degradation is observed until DS reached a value of 2. Together with typical yields above 90% and no increase in the PDI, indicates that synthesis of HPC-esters here has some significant advantage over the ones reported in the literature using acid chlorides in acetone.

In a second part of our work, we transferred HPCC18DS3 to nanoscale hydrophobic particles, by using a nanoprecipitation strategy in dilute solution. In contrast to literature known protocols, which often use organic solvents for stabilization of the particles, here we use a system, where the organic solvent can be completely replaced by water. As such water-based NP formulation are accessible, which are not trivial to obtain with other biogenic hydrophobic polymers. The accessibility and the use of water-born formulations now offers a large number of possible applications as for example barrier-coating material. As a model, we therefore studied in a conceptual work coatings on planar solid model-substrates of the HPCC18DS3-NPs. Such coatings showed in particular interesting wetting behavior that can be switched by a thermal trigger, and which points to possible future applications of these biogenic polymers, e.g., as stimuli-responsive barrier coatings.

Acknowledgments The authors would like to thank Martina Ewald and Heike Herbert for technical support and GPC measurements. Furthermore, we would like to thank Christian Rüttiger for conducting DSC measurements, and we would like to thank Dr. A. Geissler for valuable scientific discussions. This work was funded in part by the DFG Collaborative Research Center 1194 (SFB1194 "Wechelseitige Beeinflussung von Transport- und Benetzungsvorgängen").

Compliance with ethical standards

Conflict of interest The authors declare no conflict of interest.

References

Chen WW, Weng WG, Fu M (2017) Hydroxypropyl cellulose-based esters for thermal energy storage by grafting with palmitic-stearic binary acids. J Appl Polym Sci 134:44949

Daruwalla EH, Nabar GM (1956) Acid hydrolysis of cellulose. J Polym Sci 20:205–208

Geissler A (2017) Charakterisierung und Applikation von Fettsäureestern der Cellulose und deren kolloidaler Systeme vol 10. Makromolekulare Chemie, 1. Auflage edn., Aachen

Geissler A, Chen L, Zhang K, Bonaccurso E, Biesalski M (2013) Superhydrophobic surfaces fabricated from nano- and microstructured cellulose stearoyl esters. Chem Commun (Camb) 49:4962–4964

Heinze T, Glasser WG (1998) The role of novel solvents and solution complexes for the preparation of highly engineered cellulose derivatives. Cellul Deriv Am Chem Soc 688:2–18

Heinze T, Koschella A (2005) Solvents applied in the field of cellulose chemistry: a mini review. Polímeros 15:84–90

Ho FFL, Ward GA, Kohler RR (1972) Determination of molar substitution and degree of substitution of hydroxypropyl cellulose by nuclear magnetic-resonance spectrometry. Anal Chem 44:178–181

Hou HQ, Reuning A, Wendorff JH, Greiner A (2000) Tuning of the pitch height of thermotropic cellulose esters. Macromol Chem Phys 201:2050–2054

Hou HQ, Reuning A, Wendorff JH, Greiner A (2001) Effect of blending of cholesteric cellulose esters on the pitch height. Macromol Biosci 1:45–48

Huang B, Ge JJ, Li YH, Hou HQ (2007) Aliphatic acid esters of (2-hydroxypropyl) cellulose—effect of side chain length on properties of cholesteric liquid crystals. Polymer 48:264–269

Hubbard P, Brittain WJ (1998) Mechanism of amine-catalyzed ester formation from an acid chloride and alcohol. J Org Chem 63:677–683

Ishizaki T, Uenuma S, Furumi S (2015) Thermotropic properties of cholesteric liquid crystal from hydroxypropyl cellulose mixed esters. Kobunshi Ronbunshu 72:737–745

Khan FZ, Shiotsuki M, Sanda F, Nishio Y, Masuda T (2008) Synthesis and properties of amino acid esters of hydroxypropyl cellulose. J Polym Sci Pol Chem 46:2326–2334

Launer HF, Wilson WK (1950) Preparing cuprammonium solvent and cellulose solutions. Anal Chem 22:455–458

Lee JL, Pearce EM, Kwei TK (1997) Side-chain crystallization in alkyl-substituted semiflexible polymers. Macromolecules 30:6877–6883

Levin D (1997) Potential toxicological concerns associated with carboxylic acid chlorination and other reactions. Org Process Res Dev 1:182

Liu YJ, Lotero E, Goodwin JG (2006) Effect of carbon chain length on esterification of carboxylic acids with methanol using acid catalysis. J Catal 243:221–228

Malm CJ, Tanghe LJ (1955) Chemical reactions in the making of cellulose acetate. Ind Eng Chem 47:995–999

Malm CJ, Barkey KT, Schmitt JT, May DC (1957) Evaluating cellulose acetylation reactivity. Ind Eng Chem 49:763–767

Meller A (1953) Studies on modified cellulose. 3. Characterization of the reactivity and supermolecular structure cellulose fibers. Tappi 36:264–267

Ostlund A, Lundberg D, Nordstierna L, Holmberg K, Nyden M (2009) Dissolution and gelation of cellulose in TBAF/DMSO solutions: the roles of fluoride ions and water. Biomacromol 10:2401–2407

Philipp B (1993) Organic-solvents for cellulose as a biodegradable polymer and their applicability for cellulose spinning and derivatization. J Macromol Sci Pure A30:703–714

Richardson S, Andersson T, Brinkmalm G, Wittgren B (2003) Analytical approaches to improved characterization of substitution in hydroxypropyl cellulose. Anal Chem 75:6077–6083

Sealey JE, Samaranayake G, Todd JG, Glasser WG (1996) Novel cellulose derivatives. 4. Preparation and thermal analysis of waxy esters of cellulose. J Polym Sci Pol Phys 34:1613–1620

Sereti V, Stamatis H, Pappas C, Polissiou M, Kolisis FN (2001) Enzymatic acylation of hydroxypropyl cellulose in organic media and determination of ester formation by diffuse reflectance infrared Fourier transform (DRIFT) spectroscopy. Biotechnol Bioeng 72:495–500

Sihtola H, Kaila E, Laamanen L (1957) Cupriethylenediamine and cuprammonium hydroxide as solvents in molecular fractionation of cellulose. J Polym Sci 23:809–824

Situ FM et al (2015) Cellulose-based polymeric liquid crystals as a biomimetic modifier for suppressing protein adsorption. J Wuhan Univ Technol 30:416–422

Steinmeier H, Zugenmaier P (1988) Formation of liquid-crystalline phases by two phenyl-alkanoyl esters of O-(hydroxypropyl)cellulose and the (3-chlorophenyl)urethane of cellulose. Carbohyd Res 173:75–88

Tseng SL, Laivins GV, Gray DG (1982) Propanoate ester of (2-hydroxypropyl)cellulose—a thermotropic cholesteric polymer that reflects visible-light at ambient-temperatures. Macromolecules 15:1262–1264

Tu M, Han WQ, Zeng R, Best SM, Cameron RE (2012) A study of surface morphology and phase separation of polymer/cellulose liquid crystal composite membranes. Colloid Surface A 407:126–132

Wüstenberg T (2014) Hydroxypropylcellulose. In: Cellulose and cellulose derivatives in the food industry. Wiley, New York, pp 319–342

Yamagishi TA, Guittard F, Godinho MH, Martins AF, Cambon A, Sixou P (1994) Comparison of thermal and cholesteric mesophase properties among the 3 kind of hydroxypropylcellulose (Hpc). Deriv Polym Bull 32:47–54

Zhang ZG, Li GN, Hu GL, Sun YY (2013) Theoretical research on the mechanism of the dimerization reactions of alkyl ketene. J Chem 2013:481586

4.2. Independent two way switching of the wetting behavior of cellulose-derived nanoparticle surface coatings by light and by temperature

The content of this chapter has been published in:

Maximilian Nau, David Seelinger, Markus Biesalski, “Independent Two Way Switching of the Wetting Behavior of Cellulose-Derived Nanoparticle Surface Coatings by Light and by Temperature”, *Adv. Mater. Interfaces* **2019**, 6, 1900378 published by John Wiley and Sons, © 2019, reprinted with permission.

During our investigation of HPC esters we followed two directions. One way was focused on increasing control over the wettability of HPC stearic acid ester nano particle coated surfaces. We were interested in the combination of different stimuli, with the aim to switch the wetting behavior of the interface in an orthogonal fashion. Since the formation of nano particles from HPC derivatives is influenced dramatically by alterations of the polymer chemistry and thus the dissolution behavior, we opted out to modified pre-formed particles in dispersion through non-covalent attachment of photo responsive moieties, using so-called donor acceptor Stenhouse adducts (DASAs). The synthesis of a range of different DASA compounds, i.e. having *N*-alkyl substituents with varying chain length for non-covalent interaction with the hydrophobic particle surface, could be carried out fast without the need for complex multi-step synthetic routes, like it would be necessary for comparable photoswitches (e.g. spiropyrane). Initially the optimal reaction system (i.e. solvent) for this reaction was determined through kinetic analysis (Figure 4-2 a), determination of the reaction rate constants and the reaction order. A range of DASAs with *N*-alkyl substituents (C_2H_5 through $C_{18}H_{37}$) were synthesized (Figure 4-2 b) and screened for their ability to influence the wetting of the super hydrophobic surfaces produced from the nano particles through switching by visible light. The investigation revealed, that di-*N*-dodecyl substituted DASA provided the ability to switch the coatings on from super hydrophobic to hydrophilic, which in combination with lab engineered paper sheets as substrate yielded the ability to induce controlled, fast, and complete imbibition of water into the super hydrophobic surface, Figure 4-2 c. Through exploitation of heating as orthogonal stimulus, the surface could then be switched back to become hydrophobic since the particles would melt and form a film, that locks the water from imbibition into the substrate, Figure 4-2 d. In conclusion, this system is a potential candidate e.g. for the control of water flow (imbibition) in microfluidic paper based systems, where a closed-open-closed valve, e.g. for timing purposes, is desired.

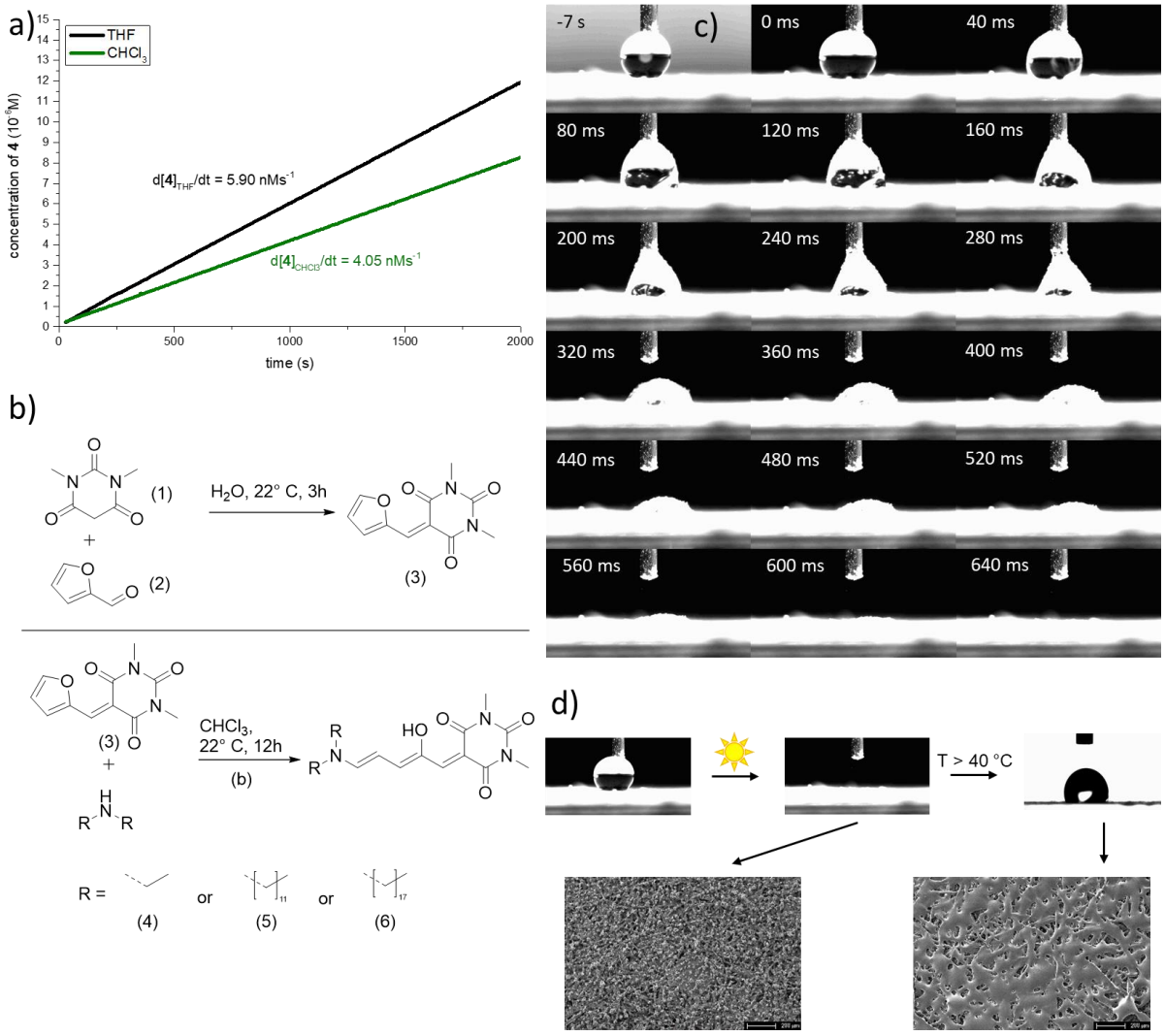

Figure 4-2: a) Reaction kinetics of Stenhouse reaction of barbituric acid derivative 3 and diethylamine to DASA **4** in THF (black line) and chloroform (green line) at 22 °C and at a stating concentration of 1.5 mM of both reactants. b) General synthetic pathways to three different DASAs (**4**, **5**, **6**). Top: Condensation of N,N'-dimethylbarbituric acid **1** and furfural **2**, in water, 22 °C, 3 h. Bottom: Reaction of **3** and different di-*N*-alkyl-amines to form DASAs **4**, **5** and **6**. c) Frame-wise depiction of the change in the wetting behavior of a paper coated with a combination of HPCC18NPs and DASA **6**. The first image shows the moment when the light is turned on, 7 s before the imbibition process starts. The second to last images depict the imbibition process, beginning at t = 0 and ending after 640 ms d) CA analysis of the DASA 6 modified NP-coatings prior to illumination, after illumination and after heating above 40 °C, SEM images corresponding to the change in the morphology of the optically switched state and once heated above 40 °C.

COMMUNICATION

Surface Coatings

ADVANCED MATERIALS INTERFACES

www.advmatinterfaces.de

Independent Two Way Switching of the Wetting Behavior of Cellulose-Derived Nanoparticle Surface Coatings by Light and by Temperature

*Maximilian Nau, David Seelinger, and Markus Biesalski**

Recently, donor acceptor Stenhouse adducts (DASAs) have received interest as photoresponsive polarity switches. In this work, a range of DASAs are synthesized and combined with nanoparticles from hydroxypropyl cellulose stearic acid ester to yield a photoresponsive composite material. This composite is spray-coated onto porous paper substrates, forming an interface that is initially superhydrophobic and can be switched by a visible light trigger to become hydrophilic. Subsequently, this hydrophilic state can be switched back to regain a hydrophobic surface by heating above the T_m of the polymer, creating a system that can exist in three stable states, which can be triggered by independent (i.e., light/heat) stimuli. If such coatings are being applied onto porous paper substrates, using such independent stimuli, water drops placed on top of the paper can be submerged (i.e., wicked) into the paper by simple illumination with light, and the surface can be "reclosed" by subsequent heating of the paper. The latter may become promising for paper-based fluid timers, e.g., in diagnostic applications.

The control of wetting behavior on solid surfaces has been a constant point of interest to academia and industry for a range of applications since the beginning of the last century.[1–5] In general, wetting is controlled by the structure and chemistry of a surface,[6–10] and surfaces that alter their wettability by an external trigger are in high demand. To achieve such switchable surfaces, a range of stimuli-responsive polymeric coating materials have been employed in the recent past, such as polymers responsive to pH, temperature, solvent, light, and mechanical stimuli.[11–16] Generally, such responsive polymers can be divided into two groups, polymers (such as poly(*N*-isopropylacrylamide) that change their macroconformation via an external trigger, where thermodynamics (e.g., demixing from a given solvent or at varying temperature) guide the interactions with the surrounding environment, and those macromolecules that carry specific functional groups, such as spiropyran groups that can be switched between nonpolar and polar states by light-induced molecular rearrangements.[17] In particular, such light-triggered changes in the polarity of a material are of interest, as the switching mechanism does not rely on diffusion, as is the case with the pH- or electrolyte-induced switching of polyelectrolytes.[18] However, one of the major challenges of light-responsive spiropyran that has yet to be solved is the rather slow dynamics of the molecular rearrangements (i.e., slow switching behavior) and the oxidative degradation that can occur during the process. Another group of photoresponsive polarity-switching materials are known as donor acceptor Stenhouse adducts (DASAs). DASAs were discovered recently and have gained an increasing amount of attention in a broad range of fields, generating literal toolboxes for the fast implementation into existing systems to add further functionalities.[19–27] These compounds are derived from furfural, a commodity chemical and plant by-product, which is a great step toward sustainable building blocks for photoswitchable compounds. Initial studies focusing on the incorporation of the photoresponsive DASA domain into polymer matrices have been carried out, and the products of which displayed a photoinduced change in wetting behavior based around the mechanism displayed in **Figure 1**a.[28,29] Both studies found that there was no observable back-switching for DASAs on surfaces, which stands in sharp contrast to the fast switching observed for these molecules in solution. A newer study has reported that second-generation DASA-containing polymers could be switched back within hours, triggered by the glass transition of the matrix polymer.[30] Very recently Zheng et al. reported the reversible switching of a silica nanoparticle bound poly dopamine based DASA system, which could, once immobilized on a polydimethylsiloxane substrate, induce a change in water contact angle (WCA) of up to ≈40°.[31]

We have been working in the recent past on cellulose-ester and hydroxypropyl cellulose (HPC)-ester polymers, which can be tailored with respect to their thermal behavior (T_g), and such materials can be applied as nanoparticle coatings on planar surfaces.[32,33] When cellulose- or HPC-ester nanoparticles are being coated onto a planar solid or porous (e.g., paper) substrate, superhydrophobic surface properties with WCAs exceeding 150° can be observed through a combination of roughness (a film consisting of nanoparticles) and low surface energy. Through thermal treatment, the nanoparticle structure

M. Nau, D. Seelinger, Prof. M. Biesalski
Technische Universität Darmstadt Ernst Berl Institut für Technische und Makromolekulare Chemie
Alarich-Weiss-Straße 8, 64287 Darmstadt, Germany
E-mail: biesalski@tu-darmstadt.de

The ORCID identification number(s) for the author(s) of this article can be found under https://doi.org/10.1002/admi.201900378.

DOI: 10.1002/admi.201900378

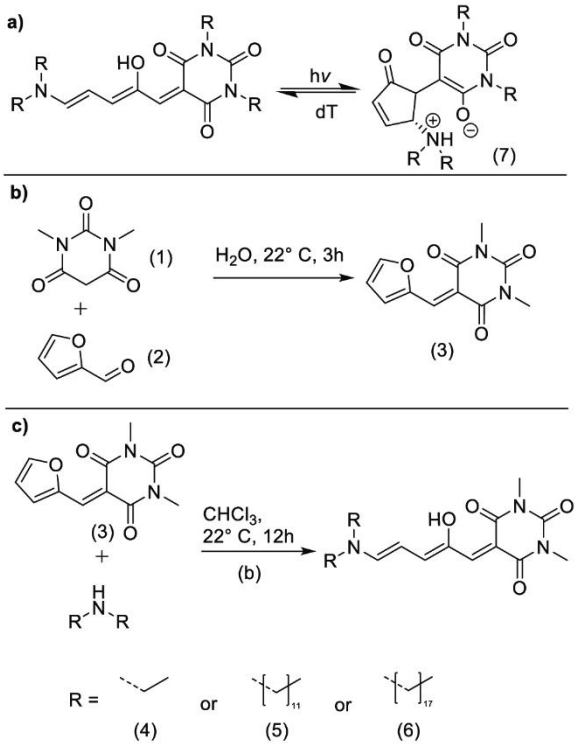

Figure 1. a) Basic mechanism of the photoinduced change in polarity of first-generation DASAs. The light stimulates an E/Z isomerization, which is followed by a Piancatelli-like rearrangement, which leads to the zwitterionic, bicyclic state. b) Condensation of *N*,*N*′-dimethylbarbituric acid **1** and furfural **2**, in water, 22 °C, 3 h. c) General synthetic pathways to three different DASAs, i.e., reaction of **3** and different di-*N*-alkyl-amines to form DASAs **4**, **5**, and **6**.

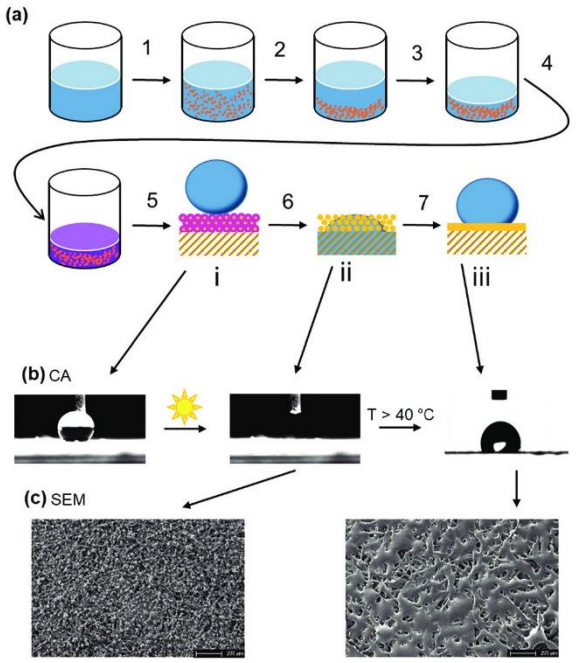

Figure 2. a) Nanoprecipitation of HPCC18NPs from THF into isopropanol (1); partial sedimentation of the formed particles (2); decantation of excess solvent (3); addition of DASA **5** (4); spray-coating of the composite onto the paper substrate (5) to form a photoresponsive coating, which is initially superhydrophobic (i); illumination with visible light (6) to yield a switching effect turning the coating, and thus, the whole system, hydrophilic (ii); and finally, heating of the sample (7) to melt produce a final, hydrophobic, state (iii). b) WCA analysis of the states (i) through (iii). c) SEM images corresponding to the change in the morphology of state (ii) once heated above 40 °C.

in the film is transformed into a smooth homogeneous coating, which exhibits hydrophobic WCAs ≈120°. To further push these triggered changes in wetting, ideally from above 150° to below 90°, one may use an additional polarity switch, such as the described DASAs, in combination with the hydrophobic, cellulose-based nanoparticles. This paper reports the combination of light-switchable DASAs and the aforementioned cellulose-based nanoparticle coatings in one composite material to create coatings on solid substrates that can be switched by visible light from superhydrophobic to hydrophilic wetting states. The hydrophobic coatings, which have been the subject of an in-depth prior investigation, are based on hydroxypropyl cellulose stearoyl ester nanoparticles (HPCC18NPs).[33] These materials present a majority of alkyl groups on their surface, which can be exploited to bind tailor-made DASAs via hydrophobic interactions. In particular, we use a surface coating based on HPCC18NPs and compound **5** (di-(*N*-dodecyl)amino-DASA, Figure 1b/c). Hydroxypropyl cellulose stearoyl ester is prepared by the esterification of hydroxypropyl cellulose with 3 equiv. of stearoyl chloride in THF, according to our recently published protocol.[33] The product is nanoprecipitated in a mixture of isopropanol and water and concentrated by decantation to increase the coating efficiency (**Figure 2**a). In the next step, **5** is produced from the barbituric acid derivative **3** and di-(*N*-dodecyl)amine. The DASA **5** is added to the HPCC18NP suspension, and the composite materials of **5** and the HPCC18NPs are applied to lab-made paper sheets via spray-coating. The resulting interfaces were analyzed via contact angle measurements. The process to yield hydrophobic HPCC18NPs has been described in detail in our prior work.[33]

To synthesize the DASAs, the general procedure, published by Helmy, was utilized. For the first step: *N*,*N*′-dimethylbarbituric acid **1** is dissolved in water, and furfural **2** is added at 22°C; the ^{1}H-NMR spectrum (Figure S1, Supporting Information) shows the distinctive signals of **3**. The second-step reaction of **3** with secondary amines in different solvents has been reported in the literature. We investigated the reaction kinetics in chloroform and tetrahydrofuran on the model-reaction with **3** and diethylamine to form the DASA **4** by in situ UV–vis spectroscopy. DASA **4** was obtained by the procedure described by Helmy (Figure S2, Supporting Information). The detailed results are displayed in the Supporting Information, in brief $CHCl_3$ was found to be the most efficient reaction medium. Based on this finding, the reactions with di-(*N*-dodecyl)- and di-(*N*-octadecyl)-amines were performed in $CHCl_3$ at higher concentrations of **3**. The subsequent products

were isolated by flash column chromatography, and the ^{1}H NMR spectra (Figures S3 and S4, Supporting Information) show all signals of the products and none of residual reactants, justifying the chemical identity of the prepared materials. After the syntheses of the DASAs, we next were interested in understanding if and which DASA would allow for the efficient light-controlled switching of the wetting behavior, once combined with the hydrophobic HPCC18NPs. DASAs **4**, **5**, and **6** were combined with a dispersion of HPCC18NPs in 2-propanol (7.7 wt% nanoparticles) to yield corresponding coating dispersions. Note, due to the hydrophobic nature of the HPCC18NPs, it was hypothesized that DASAs with enlarged nonpolar domains, i.e., longer *N*-alkyl moieties, would more easily associate with the particles by van der Waals interactions. A direct experimental proof of this, however, is not trivial and was therefore not pursued in these initial studies. Different amounts of DASA were added to the coating solution, and 2 g m^{-2} of each coating was applied onto a laboratory-formed paper sheet (eucalyptus sulfate pulp, 80 g m^{-2}, no additives) via spray-coating. For this procedure, we followed the protocol reported in our prior work, as illustrated in Figure 2a (steps 1–3 and 5).[26] Obviously these coatings may, without the addition of a binder like acrylic latex, susceptible to mechanical damage. However, at this point it is not of major concern since, in the long run, such paper hybrid materials may be implemented, e.g., into paper based microfluidic systems which are inherently disposable and sealed items, where mechanical and chemical stability of the coatings are not of primary importance.

After drying under ambient conditions, we characterized the obtained layers on paper sheets using SEM (Figure 2c, left) and WCA analysis (**Table 1**). The thermal behavior of the composite films is very similar to the bulk HPC ester behavior, i.e., when the temperature exceeds 40 °C, the particles melt and the roughness on the paper surface is significantly decreased. To switch the DASA into the polar, charged state, nanoparticle sample-coatings (Figure 2b,i) were illuminated by visible light from a Lumatec light source for 10 min, while parts of the surface were covered with a nontransparent foil. The change in wetting was then evaluated by contact angle analysis of the illuminated and nonilluminated areas. As a reference, surfaces prepared in the same manner from pure HPCC18NPs without DASA were also analyzed. As a result of this empiric approach, it is found that DASA **5** is capable of achieving the desired switching to a hydrophilic surface, and the detailed results are displayed in Table 1. A possible explanation can be that with **5**, the length of the hydrophobic alkyl tails connected to the DASA allows for a simple association to the nonpolar particle surface via hydrophobic interactions with the alkyl residues of the tertiary amine moieties, as depicted schematically in Figure S5 (Supporting Information).

Table 1. Contact angle measurements of paper substrates coated with composites from HPCC18NPs and different DASAs in varying concentrations relative to the particle mass. Total coating weight was always adjusted to 2 ± 0.2 g m^{-2}.

DASA	wt%	WCA (prior to illumination) [°]	WCA (after illumination) [°]	WCA (after heating) [°]
Reference	0	154.1 ± 2.9	154.5 ± 2.3	111.2 ± 4.0
[4]	2	153.2 ± 0.9	153.0 ± 1.1	103.5 ± 6.7
[4]	10	148.5 ± 2.8	150.7 ± 3.3	110.4 ± 3.2
[4]	40	147.5 ± 2.2	149.7 ± 2.9	104.7 ± 5.2
[5]	2	152.0 ± 3.2	0[a)]	105.3 ± 8.4
[5]	10	154.8 ± 4.0	0[a)]	117.7 ± 4.9
[5]	40	148.7 ± 2.3	0[a)]	113.1 ± 5.1
[6]	2	151.6 ± 3.9	150.4 ± 1.7	118.4 ± 2.8
[6]	10	147.2 ± 2.1	152.7 ± 2.3	113.5 ± 7.7
[6]	40	149.7 ± 2.4	146.7 ± 3.7	111.9 ± 5.4

[a)]Samples show complete imbibition of the water droplet into the substrate.

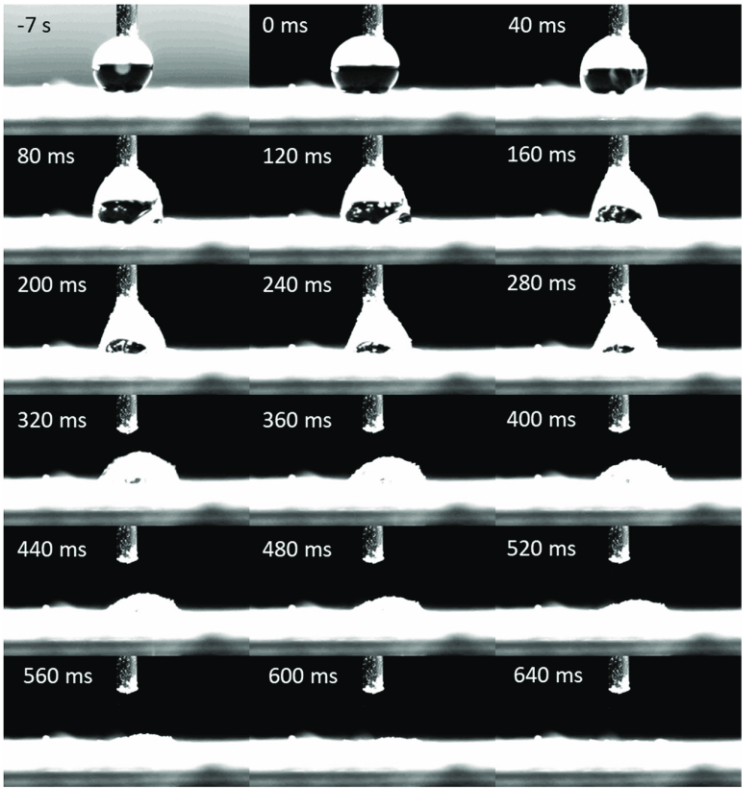

Figure 3. Frame-wise depiction of the change in the wetting behavior of a paper coated with a combination of HPCC18NPs and DASA **5**. The first image shows the moment when the light is turned on, 7 s before the imbibition process starts. The second to last images depict the imbibition process, beginning at $t = 0$ and ending after 640 ms.

If the alkyl chain is significantly shorter, the solubility of the DASA in isopropanol/water may not allow for a stable modification of the nanoparticles. Similarly, if the alkyl chains are substantially longer, the DASA may form stable micelles by itself. This could, in theory, lead to an inhibition of the targeted DASA-particle surface association. Nevertheless, at this point this hypothesis is just one of several possible explanations, and needs further clarification in future work. Further testing with different ratios of DASA **5** to HPCC18NPs reveals that at 40 wt% (relative to the nanoparticles), the switching of the surface polarity is achieved after a short period of time (<10 s) in a well-reproducible fashion (**Figure 3**). This fast switching process from superhydrophobic to hydrophilic allows a change in the WCA on the solid substrate. Because we used paper sheets as a porous solid substrate, the switching of the NP-DASA associates affords complete imbibition of the water droplet into the underlying paper sheet, as depicted in Figures 2b and 3. To facilitate this analysis in detail, a DataPhysics Contact Angle System was combined with a Lumatec SUV-DC light source (200 W mercury arc lamp, irradiance spectrum in Figure S6, Supporting Information) equipped with a UV-filter to provide light for the switching process via an optical fiber (Figure S7, Supporting Information). The fast and drastic change in wettability could then be studied by wicking effects: Once the thin layer of nanoparticles starts to wet, they allow the water to pass through and be taken up by the paper substrate due to capillary forces coming into action. When this process starts, the wetting is thus governed by the capillary-driven flow of the water into the paper substrate. This of course opens the opportunity to tune the wetting after the switching of the DASA since the flow rate, as reported by Böhm et al., in paper can be adjusted by alterations of the paper properties such as fiber length, pore size and porosity.[34] The light-switched coating containing **5** stays hydrophilic and discolored after several months under standard conditions (23 °C and 50% r.h.). The latter can be seen by the naked eye (**Figure 4**a). Using a lithographic mask becomes therefore a simple application to photopattern the surface of paper substrates (Figure 4b/c) and to prepare long-term thermally stable surface coatings with desired polarities. The latter may become interesting for emerging applications with functional paper devices. Note, the purple color can also be taken as an indirect proof of the existence of the DASA on top of the paper substrates. In our case no back-switching to the nonpolar state is observed, even if the samples were stored in the dark for such a long time or heated up to 80 °C. This behavior is similar to the irreversible switching in the solid state reported by Singh, but stands in contrast to the findings reported by Zheng et al.[29,31] One possible explanation for this behavior for this finding can be that the HPC ester matrix stabilizes the cyclic form of the DASA. While photo bleaching cannot be ruled out completely, the addition of solvent (THF) does lead to the re-coloration of the "wetted" area indicating the ability of the DASA to switch back when the DASA and the polymer matrix are dissolved and thus separated (Figure S8, Supporting Information). Subsequent illumination shows that the DASA then is stabilized in the polymermatrix and does in fact not switch to the cyclic form in the same way as the initial surface bound DASA. (Figure S8d, Supporting Information) The irreversible behavior might be mitigated via the incorporation of second-generation DASAs, which utilize aromatic amines and Meldrum's acid instead of barbituric acid, that have recently been reported by Ulrich et al. to show the potential of reversing the photoisomerization in solid state by inducing a glass transition in the matrix material.[30] Fortunately, at this stage, the intrinsic properties of the HPCC18NP coatings give a direct alternative: Once heated above 40 °C, the nanoparticles melt and form a hydrophobic polymer coating on the paper (Figure 2b,c, Table 1 last column). This method, depending on the heating operations, enables the system to be switched almost instantly from highly hydrophilic to hydrophobic again, exhibiting water contact angles in the range of 100°–120° (Figure 1b). The latter results in a system that is initially superhydrophobic (WCA > 150°), then becomes completely hydrophilic by light-switch that is evident from the observation of droplet imbibition, and finally, through an independent second stimulus (heat) regains very hydrophobic properties with static WCA of about 100°–120°, respectively.

In conclusion, we prepared and characterized surface coatings consisting of a novel composite material, which carries light-sensitive hydrophobized DASA molecules associated with preformed hydrophobic HPC ester nanoparticles. The synthesis of the hydrophobized DASA was easily established

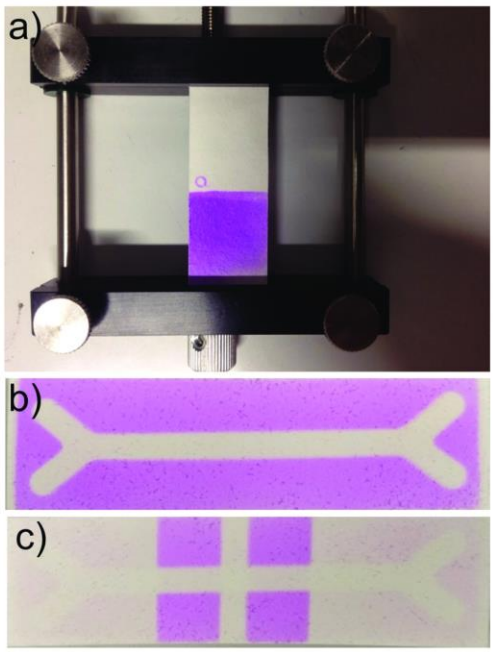

Figure 4. a) Paper sample coated with HPCC18NPs and DASA 5. The sample was illuminated while about half was covered with a mask and a water droplet was present. The lens effect produced by the droplet led to the ring of un-switched DASA; b) demonstration of the possibility to generate a surface pattern through photolithographic means. A photomask with a negative image of a handlebar was placed over the paper sample coated with HPCC18NPs and DASA 5 and illuminated using the Lumatec light source, leading to the displayed pattern; c) The mask used in creating the first pattern was turned 90° and a second illumination cycle was carried out to generate a second pattern.

in $CHCl_3$ at very high conversion rates. The composite nanoparticles are applied by spray-coating onto lab engineered paper sheets, and the resulting NP-DASA-coated paper exhibits a dramatic change in wettability upon irradiation with visible light, from an initial superhydrophobic to a completely hydrophilic state. Because the paper substrate underlying the NP-DASA coating is porous and hydrophilic in nature, the change in wettability of a water drop on top of the paper sheet leads to a complete wicking of the aqueous fluid into the substrate. This stable hydrophilic state again can subsequently be switched by a thermal stimulus to become hydrophobic again (WCA: 110°–120°), achieved through an exploit of the intrinsically low melting point of the polymer nanoparticles (T_m: 40 °C). While the irreversible nature may be limiting in some regards, possible applications for this material are photocontrolled valves in (paper-based) microfluidic systems, where a closed-open-closed sequence of fluid-timing is of interest (for instance, as a modular dosing system for diagnostic applications). Furthermore, a simple photo patterning via lithographic means can be used to form chemically structured surfaces. These types of devices are inherently disposable in nature and would thus have no need for a reversible system.[35,36]

Supporting Information

Supporting Information is available from the Wiley Online Library or from the author.

Acknowledgements

The authors gratefully acknowledge the financial support by the German Research Foundation (DFG) within the Collaborative Research Centre 1194 "Interaction of Transport and Wetting Processes," Project A05.

Conflict of Interest

The authors declare no conflict of interest.

Keywords

donor acceptor Stenhouse adduct, hydroxypropyl cellulose, stimulus responsive coatings, superhydrophobic, wetting control

Received: February 28, 2019
Revised: May 22, 2019
Published online: July 10, 2019

[1] F. E. Bartell, J. W. Shepard, *J. Phys. Chem.* **1953**, *57*, 211.
[2] D. L. Tian, Y. L. Song, L. Jiang, *Chem. Soc. Rev.* **2013**, *42*, 5184.
[3] Y. Tian, B. Su, L. Jiang, *Adv. Mater.* **2014**, *26*, 6872.
[4] L. P. Wen, Y. Tian, L. Jiang, *Angew. Chem., Int. Ed.* **2015**, *54*, 3387.
[5] P. Olin, S. B. Lindström, T. Pettersson, L. Wågberg, *Langmuir* **2013**, *29*, 9079.
[6] C. Dorrer, J. Ruhe, *Soft Matter* **2009**, *5*, 51.
[7] M. Callies, D. Quere, *Soft Matter* **2005**, *1*, 55.
[8] L. Kubus, H. Erdogan, E. Piskin, G. Demirel, *Soft Matter* **2012**, *8*, 11704.
[9] O. Werner, C. Quan, C. Turner, B. Pettersson, L. Wagberg, *Cellulose* **2010**, *17*, 187.
[10] S. Spirk, H. M. Ehmann, R. Kargl, N. Hurkes, M. Reischl, J. Novak, R. Resel, M. Wu, R. Pietschnig, V. Ribitsch, *ACS Appl. Mater. Interfaces* **2010**, *2*, 2956.
[11] Y. C. Fu, B. Y. Jin, Q. H. Zhang, X. L. Zhan, F. Q. Chen, *ACS Appl. Mater. Interfaces* **2017**, *9*, 30161.
[12] M. Heskins, J. E. Guillet, *J. Macromol. Sci., Part A: Chem.* **1968**, *2*, 1441.
[13] Y. G. Takei, T. Aoki, K. Sanui, N. Ogata, Y. Sakurai, T. Okano, *Macromolecules* **1994**, *27*, 6163.
[14] Q. Yu, Y. X. Zhang, H. Chen, F. Zhou, Z. Q. Wu, H. Huang, J. L. Brash, *Langmuir* **2010**, *26*, 8582.
[15] K. Fries, S. Samanta, S. Orski, J. Locklin, *Chem. Commun.* **2008**, 6288.
[16] J. Lee, B. He, N. A. Patankar, *J. Micromech. Microeng.* **2005**, *15*, 591.
[17] S. Samanta, J. Locklin, *Langmuir* **2008**, *24*, 9558.
[18] M. Biesalski, D. Johannsmann, J. Ruhe, *J. Chem. Phys.* **2002**, *117*, 4988.
[19] S. Helmy, J. R. de Alaniz, *Abstr. Pap. Am. Chem. Soc.* **2012**, *244*, 659.
[20] S. Helmy, S. Oh, F. A. Leibfarth, C. J. Hawker, J. R. de Alaniz, *J. Org. Chem.* **2014**, *79*, 11316.
[21] M. M. Lerch, S. J. Wezenberg, W. Szymanski, B. L. Feringa, *J. Am. Chem. Soc.* **2016**, *138*, 6344.
[22] N. Mallo, P. T. Brown, H. Iranmanesh, T. S. C. MacDonald, M. J. Teusner, J. B. Harper, G. E. Ball, J. E. Beves, *Chem. Commun.* **2016**, *52*, 13576.
[23] J. Ahrens, T. Bian, T. Vexler, R. Klajn, *ChemPhotoChem* **2017**, *1*, 230.
[24] M. Di Donato, M. M. Lerch, A. Lapini, A. D. Laurent, A. Iagatti, L. Bussotti, S. P. Ihrig, M. Medved, D. Jacquemin, W. Szymanski, W. J. Buma, P. Foggi, B. L. Feringa, *J. Am. Chem. Soc.* **2017**, *139*, 15596.
[25] D. Zhong, Z. Q. Cao, B. Wu, Q. Zhang, G. J. Wang, *Sens. Actuators, B* **2018**, *254*, 385.
[26] M. M. Lerch, W. Szymanski, B. Feringa, *Chem. Soc. Rev.* **2018**, *47*, 1910.
[27] B. P. Mason, M. Whittaker, J. Hemmer, S. Arora, A. Harper, S. Alnemrat, A. McEachen, S. Helmy, J. R. de Alaniz, J. P. Hooper, *Appl. Phys. Lett.* **2016**, *108*, 041906.
[28] G. Sinawang, B. Wu, J. L. Wang, S. Li, Y. N. He, *Macromol. Chem. Phys.* **2016**, *217*, 2409.
[29] S. Singh, K. Friedel, M. Himmerlich, Y. Lei, G. Schlingloff, A. Schober, *ACS Macro Lett.* **2015**, *4*, 1273.
[30] S. Ulrich, J. R. Hemmer, Z. A. Page, N. D. Dolinski, O. Rifaie-Graham, N. Bruns, C. J. Hawker, L. F. Boesel, J. R. de Alani, *ACS Macro Lett.* **2017**, *6*, 738.
[31] H. Q. Zhao, D. S. Wang, Y. Fan, M. R. Ren, S. M. Dong, Y. H. Zheng, *Langmuir* **2018**, *34*, 15537.
[32] A. Geissler, L. Q. Chen, K. Zhang, E. Bonaccurso, M. Biesalski, *Chem. Commun.* **2013**, *49*, 4962.
[33] M. Nau, D. Seelinger, M. Biesalski, *Cellulose* **2018**, *25*, 5769.
[34] A. Böhm, F. Carstens, C. Trieb, S. Schabel, M. Biesalski, *Microfluid. Nanofluid.* **2014**, *16*, 789.
[35] A. Böhm, M. Gattermayer, C. Trieb, S. Schabel, D. Fiedler, F. Miletzky, M. Biesalski, *Cellulose* **2013**, *20*, 467.
[36] A. Böhm, M. Biesalski, *MRS Bull.* **2017**, *42*, 356.

4.3. Spatially resolved crosslinking of hydroxypropyl cellulose esters for the generation of functional surface-attached organogels

The content of this chapter has been published in:

Maximilian Nau, Simon Trosien, David Seelinger, Anna K. Boehm, Markus Biesalski, "Spatially resolved crosslinking of hydroxypropyl cellulose esters for the generation of functional surface-attached organogels", *Front. Chem*., **2019**, 7, 367, published by Frontiers under the CC-BY 4.0 license, reprint does not require explicit permission

A second follow-up strategy based on the findings in section 4.1 was focused on the incorporation of reactive moieties into the HPC chains. The aim was to generate a flexible, cross linkable system which would allow us, to generate polymer gels with adjustable polarity and netpoint density with the option to generate patterns (e.g. for microfluidic purposes) without the need for lithographic methods. This was facilitated through esterification of HPC with 10-undecenoyl chloride, and for the hydrophobic version additionally with stearic acid(Figure 4-3 a). The unsaturated side-chains could now be utilized as crosslinking points; which was utilized through the employment of 4,4′-bis(diethylamino)benzophenone (DEABP) as radical generator in combination with a x/y-movable laser diode (405 nm). As substrate for this investigations we used a glass slide which was dip-coated with a mixture of allyltriethoxysilane and tetraethoxysilane, and subsequently cured to provide allyl groups as anchor points for the polymer network. After solvent casting of a film consisting of modified HPC and DEABP onto these functionalized glass slides the coatings were illuminated locally with the laser diode and unbound polymer was removed via solvent extraction (Figure 4-3 b). Through variation of the laser illumination time, i.e. deposited energy, the crosslinking density could be adjusted, which was confirmed through in-situ confocal laser scanning microscopy of polymer patches in swelling experiments. The achieved linear deformation of surface bound networks ranged between 2 and 6 relative to the initial film thickness, which correlates to netpoint densities between 2.35 μmol/cm^3 and 177 μmol/cm^3, respectively, demonstrating the wide tuneability of this system (Figure 4-3 c). In a proof of principle application, we subsequently designed two microfluidic channels, one with the hydrophilic and another with the hydrophobic HPC polymer network and demonstrated the ability to selectively concentrate a model-pollutant (pyrene) from water (Figure 4-3 d). The results serve as another example of the versatility of HPC as basic building block for functional surface coatings and concludes the work on this material within the scope of this thesis.

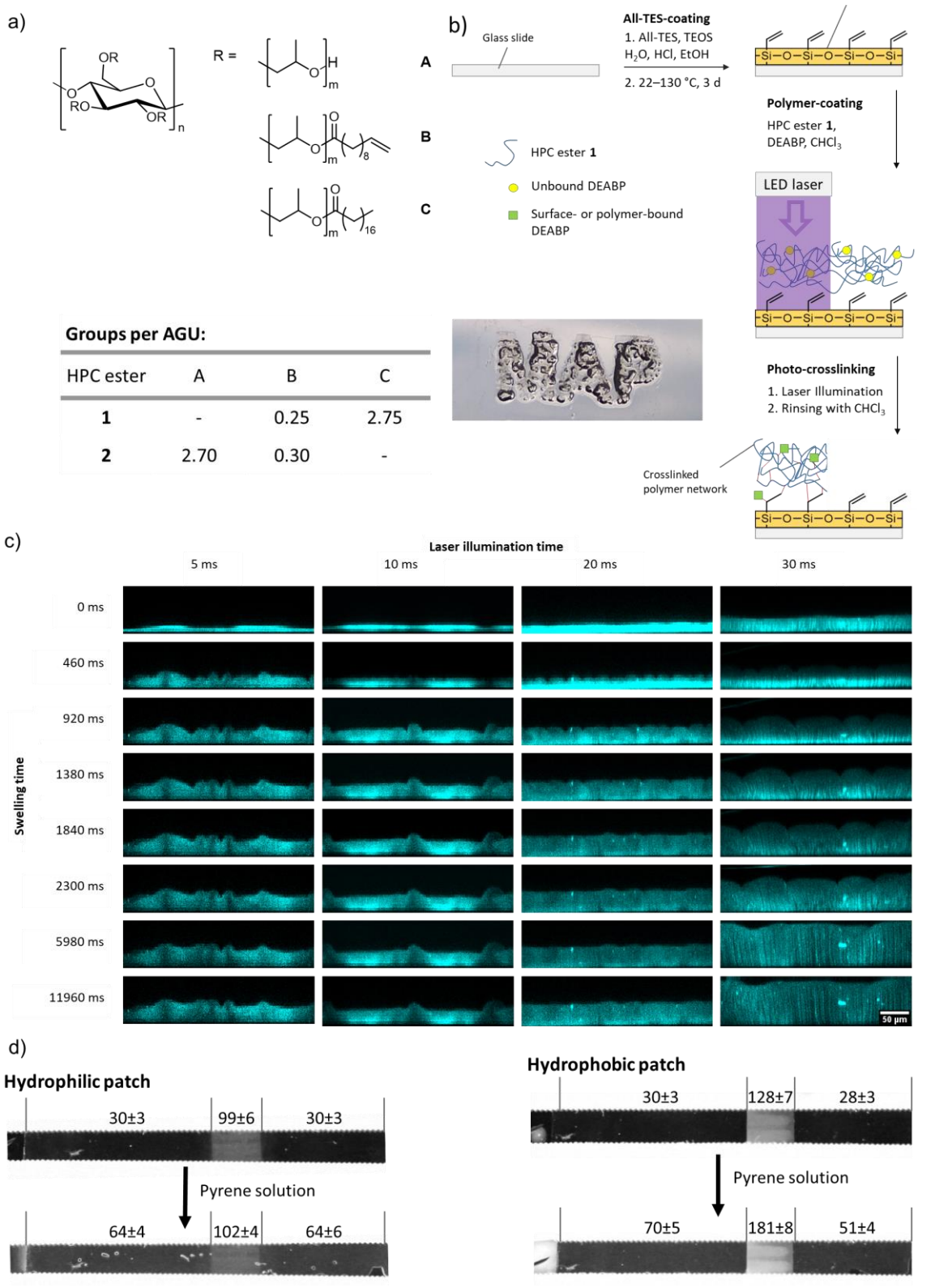

Figure 4-3: a) Synthesis of HPC esters **1** and **2**: Hydrophobic ester **1** exhibits 0.25 undecenoyl (B) and 2.75 stearoyl groups (C) per AGU, and hydrophilic ester **2** is esterified by 0.30 undecenoyl groups (B) per AGU, whereas 2.70 OH groups per AGU remain unmodified (A). b) Schematic of the production of surface-bound polymer network **1** crosslinked via laser treatment and a photograph of the surface-attached polymer network swollen in $CHCl_3$ spelling "MAP". c) Single frames from the in situ monitored swelling of polymer **1** in $CHCl_3$, obtained by dynamic CLSM analysis in xzt mode. d) Microfluidic proof-of-principle device. A network of the hydrophobic polymer **1** is generated within a microfluidic channel and used to collect pyrene from an aqueous pyrene solution, indicated by the changes in grey value. The hydrophilic polymer 2 acts a reference, where now change in mean grey value before and after the patch is measurable.

frontiers in Chemistry

ORIGINAL RESEARCH
published: 24 May 2019
doi: 10.3389/fchem.2019.00367

Spatially Resolved Crosslinking of Hydroxypropyl Cellulose Esters for the Generation of Functional Surface-Attached Organogels

*Maximilian Nau, Simon Trosien, David Seelinger, Anna K. Boehm and Markus Biesalski**

Laboratory of Macromolecular Chemistry and Paper Chemistry, Ernst-Berl Institute of Chemistry, Technische Universität Darmstadt, Darmstadt, Germany

Chemistry, geometric shape and swelling behavior are the key parameters that determine any successful use of man-made polymeric networks (gels). While understanding of the swelling behavior of both water-swellable hydrogels and organogels that swell in organic solvents can be considered well-advanced with respect to fossil fuel-based polymer networks, the understanding, in particular, of wood-derived polymers in such a network architecture is still lacking. In this work, we focus on organogels derived from hydroxypropyl cellulose (HPC) ester. The latter polymer was functionalized with saturated and unsaturated fatty acids, respectively. Due to their tailored chemical constitution, we demonstrated that such polysaccharide can be crosslinked and simultaneously surface-bound by using a photo-induced radical reaction using a photo-initiator. Based on the choice of fatty acid used in the design of the HPC ester, and by controlling the degree of substitution (DS) obtained during the esterification of the polysaccharide, modular manipulation of the physical properties (e.g., polarity) of the resulting gel is possible. Depending on the initiator employed, different wavelengths of light, from UV to visible, can be utilized for the crosslinking reaction, which facilitates the deployment of a range of light sources and different lithographic methods. Additionally, we showed that altering of the illumination time allows to tailor the netpoint density, and thus, the degree of linear deformation in equilibrium and the swelling kinetics. Finally, we performed a proof-of-principle experiment to demonstrate the application of our material for the generation of spatially resolved polymer patches to enrich organic molecules from a solution within a microfluidic channel.

Keywords: hydroxypropyl cellulose, surface modification, organo gels, surface patterning, photo-crosslinking

OPEN ACCESS

Edited by:
Eero Kontturi,
School of Chemical Technology, Aalto University, Finland

Reviewed by:
Bruno Jean,
UPR5301 Centre de Recherches sur les Macromolecules Végétales (CERMAV), France
Tamilselvan Mohan,
University of Maribor, Slovenia

****Correspondence:***
Markus Biesalski
biesalski@tu-darmstadt.de

Specialty section:
This article was submitted to Polymer Chemistry, a section of the journal Frontiers in Chemistry

Received: *18 January 2019*
Accepted: *03 May 2019*
Published: *24 May 2019*

Citation:
Nau M, Trosien S, Seelinger D, Boehm AK and Biesalski M (2019) Spatially Resolved Crosslinking of Hydroxypropyl Cellulose Esters for the Generation of Functional Surface-Attached Organogels. Front. Chem. 7:367. doi: 10.3389/fchem.2019.00367

INTRODUCTION

Swellable polymer networks have been extensively studied in recent decades, with subsequent development for use in a wide range of applications (Osada and Gong, 1998). In addition to hydrogels (networks that swell in water), which gained considerable attention during the last decades, because of their great potential in medicinal applications [e.g., tissue engineering (Annabi et al., 2014), drug delivery, and point-of-care diagnostics] (Rivest et al., 2007; van Tomme et al., 2008; Jagur-Grodzinski, 2009), organogels, which swell in organic solvents (Suzuki and Hanabusa, 2010), are highly interesting and offer promising perspectives in areas such as drug delivery

(Vintiloiu and Leroux, 2008; Esposito et al., 2018), food applications (Marangoni, 2012; Chaves et al., 2018), cosmetics (Kirilov et al., 2014), separation, and purification processes (Venkatesan and Sarles, 2016; Lai et al., 2018; Prati et al., 2018), as well as analytics (Hinze et al., 1996; Mukhopadhyay et al., 2006; Xue et al., 2015). In general, the three-dimensional network structure of a polymer gel can be stabilized by various molecular interactions, in which the individual molecules are connected to each other by secondary forces [such as arene-arene interactions (Ajayaghosh and Praveen, 2007), halogen (Meazza et al., 2013), van der Waals forces, hydrogen bonds, and combinations thereof (Sangeetha and Maitra, 2005; George and Weiss, 2006; Hirst et al., 2008; Datta and Bhattacharya, 2015)] or covalent chemical bonds (Segarra-Maset et al., 2013; García et al., 2014). While adjusting the structure and the properties of gels is not trivial, when they are based on small molecules that are non-covalently connected, the design of covalently bound gels is considered more modular since various functionalities can be easily introduced, e.g., by the co-polymerization of functional groups or by the control of crosslinking density through the adjustment of potential cross-linking moieties in the gel constituting molecules. Furthermore, the use of covalently linked molecules implies highly stable materials whose macroscopic shapes are easily controllable when network formation is triggered by an external stimulus, e.g., by light (Hennink and van Nostrum, 2002). To create such a polymer network photochemically, one possibility is the reaction of double bonds in a radical reaction, e.g., by using a photo-initiator systems, such as camphor quinone/tertiary amine systems (Jakubiak et al., 2003), borates (Toba et al., 1997), or benzophenone derivatives (Merlin et al., 1980).

A variety of materials have been studied for the synthesis of such gels; among these, bio-based polymers such as cellulose and cellulose derivatives have been popular (Larsson et al., 2017; Wang and Zhang, 2018). Cellulose is a highly interesting compound because it provides a large number of valuable benefits: For example, as the most abundant polymer on earth, cellulose is highly available in bulk and originates from well-developed wood-disintegration processes (Klemm et al., 2005). However, because of the low solubility of unmodified cellulose in common organic solvents (i.e., alcohols, THF, chloroform, etc.), the controlled modification of the polysaccharide is highly challenging. Typically, harsh reaction conditions are necessary for heterogeneous functionalization, and the controlled partial substitution of the biomolecule is not trivial (Klemm et al., 2005). Therefore, various solvent systems have been established to improve a specific cellulose reaction, but all of these systems entail a range of challenges (e.g., toxicity, complex workup procedures, or limited scope of the chemical reactions; Heinze and Koschella, 2005). Due to this complexity, many scientists use cellulose derivatives rather than unmodified cellulose. Presently, a variety of cellulose-derived polymers are commercially available as bulk material. One important example is hydroxypropyl cellulose (HPC), which is readily available because of its industrial use in coatings and food applications (Wüstenberg, 2014). Like native cellulose, HPC provides 3 hydroxy groups per anhydroglucose unit (AGU) and exhibits a significantly higher solubility in many common organic solvents compared to the unmodified polysaccharide. Due to this property, further modification is technologically simplified, and the molecule can be, for example, esterified with various carboxylic acids in a one-step reaction while retaining good control of the degree of substitution (DS; Nau et al., 2018). Therefore, the polysaccharide can be easily equipped with various functions, such as fluorescence labels (e.g., pyrene; Winnik et al., 1987), that can be used as macro initiators for further polymerization (Ostmark et al., 2007), and control of the film formation properties and optical properties, amongst others, is possible (Bhadani and Gray, 1983). To use HPC as a base material for functional polymer gels, different approaches have been described in the literature. Gehrke et al. chemically crosslinked HPC by treatment with divinyl sulfone and analyzed the resulting microstructure and swelling characteristics (Harsh and Gehrke, 1991; Kabra et al., 1998). Other strategies that achieved covalent network formation of HPC include reaction with methacrylic anhydride (Hoo et al., 2013), *p*-formaldehyde (Suto, 1989), dialdehydes (Suto and Yoshinaka, 1993), and isocyanates (Suto et al., 1992), the formation of disulfide bonds (Tan et al., 2011), and gamma ray or electron beam irradiation (Wach et al., 2002). With respect to the light-induced formation of swellable HPC polymer gels, very few reports have been published to date. Bhadani and Gray esterified HPC with acryloyl chloride followed by photo-crosslinking already to stabilize the mesophase structure of a cholesteric film (Bhadani and Gray, 1984). The polymer was effectively crosslinked, and the structure was stable over a broad range of temperatures, but the mechanical properties of the resulting films were not optimal. An elegant approach was very recently described by Teramoto et al. (Yano et al., 2018). In their work, HPC was first esterified with cinnamoyl chloride, which can be crosslinked by illumination with UV light. The degree of crosslinking can be controlled either by adjusting the DS or by modulating the irradiation time. However, UV light (280 nm) is required for the crosslinking reaction, and relatively high DS values (1.3–3) are necessary for efficient network formation, which dramatically limits the flexibility of the system. Therefore, it is highly desirable to develop an alternative method that is more modular regarding polarity and light source.

In the present manuscript, we report a different approach for the photo-induced chemical crosslinking of HPC as films on solid model-surfaces using radical initiators. The approach is highly efficient and versatile with respect to the light source and thus allows for spatially resolved network formation in well-defined areas by using a commercially available 405 nm laser diode combined with an x/y movement system. In contrast to lithographic methods based on the use of photomasks (Böhm et al., 2013; Kargl et al., 2013), this method provides more versatile and faster approach tosurface patterning with less instrumental effort. In the first step, we functionalized HPC in a controlled fashion with unsaturated fatty acids, which can be crosslinked by using a photo-induced radical reaction. Via subsequent co-esterification steps, various functionalities can be introduced, yielding different and tailored functions of this polysaccharide. During the crosslinking process, *in situ* attachment of the polymer network to a model surface exposing

allyl groups is possible. Consequently, we investigated the influence of the illumination time on network formation. For this purpose, the swelling process of the surface-bound gels was monitored via time-resolved confocal fluorescence microscopy. Finally, a microfluidic device was developed as a simple demonstration, in which a surface-attached functional HPC gel was used for the local upconcentration of organic model analytes, giving an interesting prospect for further research into low-instrumented sensing and/or purification devices.

MATERIALS AND METHODS

In this section, the most relevant results of the polymer synthesis are shown. For the clarity of the manuscript, further details for the syntheses and preparation procedures, a complete list of all solvents and reagents (including suppliers and purities), detailed information of all instruments and measurement methods, and details on reference experiments (bulk swelling) are shown in the **Supplementary Material**.

Polymer Synthesis

To synthesize the photo-crosslinkable polymers, we first dissolved HPC in THF (tetrahydrofuran) and then brought it to reaction with fatty acid chlorides. To generate a hydrophobic polymer, HPC was treated with stearoyl chloride (6 equiv.) and 10-undecenoyl chloride (1 equiv.) in a one-pot synthesis to afford a mixed HPC ester **1**. Details of the synthesis can be found in the **Supplementary Material**. The reaction led to degrees of substitution of 2.75 for stearoyl and 0.25 for undecenoyl moieties (DS were determined by NMR, see the **Supplementary Material**; **Figure 1**). In addition to this non-polar mixed ester, we synthesized a polar, hydrophilic polymer via the same method, which after cross-linking yielded a hydrogel rather than an organogel. To this end, we treated HPC with small amounts (0.5 equiv.) of 10 undecenoyl chloride so that hydrophilic reference ester **2** was obtained in quantitative yield, exhibiting a DS of 0.3 (**Figure 1**). Finally, the chemical structure of each polymer was characterized according to our recently published work (for details see **Supplementary Material**).

Note that stearoyl esters of cellulose are capable to form complexes with proteins such as bovine serum albumin (Niegelhell et al., 2017). For this reason, the formation of stearoyl esters, and tailored networks thereof is of particular interest.

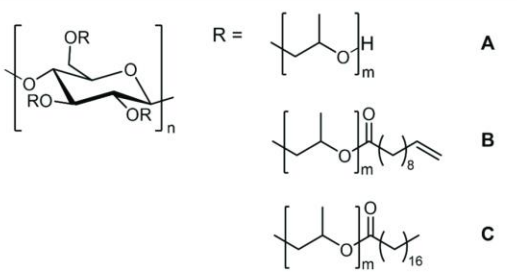

Groups per AGU:

HPC ester	A	B	C
1	-	0.25	2.75
2	2.70	0.30	-

FIGURE 1 | Synthesis of HPC esters **1** and **2**: Hydrophobic ester **1** exhibits 0.25 undecenoyl (B) and 2.75 stearoyl groups (C) per AGU, and hydrophilic ester **2** is esterified by 0.30 undecenoyl groups (B) per AGU, whereas 2.70 OH groups per AGU remain unmodified (A).

RESULTS AND DISCUSSION

Spatially Resolved Crosslinking and *in situ* Surface Attachment

Next, we were interested in designing organogels by attaching polymer **1** to the surface of a planar solid substrate in a spatially controlled fashion using a photo-initiator. Benzophenone derivatives, amongst others, are capable of generating radicals by illumination. These well-established photo-initiators provide various highly beneficial properties for the crosslinking of many systems: The activation and radical formation of benzophenone (BP) itself can be accomplished at relatively high wavelengths when compared to similar compounds (the upper absorption maximum of BP is located at $\lambda = 340$ nm; Allen et al., 1990). Consequently, it is not necessary to use high-energy light, which would otherwise be likely to damage sensitive molecules (Riga et al., 2017). Furthermore, radical formation with BP is a reversible process, implying high efficiency as an initiator (Dorman and Prestwich, 1994). If BP is functionalised with electron-donating or electron-withdrawing groups, the activation wavelength can be shifted, which allows the use of a broad range of light sources (Allen et al., 1990). To form the spatially controlled network of **1**, we decided to use a commercial laser diode ($\lambda = 405$ nm) as the light source because it is readily available and inexpensive. In addition, 405 nm light can be produced by light emitting diodes (LEDs), which opens the opportunity for the high-efficiency implementation of this method in a larger scale setting, in contrast to the use of mercury vapor lamps to generate UV radiation. Therefore, Michler's ketone [4,4′-bis(diethylamino)-benzophenone, DEABP] was found to be the most suitable initiator (see the **Supplementary Material**). To cross-link the reactive groups within the polysaccharide with functional groups on the solid substrate, appropriate pre-functionalization of the planar surface was carried out. We treated a glass slide with a mixture of allyltriethoxysilane (All-TES) and tetraethyl orthosilicate (TEOS; Ratio 15:85) by the method of Andrieu-Brunsen and co-workers (Krohm et al., 2016). Extensive characterization of this surface was reported in the literature (Krohm et al., 2016). Thus, a stable and homogeneous surface providing allyl functionalities was obtained. Note, allyl groups of All-TES are predestined for radical reactions and thus enable the polymer to be attached to the surface by a radical reaction pathway (Burkhard, 1950).

A DEABP-containing polymer solution in chloroform was solvent-casted onto the allyl-modified glass slide followed by

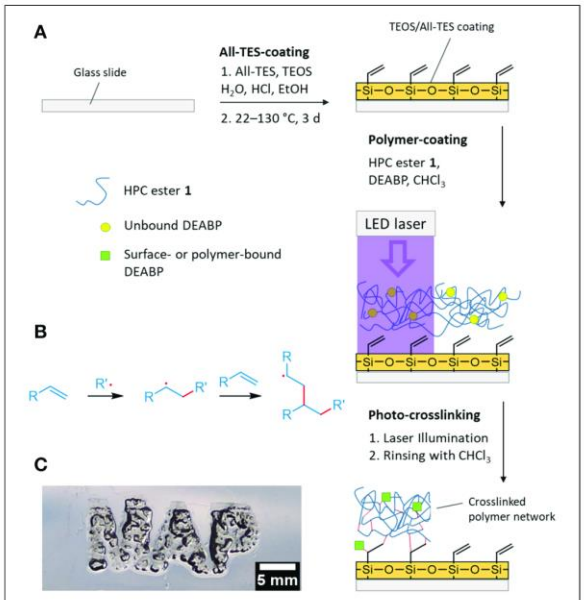

FIGURE 2 | (A) Schematic of the production of surface-bound polymer network 1 crosslinked via laser treatment; **(B)** reaction scheme of the radical reaction between generated polymer radicals and double bonds of the polymer or the All-TES surface; **(C)** photograph of the surface-attached polymer network swollen in $CHCl_3$. The illumination time used to generate the network was 20 ms with a 405 nm laser diode.

air drying and treatment with short pulses of laser light (laser-diode, 1,000 mW, 100 µm spot dia., $\lambda = 405$ nm). The actual spatial resolution of this setup is currently limited by said spot diameter. A scheme of this process is shown in **Figure 2A**. By installing the laser in a computer numerically controlled (CNC) x/y movement system (see **Supplementary Material**), the production of polymer networks with well-defined geometries was easily accomplished (resolution: 350 DPI, limited by the control system; see **Figure 2B**). Finally, any unbound polymer was removed by rinsing with $CHCl_3$, yielding a surface-bound swellable polymer network in well-defined regions (see **Figure 2**).

Next, we examined the influence of the illumination time on the generation of the polymer network by laser light. To this end, the pulse-lengths during illumination were altered between 5 and 40 ms, and the swelling behavior of the spatially confined and surface-attached polymer networks was characterized by analyzing the linear deformation parameter α (one-dimensional relative swelling degree: the thickness of the swollen polymer film divided by the thickness of the dry polymer film) in equilibrium swelling. While α refers to the linear deformation in general we introduce α_m to as an additional parameter to denote α in equilibrium state. Therefore, the film thicknesses were determined by confocal laser scanning microscopy (CLSM; for details of the analysis see the **Supplementary Material**, for still frames captured at different times see **Figure 3A**). Note that DEABP itself is non-fluorescent when excited at a wavelength of 488 nm (the wavelength used in the CLSM measurements, see below) but becomes fluorescent after the crosslinking reaction due to alteration of the electronic structure of the molecule. The use of CLSM not only allows a static determination of the film thickness in equilibrium swelling but also enables dynamic monitoring of the swelling process (resolution: 460 ms; **Figure 3B**). For the comparison of the different samples, the parameter α is always referenced to their respective dry film thickness. By illuminating the deposited polymer film with laser light for 5 ms per spot, sufficient network points can be generated to form a surface-bound polymer network. If the illumination time is increased to approximately 30 ms, the degree of equilibrium linear deformation α_m of the polymer network exponentially decreases from $\alpha_{m,5ms} = 5.8$ to $\alpha_{m,30ms} = 2.2$, to a value that is in good agreement with the theoretical value of a quantitatively crosslinked polymer network in bulk (for details of the calculation of this particular value, see **Supplementary Material**; **Figure 3C**, square symbols). If the illumination time is further increased to 40 ms, the polymer network detaches from the surface. The latter phenomenon may be caused by decreased network flexibility, which leads to high mechanical forces and cohesive failure during swelling.

Because of their differences in chemical network structure, the individual samples show distinctly different swelling kinetics: If the netpoint density n is low, the diffusion of the solvent molecules to the substrate near the polymer layers is essentially unhindered by diffusion through the gel. Thus, the swelling behavior appears to follow first-order kinetics, as discussed for a similar system in the literature (**Figure 3B**, black line; Schott, 2006). If the netpoint density is increased, then the local viscosity increases, and the swelling kinetics becomes a product of the actual thermodynamically controlled swelling and diffusion processes, leading to a more complex behavior that may no longer be described by simple first-order kinetics (**Figure 3B**, purple line; Schott, 2006).

To learn more about the network structure from the swelling behavior, the netpoint density n of the surface-attached polymer gel can be estimated by using the Flory-Rhener equation. Because swelling is hindered by surface linkages, only one-dimensional swelling can occur. Consequently, to determine n, the linear deformation α_m may be considered instead of using the volumetric degree of swelling q_m (Toomey et al., 2004). Rühe and co-workers demonstrated that with surface-attached polymer networks, q_m scales as $\alpha_m^{9/5}$ and not as α_m^3, as could be expected, because the surface-attached networks can only swell in one direction, i.e., away from the surface (Toomey et al., 2004). Finally, the Flory-Rhener equation can be transformed into equation 1 for the determination of the netpoint density of our polymer (for further details, see **Supplementary Material**).

$$n = \frac{-\left[\ln\left(1-\frac{1}{\alpha_m^{9/5}}\right)+\frac{1}{\alpha_m^{9/5}}+\chi\left(\frac{1}{\alpha_m^{9/5}}\right)^2\right]}{V_1\left(\sqrt[3]{\frac{1}{\alpha_m^{9/5}}}-\frac{1}{2\alpha_m^{9/5}}\right)} \quad (1)$$

In equation 1, V_1 represents the molar volume of the solvent (i.e., 80.66 cm^3/mol for chloroform), and χ is the characteristic Flory-Huggins polymer-solvent interaction parameter. In our

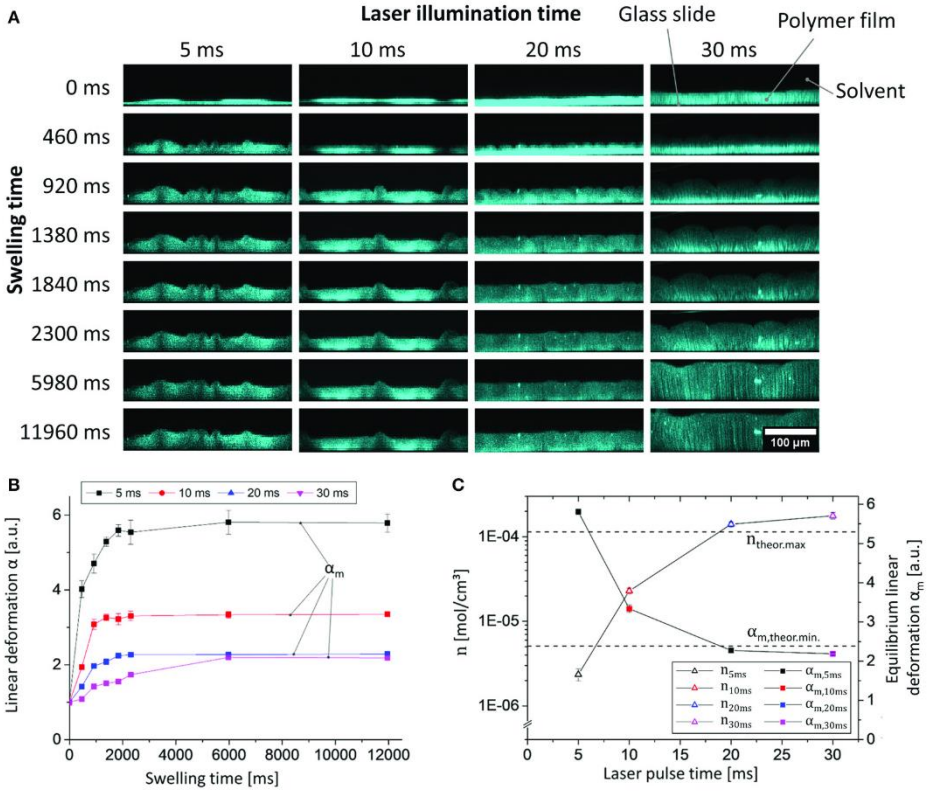

FIGURE 3 | Data from experiments of the swelling of polymer **1** in chloroform photo-crosslinked by different laser illumination times (5, 10, 20, and 30 ms) measured via CLSM: **(A)** Still images of the dynamic x/z CLSM measurements (the microscopic morphology (i.e., non-flat) structure is the result of the spotwise laser illumination); **(B)** plot of linear deformation α vs. swelling time; **(C)** plot of linear deformation in equilibrium α_m vs. laser pulse time (blue plot); netpoint density calculated by equation 1 vs. laser pulse time (black plot) (theoretical maximum/minimum values are visualized as straight horizontal dashed lines).

case here, this parameter was estimated to be $\chi = 0.48$ for **1** in chloroform at 22°C, according to incremental calculations by the method of Hoy (as shown in the **Supplementary Material**; van Krevelen and te Nijenhuis, 2009). As calculated from equation 1, the netpoint density of the polymer gel increases from $n_{5ms} = 2.4 \times 10^{-6}$ mol/cm^3 to $n_{30ms} = 1.8 \times 10^{-4}$ mol/cm^3 (**Figure 3C**, triangular symbols). Note that the latter apparently corresponds to the calculated maximum of n ($n_{theor.max} = 1.1 \times 10^{-4}$ mol/cm^3, determined from the number of crosslinkable double bonds, see **Supplementary Material**) if the numerous approximations within the Flory-Rhener theory and Hoy's incremental calculation are taken into account (Valentín et al., 2008). Based on these findings, we are able to tailor the netpoint density to desired values simply by modifying the crosslinking parameters, without alteration of the polymer itself. This result demonstrates the versatility of our surface-attached cellulose-derived polymer network.

Application in a Microfluidic Channel

Because the prepared organogels can be attached to solid substrates, we were also interested in using the gels in a microfluidic demonstration device for the separation of an organic model pollutant from an aqueous solution. For this proof of principle a polymer patch, either made from polymer **1** or **2** was generated within a microfluidic channel comprising two glass slides held together by double-sided adhesive tape and with a capillary gap of 100 µm (**Figure 4A**). As a model substance for organic molecules ("pollutants") in water, a saturated aqueous solution of pyrene was transported through the channel via capillary flow, and the gray values at different channel areas were determined during the experiment (**Figure 4B**; **Supplementary Material**). Note that the use of pyrene at the same time serves as a sensor due to its intrinsic fluorescence. If the solution comes into contact with the patch of crosslinked polymer **1**, pyrene accumulates within the patch to a very large extent, and the gray value (i.e., fluorescence) of the polymer patch increases as a result. Consequently, the mean gray value in the same area before the solution has passed through the patch is significantly higher than the value afterwards (**Figure 4B**), demonstrating the absorption and upconcentration of the pyrene in the patch. Note that pyrene did not accumulate in the channels that were composed of hydrophilic network patches of polymer **2**,

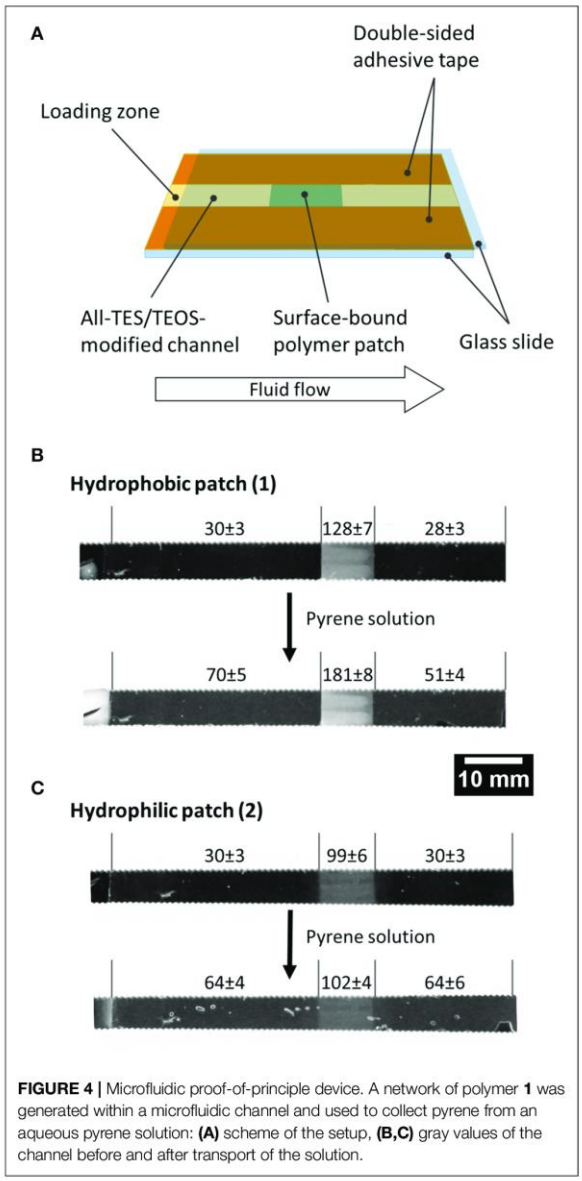

FIGURE 4 | Microfluidic proof-of-principle device. A network of polymer **1** was generated within a microfluidic channel and used to collect pyrene from an aqueous pyrene solution: **(A)** scheme of the setup, **(B,C)** gray values of the channel before and after transport of the solution.

because hydrophobic interactions are intrinsically prevented due to missing hydrophobic side chains as compared to the network composed of polymer **1** (see **Figure 4C**). Although the results reported here are qualitative, nonetheless, this simple experiment demonstrates that the surface-attached organogel is capable of upconcentrating non-polar organic molecules from solution.

CONCLUSION

In conclusion, we developed a novel and versatile method to efficiently photo-crosslink hydroxypropyl cellulose derivatives for the generation of swellable polymer networks with a focus on organogels. The method is highly versatile and allows for the synthesis of organogels by esterification of the cellulose biomolecule with different fatty acids. By using DEABP as a photo-initiator, network formation can be induced by illumination with a conventional 405 nm laser [equipped with a computer numerically controlled (CNC) x/y movement system]. As a result, spatially resolved crosslinking of the polymer via laser illumination is possible. The swelling behavior (degree of swelling) and, thus, the netpoint density (estimated by the Flory-Rhener equilibrium swelling theory) of the surface-linked network, was determined via confocal fluorescence microscopy, yielding results that matched the theoretical estimation. This method allows the dynamic monitoring of the swelling process and, hence, the determination of the swelling kinetics. As a result, gels providing low netpoint densities swell through first-order kinetics, whereas the swelling of networks with higher crosslinking degrees follows a more complex mechanism. Finally, as a proof of principle, we generated a microfluidic channel based on a hydrophobic polymer network patch; our channel is able to concentrate an organic model dye within the patch, as opposed to a reference channel that is incorporating a hydrophilic polymer network patch. This is a promising starting point to increase the sensitivity of analytical devices, by locally increasing the analyte concentration. Via specific adjustment of the netpoint density, the control of the swelling behavior, and therefore, the flow speed and the dye-gel interaction, will be investigated in future trials.

AUTHOR CONTRIBUTIONS

All authors listed, have made substantial, direct, and intellectual contribution to the work. MN, DS, and AB performed all experiments. MN, MB, and ST analyzed the data, reviewed the literature, and wrote the manuscript. MB coordinated the complete project. All authors discussed and reviewed the results and approved the manuscript.

FUNDING

We gratefully acknowledge the financial support by the German Research Foundation (DFG) within the Collaborative Research Centre 1194 Interaction of Transport and Wetting Processes, Project A05.

ACKNOWLEDGMENTS

We thank Tobias Meckel for discussion and help concerning microscopy.

SUPPLEMENTARY MATERIAL

The Supplementary Material for this article can be found online at: https://www.frontiersin.org/articles/10.3389/fchem.2019.00367/full#supplementary-material

REFERENCES

Ajayaghosh, A., and Praveen, V. K. (2007). Pi-organogels of self-assembled p-phenylenevinylenes: Soft materials with distinct size, shape, and functions. *Account. Chem. Res.* 40, 644–656. doi: 10.1021/ar7000364

Allen, N. S., Lam, E., Kotecha, J. L., Green, W. A., Timms, A., Navaratnam, S., et al. (1990). Photochemistry of novel 4-alkylamino benzophenone initiators: a conventional laser flash photolysis and mass spectrometry study. *J. Photochem. Photobiol. A* 54, 367–388. doi: 10.1016/1010-6030(90)85009-L

Annabi, N., Tamayol, A., Uquillas, J. A., Akbari, M., Bertassoni, L. E., Cha, C., et al. (2014). 25th anniversary article: rational design and applications of hydrogels in regenerative medicine. *Adv. Mater.* 26, 85–124. doi: 10.1002/adma.201303233

Bhadani, S. N., and Gray, D. G. (1983). Cellulose-based liquid crystalline polymers; esters of (Hydroxypropyl) cellulose. *Mol. Cryst. Liq. Cryst.* 99, 29–38. doi: 10.1080/00268948308072026

Bhadani, S. N., and Gray, D. G. (1984). Crosslinked cholesteric network from the acrylic acid ester of (Hydroxypropyl)cellulose. *Mol. Cryst. Liq. Cryst.* 102, 255–260. doi: 10.1080/01406568408070536

Böhm, A., Gattermayer, M., Trieb, C., Schabel, S., Fiedler, D., Miletzky, F., et al. (2013). Photo-attaching functional polymers to cellulose fibers for the design of chemically modified paper. *Cellulose* 20, 467–483. doi: 10.1007/s10570-012-9798-x

Burkhard, C. A. (1950). The reaction of mercaptans with alkenyl silanes. *J. Am. Chem. Soc.* 72, 1078–1080. doi: 10.1021/ja01159a007

Chaves, K. F., Barrera-Arellano, D., and Ribeiro, A. P. B. (2018). Potential application of lipid organogels for food industry. *Food Res. Inter.* 105, 863–872. doi: 10.1016/j.foodres.2017.12.020

Datta, S., and Bhattacharya, S. (2015). Multifarious facets of sugar-derived molecular gels: Molecular features, mechanisms of self-assembly and emerging applications. *Chem. Soc. Rev.* 44, 5596–5637. doi: 10.1039/c5cs00093a

Dorman, G., and Prestwich, G. D. (1994). Benzophenone photophores in biochemistry. *Biochemistry* 33, 5661–5673. doi: 10.1021/bi00185a001

Esposito, C. L., Kirilov, P., and Roullin, V. G. (2018). Organogels, promising drug delivery systems: An update of state-of-the-art and recent applications. *J. Control. Release* 271, 1–20. doi: 10.1016/j.jconrel.2017.12.019

García, J. M., Jones, G. O., Virwani, K., McCloskey, B. D., Boday, D. J., ter Huurne, G. M., et al. (2014). Recyclable, strong thermosets and organogels via paraformaldehyde condensation with diamines. *Science* 344, 732–736. doi: 10.1126/science.1251484

George, M., and Weiss, R. G. (2006). Molecular organogels. Soft matter comprised of low-molecular-mass organic gelators and organic liquids. *Account. Chem. Res.* 39, 489–497. doi: 10.1021/ar0500923

Harsh, D. C., and Gehrke, S. H. (1991). Controlling the swelling characteristics of temperature-sensitive cellulose ether hydrogels. *J. Control. Release* 17, 175–185. doi: 10.1016/0168-3659(91)90057-K

Heinze, T., and Koschella, A. (2005). Solvents applied in the field of cellulose chemistry - a mini review. *Polim. Cienc. Tecnol.* 15, 84–90. doi: 10.1590/S0104-14282005000200005

Hennink, W. E., and van Nostrum, C. F. (2002). Novel crosslinking methods to design hydrogels. *Adv. Drug Deliv. Rev.* 54, 13–36. doi: 10.1016/S0169-409X(01)00240-X

Hinze, W. L., Uemasu, I., Dai, F., and Braun, J. M. (1996). Analytical and related applications of organogels. *Curr. Opin. Coll. Interface Sci.* 1, 502–513. doi: 10.1016/S1359-0294(96)80119-1

Hirst, A. R., Escuder, B., Miravet, J. F., and Smith, D. K. (2008). High-tech applications of self-assembling supramolecular nanostructured gel-phase materials: From regenerative medicine to electronic devices. *Angew. Chem.* 47, 8002–8018. doi: 10.1002/anie.200800022

Hoo, S. P., Loh, Q. L., Yue, Z., Fu, J., Tan, T. T. Y., Choong, C., et al. (2013). Preparation of a soft and interconnected macroporous hydroxypropyl cellulose methacrylate scaffold for adipose tissue engineering. *J. Mater. Chem. B* 1, 3107–3117. doi: 10.1039/c3tb00446e

Jagur-Grodzinski, J. (2009). Polymeric gels and hydrogels for biomedical and pharmaceutical applications. *Polym. Adv. Technol.* 21, 27–47. doi: 10.1002/pat.1504

Jakubiak, J., Allonas, X., Fouassier, J. P., Sionkowska, A., Andrzejewska, E., Linden, L. Å., et al. (2003). Camphorquinone–amines photoinitating systems for the initiation of free radical polymerization. *Polymer* 44, 5219–5226. doi: 10.1016/S0032-3861(03)00568-8

Kabra, B. G., Gehrke, S. H., and Spontak, R. J. (1998). Microporous, responsive hydroxypropyl cellulose Gels. 1. Synthesis and microstructure. *Macromolecules* 31, 2166–2173. doi: 10.1021/ma970418q

Kargl, R., Mohan, T., Köstler, S., Spirk, S., Doliška, A., Stana-Kleinschek, K., et al. (2013). Functional patterning of biopolymer thin films using enzymes and lithographic methods. *Adv. Funct. Mater.* 23, 308–315. doi: 10.1002/adfm.201200607

Kirilov, P., Rum, S., Gilbert, E., Roussel, L., Salmon, D., Abdayem, R., et al. (2014). Aqueous dispersions of organogel nanoparticles - potential systems for cosmetic and dermo-cosmetic applications. *Int. J. Cosm. Sci.* 36, 336–346. doi: 10.1111/ics.12131

Klemm, D., Heublein, B., Fink, H.-P., and Bohn, A. (2005). Cellulose: fascinating biopolymer and sustainable raw material. *Angew. Chem.* 44, 3358–3393. doi: 10.1002/anie.200460587

Krohm, F., Kind, J., Savka, R., Alcaraz Janßen, M., Herold, D., Plenio, H., et al. (2016). Photochromic spiropyran- and spirooxazine-homopolymers in mesoporous thin films by surface initiated ROMP. *J. Mater. Chem. C* 4, 4067–4076. doi: 10.1039/C5TC04054J

Lai, H. Y., Leon, A., d., Pangilinan, K., and Advincula, R. (2018). Superoleophilic and under-oil superhydrophobic organogel coatings for oil and water separation. *Progr. Org. Coat.* 115, 122–129. doi: 10.1016/j.porgcoat.2017.11.001

Larsson, M., Johnsson, A., Gårdebjer, S., Bordes, R., and Larsson, A. (2017). Swelling and mass transport properties of nanocellulose-HPMC composite films. *Mater. Des.* 122, 414–421. doi: 10.1016/j.matdes.2017.03.011

Marangoni, A. G. (2012). Organogels: an alternative edible oil-structuring method. *J. Am. Oil Chem. Soc.* 89, 749–780. doi: 10.1007/s11746-012-2049-3

Meazza, L., Foster, J. A., Fucke, K., Metrangolo, P., Resnati, G., and Steed, J. W. (2013). Halogen-bonding-triggered supramolecular gel formation. *Nat. Chem.* 5, 42–47. doi: 10.1038/nchem.1496

Merlin, A., Lougnot, D.-J., and Fouassier, J.-P. (1980). Laser spectroscopy of substituted benzophenone used as photo-initiators of vinyl polymerization. *Polymer Bull.* 2, 847–853. doi: 10.1007/BF00255514

Mukhopadhyay, P., Iwashita, Y., Shirakawa, M., Kawano, S.-I., Fujita, N., and Shinkai, S. (2006). Spontaneous colorimetric sensing of the positional isomers of dihydroxynaphthalene in a 1D organogel matrix. *Angew. Chem.* 45, 1592–1595. doi: 10.1002/anie.200503158

Nau, M., Seelinger, D., and Biesalski, M. (2018). Functional surface coatings from tailor-made long-chain hydroxypropyl cellulose ester nanoparticles. *Cellulose* 134:44949. doi: 10.1007/s10570-018-1981-2

Niegelhell, K., Süßenbacher, M., Sattelkow, J., Plank, H., Wang, Y., Zhang, K., et al. (2017). How bound and free fatty acids in cellulose films impact nonspecific protein adsorption. *Biomacromolecules* 18, 4224–4231. doi: 10.1021/acs.biomac.7b01260

Osada, Y., and Gong, J.-P. (1998). Soft and wet materials: polymer gels. *Adv. Mater.* 10, 827–837.

Ostmark, E., Harrisson, S., Wooley, K. L., and Malmström, E. E. (2007). Comb polymers prepared by ATRP from hydroxypropyl cellulose. *Biomacromolecules* 8, 1138–1148. doi: 10.1021/bm061043w

Prati, S., Volpi, F., Fontana, R., Galletti, P., Giorgini, L., Mazzeo, R., et al. (2018). Sustainability in art conservation: a novel bio-based organogel for the cleaning of water sensitive works of art. *Pure Appl. Chem.* 90, 239–251. doi: 10.1515/pac-2017-0507

Riga, E., Saar, J., Erath, R., Hechenbichler, M., and Lienkamp, K. (2017). On the Limits of benzophenone as cross-linker for surface-attached polymer hydrogels. *Polymers* 9:686. doi: 10.3390/polym9120686

Rivest, C., Morrison, D. W. G., Ni, B., Rubin, J., Yadav, V., Mahdavi, A., et al. (2007). Microscale hydrogels for medicine and biology: synthesis, characteristics and applications. *J. Mech. Mater. Struct.* 2, 1103–1119. doi: 10.2140/jomms.2007.2.1103

Sangeetha, N. M., and Maitra, U. (2005). Supramolecular gels: functions and uses. *Chem. Soc. Rev.* 34, 821–836. doi: 10.1039/b417081b

Schott, H. (2006). Swelling kinetics of polymers. *J. Macromol. Sci. Part B* 31, 1–9. doi: 10.1080/00222349208215453

Segarra-Maset, M. D., Nebot, V. J., Miravet, J. F., and Escuder, B. (2013). Control of molecular gelation by chemical stimuli. *Chem. Soc. Rev.* 42, 7086–7098. doi: 10.1039/c2cs35436e

Suto, S. (1989). Crosslinked hydroxypropyl cellulose solid films cast from liquid crystalline solutions. *J. Appl. Polym. Sci.* 37, 2781–2784. doi: 10.1002/app.1989.070370927

Suto, S., Tashiro, H., and Karasawa, M. (1992). Preparation and mechanical properties of chemically cross-linked hydroxypropyl cellulose solid films retaining cholesteric liquid crystalline order. *J. Appl. Polym. Sci.* 45, 1569–1585. doi: 10.1002/app.1992.070450908

Suto, S., and Yoshinaka, M. (1993). Chemical cross-linking of cholesteric liquid-crystalline hydroxypropyl cellulose with dialdehydes. *J. Mater. Sci.* 28, 4644–4650. doi: 10.1007/BF00414253

Suzuki, M., and Hanabusa, K. (2010). Polymer organogelators that make supramolecular organogels through physical cross-linking and self-assembly. *Chem. Soc. Rev.* 39, 455–463. doi: 10.1039/b910604a

Tan, J., Kang, H., Liu, R., Wang, D., Jin, X., Li, Q., et al. (2011). Dual-stimuli sensitive nanogels fabricated by self-association of thiolated hydroxypropyl cellulose. *Polym. Chem.* 2, 672–678. doi: 10.1039/C0PY 00348D

Toba, Y., Yasuike, M., and Usui, Y. (1997). The 'onium butyltriphenylborates as novel donor-acceptor initiators for free radical photopolymerization. *Chem. Commun.* 1997, 675–676. doi: 10.1039/A700579B

Toomey, R., Freidank, D., and Rühe, J. (2004). Swelling behavior of thin, surface-attached polymer networks. *Macromolecules* 37, 882–887. doi: 10.1021/ma034737v

Valentín, J. L., Carretero-González, J., Mora-Barrantes, I., Chassé, W., and Saalwächter, K. (2008). Uncertainties in the determination of cross-link density by equilibrium swelling experiments in natural rubber. *Macromolecules* 41, 4717–4729. doi: 10.1021/ma8005087

van Krevelen, D. W., and te Nijenhuis, K. (2009). *Properties of Polymers*. Amsterdam: Elsevier.

van Tomme, S. R., Storm, G., and Hennink, W. E. (2008). *In situ* gelling hydrogels for pharmaceutical and biomedical applications. *Int. J. Pharmac.* 355, 1–18. doi: 10.1016/j.ijpharm.2008.01.057

Venkatesan, G. A., and Sarles, S. A. (2016). Droplet immobilization within a polymeric organogel improves lipid bilayer durability and portability. *Lab Chip* 16, 2116–2125. doi: 10.1039/c6lc00391e

Vintiloiu, A., and Leroux, J.-C. (2008). Organogels and their use in drug delivery–a review. *J. Control. Release* 125, 179–192. doi: 10.1016/j.jconrel.2007.09.014

Wach, R. A., Mitomo, H., Yoshii, F., and Kume, T. (2002). Hydrogel of radiation-induced cross-linked hydroxypropylcellulose. *Macromol. Mater. Eng.* 287, 285–295. doi: 10.1002/1439-2054(20020401)287:4<285:AID-MAME285>3.0.CO;2-3

Wang, J., and Zhang, K. (2018). Modular adjustment of swelling behaviors of surface-modified solvent-responsive polymeric nanoparticles based on cellulose 10-undecenoyl ester. *J. Phys. Chem. C* 122, 7474–7483. doi: 10.1021/acs.jpcc.7b11521

Winnik, F. M., Winnik, M. A., Tazuke, S., and Ober, C. K. (1987). Synthesis and characterization of pyrene-labeled hydroxypropyl cellulose and its fluorescence in solution. *Macromolecules* 20, 38–44. doi: 10.1021/ma00167a008

Wüstenberg, T. (2014). *Cellulose and Cellulose Derivatives in the Food Industry: Fundamentals and Applications*. New York, NY: Wiley-VCH.

Xue, P., Yao, B., Wang, P., Gong, P., Zhang, Z., and Lu, R. (2015). Strong fluorescent smart organogel as a dual sensing material for volatile acid and organic amine vapors. *Chemistry* 21, 17508–17515. doi: 10.1002/chem.201502401

Yano, S., Iwase, T., Teramoto, N., Shimasaki, T., and Shibata, M. (2018). Synthesis, thermal properties and cell-compatibility of photocrosslinked cinnamoyl-modified hydroxypropyl cellulose. *Carbohyd. Polymers* 184, 418–426. doi: 10.1016/j.carbpol.2017.12.087

Conflict of Interest Statement: The authors declare that the research was conducted in the absence of any commercial or financial relationships that could be construed as a potential conflict of interest.

4.4. Design of friction, morphology, wetting and protein affinity by cellulose blend thin film composition

The content of this chapter has been published in:

Caterina Czibula, Gundula Teichert, Maximilian Nau, Mathias Hobisch, Chonnipa Palasingh, Markus Biesalski, Stefan Spirk, Christian Teichert and Tiina Nypelö, “Design of friction, morphology, wetting and protein affinity by cellulose blend thin film composition”, *Front. Chem.*, **2019**, 7, 239, published by Frontiers under the CC-BY 4.0 license, reprint does not require explicit permission.

Following the research on HPC esterification in section 4.1 a multilateral and international cooperation with Prof. Stefan Spirk (Graz University of Technology, Austria), Prof. Christian Teichert (University of Leoben, Austria) and Prof. Tiina Nypelö (Chalmers University of Technology, Sweden) was started. We were interested in possible applications of HPC stearic acid esters in the formation of blend films with trimethylsilyl cellulose (TMSC) and the resulting surface properties. For readability the blends are referred to by their fractional composition in the format TMSC:HPCE, i.e. a composition of 3 parts TMSC and 1 part HPCE would be 3:1. During this research the phase separation of blends formed from the HPCE and TMSC were exploited to generate both, chemically and morphologically, unique surface structures This was facilitated through the variation of the ratio of TMSC and HPCE, both dissolved in chloroform, and subsequent spin-coating onto either SPR-substrates or silicone wavers. The surfaces generated after evaporation of the solvent were characterized via AFM (Figure 4-4 a and b) to determine the morphology and localization of both polymers. Through regeneration of the cellulose in one set of the samples, identification of the respective protrusions and cavities became trivial since the loss in mass of TMSC during regeneration leads to obvious morphological changes in the film (Figure 4-4 b). The coatings with a ratio of 3:1 exhibited valleys of HPCE in a matrix comprised of TMCS, which after regeneration of the cellulose led to HPCE protrusions on the now collapsed cellulose. This arrangement was inverted when the for a ratio of 1:3, where initially TMSC protrusions are presented in a HPCE matrix that, after regeneration, form cellulose valleys. Contact mode friction force microscopy revealed further that the friction coefficient, as well as the adhesion force, was lower for the blend film than for the respective coatings prepared from the pure polymer (Figure 4-4 c). The final point of interest was, if the roughness or chemical composition of the coatings could be used to tune the unspecific protein adsorption. For this purpose, BSA was selected as model analyte and QCM-D measurements (to determine total adsorption) as well as SPR spectroscopy (dry mass, utilizing the de Feijter equation) were carried out and correlated with the ratio of the polymers (Figure 4-4 d). In brief, an increase in HPCE content led to an increased protein adsorption and the roughness, as well as friction appeared to showed no correlation to the protein adsorption, leading to the conclusion, that the surface free energy (Figure 4-4 e) appeared to be the dominating factor.

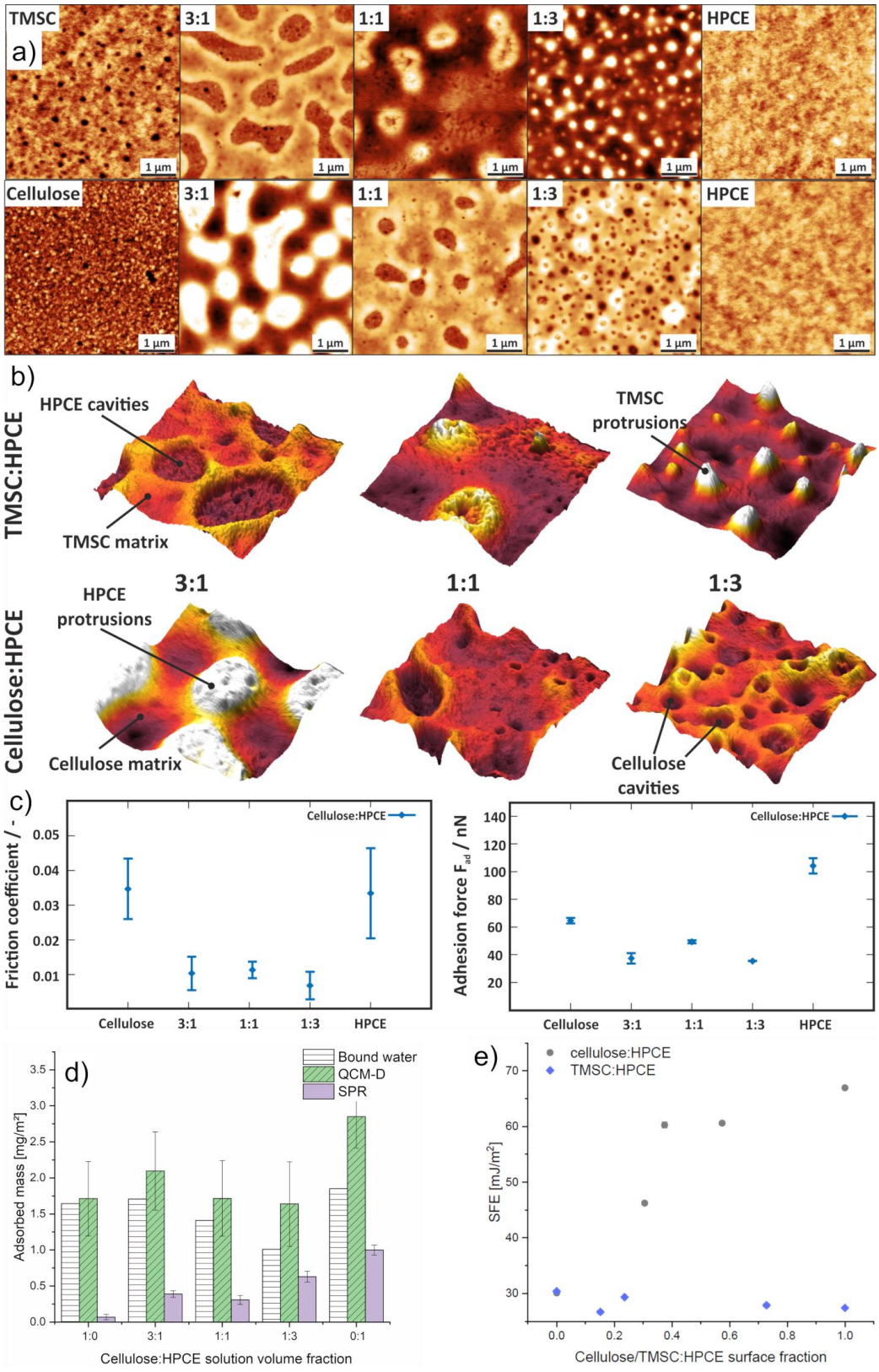

Figure 4-4: a) AFM topography imaging of polymer-blend coatings comprised of TMSC and HPC stearic acid ester with different blend ratio. On top the neat films after casting are displayed, while the bottom shows the same films after regeneration of cellulose from the TMSC b) High resolution 3D Images of the 2 x 2 µm sections of the AFM topography displayed in a), the distinct changes in morphology induced by the variation of the can be easily identified, z-scale is 60 nm. c) Friction coefficient and adhesion force measurements of coatings with different ratios, the data was obtained through contact mode AFM analysis. d) Analysis of BSA adsorption onto the different cellulose:HPCE coatings as well as total adsorption determined through QCM-D and SPR, showing a steady increase in BSA adsorption with increasing HPCE content. e) Plot of the BSA adsorption with the surface free energy.

frontiers in Chemistry

ORIGINAL RESEARCH
published: 03 May 2019
doi: 10.3389/fchem.2019.00239

Design of Friction, Morphology, Wetting, and Protein Affinity by Cellulose Blend Thin Film Composition

Caterina Czibula[1,2†], *Gundula Teichert*[3†], *Maximilian Nau*[4], *Mathias Hobisch*[3], *Chonnipa Palasingh*[5], *Markus Biesalski*[4], *Stefan Spirk*[2,3], *Christian Teichert*[1,2*] *and Tiina Nypelö*[5,6*]

[1] *Institute of Physics, Montanuniversität Leoben, Leoben, Austria,* [2] *Christian Doppler Laboratory for Fiber Swelling and Paper Performance, Graz University of Technology, Graz, Austria,* [3] *Institute of Paper, Pulp and Fiber Technology, Graz University of Technology, Graz, Austria,* [4] *Macromolecular Chemistry and Paper Chemistry, Technical University Darmstadt, Darmstadt, Germany,* [5] *Division of Applied Chemistry, Department of Chemistry and Chemical Engineering, Chalmers University of Technology, Gothenburg, Sweden,* [6] *Wallenberg Wood Science Center, Gothenburg, Sweden*

OPEN ACCESS

Edited by:
Giuseppe Mensitieri, University of Naples Federico II, Italy

Reviewed by:
Artur J. M. Valente, University of Coimbra, Portugal
Ram Gupta, Pittsburg State University, United States

***Correspondence:**
Christian Teichert
christian.teichert@unileoben.ac.at
Tiina Nypelö
tiina.nypelo@chalmers.se

†These authors have contributed equally to this work

Specialty section:
This article was submitted to Polymer Chemistry, a section of the journal Frontiers in Chemistry

Received: *28 January 2019*
Accepted: *26 March 2019*
Published: *03 May 2019*

Citation:
Czibula C, Teichert G, Nau M, Hobisch M, Palasingh C, Biesalski M, Spirk S, Teichert C and Nypelö T (2019) Design of Friction, Morphology, Wetting, and Protein Affinity by Cellulose Blend Thin Film Composition. Front. Chem. 7:239. doi: 10.3389/fchem.2019.00239

Cellulose derivate phase separation in thin films was applied to generate patterned films with distinct surface morphology. Patterned polymer thin films are utilized in electronics, optics, and biotechnology but films based on bio-polymers are scarce. Film formation, roughness, wetting, and patterning are often investigated when it comes to characterization of the films. Frictional properties, on the other hand, have not been studied extensively. We extend the fundamental understanding of spin coated complex cellulose blend films via revealing their surface friction using Friction Force Microscopy (FFM). Two cellulose derivatives were transformed into two-phase blend films with one phase comprising trimethyl silyl cellulose (TMSC) regenerated to cellulose with hydroxyl groups exposed to the film surface. Adjusting the volume fraction of the spin coating solution resulted in variation of the surface fraction with the other, hydroxypropylcellulose stearate (HPCE) phase. The film morphology confirmed lateral and vertical separation and was translated into effective surface fraction. Phase separation as well as regeneration contributed to the surface morphology resulting in roughness variation of the blend films from 1.1 to 19.8 nm depending on the film composition. Friction analysis was successfully established, and then revealed that the friction coefficient of the films could be tuned and the blend films exhibited lowered friction force coefficient compared to the single-component films. Protein affinity of the films was investigated with bovine serum albumin (BSA) and depended mainly on the surface free energy (SFE) while no direct correlation with roughness or friction was found. BSA adsorption on film formed with 1:1 spinning solution volume ratio was an outlier and exhibited unexpected minimum in adsorption.

Keywords: blend films, spinodal decomposition, cellulose, friction, protein adsorption, adhesion

INTRODUCTION

Spinodal decomposition of polymer blends can generate thin films with multi-phase surface composition, and often, complex morphology (Heriot and Jones, 2005). Lateral separation of the phases on a substrate results in patterns where islands of one phase reside within the other phase. Vertical separation can lead to heterogeneous distribution in the film's z-direction induced by surface energy differences of the components and can influence the surface morphology (Karim et al., 1998).

An intriguing area of research is the exploration of blend thin films obtained with spin coating. During the spin coating step, macroscopically homogeneous solutions of two polymers phase separate into the domains (Dalnoki-Veress et al., 1997). The ratio of the two polymers, molecular weight, solvent and spin coating conditions define the feature sizes and shapes (Xue et al., 2012). Synthetic polymer phase separation is exploited in coatings and organic electronics (Halls et al., 1995), while for biopolymer blend thin films their utilization and fundamentals, are still in their origins.

Cellulose synthetized by nature is notorious for insolubility having only few one-component solvents such as N-methylmorpholine-N-oxide (Medronho et al., 2012). In industrial fiber production, cellulose insolubility has been circumvented by derivatization followed by conversion to cellulose commonly referred to as regeneration. Similar approaches have been applied in thin film manufacturing involving derivatization, dissolution, film formation, and regeneration of the derivatized film to cellulose (Schaub et al., 1993; Kontturi et al., 2003a,b). Spin coating, and propagation of repeating submicron patterns, requires volatile and good solvents for the blend components. Trimethylsilyl cellulose (TMSC) dissolved in toluene or chloroform has been used for single-component cellulose films as well as for blend films (Kontturi et al., 2009, 2010; Nyfors et al., 2009; Niegelhell et al., 2016, 2017; Strasser et al., 2016). Regeneration takes place upon exposure to hydrochloric acid vapor (Schaub et al., 1993).

Cellulose in products is often an inert component intended to protect or seal, such as package products, or to carry functionalities as in paper-based diagnostics (Pelton, 2009). As a substrate it can be used to accommodate follow-up chemistries, for example, to bind peptides to further tune it for specific protein or antibody affinity and sensing of biological molecules (Orelma et al., 2012a,b; Zhang et al., 2013). In addition to detection, protein adsorption is a way to design medical materials or to control fouling of surfaces. The inhibition of protein deposition, on the other hand, is an asset when bacterial growth and biofilm formation are required to be blocked.

Biofilm formation on surfaces takes place in two phases where the first one includes reversible physical attachment of bacteria and the second irreversible, cellular phase. Surface roughness, wetting and surface configuration have been identified as key parameters for bacterial adhesion (An and Friedman, 1998). The effect of hydrophobicity is directly in connection with the properties of the bacteria while with respect to roughness there is direct evidence that increase in roughness—and hence, in the surface area—promotes bacterial adhesion. Roughness is different from surface configuration that refers to patterning on the surface. The periodicity and size of surface patterns has been found to be a parameter to inhibit bacterial adhesion. While bacteria preferentially adhere to irregularities that conform to their size since this maximizes bacteria-surface area (Katsikogianni and Missirlis, 2004), there is evidence that specific surface pattern design can prevent the attachment. A pattern mimicking a skin of shark was able to significantly reduce biofilm formation (Chung et al., 2007). The key parameters of the biofilm inhibiting films are non-random patterns with a hierarchy where the size is optimized to the size of a specific bacteria (Schumacher et al., 2007a,b). Here, we apply spinodal separation to generate periodical cellulose blend film hierarchies and evaluate the morphology and configuration and discuss their relation to antifouling surfaces.

Atomic force microscopy (AFM) is a non-destructive analytical tool applying low forces and is therefore suited for nanoscale characterization of soft polymer and biological surfaces. Apart from morphology studies, phase contrast in tapping mode imaging (Tamayo and Garcia, 1996), chemical contrast with functionalized AFM tips (Frisbie et al., 1994), and mechanical contrasts (Chyasnavichyus et al., 2015; Kocun et al., 2017) are established investigation routines. Phase and adhesion contrast measurements have been explored also on cellulosic films to achieve chemical contrast with functionalized probes (Ganser et al., 2016). Friction behavior of blend films can be studied on the nanoscale by friction force microscopy (FFM) (Mate et al., 1987; Marti et al., 1990; Meyer and Amer, 1990). In FFM, the AFM tip scans in contact mode normal to the cantilever's long axis, and the resulting cantilever torsion is related to the friction coefficient. Friction contrast for polymers by FFM has been demonstrated for phase-separated thin organic films (Overney et al., 1992, 1994) where differences in the friction signal between hydrocarbon and fluorocarbon containing domains were found. More recently, FFM was employed to correlate friction to viscoelastic relaxation (Hammerschmidt et al., 1996; Sondhauß et al., 2015) and to characterize photoreactive organic surface patterns of spin casted thin films (Hlawacek et al., 2009; Shen et al., 2014). Polyisoprene and polystyrene blend coatings were recently reported to show an unexpected tribological synergy (Emerson et al., 2017). By varying the composition of the blend films, it was possible to tune the tribological properties and achieve friction coefficients which are much lower than for the pure films.

A blend of TMSC (regenerable to cellulose) and hydroxypropylcellulose stearate (HPCE) resulted in micropatterned films with varying aliphatic surface concentration. HPCE, a cellulose derivative, exhibits long alkyl side chains which may act as brushes and in combination with cellulose impact, wetting, adhesion, and protein adsorption. The surface morphology, roughness and lateral correlation length, of the films was quantitatively studied using AFM. The friction behavior was analyzed by FFM and compared to the adhesive properties of the surfaces of the pure and blend films obtained from AFM force spectroscopy. Finally, the comprehensive information obtained by surface characterization was employed to determine the influence of adhesive and

tribological surface properties of the cellulose-HPCE blend films on bovine serum albumin (BSA) adsorption investigated by surface plasmon resonance spectroscopy (SPR) and Quartz Crystal Microbalance with Dissipation monitoring (QCM-D).

MATERIALS AND METHODS

Materials

Hydroxypropylcellulose stearate (HPCE, M_w 134,700 g mol^{-1}, M_n 107,400 g mol^{-1}, polydispersity index 1.25, degree of substitution (DS) 3.0) was synthesized according to a literature protocol (Nau et al., 2018). Trimethylsilyl cellulose (TMSC, From Avicel, M_w 185,000 g mol^{-1}, M_n 30,400 g mol^{-1}, polydispersity index 6.1, DS 2.8) was purchased from TITK (Thuringian Institute of Textile and Plastics Research, Germany). The structures are shown in **Figure 1**. Chloroform (99.3%), disodium phosphate heptahydrate ($Na_2HPO_4{\cdot}7H_2O$), sodium dihydrogen phosphate monohydrate ($NaH_2PO_4{\cdot}H_2O$), hydrochloric acid (37%), and bovine serum albumin (BSA) were purchased from Sigma-Aldrich and were used as received. Silicon wafers used as film substrates were cut 1 cm × 2 cm. Surface plasmon resonance (SPR) gold sensor slides (CEN102 AU) were purchased from Cenibra (Germany). Milli-Q water (resistivity = 18.2 Ω^{-1} cm^{-1} at 25°C) from a Millipore water purification system (Millipore, U.S.A.) was used for contact angle, SPR, and QCM-D investigations.

Substrate Cleaning and Film Preparation

The film substrates were cleaned by immersing them in an *in-situ* produced peroxymonosulfuric acid containing H_2O_2 (30 wt%)/ H_2SO_4 (1:3 v/v) for 10 min for SPR spectroscopy slides or 30 min for silicon wafers, respectively. After rinsing with deionized water, the wafers were dried with nitrogen gas, rinsed and stored in deionized water. TMSC and HPCE were dissolved in chloroform in a concentration of 0.75 wt%, using a water bath heated to 30°C, and 120 h on a magnetic stirrer. Right before use the solutions were filtered through 0.45 μm PVDF filters (Chromafil) and mixed in volumetric ratios labeled further on as TMSC:HPCE 1:0, 1:3, 1:1; 3:1, and 0:1. A volume of 100 μl was used for spin coating and operated for 60 s with an acceleration of 2,500 rpm s^{-1} and a speed of 4,000 rpm.

The conversion of TMSC into cellulose was implemented in a polystyrene petri dish (5 cm in diameter) containing 3 ml of 10 wt% HCl. The substrates were exposed to HCl vapor for 12 min. The regeneration of cellulose from TMSC was verified by contact angle and ATR-IR measurements (Alpha FT-IR spectrometer, Bruker, U.S.A.) using an attenuated total reflection attachment and obtaining spectra between 4,000 and 400 cm^{-1} with 48 scans and a resolution of 4 cm^{-1}. The data was analyzed with OPUS 4.0 software.

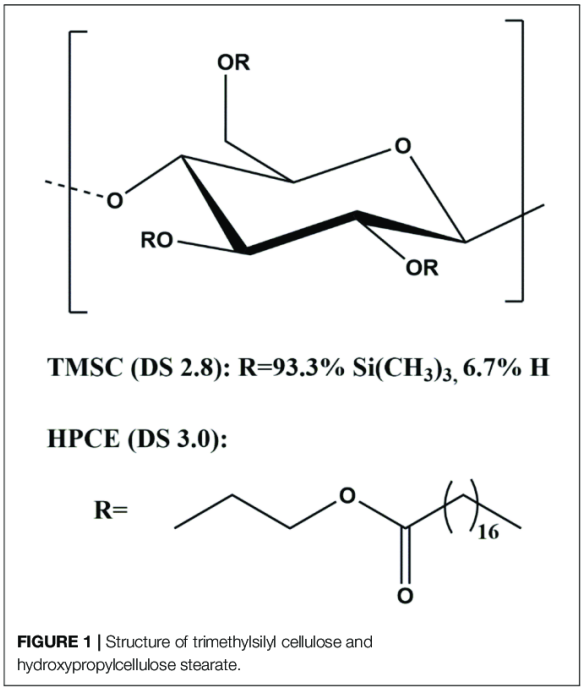

FIGURE 1 | Structure of trimethylsilyl cellulose and hydroxypropylcellulose stearate.

Profilometry

Thickness of the thin films was determined by scratching the films with a scalpel and measuring the profile of a scan length of 1,000 μm and a duration of 3 s using a DETAK 150 Stylus Profiler from Veeco (Bruker, USA) on a hydraulic balanced stone table with a diamond stylus with a radius of 12.5 μm and a force of 3 mg. Three films of each sample were measured at 6 locations before and after regeneration. Film thickness and film roughness was calculated from the resulting profile using Software Vision 64.

Contact Angle (CA) and Surface Free Energy (SFE) Determination

Static contact angle measurements were performed with a Drop Shape Analysis System DSA100 (Krüss GmbH, Germany) with a T1E CCD video camera (25 frames per second) and the DSA1 v 1.90 software. All measurements were performed at least three times on minimum two manufactured films with Milli-Q water and diiodomethane using a droplet size of 3 μL and a dispense rate of 400 μL min^{-1}. Static CAs were calculated with the Young-Laplace equation, and the SFE was determined with the Owen-Wendt-Rabel-Kaelble (OWRK) method. Surface tension of 50.80 and 72.80 mN m^{-1} for diidomethane and water were used, respectively.

Adsorption Experiments

A phosphate buffer containing 8.1 mM disodium phosphate, 1.9 mM sodium phosphate and 100 mM sodium chloride at pH 7.4 was used to carry out the adsorption experiments of BSA on the films. Surface Plasmon Resonance Spectroscopy (SPR) was performed with a MP-SPR Navi 200 from Bionavis Ltd (Finland), using 785 nm laser in both measurement channels. The attached autosampler MP-SPR Navi 210A was set to 20 μl min^{-1} flow rate. The equilibration of the thin films was observed by measuring the spectra with full angular scan (39–78°) and scan speed of 8° s^{-1} at 24.5° and plot the SPR-angle over time. A concentration

of 1.0 mg ml^{-1} of BSA was dissolved in the buffer and exposed to the thin films for 10 min. Adsorbed mass (Γ) was calculated with the de Feijter equation,

$$\Gamma = \frac{\Delta\Theta^* \kappa^* d_p}{dn/dc} \quad (1)$$

using the refractive index increment (dn/dc) 0.182 cm^3 g^{-1}. The $\Delta\Theta$ is the angular response of the surface plasmon resonance. For thin layers (<100 nm), k × d_p can be considered constant and can be obtained by calibration of the instrument by determination of the decay wavelength l_d. Here it was 1.09 × 10^{-7} cm/° (at 670 nm) and 1.9 × 10^{-7} cm/° (at 785 nm) in aqueous systems.

Quartz Crystal Microbalance and Dissipation (QCM-D) instrument (model E4) from Q-Sense (Sweden) was used with gold sensors purchased from QuartzPro (Sweden). The attached peristaltic pump was set to 0.1 ml min^{-1}. Adsorption was performed in the same conditions as the SPR analyses. The data was analyzed using Johannsmann modeling (Johannsmann et al., 1992; Naderi and Claesson, 2006).

Atomic Force Microscopy

Most AFM and all FFM measurements were acquired using an Asylum Research MFP-3D AFM (USA). The instrument is equipped with a closed-loop planar x-y-scanner with a scanning range of 85 µm × 85 µm and a z-range of 15 µm. The tapping mode AFM images were recorded with standard silicon probes (Olympus AC160TS, cantilever spring constant ~30 N m^{-1}, tip radius ~10 nm). The measurements were obtained in ambient conditions at 50 ± 8% relative humidity and a temperature of 22 ± 1°C. Topography images of three independent positions were recorded for each sample. All the data was processed in the open-source software Gwyddion (Necas and Klapetek, 2012). For the 5 µm × 5 µm images, a roughness analysis (Teichert, 2002) was performed by calculating the 1D height-height correlation function:

$$C(x) = \langle [z(x_0 + x) - \langle z \rangle][z(x_0 - \langle z \rangle)] \rangle \quad (2)$$

of each scan line and then averaging over all lines. The resulting values were fitted with the function:

$$C(x) = \sigma^2 e^{-\left(\frac{|x|}{\xi}\right)^{2\alpha}} \quad (3)$$

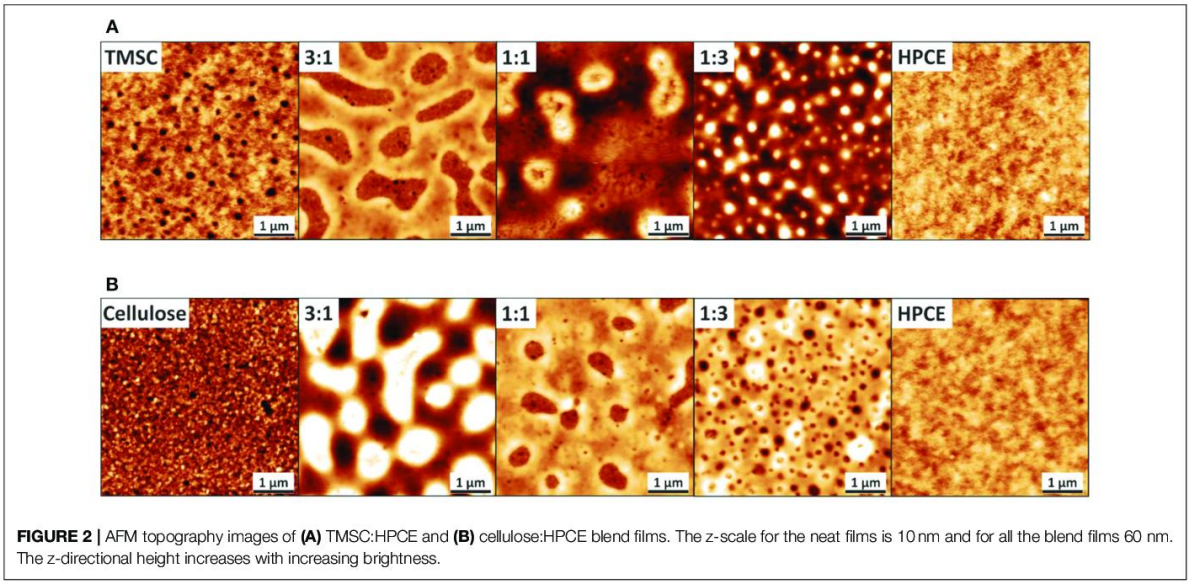

FIGURE 2 | AFM topography images of **(A)** TMSC:HPCE and **(B)** cellulose:HPCE blend films. The z-scale for the neat films is 10 nm and for all the blend films 60 nm. The z-directional height increases with increasing brightness.

TABLE 1 | RMS roughness and lateral correlation length of the roughness of the blend films prior (TMSC:HPCE) and after (cellulose:HPCE) regeneration.

	RMS roughness σ [nm]	Lateral correlation length ξ [nm]		RMS roughness σ [nm]	Lateral correlation length ξ [nm]
TMSC	1.50 ± 0.05	95 ± 5	Cellulose	1.50 ± 0.20	55 ± 10
3:1	7.60 ± 0.30	185 ± 15	3:1	19.80 ± 0.30	310 ± 10
1:1	12.60 ± 0.80	320 ± 20	1:1	8.00 ± 0.40	180 ± 5
1:3	14.15 ± 0.75	145 ± 10	1:3	10.20 ± 0.10	155 ± 5
HPCE	1.10 ± 0.05	120 ± 10	HPCE	1.10 ± 0.10	140 ± 10

The data is obtained from analysis of the 5 µm × 5 µm topography images.

The parameters σ, ξ, and α are used to characterize the surface roughness (Teichert, 2002). The σ denotes the root mean square (RMS) roughness, i.e., the standard deviation of the height values, which is a common measure for the vertical roughness. The lateral correlation length ξ describes the lateral fluctuation of the height values and α is the so-called Hurst parameter or roughness exponent. It determines the shape of C(x) and quantifies the jaggedness of the surface.

For FFM, which is recorded in contact mode, NT-MDT CSG10/Au probes with a tip radius of about 30 nm and a low cantilever spring constant of 0.1 N m^{-1} were employed. Images with frame size of 5 μm × 5 μm were obtained with a constant scan speed of 2.5 μm s^{-1}. A vertical force of about 10 nN was applied during the measurements. For acquisition of an FFM image, standard contact mode AFM scan including the lateral trace and retrace channel were recorded. The raw lateral signals were converted to friction images by subtracting the lateral retrace from the lateral trace signal and dividing it by two for each image (Kalihari et al., 2010; Shen et al., 2014). This eliminates topography artifacts and a possible offset.

The quantitative interpretation in terms of friction coefficient is not straightforward, and literature includes several calibration methods (Klapetek, 2018). Lateral force sensitivity calibration was done here according to the wedge calibration method of Varenberg et al. (2003). Quantitative friction images were obtained by multiplying the resulting friction image data with the lateral force sensitivity using the Gwyddion software.

AFM force spectroscopy measurements to investigate the adhesion properties of the film surfaces were performed with a scan rate of 2 Hz and a force distance of 0.5 μm. For these measurements, HSC60 probes from Team Nanotec (Germany) were used which have a cantilever spring constant of about 50 N/m and a tip radius of 60 nm. Here, 32 × 32 px^2 maps were obtained on 5 μm × 5 μm topography scans.

A Veeco Multimode Quadrax MM AFM (Bruker, USA) in tapping mode using standard silicon probes (NCH-VS1-W, NanoWorld AG) was used for recording film topography after they were rinsed with chloroform.

Surface Morphology and Area Determination

To quantify the observed surface features for the individual blend films, ten individual cross-sections of the features were obtained from the topography images for each film with the Gwyddion software to determine the height and width of the features. The values are given as mean ± standard deviation.

The AFM topography images were used for calculating effective surface fractions of the blend films. These are referred to as "effective surface fraction" or "surface fraction" later in the manuscript. The film component fraction derived from spinning solution is referred to as "volume fraction" or "volume ratio." Masked surfaces were evaluated by the surface area estimate method in Gwyddion, computed by simple triangulation that considers heights and spatial relations in the surface. For this purpose, additional points were added in-between four neighboring points using the mean values of these pixels. Four triangles are formed, and the surface area is approximated by summing their areas. Masking was done by threshold in *z*-value and adjusting with a pen tool. Single noise pixel was removed by grain filtering function. For films that showed a reliable phase contrast in the tapping mode topography analysis, the masks were determined from the phase information.

RESULTS AND DISCUSSION

Spin coated TMSC and HPCE films formed into smooth one-component film morphologies—indicating a uniform film formation—while the blend films containing both derivatives resulted in films with spinodal decomposition and are presented via three composition ratios, 3:1, 1:1, and 1:3 (**Figure 2A**). These TMSC:HPCE blend film surfaces consisted of domains which either formed cavities (TMSC:HPCE 3:1) or protrusions in lower

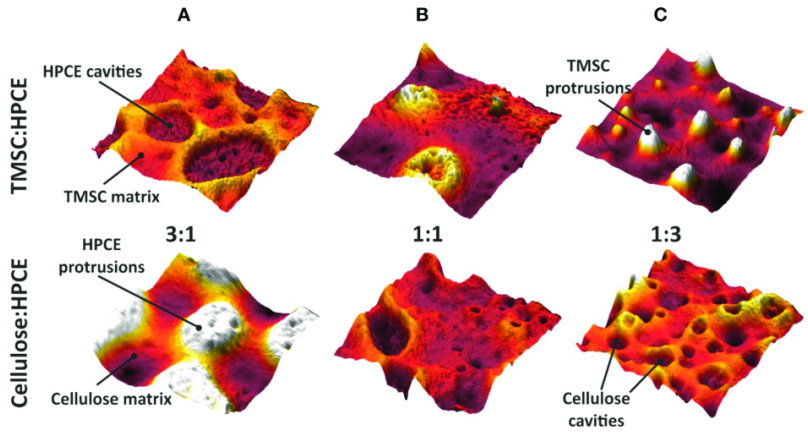

FIGURE 3 | Three-dimensional (2 μm × 2 μm) AFM topography images of the TMSC:HPCE (top row) and cellulose:HPCE (bottom row) blend films. **(A)** 3:1, **(B)** 1:1, and **(C)** 1:3. The z-scale is 60 nm in all cases.

sub-micrometer range. Protrusions with height 35 ± 10 nm and width of 780 ± 130 nm were determined for TMSC:HPCE 1:1 and of height of 55 ± 10 nm and width of 340 ± 50 nm for TMSC:HPCE 1:3. The protrusions increased in height with increasing HPCE content but decreased in lateral size.

The regeneration of TMSC into cellulose is accompanied by the cleavage of the silyl groups and simultaneous formation of hydrogen bonds of the created hydroxyl groups. This led to densification and reduction in film thickness (**Figure S1**), similar to reported elsewhere (Wolfberger et al., 2015), of the regenerated parts and consequently, more complex morphology (**Figure 2B**). HPCE is unaffected by the treatment (compare **Figures 2A,B**). After conversion to cellulose, the blend film cellulose fraction mass was reduced which translated into an inverted morphology compared to the TMSC:HPCE blend films. The cellulose:HPCE 3:1 surface was characterized by protrusions with arbitrary size and a height of 40 ± 10 nm, whereas the cellulose:HPCE 1:1 and 1:3 films contained cavities which decrease in lateral size. The 1:1 sample showed random-shaped surface features with a lateral width of 660 ± 80 nm, but the more spherical-shaped features on the 1:3 blend film surface had a width of only 250 ± 25 nm. An overview of this data is presented in **Table 1**.

The phase assignment was confirmed by treating the cellulose:HPCE blend films with chloroform that removed the HPCE phase. The remaining cellulose matrix was visualized and confirmed that the cellulose was the continuous phase in 3:1 blends, and the discontinuous one in 1:1 and 1:3 films (see **Figure S2A**). The phase assignments were incorporated in three-dimensional AFM topography images (**Figure 3**). The TMSC:HPCE 3:1 blend film consisted of a continuous TMSC matrix with HPCE cavities. Regeneration of the TMSC to cellulose resulted in a shrinkage of the TMSC domains. Therefore, the HPCE domains were protruding from the surface of the cellulose:HPCE blend films. With increasing HPCE amount, the matrix increasingly consisted of HPCE and the TMSC domains formed protrusions, which collapsed during cellulose regeneration (**Figures 3B,C**).

The visualization of the blend film after removal of the HPCE phase of 1:1 film did not only reveal the cellulose left behind in islands (**Figure S2A**). Lateral phase separation is chiefly responsible for the phase separation patterns that were observed upon the spinodal decomposition (**Figure 2**). This can take place independently or simultaneously with vertical separation which results in heterogeneous layer formation in the z-direction (Karim et al., 1998; Heriot and Jones, 2005). Dissolution of the HPCE phase revealed the cellulose skeleton left behind creating roughness beyond the apparent cellulose islands (**Figure S2A**).

The vertical separation and z-directional morphology evidently had an impact on the surface composition of the films meaning that the volume fraction did not necessarily equal to a surface area fraction. We used the AFM analyses to calculate effective surface area taking into consideration the surface roughness. The calculated surface areas were converted into surface fraction so that the TMSC or regenerated cellulose phase area was divided by the total area. The surface area could not be solely determined from the topography analysis (**Figure S2B**) but required phase imaging to reveal additional cellulose domains (**Figure S2C**). These were counted in to the cellulose surface fraction. Neither the TMSC:HPCE (diamonds) nor cellulose:HPCE (circles) surface fraction correlated directly with the volume fraction of the polymer blends used in spin coating (**Figure 4**). The surface fraction decreased upon regeneration in the case of high cellulose dominant blend films and increased with HPCE dominant ones. The differences in surface fraction of cellulose between the 1:3 and 1:1 sample is small (30% vs. 37%), but the resulting microstructures are very different (**Figures 3B,C**, lower row).

The roughness σ of the resulting blend thin films increased by factors of 4 to 20 compared to the neat films (**Table 1**). For the TMSC:HPCE blend films, the 1:3 composition featured the largest σ while after regeneration by HCl vapors, the cellulose:HPCE 3:1 film exhibited largest σ. The lateral correlation lengths ξ were lowest for the pure films. For the blend films, ξ increased by up to a factor of 3. TMSC:HPCE 1:1 and cellulose:HPCE 3:1 showed the highest values.

Derivatization of cellulose with the hydroxypropyl stearyl side chain (**Figure 1**) modifies the hydrophobicity of the molecule and this should reflect to the water contact angle and the surface free energy (SFE) of the films. The water contact angle of the cellulose film was 36.6 ± 0.3 degrees, TMSC film 94.6 ± 0.1 degrees, and that of the HPCE film 77.9 ± 0.5 degrees. The SFE of the blend films increased with increasing cellulose fraction (**Figure S3**) while prior to regeneration SFE was below 30 mJ m^{-2} for all the films. Consequently, the polar contribution decreased with the same trend (**Figure S4**).

Correlation of Friction Coefficient, Adhesion Force, Surface Roughness to Surface Free Energy and Protein Affinity of the Cellulose/HPCE Blend Films

The contact mode FFM images (**Figure 5A**) enclose the distinct differences between the neat and the cellulose/HPCE blend films' friction (indicated by the contrast differences). The average friction coefficients (Klunsner et al., 2010) were lower for the blend films than for the pure films (**Figure 5B**). The same applied for the adhesion forces (**Figure 5C**) where the blends featured lower values (20–50 nN) than the cellulose and HPCE films (65 ± 2 nN, and 104 ± 5 nN, respectively). It should be noted here that friction force data is in good agreement with those reported for cellulose spheres interacting with modified silica surfaces in a similar applied force range (∼5 nN) (Bogdanovic et al., 2001).

Non-specific Protein Deposition—BSA Adsorption

Cellulose in general is not very prone to non-specific protein adsorption. This originates from the highly hydrated, hydrophilic cellulosic material, having hydrogel characteristics. Upon protein deposition, the water that is close to the surface of the cellulose and on the surface of the protein needs to be replaced—a process which is, if there are not any specific contributions—entropically unfavorable. Several approaches have shown that either anionic or cationic coatings on cellulose thin films may alter the adsorption behavior of proteins (Orelma et al., 2011;

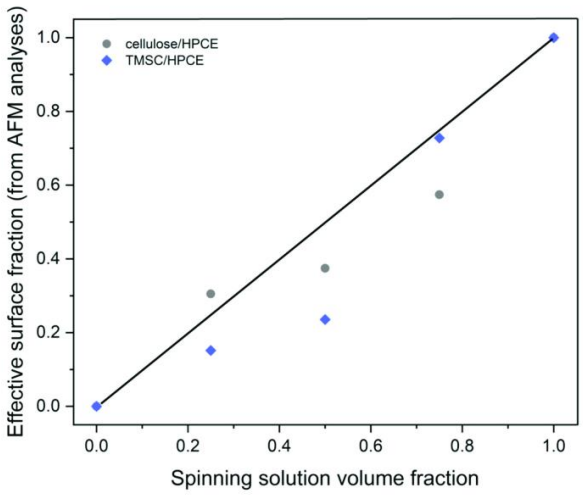

FIGURE 4 | Relationship of the TMSC:HPCE blend spinning solution volume fraction and experimentally determined effective surface fraction of the TMSC:HPCE (diamonds) and cellulose:HPCE films (circles). The black line represents identical volume and surface fraction.

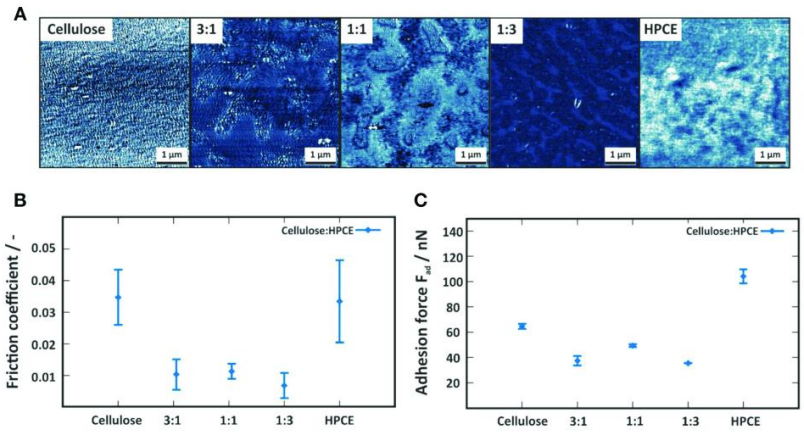

FIGURE 5 | (A) Contact mode friction force images of the cellulose, cellulose:HPCE and HPCE films. The z-scale of all images is 5 mV. **(B)** Friction coefficient and **(C)** adhesion force for the cellulose, cellulose:HPCE and HPCE films.

Mohan et al., 2013, 2014) depending on the employed pH during adsorption and the isoelectric point of the protein. On hydrophobic surfaces, proteins adhere spontaneously in a non-specific fashion and often they (partially) lose their ternary or quaternary structure and denaturate during deposition (Norde and Lyklema, 1991; Sagvolden et al., 1998). One would expect that the incorporation of a hydrophobic component such as HPCE into the cellulose film would trigger non-specific adsorption different from affinity to the cellulose regions. We chose BSA (pH 7.4) as a demonstrator probe for non-specific protein interactions of the blend films and studied the adsorption process using a combination of SPR spectroscopy and QCM-D. The combination of these techniques gives complementing insight into the amount of adsorbed protein. While QCM-D is a gravimetric technique capable of sensing any type of mass (i.e., water, and BSA, Γ^{QCM}) on the surface, SPR spectroscopy allows for determination of dry mass (Γ^{SPR}) by employing the de Feijter equation (1). The difference between Γ^{QCM} and Γ^{SPR} is the amount of water in the film. This amount of water decreased with lowering the cellulose content in the films and reaches its minimum for the 1:3 cellulose:HPCE film (**Figure 6A**). The HPCE film should swell the least, and hence, the major fraction of water can be assumed to be associated with the BSA on the surface. The amount of water in the BSA layer is 65%.

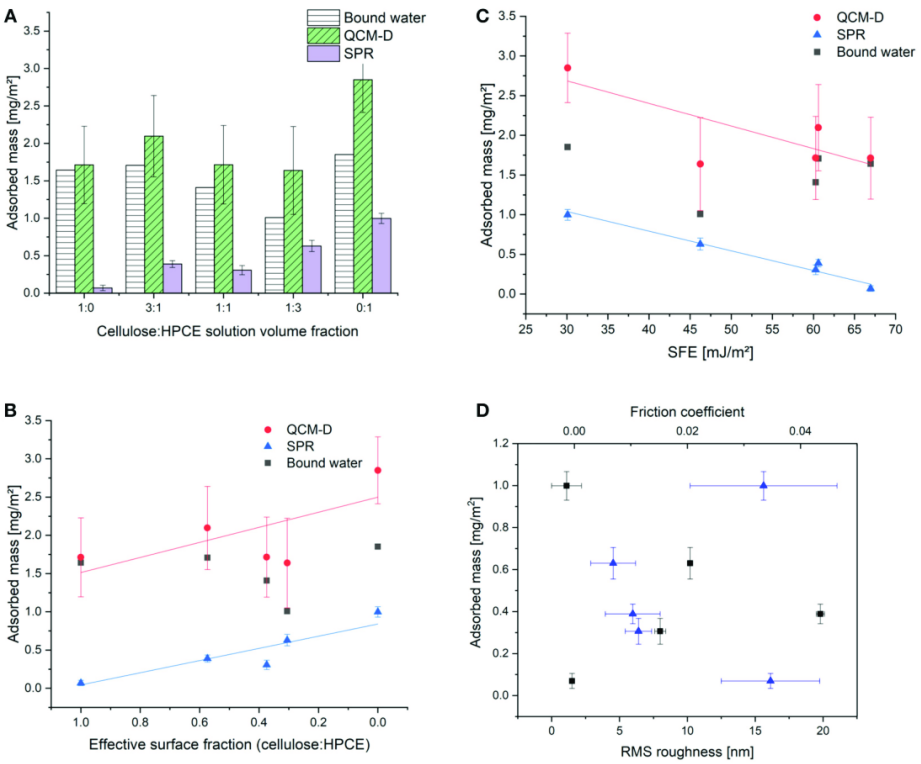

FIGURE 6 | (A) Adsorbed mass (mg m^{-2}) of BSA on the cellulose:HPCE blend films determined by SPR and QCM-D. Adsorbed masses with respect to the **(B)** surface fraction, and **(C)** surface free energy. **(D)** RMS roughness (squares) from the AFM measurements and friction coefficients (triangles) from the FFM analysis contrasted to the adsorbed amount based on SPR analyses.

The HPCE film experiences the highest BSA adsorbed amount (based on SPR) of 1 mg m^{-2}. The other extreme is the neat cellulose film that features low BSA adsorption (Γ^{SPR} 0.1 mg m^{-2}) which is in good agreement with other reports in these conditions (Niegelhell et al., 2017; Weißl et al., 2018). The highly swollen hydrogel character is revealed in the QCM-D data for the pure cellulose film, showing 1.7 mg m^{-2} water in the layer corresponding to 96% of hydration.

The increase in volume fraction of the HPCE led to a linear increase in the amount of adsorbed BSA on the surfaces. Contrasting the SPR adsorbed mass to the effective surface fraction revealed that the 1:1 blend film (volumetric) was an outlier in the adsorption trend and a lower amount of protein was deposited than what would have been expected (**Figure 6B**). Comparing this data to the other few reports on protein adsorption on cellulose based blend films revealed that also for the other systems protein adsorption minima were determined close to the 1:1 volume ratio (Niegelhell et al., 2016, 2017; Strasser et al., 2016). The cellulose:HPCE 3:1 film contains 57% of cellulose based on surface fraction, but still, it shows a higher BSA adsorption (0.39 mg m^{-2}) than the cellulose:HPCE 1:1 film (0.30 mg m^{-2}) with lower cellulose content (37% surface fraction).

The influence of surface free energy, roughness, and friction coefficient on the BSA adsorption is plotted against Γ^{QCM}, Γ^{SPR} and bound water (**Figures 6C,D**). The SFE has a decisive influence on the BSA adsorption (**Figure 6C**). For the neat cellulose and HPCE films, surface roughness as well as friction coefficient were similar, but the SFE significantly differed. For the blend films however, the correlation between SFE and adsorbed mass was straightforward at first glance: lower surface energy translated to more hydrophobic surface resulting in higher non-specific protein deposition (**Figure 6C**). However, the SFE development did not correlate linearly with the effective surface fraction (**Figure S3**). There is a plateau in the SFE development with surface fraction of 0.37 (1:1) after which the cellulose dominated the SFE. One would expect much lower SFEs due to the actual surface fraction of just 37% of cellulose which would lead to higher non-specific protein adsorption. It is therefore rather the wetting properties of the blend films that are tuned by the morphology and configuration and these further affect the

adsorption. The roughness did not have a direct correlation to the adsorbed mass through the series, and neither did the friction coefficient (**Figure 6D**). Since the adsorbed mass and the SFE exhibited a linear correlation, it is clear that the roughness and friction coefficient correlation with SFE is similar to the adsorbed mass (**Figure S5** vs. **Figure 6D**).

CONCLUSIONS

Friction of cellulose films could be altered by blend composition including a low surface energy derivative. A surface fraction of 37% of cellulose (1:1 volume fraction) exhibited outlier adsorption inhibiting the protein adsorption. Surface energy rather than friction was a decisive factor for protein adsorption on the films. However, the SFE did not follow linearly the component surface area fraction. Wetting and adhesion typically correlate with surface friction. However, this correlation was not verified here to provide a correlation of friction to protein adsorption on the surface. Surface configuration—periodicity of the structure and feature size—might be an underlying factor.

AUTHOR CONTRIBUTIONS

CC was responsible of FFM and some of the AFM measurements, FFM data analysis, area calculations, and contributed in writing of the manuscript. GT was responsible of the SPR and QCM-D measurements, area calculations, and writing. MN and MB contributed with HPCE synthesis and characterization and MH with AFM measurements. CP assisted with QCM-D measurements and corresponding data analysis. SS and CT contributed in data analysis and writing. TN contributed with experimental analyses and writing the manuscript.

FUNDING

TN acknowledges Wallenberg Wood Science Center and Chalmers Area of Advance Materials for funding. The members of the Christian Doppler Laboratory for Fiber Swelling and Paper Performance gratefully acknowledge the financial support of the Austrian Federal Ministry of Economy, Family and Youth and the National Foundation for Research, Technology and Development.

SUPPLEMENTARY MATERIAL

The Supplementary Material for this article can be found online at: https://www.frontiersin.org/articles/10.3389/fchem.2019.00239/full#supplementary-material

REFERENCES

An, Y. H., and Friedman, R. J. (1998). Concise review of mechanisms of bacterial adhesion to biomaterial surfaces. *J. Biomed. Mater. Res.* 43, 338–348.

Bogdanovic, G., Tiberg, F., and Rutland, M. W. (2001). Sliding friction between cellulose and silica surfaces. *Langmuir* 17, 5911–5916. doi: 10.1021/la010330c

Chung, K. K., Schumacher, J. F., Sampson, E. M., Burne, R. A., Antonelli, P. J., and Brennan, A. B. (2007). Impact of engineered surface microtopography on biofilm formation of *Staphylococcus aureus*. *Biointerphases* 2, 89–94. doi: 10.1116/1.2751405

Chyasnavichyus, M., Young, S. L., and Tsukruk, V. V. (2015). Recent advances in micromechanical characterization of polymer, biomaterial, and cell surfaces with atomic force microscopy. *Japan. J. Appl. Phys.* 54:08LA02. doi: 10.7567/JJAP.54.08LA02

Dalnoki-Veress, K., Forrest, J., Stevens, J., and Dutcher, J. (1997). Phase separation morphology of spin-coated polymer blend thin films. *Phys A Stat. Mech. Appl.* 239, 87–94. doi: 10.1016/S0378-4371(96)00471-2

Emerson, J. A., Garabedian, N. T., Moore, A. C., Burris, D. L., Furst, E. M., and Epps, T. H. (2017). Unexpected tribological synergy in polymer blend coatings: leveraging phase separation to isolate domain size effects and reduce friction. *ACS Appl. Mater. Interfaces* 9, 34480–34488. doi: 10.1021/acsami.7b10170

Frisbie, C. D., Rozsnyai, L. F., Noy, A., Wrighton, M. S., and Lieber, C. M. (1994). Functional group imaging by chemical force microscopy. *Science* 265, 2071–2074. doi: 10.1126/science.265.5181.2071

Ganser, C., Niegelhell, K., Czibula, C., Chemelli, A., Teichert, C., Schennach, R., et al. (2016). Topography effects in AFM force mapping experiments on xylan-decorated cellulose thin films. *Holzforschung* 70, 1115–1123. doi: 10.1515/hf-2016-0023

Halls, J. J. M., Walsh, C. A., Greenham, N. C., Marseglia, E. A., Friend, R. H., Moratti, S. C., et al. (1995). Efficient photodiodes from interpenetrating polymer networks. *Nature* 376, 498–500. doi: 10.1038/376498a0

Hammerschmidt, J. A., Moasser, B., Gladfelter, W. L., Haugstad, G., and Jones, R. R. (1996). Polymer viscoelastic properties measured by friction force microscopy. *Macromolecules* 29, 8996–8998. doi: 10.1021/ma9603239

Heriot, S. Y., and Jones, R. A. (2005). An interfacial instability in a transient wetting layer leads to lateral phase separation in thin spin-cast polymer-blend films. *Nat. Mater.* 4, 782–786. doi: 10.1038/nmat1476

Hlawacek, G., Shen, Q., Teichert, C., Lex, A., Trimmel, G., and Kern, W. (2009). Hierarchy of adhesion forces in patterns of photoreactive surface layers. *J. Chem. Phys.* 130:044703. doi: 10.1063/1.3062841

Johannsmann, D., Mathauer, K., Wegner, G., and Knoll, W. (1992). Viscoelastic properties of thin films produced with a quartz-crystal resonator. *Phys. Rev. B* 46, 7808–7815. doi: 10.1103/PhysRevB.46.7808

Kalihari, V., Haugstad, G., and Frisbie, C. D. (2010). Distinguishing elastic shear deformation from friction on the surfaces of molecular crystals. *Phys. Rev. Lett.* 104:086102. doi: 10.1103/PhysRevLett.104.086102

Karim, A., Slawecki, T., Kumar, S., Douglas, J., Satija, S., Han, C., et al. (1998). Phase-separation-induced surface patterns in thin polymer blend films. *Macromolecules* 31, 857–862. doi: 10.1021/ma970687g

Katsikogianni, M., and Missirlis, Y. (2004). Concise review of mechanisms of bacterial adhesion to biomaterials and of techniques used in estimating bacteria-material interactions. *J. Eur. Cell Mater.* 8, 37–57. doi: 10.22203/eCM.v008a05

Klapetek, P. (2018). *Quantitative Data Processing in Scanning Probe Microscopy: SPM Applications for Nanometrology*. Amsterdam: Elsevier.

Klunsner, T., Shen, Q., Hlawacek, G., Teichert, C., Fateh, N., Fontalvo, G. A., et al. (2010). Morphology characterization and friction coefficient determination of sputtered V2O5 films. *Thin Solid Films* 519, 1416–1420. doi: 10.1016/j.tsf.2010.09.040

Kocun, M., Labuda, A., Meinhold, W., Revenko, I., and Proksch, R. (2017). Fast, high resolution, and wide modulus range nanomechanical mapping with bimodal tapping mode. *ACS Nano* 11, 10097–10105. doi: 10.1021/acsnano.7b04530

Kontturi, E., Johansson, L.-S., and Laine, J. (2009). Cellulose decorated cavities on ultrathin films of PMMA. *Soft Matter* 5, 1786–1788. doi: 10.1039/b901059a

Kontturi, E., Nyfors, L., and Laine, J. (2010). Utilizing polymer blends to prepare ultrathin films with diverse cellulose textures. *Macromol. Symp.* 294, 45–50. doi: 10.1002/masy.200900032

Kontturi, E., Thune, P. C., and Niemantsverdriet, J. W. (2003a). Cellulose model surfaces-simplified preparation by spin coating and characterization by X-ray photoelectron spectroscopy, infrared spectroscopy, and atomic force microscopy. *Langmuir* 19, 5735–5741. doi: 10.1021/la0340394

Kontturi, E., Thune, P. C., and Niemantsverdriet, J. W. (2003b). Novel method for preparing cellulose model surfaces by spin coating. *Polymer* 44, 3621–3625. doi: 10.1016/S0032-3861(03)00283-0

Marti, O., Colchero, J., and Mlynek, J. (1990). Combined scanning force and friction microscopy of mica. *J. Nanotechnol.* 1:141. doi: 10.1088/0957-4484/1/2/003

Mate, C. M., Mcclelland, G. M., Erlandsson, R., and Chiang, S. (1987). Atomic-scale friction of a tungsten tip on a graphite surface. *Phys. Rev. Lett.* 59, 1942–1945.

Medronho, B., Romano, A., Miguel, M. G., Stigsson, L., and Lindman, B. (2012). Rationalizing cellulose (in)solubility: reviewing basic physicochemical aspects and role of hydrophobic interactions. *Cellulose* 19, 581–587. doi: 10.1007/s10570-011-9644-6

Meyer, G., and Amer, N. M. (1990). Simultaneous measurement of lateral and normal forces with an optical-beam-deflection atomic force microscope. *J Appl. Phys. Lett.* 57, 2089–2091. doi: 10.1063/1.103950

Mohan, T., Niegelhell, K., Zarth, C. S., Kargl, R., Köstler, S., Ribitsch, V., et al. (2014). Triggering protein adsorption on tailored cationic cellulose surfaces. *Biomacromolecules* 15, 3931–3941. doi: 10.1021/bm500997s

Mohan, T., Ristić, T., Kargl, R., Doliska, A., Köstler, S., Ribitsch, V., et al. (2013). Cationically rendered biopolymer surfaces for high protein affinity support matrices. *Chem. Comm.* 49, 11530–11532. doi: 10.1039/c3cc46414h

Naderi, A., and Claesson, P. M. (2006). Adsorption properties of polyelectrolyte-surfactant complexes on hydrophobic surfaces studied by QCM-D. *Langmuir* 22, 7639–7645. doi: 10.1021/la061118h

Nau, M., Seelinger, D., and Biesalski, M. (2018). Functional surface coatings from tailor-made long-chain hydroxypropyl cellulose ester nanoparticles. *Cellulose* 25, 5769–5780. doi: 10.1007/s10570-018-1981-2

Necas, D., and Klapetek, P. (2012). Gwyddion: an open-source software for SPM data analysis. *Cent. Eur. J. Phys.* 10, 181–188. doi: 10.2478/s11534-011-0096-2

Niegelhell, K., Süßenbacher, M., Jammernegg, K., Ganner, T., Schwendenwein, D., Schwab, H., et al. (2016). Enzymes as biodevelopers for nano- and micropatterned bicomponent biopolymer thin films. *Biomacromolecules* 17, 3743–3749. doi: 10.1021/acs.biomac.6b01263

Niegelhell, K., Süßenbacher, M., Sattelkow, J., Plank, H., Wang, Y., Zhang, K., et al. (2017). How bound and free fatty acids in cellulose films impact nonspecific protein adsorption. *Biomacromolecules* 18, 4224–4231. doi: 10.1021/acs.biomac.7b01260

Norde, W., and Lyklema, J. (1991). Why proteins prefer interfaces. *J. Biomater. Sci. Polymer Edn.* 2, 183–202. doi: 10.1080/09205063.1991.9756659

Nyfors, L., Suchy, M., Laine, J., and Kontturi, E. (2009). Ultrathin cellulose films of tunable nanostructured morphology with a hydrophobic component. *Biomacromolecules* 10, 1276–1281. doi: 10.1021/bm900099e

Orelma, H., Filpponen, I., Johansson, L.-S., Laine, J., and Rojas, O. J. (2011). Modification of cellulose films by adsorption of CMC and chitosan for controlled attachment of biomolecules. *Biomacromolecules* 12, 4311–4318. doi: 10.1021/bm201236a

Orelma, H., Filpponen, I., Johansson, L. S., Osterberg, M., Rojas, O. J., and Laine, J. (2012a). Surface functionalized Nanofibrillar Cellulose (NFC) film as a platform for immunoassays and diagnostics. *Biointerphases* 7:61. doi: 10.1007/s13758-012-0061-7

Orelma, H., Johansson, L. S., Filpponen, I., Rojas, O. J., and Laine, J. (2012b). Generic method for attaching biomolecules via avidin-biotin complexes immobilized on films of regenerated and nanofibrillar cellulose. *Biomacromolecules* 13, 2802–2810. doi: 10.1021/bm300781k

Overney, R. M., Meyer, E., Frommer, J., Brodbeck, D., Luthi, R., Howald, L., et al. (1992). Friction measurements on phase-separated thin-films with a modified atomic force microscope. *Nature* 359, 133–135. doi: 10.1038/359133a0

Overney, R. M., Meyer, E., Frommer, J., Guntherodt, H. J., Fujihira, M., Takano, H., et al. (1994). Force microscopy study of friction and elastic compliance of phase-separated organic thin-films. *Langmuir* 10, 1281–1286. doi: 10.1021/la00016a049

Pelton, R. (2009). Bioactive paper provides a low cost paltform for diagnostics. *Trends Anal. Chem.* 8, 925–942. doi: 10.1016/j.trac.2009.05.005

Sagvolden, G., Giaever, I., and Feder, J. (1998). Characteristic protein adhesion forces on glass and polystyrene substrates by atomic force microscopy. *Langmuir* 14, 5984–5987. doi: 10.1021/la980271b

Schaub, M., Wenz, G., Wegner, G., Stein, A., and Klemm, D. (1993). Ultrathin films of cellulose on silicon wafers. *Adv. Mater.* 5, 919–922. doi: 10.1002/adma.19930051209

Schumacher, J. F., Aldred, N., Callow, M. E., Finlay, J. A., Callow, J. A., Clare, A. S., et al. (2007a). Species-specific engineered antifouling topographies: correlations between the settlement of algal zoospores and barnacle cyprids. *Biofouling* 23, 307–317. doi: 10.1080/08927010701393276

Schumacher, J. F., Carman, M. L., Estes, T. G., Feinberg, A. W., Wilson, L. H., Callow, M. E., et al. (2007b). Engineered antifouling microtopographies–effect of feature size, geometry, and roughness on settlement of zoospores of the green alga Ulva. *Biofouling* 23, 55–62. doi: 10.1080/08927010601136957

Shen, Q., Edler, M., Griesser, T., Knall, A. C., Trimmel, G., Kern, W., et al. (2014). *Ex situ* and *in situ* characterization of patterned photoreactive thin organic surface layers using friction force microscopy. *Scanning* 36, 590–598. doi: 10.1002/sca.21159

Sondhauß, J., Lantz, M., Gotsmann, B., and Schirmeisen, A. (2015). β-relaxation of PMMA: tip size and stress effects in friction force microscopy. *Langmuir* 31, 5398–5405. doi: 10.1021/acs.langmuir.5b00735

Strasser, S., Niegelhell, K., Kaschowitz, M., Markus, S., Kargl, R., Stana-Kleinschek, K., et al. (2016). Exploring nonspecific protein adsorption on lignocellulosic amphiphilic bicomponent films. *Biomacromolecules* 17, 1083–1092. doi: 10.1021/acs.biomac.5b01700

Tamayo, J., and Garcia, R. (1996). Deformation, contact time, and phase contrast in tapping mode scanning force microscopy. *Langmuir* 12, 4430–4435. doi: 10.1021/la960189l

Teichert, C. (2002). Self-organization of nanostructures in semiconductor heteroepitaxy. *Phys. Rep.* 365, 335–432. doi: 10.1016/S0370-1573(02)00009-1

Varenberg, M., Etsion, I., and Halperin, G. (2003). An improved wedge calibration method for lateral force in atomic force microscopy. *Rev. Sci. Instruments* 74, 3362–3367. doi: 10.1063/1.1584082

Weißl, M., Niegelhell, K., Reishofer, D., Zankel, A., Innerlohinger, J., and Spirk, S. (2018). Homogeneous cellulose thin films by regeneration of cellulose xanthate: properties and characterization. *Cellulose* 25, 711–721. doi: 10.1007/s10570-017-1576-3

Wolfberger, A., Petritz, A., Fian, A., Herka, J., Schmidt, V., Stadlober, B., et al. (2015). Photolithographic patterning of cellulose: a versatile dual-tone photoresist for advanced applications. *Cellulose* 22, 717–727. doi: 10.1007/s10570-014-0471-4

Xue, L. J., Zhang, J. L., and Han, Y. C. (2012). Phase separation induced ordered patterns in thin polymer blend films. *Prog. Polym. Sci.* 37, 564–594. doi: 10.1016/j.progpolymsci.2011.09.001

Zhang, Y., Carbonell, R. G., and Rojas, O. J. (2013). Bioactive cellulose nanofibrils for specific human IgG binding. *Biomacromolecules* 14, 4161–4168. doi: 10.1021/bm4007979

Conflict of Interest Statement: The authors declare that the research was conducted in the absence of any commercial or financial relationships that could be construed as a potential conflict of interest.

4.5. Janus-type hybrid paper membranes

The content of this chapter has been published in:

Maximilian Nau and Nicole Herzog, Johannes Schmidt, Tobias Meckel, Annette Andrieu-Brunsen and Markus Biesalski, “Janus-Type Hybrid Paper Membranes“ *Adv. Mater. Interfaces* **2019**, 6, 1900892 published by John Wiley and Sons, © 2019, reprinted with permission.

In cooperation with the group of Prof. Andrieu-Brunsen (SmartMembranes), we were interested in the investigation of functional paper coatings with tailor-made and modular wetting properties, respectively. With initial attempts to establish silica based DASA-coatings on paper, we aimed to produce papers coated with neat silica first, in order to establish a baseline for the interface properties. During this trials we were surprised by the discovery that small amounts of silica, which is inherently hydrophilic, were able to inhibit the imbibition of water into the paper substrate and resulted in apparent water contact angles in excess of 120° (Figure 4-5 a). Intrigued by this discovery we also found that we were able to control the wettability of both sides of the paper through the concentration of the dip-coating solution and the drying methods employed (Figure 4-5 b). Subsequent analysis of the paper coatings using CLSM revealed that the silica distribution was in fact the driving force between the different observed wetting behaviors (Figure 4-5 c). Through correlation of the CLSM data, thermogravimetric analysis, and Kr-BET measurements we were further able to determine that the actual thickness of the coatings ranged below 50 nm, and the local gravimetric threshold was found to range between 1.85 and 2.05 wt. % silica relative to the mass of cellulose. The control of the silica distribution enabled us further to produce Janus type membranes, with one hydrophobic and one hydrophilic surface. Such membranes are typically only achievable through multistep processes, involving laborious routines and highly unsustainable (i.e. perfluorinated) compounds. Our work, in comparison, produced a porous hybrid material with Janus type interfaces, which is basically composed of wood fibers and glass. Notably these membranes were able to separate oil and water, because they would only let the respective liquids permeate through in one direction, thus effectively working as a double diode (Figure 4-5 d).

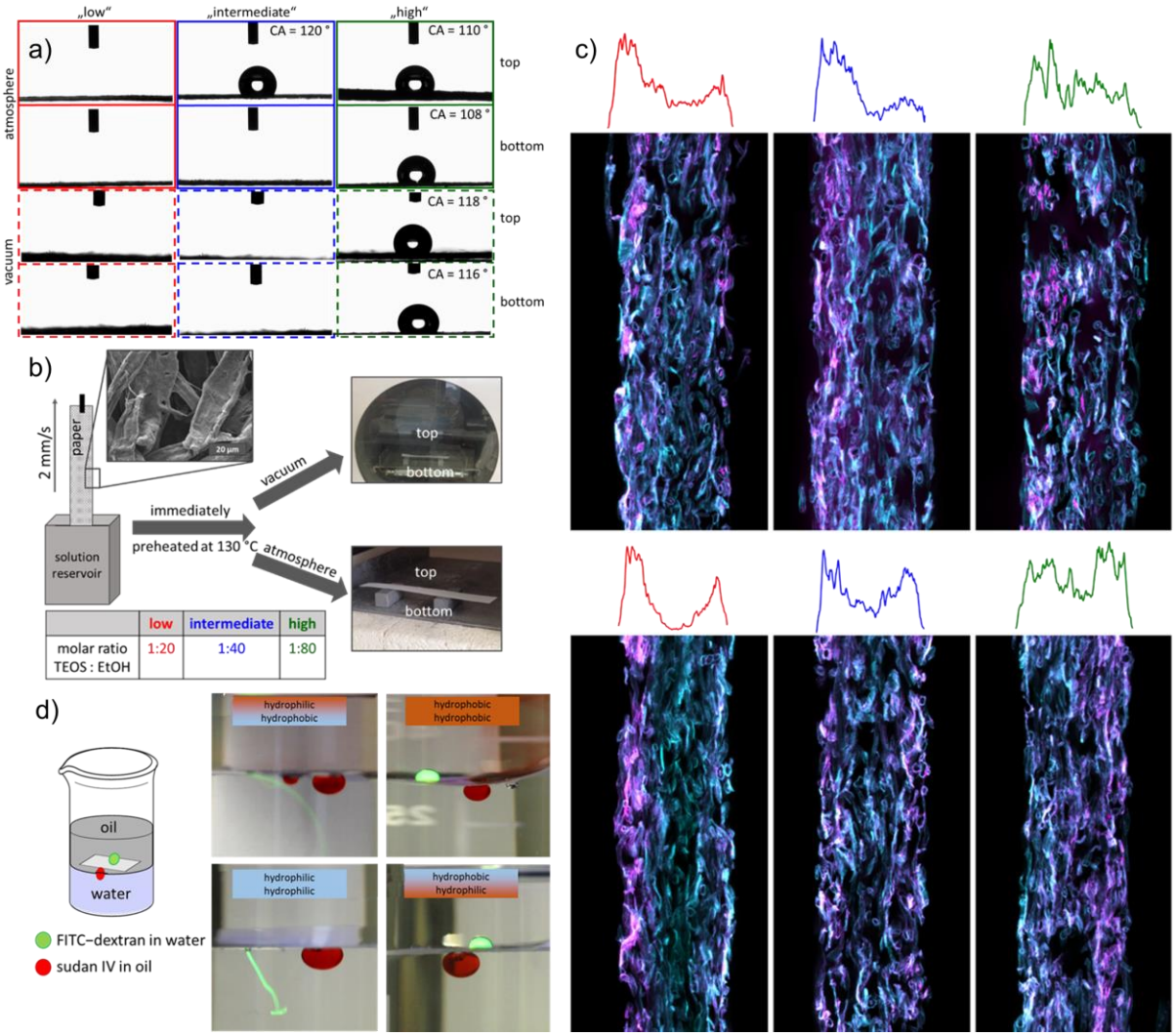

Figure 4-5: a) Static contact angle measurements of 2 µL water (MiliQ) droplets on silica coated eucalyptus-sulfate paper sheets (~80 g/m²). The papers are coated with the three different TEOS concentrations, "low", "intermediate", and "high". b) Schematic illustration of the preparation of silica coated paper sheets. The paper sheet is dip coated in three different precursor solutions having defined amounts of dissolved TEOS given in the inserted table. Subsequently, the samples are cured in preheated ovens at 130 °C under atmospheric pressure and vacuum, respectively. c) CLSM images of cross sections of hybrid papers prepared and the corresponding relative silica distribution from left to right increasing TOES concentration and cured under ambient pressure (top) and vacuum (bottom). All images are z-projections of stacks with 20 to 25 individual images, respectively. d) Experimental set-up with a membrane between water phase on the bottom and oil phase on the top. An oil droplet colored with Sudan IV or and water droplet colored with FITC-dextran are positioned on the opposite side to take a look on droplet permeation. Images of the four combinations of permeation/exclusion on the right.

FULL PAPER

Hybrid Paper Membrane

ADVANCED MATERIALS INTERFACES

www.advmatinterfaces.de

Janus-Type Hybrid Paper Membranes

Maximilian Nau, Nicole Herzog, Johannes Schmidt, Tobias Meckel, Annette Andrieu-Brunsen, and Markus Biesalski**

Functional paper-based materials and devices have been increasingly attractive to scientists in the recent past. In particular, the possibility to functionalize the surface of paper fibers with tailor-made coatings has broadened a possible scope of emerging application considerably. This work introduces novel functional paper membranes with adjustable gradient and Janus-type wettability based on gradient and Janus-type silica coating distribution along the paper cross-section. Correlation of CLSM (distribution), thermogravimetric analysis (silica amount), and Kr-BET (surface area; BET: Brunauer–Emmett–Teller) reveals an extremely low coating thickness, in the range of just a few nanometers, being sufficient to fully inverse paper wettability from hydrophilic to very hydrophobic excluding water. This asymmetric wettability, originating from an asymmetric silica distribution along the paper cross-section, is established by synchronizing silane hydrolysis and condensation reaction rates with silane transport rates in paper within a simple and scalable one-step drying process after having immersed a paper sheet into a tetraethoxysilane-containing precursor solution. As silica by itself, like paper, is a hydrophilic material, the observed hydrophobicity is related to a reduction in cellulose fiber nanoscale porosity controlling water imbibition. While being relevant in manifold applications, these ultrathin, Janus-type hybrid paper membranes are demonstrated to show directed gating and selective oil–water separation.

1. Introduction

In the recent past, research in various cross-disciplinary fields has been inspired by nature, and consequently, attempts to mimic material properties found in plants and animals are widespread. Natural cactus, spider silk, lotus leafs, and desert beetles are some examples showing fascinating performance that is strongly based on their asymmetric physical structure or asymmetric chemical properties, both in bulk and in surface-confined coatings.[1–5] Referencing their two-faced nature, such asymmetric material properties are often named after the Roman god Janus. In particular, the behavior of membranes, particles, rods, or micelles with two orthogonal sides shows high potential for different applications, such as oil/water separation, droplet manipulation, fog collection, unidirectional water flow design, bubble aeration, ion gating, and energy harvesting.[6–12] In particular, asymmetrically designed membranes show strong potential for improved transport design and thus improved application performance. Directed oil–water transport in the context of oil–water separation and directed gas–water transport in the context of fuel cell gas diffusion layers are two specific application examples.[13,14] Therefore, enhancing control of material design and reducing the amount of material needed to achieve asymmetric material characteristics such as wettability are still an ongoing challenge. To make this situation even more stimulating, applying biocompatible and degradable materials while retaining needed stability and doing this in simple, ideally single-step, scalable fabrication processes are of increasing demand.

Janus materials in general are well known since the Nobel Prize lecture of de Gennes in 1991, but they were first mentioned in 1898 by the group of Veyssié.[15,16] The general definition of Janus materials is diverse and includes all materials with asymmetric surfaces as well as composite bulk materials. In 2016, the group of Xu reshaped the definition of materials having opposing properties at two respective interfaces and proposed three configurations of so-called Janus membranes.[5] One is the "A to B"-type material, which shows a physical and/or chemical gradient across a membrane cross-section. Alternatively, A-to-B or A- and B-type Janus membranes are defined as having a clear interface between the layers. Within the last few years, the Jiang group developed a coating and peeling strategy for the facile preparation of multifunctional Janus membranes based on synthetic polymers such as polyethylene terephthalate (PET)/polytetrafluoroethylene (PTFE).[1] After membrane modification by tannic acid (TA) and diethylenetriamine to form a hydrophilic coating on the surface, peeling off the top PTFE layer from the hydrophilic membrane results in a Janus membrane showing unidirectional water permeation properties at

M. Nau, N. Herzog, Dr. T. Meckel, Prof. A. Andrieu-Brunsen, Prof. M. Biesalski
Ernst-Berl Institut für Technische und Makromolekulare Chemie
Technische Universität Darmstadt
Alarich-Weiss-Strasse 8, D-64287 Darmstadt, Germany
E-mail: andrieu-brunsen@smartmem.tu-darmstadt.de; biesalski@tu-darmstadt.de

Dr. J. Schmidt
Fakultät II
Institut für Chemie
Technische Universität Berlin
Hardenbergstr. 40, D-10623 Berlin, Germany

The ORCID identification number(s) for the author(s) of this article can be found under https://doi.org/10.1002/admi.201900892.

DOI: 10.1002/admi.201900892

an oil/water interface.[1] Despite their interesting side-specific separation performance, these materials are fully synthetic with respect to their origin. In 2014, the group of Ikkala presented a membrane consisting of cotton modified on one side by chemical vapor deposition (CVD) of perfluorooctyltrichlorosilane, resulting in a Janus-type material via a single-step preparation.[8] These composite materials exhibit a directional gating to water droplets at the air–water interface as well as oil–water systems with integrated selectivity for oil or water inspired by the passive transport across cell membranes based on transmembrane hydrophilic/hydrophobic interactions.[17,18] As demonstrated, for example, by the work of Ikkala, a hydrophobic interface can be designed by using silanes that chemically bind to the hydroxyl groups at the surface of cotton fibers. Control wetting through silane-based coatings has been a broad area of research since silanes represent a facile way to modulate the interfacial properties of surfaces.[19–24] Additionally, the utilization of poly(dimethylsiloxane) (PDMS) in combination with silica particles on cellulose fibers has yielded some promising results in regard to mechanically stable coatings, a challenge that still faces a number of micro/nanostructured surfaces.[25,26] While these strategies evidently have proven track records, the production of the material is rather laborious, including delicate sol/gel processes and the necessity for several steps to produce the interface.[26,27] In addition, the use of perfluorinated compounds in surface modification should raise concerns with respect to the environmental impact, especially if these coatings should be implemented on an industrial scale.[28] Furthermore, if silanes are implemented without the generation of a micro- or nanostructure, for example, on cellulosic substrates, the wettability of surfaces can only be modulated by alteration of the silane derivatives used and thus of the final surface energy of the chemically modified substrate.[29,30] These techniques again all utilize a range of organo- and perfluorinated compounds.[31] Interestingly, a study from Cappelletto et al. on nonwoven cellulose fiber webs, such as paper, reports that coating tetraethoxysilane (TEOS) without further modification increases hydrophobicity. When relatively high silica amounts, namely, 20 and 40 wt% (by thermal analysis), were deposited on paper fibers, the static contact angle was increased; however, the samples were still classified as hydrophilic, and only the introduction of methyl groups through the use of methyl-substituted precursors instead of TEOS led to hydrophobic materials.[32] Due to the large amounts of silica deposited, the fiber microstructure is consequently masked, and contact angle (CA) analysis effectively sampled a slightly structured silica surface rather than an open porous paper structure. An interesting application shown by Kehr and Motealleh in 2017 was the use of Janus-type paper sheets as a 3D cell culture system.[33] Spatially resolved functionalization of the paper substrate is not reported with this particular strategy. However, for any successful design of Janus-type (paper-based) membranes, gradients of the surface chemistry within the substrate are perhaps the key parameter to guide wettability within defined areas of the hybrid material.

Here, we present a novel cellulose-based hybrid material that addresses the above outlined challenges of known Janus-type membranes through a facile production method using a single-step process. Highly controlled deposition of very small amounts of silica on lab-engineered paper substrates enables us to avoid the use of perfluorinated or organo-modified silanes, providing a cheap, easy, sustainable and biobased route to generate highly functional asymmetric, i.e., Janus-type, hybrid materials.

2. Results and Discussion

To design Janus-type paper hybrid materials with asymmetric wettability and capillary-driven fluid flow, we modified lab-engineered eucalyptus sulfate paper with extremely low amounts of silica. Asymmetric silica coating distribution and thus wetting and fluid flow gradients are achieved through a dip-coating process in a tetraethoxysilane-containing ethanol-water-based solution, adapted from our prior work, together with a subsequent heat treatment at 130 °C at atmospheric pressure or at reduced pressure (**Figure 1**a–c).[34] The temperature of 130 °C was chosen because it is known to be nondestructive to eucalyptus paper while allowing acid (i.e., HCl)-catalyzed hydrolysis and condensation of TEOS, resulting in silica formation.[34,35] By using a simple dip-coating process and tuning the initial TEOS concentration in the coating solution, the wetting characteristics progress from hydrophilic to Janus type and hydrophobic in a controlled fashion by adjusting a precise and simple gradient design. Investigation by eye, microscope, and scanning electron microscopy (SEM) did not show macroscopic changes in the eucalyptus paper structure or alterations on the micrometer scale (Figure 1b,c) compared to unmodified paper sheets (Figure 1a). This apparent lack of discernible topographical and morphological differences indicates that the relevant features of the coating and its thickness must be smaller than the resolution limit of the SEM under the given conditions (2500×76 nm^{-2}). In comparison, the work of Cappelletto et al. showed obvious masking of the paper structure already when 20 wt% silica was applied to paper surfaces and still yielded materials considered hydrophilic.[32] Unfortunately, SEM nanoscale analysis of the silica-coated eucalyptus paper sheets is not trivial due to the high energy needed for imaging, which can destroy the organic matrix of the hybrid material. Consequently, further studies are conducted via correlated thermogravimetric analysis (TGA), confocal laser scanning microscopy (CLSM), and Brunauer–Emmett–Teller (BET) analysis to gather information at the submicron scale.

Macroscopic static contact angle measurements of the top and bottom surfaces of all silica-coated eucalyptus sulfate paper samples (**Figure 2**) prepared in this study were carried out to study the influence of the silica coating on the wetting behavior of the hybrid paper. All samples prepared with high TEOS concentrations (for solution composition, please refer to the Experimental Section) exhibit hydrophobic wetting characteristics with static contact angles of 120°–130°. Note that the chemical surface of cured TEOS is composed solely of hydrophilic hydroxyl functions. No difference between the macroscopic static water contact angles of the top and bottom surface is observed, regardless of the orientation during curing and curing pressure, i.e., ambient pressure versus vacuum oven. In contrast, all eucalyptus paper sheets coated with low TEOS concentrations in the dip-coating process do exhibit hydrophilic wetting behavior. We found no difference between top and bottom side wetting behavior, nor any differences in the

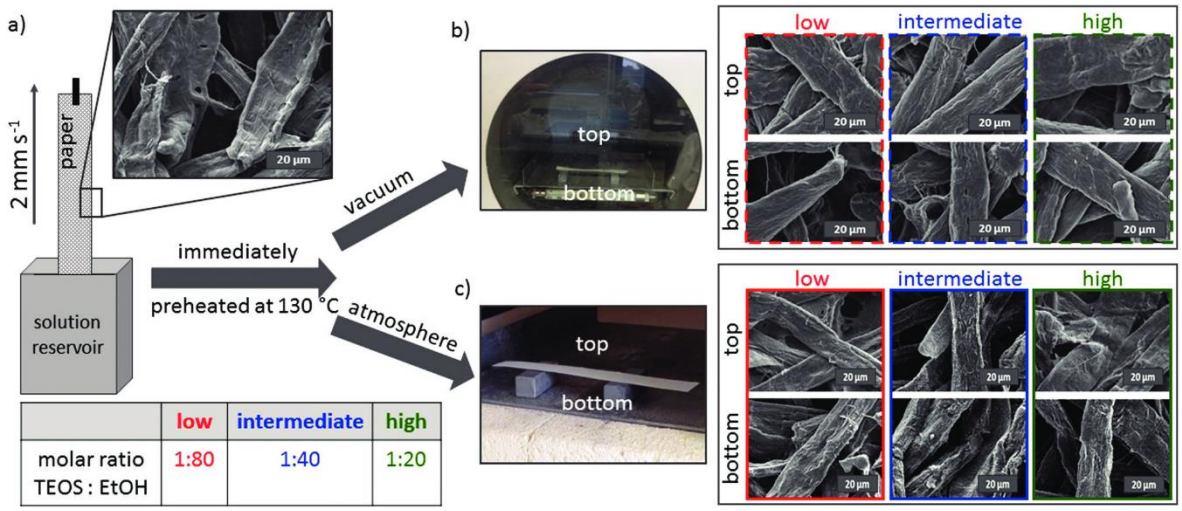

Figure 1. a) Schematic illustration of the preparation of silica-coated paper sheets. The paper sheet is dip-coated in three different precursor solutions having defined amounts of dissolved TEOS given in the inserted table. Subsequently, the samples are cured in preheated ovens at 130 °C under b) vacuum and c) atmospheric pressure, respectively. The inserted scanning electron microscopy images show examples of nonmodified eucalyptus sulfate paper (80 g m^{-2}, (a)) and silica-modified eucalyptus sulfate paper (80 g m^{-2}, (b,c)).

wetting of the hybrid materials using the two different curing strategies (at atmospheric pressure vs under reduced pressure). Interestingly, the eucalyptus paper sheets coated with intermediate TEOS concentrations show a very different and curing process-dependent wetting behavior: if these samples are cured in an oven under ambient pressure, the top side exhibits hydrophobic wetting behavior with static contact angles of ≈120°, whereas the bottom side exhibits hydrophilic macroscopic static contact angles of 0° along with water exclusion at the top side and instant and complete water imbibition at the bottom side (Figure 2, blue). As the top surface is water repellent, while the bottom side absorbs water immediately, a Janus-type or amphiphilic membrane has been created. This result can be explained by the positioning of the sample in the oven and by considering migration of the TEOS during the drying procedure. The sample is placed in an oven during drying in a horizontal position (Figure 1b), favoring a directed migration of TEOS due to the preferred ethanol evaporation at the top of the paper sheet. If ethanol evaporation and silane hydrolysis as well as condensation now occur on similar time scales, a gradient in

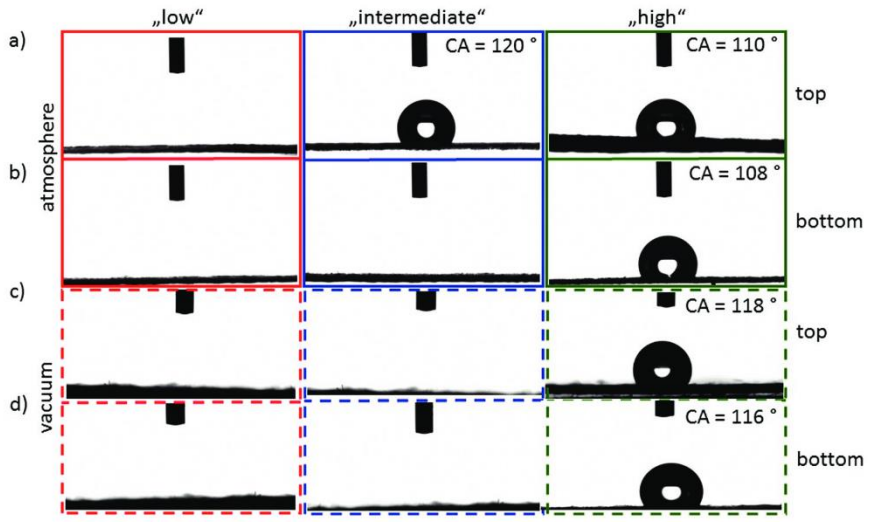

Figure 2. Static contact angle measurements of 2 µL water (MilliQ) droplets on silica-coated eucalyptus sulfate paper sheets (≈80 g m^{-2}). The papers were coated with the three different TEOS concentrations, "low," "intermediate," and "high." a) Shows the top surface and b) the bottom side of the paper after curing in a preheated oven, c) shows the top surface and d) the bottom side of the paper after curing in a vacuum oven.

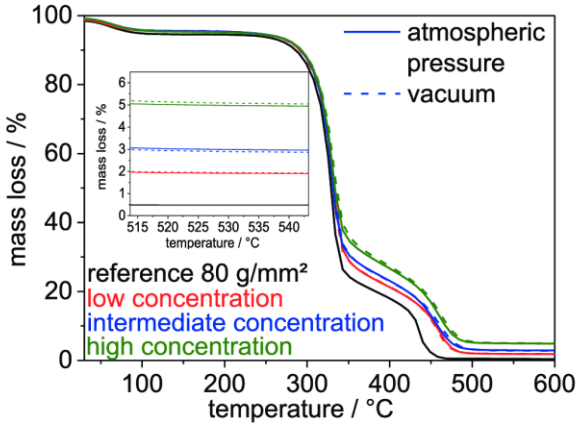

Figure 3. Thermogravimetric analysis of silica-coated eucalyptus sulfate paper (80 g m^{-2}) sheets. The amount of coating is determined by the TEOS concentration in the initial coating (red, blue, and green) and, to a much smaller degree, by the curing process (atmospheric pressure = line and vacuum = dotted line).

silica distribution along the eucalyptus paper cross-section is obtained. Curing eucalyptus paper sheets coated with identical intermediate TEOS concentrations in an oven under reduced pressure results in hydrophilic wetting behavior on both sides of the paper sheets. This result can be explained by the fact that evaporation of the solvent is now much faster than migration of TEOS, and thus, homogeneous paper characteristics with respect to the silica coating are obtained.

To understand the findings outlined above in more detail, we next addressed the following questions: how much silica is deposited on the respective paper sheets, what does the silica distribution look like, and is there an effective coating thickness necessary in order to achieve hydrophobic wetting characteristics?

The amount of deposited silica within the eucalyptus paper sheet was determined via TGA (**Figure 3**). Due to the apparently very low amount of silica, TGA is the method of choice because of the very small errors compared to those of alternative methods such as standard gravimetric analysis, especially for small sample amounts. During a TGA measurement, the silica content of coated paper sheets was determined by thermal removal of the paper, which only leaves silica (stable up to 1700 °C) and ash. The determined amount of silica is calculated considering the ash content, 5.8 wt%, of the base paper deduced from a reference measurement. This finding shows that the silica content in the low TEOS concentration coated papers is 0.5 wt%; in the intermediate TEOS concentration coated papers, 1.5 wt%; and in the high TEOS concentration coated papers, ≈3.7 wt% (Table S1, Supporting Information).

Further analysis using Krypton sorption reveals a specific surface area (BET) for uncoated samples of 0.54 $m^2\ g^{-1}$. While eucalyptus fiber macropores are unaffected by the aforementioned silica coating, as is evident through SEM imaging (Figure 1), the Kr-BET specific surface area progressively changed from 0.59 (low), over 0.43 (intermediate), to 0.27 $m^2\ g^{-1}$ (high).

This decrease in surface area indicates that the mechanism of the silica induced hydrophobization is not based on the generation of micro- or nanostructure. Mechanistically, we rather suggest a mechanism based on pinning on the three-phase contact line on the microrough paper which is facilitated through the fact that coated fibers cannot undergo subsequent swelling of the cellulosic material. The pinning mechanism with respect to water on hydrophilic surfaces has been described in detail by Hensel et al. and is facilitated through the inhibition of fiber swelling and masking of the internal and external fiber surface.[36] This hypothesis is supported by a rather miniscule decrease in free surface energy from cellulose (63.8 mN m^{-1}) to silica (59.2 mN m^{-1}) that were determined on model surfaces (Table S2, Supporting Information).

2.1. Silica Distribution Analysis

To further support this interpreation we further investigated the Janus paper characteristics. We determined the cross-sectional silica distribution to address possible threshold concentrations of silica deposited at the fiber surfaces that is needed to render the hybrid material hydrophobic (i.e., where no further wicking of a water drop into the material can be observed). The relative silica distribution is obtained by using CLSM imaging. This technique is based on our prior investigations regarding localized modifications of paper and functionalization of fiber surfaces.[37,38] Examples of CLSM image stacks of cross-sections of the hybrid paper material are displayed in **Figure 4**. The untreated cellulose sheets were stained with Calcofluor white prior to dip-coating with Rhodamine B-labeled silica precursor solution. The silica (Rhodamine B channel) is colored magenta, while the eucalyptus fibers (CFW channel) are colored cyan.

For the three different TEOS concentrations applied during dip-coating (compare Figure 4a–c and Figure 4d–f) and the two curing methods (ambient pressure and reduced pressure, Figure 4a,d; Figure 4b,e; Figure 4c,f), similar silica distributions are observed (Figures S1 and S2, Supporting Information). TEOS-coated eucalyptus paper sheets cured under vacuum show bathtub-like silica distribution along the cross-section with an increased silica amount at the top and bottom surfaces of the paper cross-section (Figure S1, Supporting Information). The relative difference in deposited silica between the outer paper sheet surfaces and the center of the cross-section increases with decreasing TEOS concentration in the dip-coating solution. This result implies that the TEOS concentration within the coating solution affects the movement of the liquid phase during TEOS hydrolysis and condensation, e.g., via changes in the fluidic properties (e.g., viscosity) and different interactions with the fibrous eucalyptus paper substrate.

On the other hand, eucalyptus paper sheets cured under ambient pressure show up to two times higher relative silica concentration on the top of the samples than on the bottom. The silica gradient along the cross-section of the hybrid paper is less pronounced if the initial coating solution contains higher TEOS concentrations. The reason for this behavior again can be found in the evaporation kinetics, and thus, the relation of material transport with hydrolysis-condensation speed determines the chemical gradient formation of the silica-modified hybrid paper (Figures S1 and S2, Supporting Information).

To gain further insight into the absolute mass distributions, the relative measurements are numerically integrated (over the

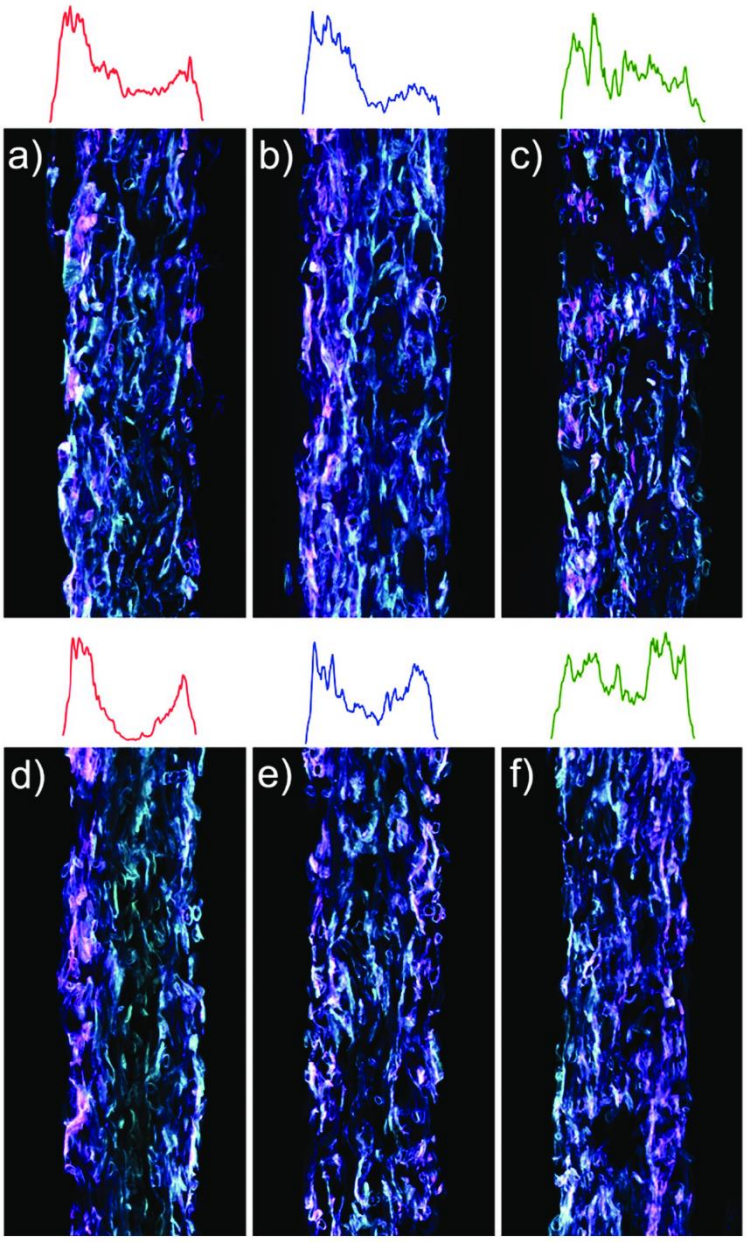

Figure 4. CLSM images of cross-sections of prepared hybrid papers and the corresponding relative silica distribution of a) samples prepared with a low TEOS concentration and cured under ambient pressure, b) samples prepared with an intermediate TEOS concentration and cured under ambient pressure, c) samples prepared with a high TEOS concentration and cured under ambient pressure, d) samples prepared with a low TEOS concentration and cured under vacuum, e) samples prepared with an intermediate TEOS concentration and cured under vacuum, and f) samples prepared with a high TEOS concentration and cured under vacuum. All images are *z*-projections of stacks with 20 to 25 individual images.

cross-section) and normalized, and the relative partial integral for each 10 µm cross-section segment of the paper sheet cross-section is calculated and multiplied by the coating weight, as determined by TGA. This procedure allows us to determine the distribution of absolute volumetric coating weights, as displayed in **Figure 5**a (cured under vacuum) and Figure 5b (cured under ambient pressure). By correlating the obtained silica distribution with the static CA values described above, a correlation between the silica amount and wetting is observed: the threshold silica amount above which the paper sheet becomes hydrophobic is located between the highest coating weight (still resulting in hydrophilic wetting) and the lowest silica coating weight (just inducing hydrophobic wetting).

The highest amount of silica in a hydrophilic sample (lower threshold boundary) is observed with the top surface of the samples coated with the intermediate TEOS concentration and cured under vacuum (Figure 5a, blue), while the lowest already hydrophobic material is observed with the corresponding sample cured under atmospheric pressure (Figure 5b, blue). While the sample cured under atmospheric pressure is still hydrophobic with a specific coating weight of 10.3 mg cm^{-3} (Figure 5b), the sample cured under vacuum is hydrophilic at a specific coating weight of 9.3 mg cm^{-3} (Figure 5a), which defines the threshold between those two boundaries. Consequently, a minimum silica content between 1.85 and 2.05 wt% with respect to eucalyptus sulfate fibers is necessary to obtain hydrophobic hybrid membrane behavior. In brief, we determined a minimal threshold amount of TEOS coating, which is necessary to induce the hydrophobic effect, samples prepared from low TEOS concentration, as shown by the data in Figure 5 did not overcome this threshold amount on either surface and thus remained hydrophilic, indicating our data to be accurate. Through correlation of these data with the Kr-BET specific surface area, the threshold in terms of coating weight is located between about 43 and 47 mg m^{-2}, respectively. The apparent absence of changes in the micrometer scale is subsequently self-explanatory because the density of silica (2.65 g cm^{-2}) corresponds to—with respect to paper coatings—ultrathin coating thicknesses between 16 and about 18 nm, respectively.

2.2. Application of TEOS-Modified Paper as Tunable Membrane

To show the versatility of asymmetric paper-based Janus membranes, we demonstrate their ability to separate oil and water as one possible application model. For this purpose, a two-phase

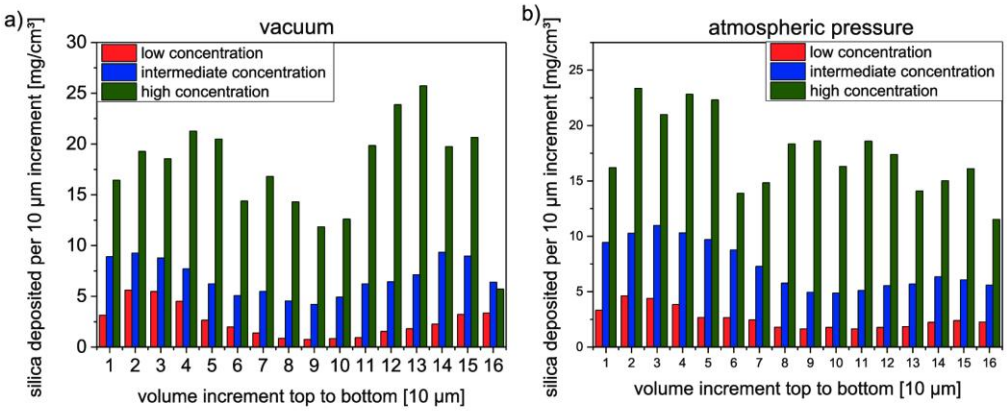

Figure 5. Absolute amount of silica per volume increment calculated through correlation of CLSM and TGA data for a) samples cured under vacuum and b) samples cured under ambient pressure.

water-oil system consisting of water and cyclohexane was used. Cyclohexane was chosen as an oil component to eliminate effects based on high viscosity. The investigated paper sheet is located at the interface between water and cyclohexane (**Figure 6**b). Through use of the three different TEOS concentrations for eucalyptus paper coating and facile orientation, all possible permeation combinations for this system can be designed, as depicted in Figure 6a. The paper sheets coated with "low" and "high" amounts of TEOS behave as expected. If an FITC-labeled water drop is placed onto the hydrophilic paper membrane (i.e., "low" TEOS coating, Figure 6e), the latter allows water permeation, as easily inferred even by the naked eye. However, the same membrane does not allow any visible permeation of the nonpolar oil. The opposite behavior is observed for the hydrophobic paper (i.e., "high" TEOS coating, Figure 6d): the Sudan IV-labeled oil droplet is capable of permeating the fibrous network, whereas the water droplet does not penetrate the surface of the paper. Most interestingly, however, the Janus-type paper (i.e., the "intermediate" TEOS coating dried under ambient pressure) is acting as a "double diode": both water and oil are capable of permeating through the membrane but only with a specific direction and in opposite directions relative to each other (Figure 6c,f). This property prohibits reverse permeation, as demonstrated by the fact that one orientation of the Janus paper (hydrophobic side facing toward the water, Figure 6c) will let water pass through from the oil side, and vice versa. In the opposite orientation (hydrophobic side facing toward the oil, Figure 6f), permeation is blocked in both directions. Note, investigation of the influence of geometric factors of the hydrophobic coating (i.e., thickness) on the permeation dynamics is a complex endeavor to be addressed in follow-up scientific studies. However, comparable properties have, to the best of our knowledge, only been realized using fluorosilanes, dodecanethiol, poly(dimethylsiloxane), or

a)	water permeation	no water permeation
oil permeation	intermediate silica concentration (hydrophobic surface on water fraction) -> c)	high silica concentration -> d)
no oil permeation	low silica concentration -> e)	intermediate silica concentration (hydrophobic surface to oil fractions) -> f)

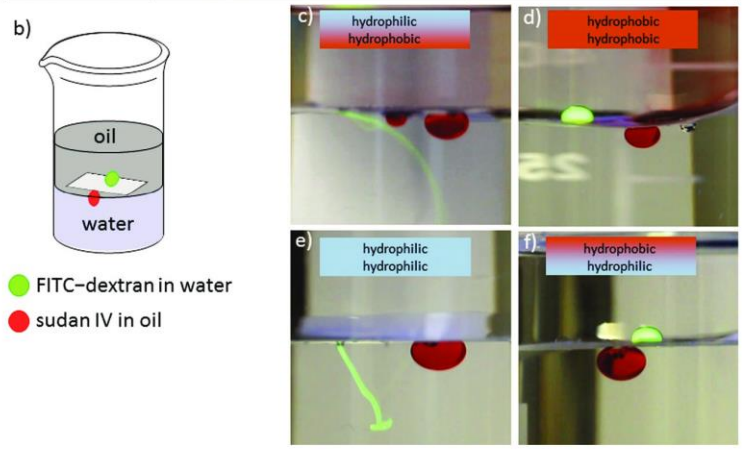

Figure 6. a) Table showing the oil/water infiltration or exclusion through different eucalyptus paper sheets prepared with different amounts of silica coating cured under atmospheric pressure. b) Experimental setup with a membrane between the water phase on the bottom and oil phase on the top. An oil droplet colored with Sudan IV or a water droplet colored with FITC-dextran was positioned on the opposite side to look at droplet permeation. Images of the four combinations of permeation/exclusion are shown in (c) through (f): c) Janus membrane, where the hydrophobic interface lays on the water phase. d) Hydrophobic silica-coated paper membrane, e) hydrophilic silica-coated paper, and f) Janus membrane, where the hydrophilic interface lays on the water phase. Time-dependent images of the systems are provided in Figure S3 in the Supporting Information.

polymers such as polyethylene terephthalate and polytetrafluoroethylene obtained through multistep, sophisticated processes. The approach presented here essentially produces paper coated with an extremely low amount of silica (i.e., SiO_2) content using nothing but an oven heated to 130 °C.[1,5,8,39–41] Moreover, due to the ease of application, even a simple scale-up to roll-to-roll coating shall in principle be possible, given the state of art technologies in papermaking and printing.

3. Conclusion

This work presents a facile, sustainable, and scalable method to create paper-based hybrid materials with designed wettability and wettability gradients ranging from very hydrophilic to fully hydrophobic. Especially paper-based hybrid membranes with Janus-type asymmetric wetting characteristics using extremely low amounts of TEOS as the only active chemical in a simple dip-and-cure process are provided. These asymmetric wetting characteristics are based on an interplay of silane reactivity and environment-controlled transport along the paper cross-section during curing. This simple process allows for tailored adjustment of the silica gradient across the paper cross-section. This inherently simple and easily scalable process produces thin silica coatings on the outer, as well as on the inner surface of the cellulose fibers within the paper sheet. The silica coating amount can be precisely adjusted through variation in the TEOS concentration in the initial coating solution together with control of the curing conditions, especially the air pressure, employed during the curing step. It has to be emphasized that an extremely low silica coating amount (1.40–3.70 wt%, with respect to the final membrane mass) results in fully hydrophobic as well as Janus-type wetting characteristics, as determined by the correlation of CLSM, TGA, and BET analysis, respectively. Thereby a low silica content of 1.85–2.05 wt% is sufficient to produce a hydrophobic interface on eucalyptus paper, by generating localized coating thicknesses of just a few nanometers. Mechanistically, the observed hydrophobization is based on nanoscale porosity reduction. The generated A–B Janus-type paper sheets are capable of separating oil and water in a double-diode fashion, allowing permeation of water from one side and permeation of oil from the opposite side and in opposite directions. The latter offers great potential for the design of simple yet efficient oil–water separation membranes for future water management concepts. In contrast to state-of-the-art membrane designs known today, our membranes consist of fully biobased compounds and can be easily disintegrated and recycled using well-established technologies with paper recycling. Finally, a simple scale-up to roll-to-roll coating will in principle be possible, given the technologies in papermaking and printing.

4. Experimental Section

Reagents: All chemicals and solvents were purchased from Fisher Scientific, Merck, Sigma-Aldrich, or Alfa Aesar and used as received unless otherwise stated.

Paper Fabrication: For the preparation of lab-engineered paper substrates, eucalyptus sulfate pulp (curl: 16.2%; fibrillation degree: 1.3%; fines content: 15.2%) was used. The pulp was refined in a Voith LR 40 laboratory refiner. Refining was performed with an effective specific energy of 16 kWh t^{-1} (750 000 revolutions). Laboratory-engineered paper substrates were prepared from said pulp with a grammage of 80 ± 0.9 g m^{-2} by using a Rapid-Köthen sheet former according to DIN 54358 and ISO 5269/2 (REF: ISO 5269-2:2004(E), Pulps—Preparation of Laboratory Sheets for Physical Testing—Part 2: Rapid Köthen Method, 2004.) No additives or filler materials were used. Prior to coating, the paper was conditioned for at least 24 h under standard conditions (23 °C, 50% r.h.).

Silica Coatings: Silica coatings were generated from three TEOS-containing dip-coating solutions that were prepared with the following molar ratios. The color code remains consistent throughout the work.

1 TEOS : 80 EtOH : 20 H2O : 0.04 HCl → low concentration

1 TEOS : 40 EtOH : 10 H2O : 0.02 HCl → intermediate concentration

1 TEOS : 20 EtOH : 5 H2O : 0.01 HCl → high concentration

The precursor solutions were stirred at 22 °C for 24 h and subsequently used for dip-coating on eucalyptus sulfate paper strips (1 cm* 8 cm) at 50% relative humidity and 23 °C at a withdrawal speed of 2 mm s^{-1}. After dip-coating, samples were directly brought into a 130 °C preheated vacuum curing oven or a muffle furnace that was heated from 23 to 130 °C. The samples were kept at 130 °C for 2 h (regardless of the heating method) before cooling to ambient temperature. The samples were marked on the top side (with respect to the orientation during the curing process) of the sheets.

Contact Angle: Contact angle measurements were carried out using a Model TBU90E from DataPhysics Instruments GmbH with the corresponding software. All samples were measured at five positions, and the average value was calculated with standard deviation. For macroscopic static contact angle measurements, a water drop volume of 2 µL was used (dispense rate: 1 µL s^{-1}). To determine the surface energy of silica and regenerated cellulose, the macroscopic static contact angles on planar model surfaces (silica coating on a glass substrate and regenerated cellulose) were determined for different solvents. The following solvents with different surface energies were used: water, *N*,*N*-dimethylformamide, dimethyl sulfoxide, *n*-hexane, and toluene. Subsequently, the respective surface energies of the model surfaces were calculated according to the Owens, Wendt, Rabel, & Kälble (OWRK) method.

Thermogravimetric Analysis: TGA analysis was performed on a TGA 1 instrument (Mettler–Toledo). The samples were heated from 25 to 600 °C at a rate of 10 K min^{-1} under a constant air flow of 30 mL min^{-1}.

Scanning Electron Microscopy: SEM micrographs were acquired using a Philips XL30 FEG scanning electron microscope operated at an acceleration voltage of 10 kV. Samples were sputtered with a platinum(80)/palladium(20) layer of 10 nm prior to analysis.

Preparation of the Paper Samples for CLSM: The paper samples for CLSM analysis were coated with different amounts of TEOS in the same fashion as described before except for the addition of fluorescence labels. For this purpose, the untreated paper was dip-coated in an ethanol (abs.) solution of 10×10^{-6} M calcofluor white (CFW). After drying at 40 °C in a vacuum oven (Heraeus, VTR 5036) for 1 h, the resulting CFW-labeled samples were coated with silica as described before except for the addition of 20×10^{-6} M Rhodamine B (based on the amount of ethanol (abs.)) to the dip-coating solutions.

Preparation of the Cross-Sections: Each sample was embedded in a mixture of 49.9875 wt% Desmodur 3200, 49.9875 wt% Albodur 956 VP, and 0.025 wt% TIB-KAT 318, which is a commercial polyurethane system. The freshly embedded samples then underwent several vacuum cycles at room temperature to remove residual air bubbles; afterward, the resin was cured for 18 h at 40 °C. The final semiflexible sample was then cut into 120 µm slices using a microtome. During all these steps, the identity of the "top" side was tracked via appropriate sample labeling.

CLSM Imaging: The microtome-cut sample slices were placed between two 25 mm round microscope cover glasses Type No. 1 from "Assistent" in a custom sample holder. Optical matching was achieved

using Type F immersion liquid from Leica. The imaging was performed on a Leica TCS SP8. The image stacks obtained for each sample were summed up to condense the information about the material distribution. A gray value analysis was performed on these summed image data for each row of pixels, i.e., the gray values of each image were added for every single pixel column. This procedure yields the relative distribution of the given material throughout the paper from top to bottom or, in terms of the images displayed in Figure 4, from left to right.

Analysis of Oil/Water Accessibility of Paper Membranes: Water was placed in a cylindrical beaker, and the sample membrane was placed on the interface and covered with cyclohexane (oil simulant), as inspired by the work of Wang et al.[1] The beaker was positioned on top of a 365 nm lamp for excitation of fluorescein. A drop of cyclohexane colored with the dye Sudan IV was added through the water phase to the membrane, and a drop of water colored with FITC-dextran was placed onto the membrane at the oil phase side. The experiment was recorded using a Canon EOS 700D camera equipped with a 55–250 mm objective and a 24 mm spacer ring.

Krypton Adsorption: Krypton adsorption measurements were performed at 77 K using an Autosorb iQ2 from Quantachrome. The samples were degassed for 12 h prior to measurement, and the surface area was calculated from the Brunauer–Emmett–Teller model by selecting adsorption points satisfying the consistency criteria for application of the BET theory.

Supporting Information

Supporting Information is available from the Wiley Online Library or from the author.

Acknowledgements

M.N. and N.H. contributed equally to this work. The authors would like to thank Dr. Martin Brodrecht (Buntkowsky Group, Technische Universität Darmstadt) for the fruitful discussion and insight regarding BET-Analysis. The authors acknowledge fruitful collaboration within the framework DFG PAK 962 “Geometrische und Chemische Struktur funktionaler Papiere.”

Conflict of Interest

The authors declare no conflict of interest.

Keywords

asymmetric material distribution, functional paper, hybrid materials, Janus membranes, ultrathin coating

Received: May 20, 2019
Revised: June 13, 2019
Published online: July 26, 2019

[1] Z. Wang, X. Yang, Z. Cheng, Y. Liu, L. Shao, L. Jiang, *Mater. Horiz.* **2017**, *4*, 701.
[2] A. Walther, A. H. E. Müller, *Chem. Rev.* **2013**, *113*, 5194.
[3] X. Tian, J. Li, X. Wang, *Soft Matter* **2012**, *8*, 2633.
[4] A. A. Shah, B. Schultz, W. Zhang, S. C. Glotzer, M. J. Solomon, *Nat. Mater.* **2015**, *14*, 117.
[5] H. C. Yang, J. Hou, V. Chen, Z. K. Xu, *Angew. Chem., Int. Ed.* **2016**, *55*, 13398.
[6] H. Zhang, X. Hou, L. Zeng, F. Yang, L. Li, D. Yan, Y. Tian, L. Jiang, *J. Am. Chem. Soc.* **2013**, *135*, 16102.
[7] M. Cao, J. Ju, K. Li, S. Dou, K. Liu, L. Jiang, *Adv. Funct. Mater.* **2014**, *24*, 3235.
[8] X. Tian, H. Jin, J. Sainio, R. H. A. Ras, O. Ikkala, *Adv. Funct. Mater.* **2014**, *24*, 6023.
[9] M. Zhang, L. Wang, Y. Hou, W. Shi, S. Feng, Y. Zheng, *Adv. Mater.* **2015**, *27*, 5057.
[10] Z. Zhang, X. Y. Kong, K. Xiao, Q. Liu, G. Xie, P. Li, J. Ma, Y. Tian, L. Wen, L. Jiang, *J. Am. Chem. Soc.* **2015**, *137*, 14765.
[11] H.-C. Yang, J. Hou, L.-S. Wan, V. Chen, Z.-K. Xu, *Adv. Mater. Interfaces* **2016**, *3*, 1500774.
[12] H. C. Yang, Y. Xie, J. Hou, A. K. Cheetham, V. Chen, S. B. Darling, *Adv. Mater.* **2018**, *30*, 1801495.
[13] A. Forner-Cuenca, J. Biesdorf, L. Gubler, P. M. Kristiansen, T. J. Schmidt, P. Boillat, *Adv. Mater.* **2015**, *27*, 6317.
[14] Z. Zhang, L. Wen, L. Jiang, *Chem. Soc. Rev.* **2018**, *47*, 322.
[15] P.-G. de Gennes, *Angew. Chem., Int. Ed. Engl.* **1992**, *31*, 842.
[16] C. Casagrande, P. Fabre, E. Raphael, M. Veyssié, *Europhys. Lett.* **1989**, *9*, 251.
[17] A. M. Seddon, D. Casey, R. V. Law, A. Gee, R. H. Templer, O. Ces, *Chem. Soc. Rev.* **2009**, *38*, 2509.
[18] K. Sugano, M. Kansy, P. Artursson, A. Avdeef, S. Bendels, L. Di, G. F. Ecker, B. Faller, H. Fischer, G. Gerebtzoff, H. Lennernaes, F. Senner, *Nat. Rev. Drug Discovery* **2010**, *9*, 597.
[19] M. Hikita, K. Tanaka, T. Nakamura, T. Kajiyama, A. Takahara, *Langmuir* **2005**, *21*, 7299.
[20] H. Yang, F. Liang, Y. Chen, Q. Wang, X. Qu, Z. Yang, *NPG Asia Mater.* **2015**, *7*, e176.
[21] B. Xia, L. Yan, Y. Li, S. Zhang, M. He, H. Li, H. Yan, B. Jiang, *RSC Adv.* **2018**, *8*, 6091.
[22] D. Liu, Q. Wu, R. L. Andersson, M. S. Hedenqvist, S. Farris, R. T. Olsson, *J. Mater. Chem. A* **2015**, *3*, 15745.
[23] Q. F. Xu, J. N. Wang, K. D. Sanderson, *J. Mater. Chem.* **2010**, *20*, 5961.
[24] P.-H. Chen, C.-C. Hsu, P.-S. Lee, C.-S. Lin, *J. Mech. Sci. Technol.* **2011**, *25*, 43.
[25] Q. P. Ke, W. Q. Fu, H. L. Jin, L. Zhang, T. D. Tang, J. F. Zhang, *Surf. Coat. Technol.* **2011**, *205*, 4910.
[26] C. Kosak Soz, S. Trosien, M. Biesalski, *ACS Appl. Mater. Interfaces* **2018**, *10*, 37478.
[27] S. Cai, Y. Zhang, H. Zhang, H. Yan, H. Lv, B. Jiang, *ACS Appl. Mater. Interfaces* **2014**, *6*, 11470.
[28] T. Stahl, D. Mattern, H. Brunn, *Environ. Sci. Eur.* **2011**, *23*, 38.
[29] B. Ding, C. Li, Y. Hotta, J. Kim, O. Kuwaki, S. Shiratori, *Nanotechnology* **2006**, *17*, 4332.
[30] J. Vasiljević, M. Gorjanc, B. Tomšič, B. Orel, I. Jerman, M. Mozetič, A. Vesel, B. Simončič, *Cellulose* **2013**, *20*, 277.
[31] F. Ferrero, M. Periolatto, *Appl. Surf. Sci.* **2013**, *275*, 201.
[32] E. Cappelletto, E. Callone, R. Campostrini, F. Girardi, S. Maggini, C. della Volpe, S. Siboni, R. Di Maggio, *J. Sol-Gel Sci. Technol.* **2012**, *62*, 441.
[33] N. S. Kehr, A. Motealleh, *Colloids Surf., B* **2017**, *156*, 236.
[34] C. Dubois, N. Herzog, C. Ruttiger, A. Geissler, E. Grange, U. Kunz, H. J. Kleebe, M. Biesalski, T. Meckel, T. Gutmann, M. Gallei, A. Andrieu-Brunsen, *Langmuir* **2017**, *33*, 332.
[35] G. De, B. Karmakar, D. Ganguli, *J. Mater. Chem.* **2000**, *10*, 2289.
[36] R. Hensel, R. Helbig, S. Aland, H.-G. Braun, A. Voigt, C. Neinhuis, C. Werner, *Langmuir* **2013**, *29*, 1100.
[37] S. Bump, A. Böhm, L. Babel, S. Wendenburg, F. Carstens, S. Schabel, M. Biesalski, T. Meckel, *Cellulose* **2015**, *22*, 73.
[38] M. Janko, M. Jocher, A. Boehm, L. Babel, S. Bump, M. Biesalski, T. Meckel, R. W. Stark, *Biomacromolecules* **2015**, *16*, 2179.
[39] F. Ren, G. Li, Z. Zhang, X. Zhang, H. Fan, C. Zhou, Y. Wang, Y. Zhang, C. Wang, K. Mu, Y. Su, D. Wu, *J. Mater. Chem. A* **2017**, *5*, 18403.
[40] J. Ju, K. Xiao, X. Yao, H. Bai, L. Jiang, *Adv. Mater.* **2013**, *25*, 5937.
[41] M. Cao, J. Xiao, C. Yu, K. Li, L. Jiang, *Small* **2015**, *11*, 4379.

5. Towards smart polysaccharide coatings and bio-based process additives in paper making

5.1. Thermally responsive paper coatings

The content of this chapter has been disclosed in the patent application DE 102018111495.8 („Thermoresponsive Papierbeschichtungen auf Basis von Cellulosederivaten“). The work presented is the result of a collaboration of the Technische Universität Darmstadt with the Papierfabrik August Koehler SE, a paper mill which is focused on specialty papers, like carbonless copy- and thermal printing paper. Thermal paper (e.g. receipts at cash registers) are printed with thermal printers, which work with an array of submillimeter resistors, that are used as heat source. This system does not heat the substrate to a defined temperature, it rather deposits a defined amount of energy per unit area.

As laid out in section 1.4, the function of thermal printing paper is currently (in almost all products) obtained by a thermo reactive coating, that forms a colored area from a leuco dye once heated beyond a certain temperature threshold. The use of potentially harmful chemicals in products of our daily lives is under constant scrutiny, be it by consumers, NGOs, or governments. Since the Bisphenol A (BPA), which was until recently the primary used developer in thermal paper, has been the focus of controversy due to its adverse effects as endocrine disrupter and potential other hazards, alternative methods to obtain thermo printable coatings have to be considered. This challenge has become significantly more pressing since BPA will be effectively banned EU-wide in thermal paper after 02.01.2020.[137] At prior stages of our work we observed, that coatings from HPC ester based nano particles showed high opacities, even at low coat weights (starting at 0.2 g/m²). This led to the hypothesis that it might be possible to use nano particles from polysaccharide based thermoplastics to create high opacity coatings on colored substrates, which could be molten locally to destroy the scattering centers and reveal the colored base paper. In initial trials, HPCC18DS3 nano particles were applied to black paper substrates and coat weights as low as 0.2 g/m² yielded an apparently white coating. As a proof-of-principle experiment, the coated paper was heated locally by an infrared laser to create the image displayed in Figure 5-1.

Figure 5-1: A coating of HPCC18DS3 nano particles (0.5 g/m²) on black cardboard. The coating was heated locally with a pulsed IR-laser (λ = 10.6 µm) depositing an energy of 0.3 mJ/mm². Through this, the highly opaque particle structure has been transferred into a translucent film, which in turn creates the impressing of a black image on a white background.

While this demonstration shows good potential behind this idea, the material exhibited a melting point at ~40°C. This would be extremely challenging in actual applications since paper machines need to remove the water, used as carrier for the coatings, with heat which leaves the material at temperatures typically between 50 and 70 °C when spun up onto the

tambour. Having a thermoplastic material in a molten state at this point of the process could, of course, lead to the formation of a massive block which essentially prohibits this route. In addition, the HPC derivative employed is not commercially available, which would pose a second major hurdle for industrial application. In a response to those challenges, the main requirements for coating materials that would be employed in this endeavor were formulated as:

1. thermal stability at process temperatures (T_m > 100 °C)
2. long term stability of the coating (to avoid unwanted coloring)
3. bio based material with thermoplastic properties, established on an industrial scale

Based on our own previous work on commercially available cellulose esters, we knew that a range of short chain CEs would exhibit thermoplastic properties and we had data to select the most promising candidate, which was a cellulose acetate butyrate (CAB) with a DS_{Ac} of 0.12, a DS_{Bu} of 2.62, a M_n of 30,000 g/mol, and a T_m of 141 °C. After this material had been identified as potential lead compound a method for the production of sufficiently concentrated – about 10–20 % by weight – nano particle dispersions on the 10–100 g scale had to be established. Based on the general procedures laid out in sections 2.2.3 and 3.2 it was suspected, that a direct precipitation of sufficiently diluted CAB could successfully produce nano particles. Furthermore, through engineering of the non-solvent it should be possible to induce partial aggregation to yield larger clusters composed of small structures, that would still scatter light similar to nano particles, but could be handled at higher concentrations without the risk of large scale aggregation. It was found, that a suitable system started with a 1 % (by weight) solution of CAB in THF. 1000 mL of this solution are precipitated in a mixture of 2800 mL isopropanol, 1200 mL distilled water, and 0.1 wt.% PVOH. After this, the resulting colloidal suspension is stirred for 24 hours to force the complete removal of solvent from the particles and foster partial aggregation, a process which is detailed with SEM imaging in Figure 5-2.

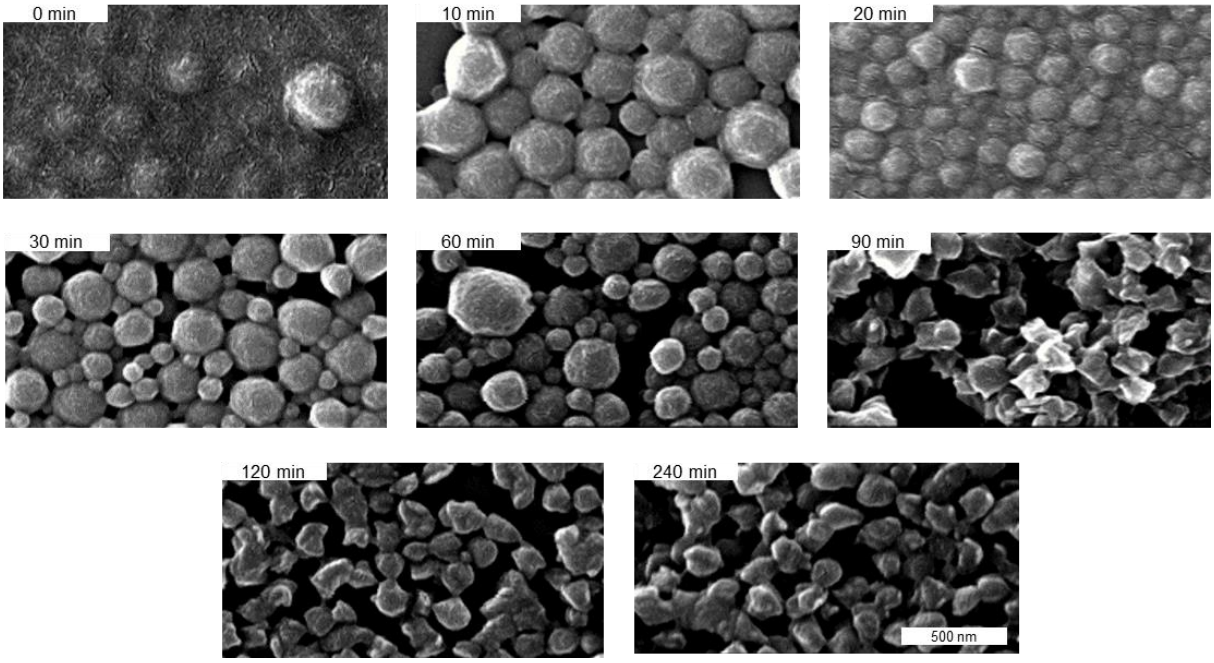

Figure 5-2: SEM images of dried samples taken from the CAB-precipitation solution at different times after the initial precipitation. It is evident, that at first (0 min) the particles still contain high amounts of solvent and disintegrate for the best part after evaporation of the surrounding medium. Subsequently the solvent is removed more and more which leads to roughly spherical particles after 60 minutes. Further curing then leads to irregular shaped particles which is a typical observation for short chain CE´s. Finally, the particles start to exhibit (wanted) partial aggregation after 2 h of stirring, since the mechanical energy supplied is sufficient to overcome the coulomb stabilization (section 3.2).

Subsequently, the formed particles would settle down to form a concentrated layer (~1–2 wt.%) at the bottom of the flask. After isolation by centrifugation, the particles could be successfully re-suspended in pure water to remove any residual organic solvent. This method could produce 40–50 g of CAB particles per day, but produced excessive amounts of solvent waste. Subsequent analysis revealed that the primary particle size (prior to aggregation) was comparable to the size of the previously used HPC-based particles. After this challenge was successfully overcome, the next step was to make a suitable coating. The general approach was to apply the formulation via blade coating to a model surface (structured Hostaphan® foil) and use the aforementioned IR-laser to apply defined energy amounts. Subsequently, the samples were analyzed via visible light microscopy (wide field). The primary challenge at this stage was to determine which coating additives were needed for the formulation to form a stable dispersion without unwanted large scale aggregation. Furthermore, the resulting coating has to form a mechanically stable film, as pure nano particles can easily be stripped off and must still exhibit a change in opacity after thermal treatment.

Over 200 formulations were evaluated, containing a broad range of typical coating additives, tuned to different pH-values (HCl, NaOH), ion concentrations (NaCl, $CaCl_2$), and solid content. During this work, synthetic binders from the Acronal® and Styronal® family by BASF were investigated. While some lead to large scale aggregation, one non-ionic styrene-butadien (SB) binder lead to stable films that are resistant to scratching and do not break when bent around a 1.5 mm radius. Furthermore, the use of partly hydrolyzed polyvinyl alcohol (PVOH) enabled us to control the viscosity, aid in binding, and stabilize the dispersion, hence this compound is acting in three roles at once. Subsequent analysis of the "optimized" coating revealed, that with coat weights below 10 g/m² the initial transparency

(according to DIN 53147) for visible light is below 40 % while the transparency values go up to 90 % after heating, yielding a good contrast, as illustrated in Figure 5-3.

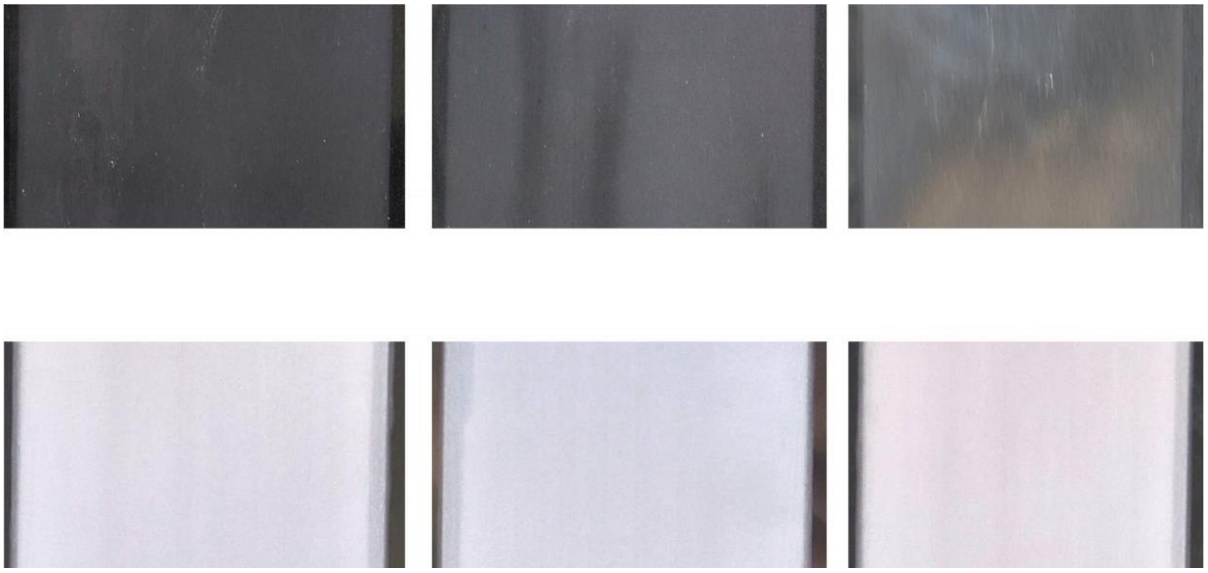

Figure 5-3: CAB-NP coated transparent Hostaphan® substrates on top of black cardboard (increasing coat weight from left to right). The top images show the material after heating above T_m, while the bottom row depicts the coatings in their native state.

During subsequent testing on a lab-scale thermal printer (Figure 5-4), it became obvious that continuous printing with this coating alone was not possible, because the coating would stick to the heating elements on occasion. This is attributed to the rather low printing speed of our setup (5 lines per second), which leads to excessive interaction between the polymer and the printing array. Nevertheless, this challenge has to be attributed in further work to yield a reliable product. It should be possible without too many issues via the addition of a transparent, flexible, non-thermoplastic layer as additional top-coating, but was beyond the scope of this project. As material of choice we identified siloxane coatings since they are already applied widely and release line on labels or adhesive tape.

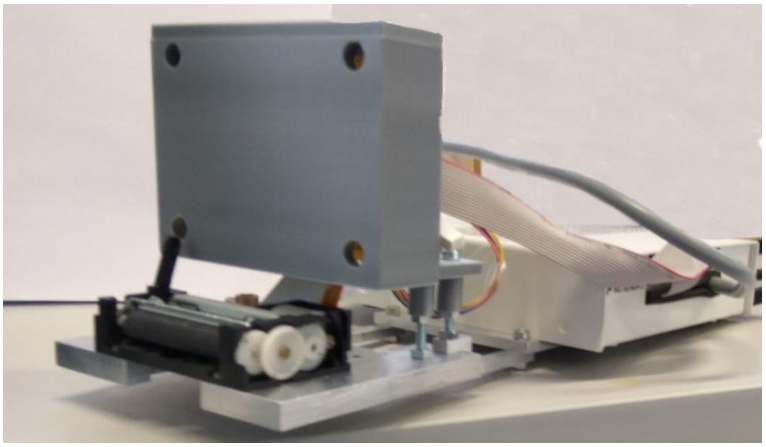

Figure 5-4: A lab-scale thermal printer based around a commercial printing unit, combined with purpose build electronics to interface with a computer running a custom LabView program to create the possibility for precise control of heating, dwell time, and speed.

In conclusion we demonstrated a facile way to produce a bio based coating with high potential for the application in thermal paper on the road to a more sustainable product, with a lower environmental impact.

5.2. Initial studies on oxidized hydroxypropyl cellulose

While oxidization of cellulose, with e.g. 2,2,6,6-Tetramethylpiperidin-1-yl)oxyl (TEMPO), is a well-documented and established technique, and even used commercially for the improvement of wound dressings (because of intrinsically low cell adhesion to oxidized cellulose), HPC has to the best of our knowledge not been investigated in the same manner. Since we found the literature lacking in this regards, we started to investigate if controlled oxidization of HPC is possible and what properties the oxidized HPC (HPC_{ox}) would exhibit.

In a first approach we investigated if the well-known Swern-oxidation, utilizing DMSO and oxalylchloride at low temperatures, would be capable to oxidize HPC in a controlled fashion. This strategy was chosen since the Swern oxidation is known to stop at the carbonyl stage and does generally not produce carboxylic acid moieties, which would leave us with the desired product. Unfortunately, the reaction, arguably because of too low reactivity of the reactive species, did not lead to oxidization of the HPC, which is why this route was quickly discarded.

Consequently, we considered the more aggressive TEMPO-mediated oxidation with sodium hypochlorite as illustrated in Figure 5-5. This reaction is carried out in a two phase system, where the oxidizing TEMPO species is present in a chloroform phase and HPC is dissolved in an aqueous phase. In combination with initially low reaction temperatures (0 °C) this method is comparably suitable for controlled oxidations. Additionally, in HPC almost all alcohol functions are present as secondary alcohols which intrinsically increases the barrier between the carbonyl and carboxyl reaction stage of oxidation.

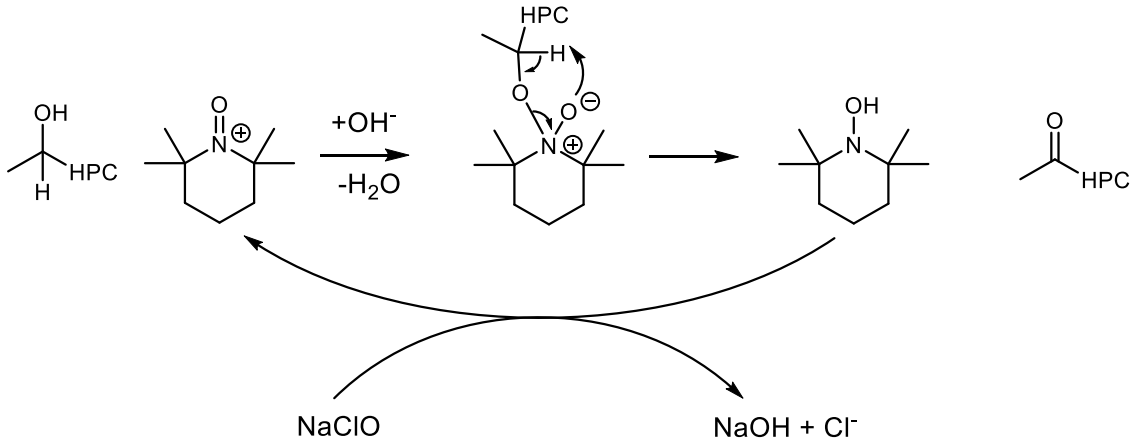

Figure 5-5: Schematic representation of the TEMPO mediated oxidation of HPC using sodium hypochlorite as oxidant. When carried out under heterogeneous, i.e. multiphase, conditions this route led to a degree of oxidation < 0.1 (according to ^{1}H-NMR analysis of a soluble fraction). The majority of the product remains insoluble in neutral water and can only be dissolved under acidic conditions, indicating a reversible crosslinking mechanism.

After isolation of the products and drying *in vacuo*, independent of the amount of oxidizer used, the product would not dissolve in any common solvent. When water was added, the product would swell by factor of 10–20, but it would not dissolve as demonstrated in Figure 5-6.

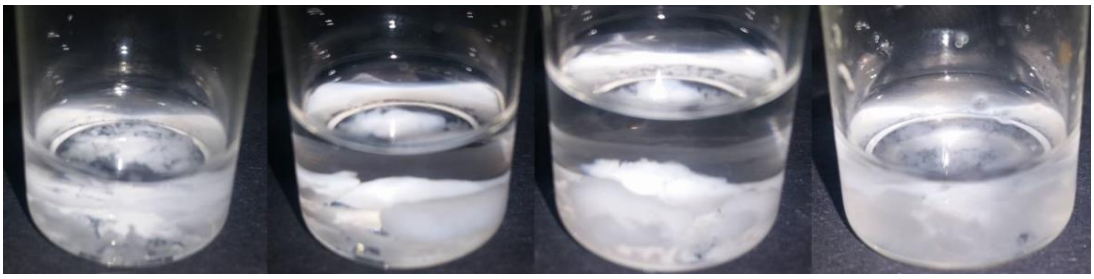

Figure 5-6: Examples of HPC_{ox} (produced with increasing amounts of oxidant from left to right) swollen in water. While there is no observable spontaneous dissolution, addition of 0.1 M acetic acid led to the formation of a homogeneous solution within minutes, further pointing towards a acetal/ketal based crosslinking between the polymer chains.

There were some "extractable" components, which were analyzed via ^{1}H-NMR and exhibited low (<0.1) degrees of oxidation. It was suggested, that the HPC_{ox} would auto-crosslink via the formation of ketal moieties (Figure 5-7). This was tested via the addition of 0.1 M acetic acid which readily dissolved the polymer within seconds. Subsequently, the now dissolved HPC_{ox} was re isolated, separated into two parts and dried *in vacuo* and under ambient conditions respectively. The sample dried *in vacuo* would again be cross-linked and only swell, revealing that this process was reversible, in contrast the sample dried under ambient conditions (for 240 h) did not exhibit the same behavior and was readily soluble in water without addition of any acid. This supports the hypothesis of ketal formation, because in the final stage of this reaction water is eliminated and thus the vacuum treatment would move the equilibrium to the product side.

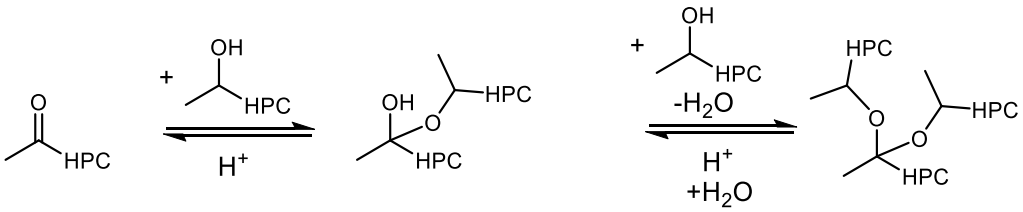

Figure 5-7: Proposed mechanism of the acetal/ketal formation involved in the reversible crosslinking of HPC_{ox}. Note that this reaction route would explain both core observations, drying induced network formation and acid induced re-dissolution.

An alternative explanation would be the aldol-reaction mechanism. This would however need a catalyst (basic or acid) to occur, which is not present, and no difference between the vacuum dried and ambient dried polymer would be expected, as no water is released during this reaction. Still, both hypotheses need to be addressed in the future.

At this point the project started to ask more questions than it answered, therefore we decided to start a stand-alone 3-year project to investigate the possibilities of HPC_{ox} in detail and explore further into the nature of its crosslinking, control and influence of D_{ox}, possible further derivatization, and finally potential applications. Nevertheless, this poses an interesting insight into the particular structure property relationships of HPC, comparable to the "inverted" reaction kinetics observed in section 4.1, because this behavior is completely different than the properties of oxidized cellulose. These, completely unexpected, properties originate simply from the fact that instead of the AGU-alcohol function, the reaction takes place on the hydroxypropyl moieties. The cause of this drastic change in outcome is beyond the scope of this work and will be studied within the mentioned follow-up project.

5.3. Cellulose based LCST-polymers as wet-end additive in paper production

The following section gives an overview of the results generated during the project INFOR 193 “Steigerung der Energieeffizienz bei der Trocknung von Papier und Papierstrichen durch intelligente, schaltbare Polymere”. This project was a cooperation between our working group and the “Papiertechnische Stiftung (PTS), Heidenau”, it was furthermore guided by a range of industry-partners from the “Verband Deutscher Papierfabriken e.V.” and the INFOR-council, which also provided funding.

Polymers that exhibit a miscibility gap in a given solvent at elevated temperatures are called lower critical solution temperature (LCST, Figure 5-8) polymers. In practice this describes, that at temperatures below the LCST the mixture is a homogeneous one phase system for all compositions, i.e. the minimum of the spinodal curve. But once the spinodal is crossed, the intramolecular interactions of the polymer chains start to dominate over the polymer-solvent interaction, which leads to the collapse of the solvated polymer chains, removal of the solvent, and subsequent phase separation.

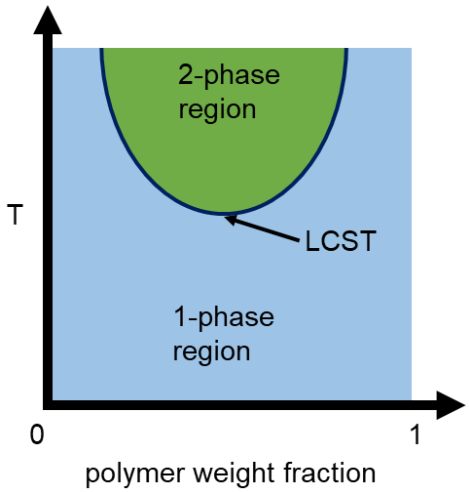

Figure 5-8: Location of the LCST in a schematically phase/temperature diagram for a polymer solution. If the system is heated above the spinodal curve, the solution demixes reversibly. This behavior can be exploited e.g. while dissolving bulk polymers, or in the case of this project, possibly to trigger the release of bound water.

During paper production drying has the highest demand on both energy and space consumption. Hence improving the drying efficiency is, from a process engineering perspective, of great interest to reduce cost and energy consumption. Typical optimization approaches focus on the mechanical drying part (vacuum dewatering and pressing) in the first step and heat reclaiming methods. In the first phases of thermal drying, the wet paper web is losing water at a constant rate through surface evaporation of the capillary water. After the capillary water is gone, the second stage begins, where water molecules that are bound to the fiber surface are removed, as illustrated in Figure 5-9. Our work focused on this later stage of the drying process, where the rate of drying decreases rapidly, because in addition to the isolated evaporation, the water has also to be dissociated from the cellulose fibers, which increases the required energy dramatically.

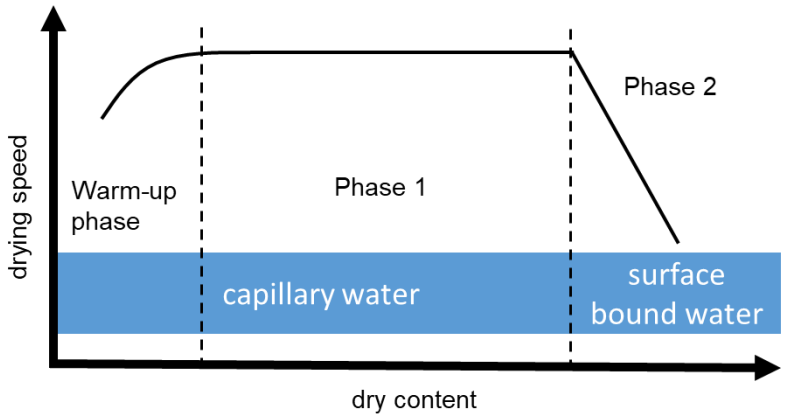

Figure 5-9: Schematic representation of the different drying phases encounter throughout the thermal drying process of a porous material like paper. Evidently the second phase is accompanied by a drastic decrease in drying speed, which is the direct result of an increase in the heat of evaporation due to the added energy needed do overcome the surface adsorption.

The aim of this project was to utilize LCST polymers in this final stage in an effort to remove bound water from the fiber surface by inducing a phase separation and thus convert the surface bound water to free water. To be useful in this fashion the LCST has to be in the temperature range present during the drying of 40 to 80 °C, which is covered by full synthetic polymers like e.g. PNiPAM and PMMA/OEG-copolymers.[158-159] Fortunately analogous LCST properties are also present in cellulose ethers like methyl, ethyl and hydroxypropyl cellulose.[160-161]

This led to the formulation of the following project goals:

1. Determination of the LCST of different CE´s
2. Analysis and optimization of CE retention in the wet-end application (with respect to different fiber materials)
3. Measuring and interpretation of drying curves with different:
    a. CE´s
    b. Application amounts
    c. Fiber materials

The selection of cellulose ethers was based on availability and focused on methyl, hydroxyl ethyl, and hydroxyl propyl (methyl) celluloses with different molar masses. Furthermore, HPC was modified with glycidyltrimethylammonium chloride to yield a permanently charged derivative for better retention. While some LCSTs for these materials are listed in literature, we decided to perform measurements on our own to guarantee reliable data. The LCSTs were determined with a combination of a photometer and a precision temperature probe, both monitored via a camera for convenience. The setup and results are displayed in Figure 5-10 and show some discrepancies between literature data and the obtained values, which can be explained by the influence of different substitution patterns and molecular weights. Note that the values obtained for HEC could not be obtained from a decrease in the photometers signal but had to be determined visually. This is due to the effect, that HEC solutions does not become cloudy, like it would be the case for the other CEs but formed large solid aggregates

when the temperature exceeds the LCST. In general, higher LCST temperatures are more favorable, since this infers, that the effect will occur later in the drying process, focusing it on the bound water.

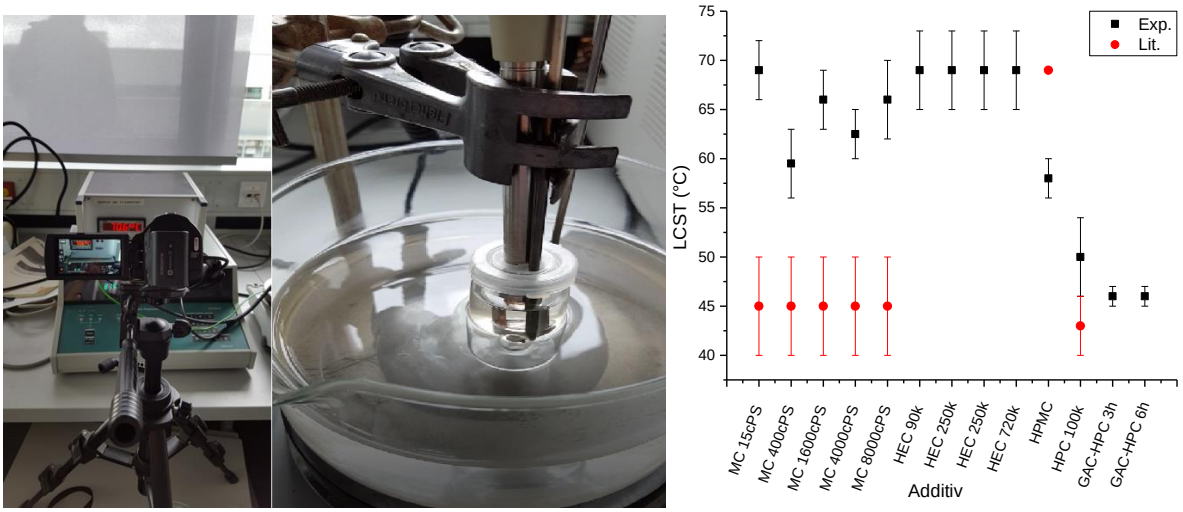

Figure 5-10: Setup used for the determination of the LCSTs exhibited by aqueous solutions of different cellulose ethers, comprised of a heated bath, a precision temperature probe, a photometer and a camera for data acquisition (left and center). Data generated using this setup (right).

As for the fiber material we selected short (SF) and long (LF) ground fibers and a mixture of both materials (SFLF) to mimic typical fiber materials used in industrial applications. The SF was composed of eucalyptus, while the LF was a blend of pine and spruce. Subsequently the retention rate, i.e. the amount of material present in the final paper (inferred from gravimetrical white water analysis) divided by the amount added to the process water was analyzed. This trial yielded broad range of results, starting with HPMC, which showed practically no retention, up to high molecular weight HEC, with a retention of almost all the material. In general retention rates rose with molecular weight, which is in agreement with prior work on polymer additives in paper.

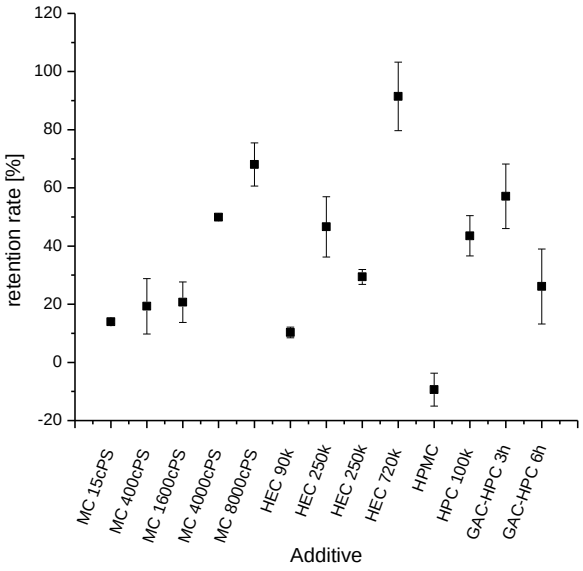

Figure 5-11: Determination of the respective retention rates exhibited by different LCST-CE´s, when the material is applied in the wet-end of a lab-scale paper production process.

Based on this, selected CE´s were analyzed towards their influence on the drying process. Since the addition of CE´s reduced the initial water content in all cases, it was deemed necessary to compare relative drying rates rather than absolute values, because absolute comparisons would always be skewed by effects of primary water retention and thus obfuscate any real effects. In these trials a laboratory scale for dry content determination with an IR-heater was used, to streamline and speed up the process, which was necessary due to the amount of tests required.

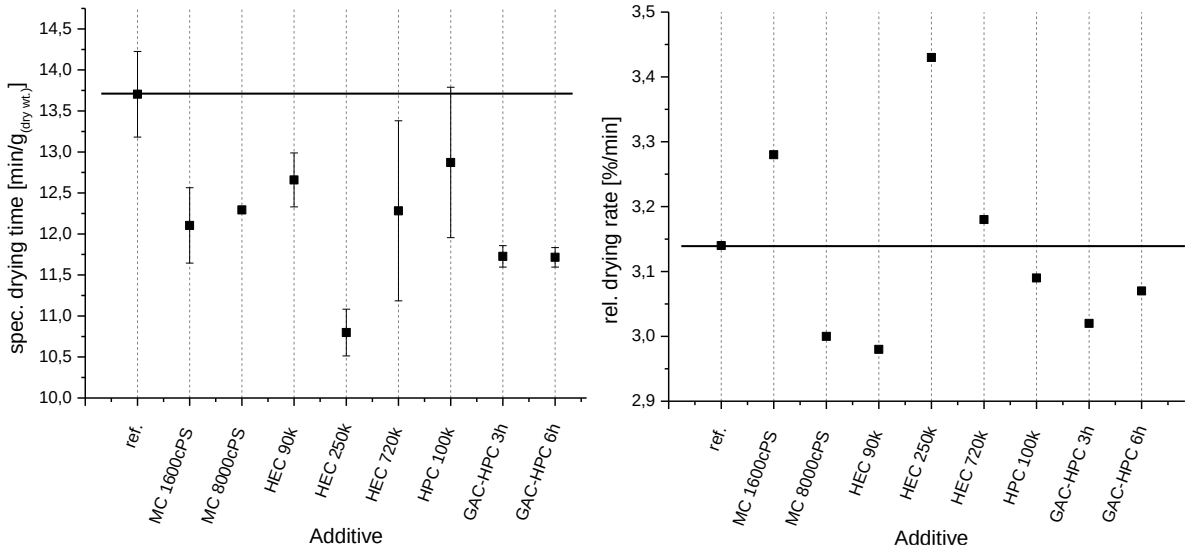

Figure 5-12: Analysis of the influence of different LCST-CEs on the drying behavior of papers. Both graphs are based on the same dataset. While the left graph shows absolute values, indicating that all polymers exhibit a positive influence on the drying process, when one is taking into account the changes in initial moisture content and thus comparing relative drying rates (right), it becomes obvious that only three promising candidates remain.

With this knowledge MC1600 Cps, HEC 250k, and HEC 720k were identified as lead components for further study using a Rapid Köthen sheet former. These “sheet former trials” were carried out in a way that for every sample (i.e. combination of fiber material and cellulose ether in a given concentration) 11 papers with a grammage of 80 g/m²were formed. Every one of these papers was dried for a specific time (0, 30, 60, 120, 180, up to 600 s) and for every sample the residual water content was analyzed via the aforementioned scale for dry content determination, providing the data for numerical analysis based on Figure 5-13.

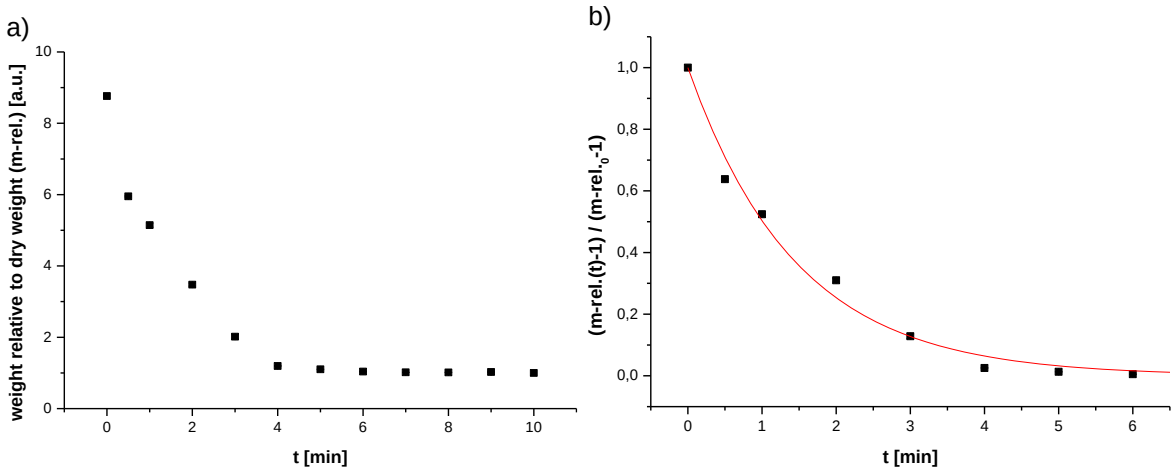

Figure 5-13: a) Example of a residual moisture curve, as produced by the trials run on a Rapid Köthen sheet former. b) Plot of the mass relative to the dry mass (m-rel.) normalized to the initial mass relative to the dry mass (m-rel.$_0$). These examples both show SF-material, with the addition of HEC 720k (5 wt.-%).

The aim of this study was to gain insight into possible effects that LCST polymers could generate in a more real world like drying process. This is mimicked through the use of a Rapid Köthen sheet former, that is equipped with a drying system far more reminiscent of an industrial drying than an enclosed IR-heated dry scale, but does under no circumstances replicate the exact conditions present on a paper machine. Based on the aforementioned data, the residual relative moisture content is calculated and plotted as shown in Figure 5-13 b. Since this follows the basic exponential decay function (equation 1), the exponential decay constant (equation **1**, parameter **b**) can be acquired via numeric fitting, with the parameters **a** and **c** fixed at 1 and 0, to represent the initial and final relative moisture content. The parameter **b**, henceforth referred as relative residual drying rate (RRDR), was determined for all three fiber materials, in combination with the three selected polymers in relative concentrations (polymer wt./ dry fiber wt.) of 5 and 10 % respectively.

$$\frac{m-rel.(t)-1}{m-rel._0-1} = a * e^{-tb} + c \qquad (1)$$

In comparison to the fiber material without additives, Figure 5-14 shows that all three polymers, in both concentrations, improve the drying performance of all three fiber types. The general improvement with an increase in concentration of the polymers is consistent with the retention rates displayed in Figure 5-11. MC 1600 Cps, and HEC 250k showed similar retention rates (in the 30 % range) and show similar improvement of the RRDR when the concentration is doubled. HEC720k however exhibited almost complete retention and hence shows no significant improvement when the concentration is increased. This leads to the conclusion, that for HEC 720k the fibers are already loaded completely at 5 wt.%.

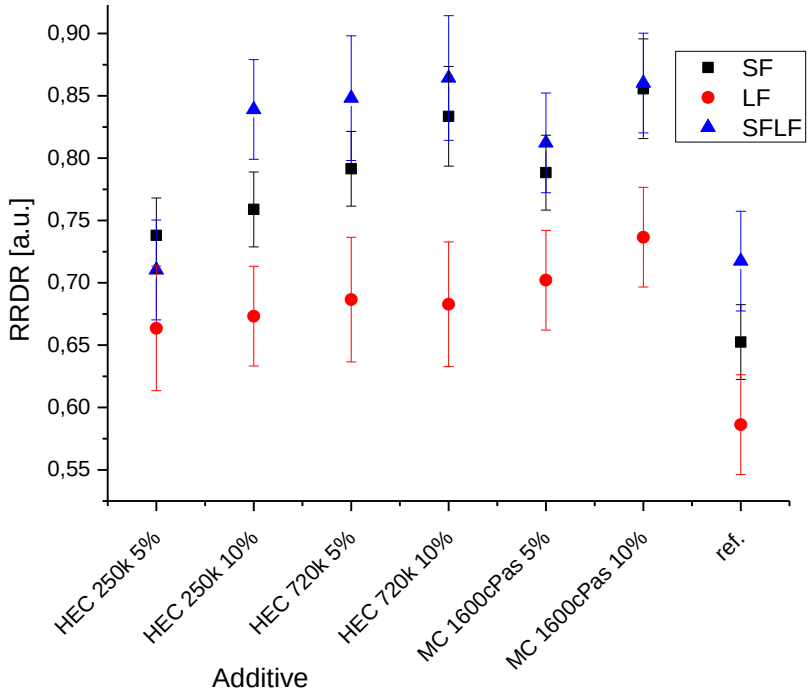

Figure 5-14: The relative residual drying rate, based on the numerical analysis of the drying experiments in Figure 5-10 b show that all three lead-polymers improve the dying rate, compared to the reference paper without additive. The effect is present for all three fiber materials, but is most prominent in short ground fibers (SF).

Due to practical limitations, i.e. viscosity related challenges, only HEC 250k and MC 1600Cps were analyzed on a pilot machine. Unfortunately, despite the promising lab scale results, the polymer additive lead to some issues on the paper machine. Foaming, which had been of minor concern in lab trials became an apparent issue on the larger scale machine, which would have to be addressed by addition of surface active agents, which would most likely impede fiber coverage. In addition, the vacuum applied in the lab scale coater was considerably higher compared to the pilot machine, this in conjunction with an increased viscosity led to challenges in the initial drying stages and a 3 % higher initial water content when the web was transferred to the heated drying rolls, in opposition to the lab scale experiments. The combination of these phenomena led to improper sheet formation and inhomogeneous fiber mats. Based on this findings additional research will have to be devoted to the transfer of this concept and to investigate, if the system can be applied to an actual production line as drop-in solution. While this is beyond the scope of this work, we successfully demonstrated that the core idea was feasible and, at least on a laboratory scale, led to an improvement in the drying properties of model-papers.

6. Summary and Outlook

During the past decades, humanity has been relying more and more on fossil based polymers in every aspect of our daily life, starting in the use as packaging materials and commodity items, over specialized barrier coatings and widespread use as high performance, low weight structural components up to essential components in medical diagnostics. Despite the immeasurable positive effect of this widespread use of crude oil based chemistry had on mankind, we have to take a hard look into the possible ramifications that a continuation of this course of action would entail. For one, crude oil will run out, even by optimistic estimations, before the end of this century given our current rate of consumption and the remaining reserves. Secondly, as of now there are already unacceptable amounts of non-biodegradable polymers released into our environment, with no natural way of decomposition, excluding painstakingly slow UV-degradation. This has sparked research into a range of approaches to produce bio-based and ideally biodegradable polymers in an effort to replace petrochemical compounds and make way to a truly closed loop economy. Notable materials in this area are polyesters like poly lactic acid and polyhydroxyalkanoates, starch derivatives, cellulose based materials like cellulose acetate (ester) or carboxymethyl cellulose (ether), and even protein based compounds. The industrial impact and thus the effect on the real world has been growing constantly with increasing prices, both monetary and environmentally, that are associated with crude oil based polymers.

Based on these developments, the need for novel bio based polymers is also increasing, which has led to a surge in research regarding functional materials derived from sustainable sources. While most of the approaches in literature are focused on a specific functionality or specific physicochemical properties, we were intrigued by the question, what could be done with a given bio based material, i.e. hydroxypropyl cellulose (HPC), through simple and straightforward modification. This shift in focus from the product to the range of possible properties that could be generated with HPC as starting material, led to the formulation of our main goals.

The main focus of this work was, in brief, to establish a good understanding of the reaction kinetics and behavior of HPC during esterification with different acid chlorides, ranging from unsaturated 10-undenoic acid to stearic acid. Once this was well understood and controlled, the materials were used in an effort to crate tailored functional interfaces aiming for the discovery of possible applications and further utility. To this end both, classical surface coating techniques, including blending, additivities, and different application methods as well as photolithographic methods were utilized, which finally led to a range of proof-of-principle and proof-of-concept stage demonstrations creating, superhydrophobic (section **4.1**) and photoresponsive (section **4.2**) coating materials, surface attached networks with tunable polarity (section **4.3**), thermo-optical coatings, coatings with tunable friction properties (section **4.4**) and finally in a spin-off cooperation Janus type membranes (section **4.5**).

To gain systematic knowledge about the esterification of HPC with fatty acid chlorides, a task the literature has until now failed to address comprehensively, we studied the reaction behavior of HPC with stearic acid chloride (model reactant) under different (homogeneous) reaction conditions and established neat and dry THF as best reaction medium with regards to toxicity, workup and reaction speed. This optimized system was then used to study reaction kinetics of HPC esterification with different fatty acid chlorides as mentioned above. The resulting polymers were studied via conventional ^{1}H-NMR analysis, which was correlated with

elemental analysis to result in a reliable and precise data-set. We found the exact inversion from the expected trend in reaction rates, which was that short chain acid chlorides would result in the fastest reaction. This was attributed to the coil-widening effect of longer chain substituents, which was further backed up by a reference experiment utilizing halfway modified starting materials. Using fully modified HPC stearic acid ester we were able to create nano particles via a precipitation process. To generate functional paper coatings, we used spray coating as a facile application method, which would allow us to deposit minimal amounts of the materials and thus to generate super hydrophobic coatings. Interestingly, these coatings were thermo responsive which, after heating, inferred a strong change in the wetting behavior, i.e. the contact angle would decrease to become just hydrophobic. This was, through SEM-Imaging, determined to be caused by the loss of the particle structure and formation of a comparatively flat surface.

Starting from this stimulus-responsive coating we were highly interested in the addition of a second, orthogonal, stimulus to generate a system which could be switched between multiple states independently. This was achieved through the targeted synthesis of different donor acceptor Stenhouse adducts, which exhibit a strong change in polarity, from a non-polar, hydrophobic state to a charged, polar state upon irradiation with visible light. In the endeavor we first established the fastest reaction system to produce the desired derivatives, based on UV-Vis monitoring of a model reaction and kinetic analysis. Subsequently, three derivatives of interest with different alkyl-substituents were synthesized, characterized by means of NMR-spectroscopy and added to the existing nano-particle dispersion, respectively. The rationale behind this was to get the alkyl-substituents on the DASA to associate to the nano-particles via van der Waals interaction which would expose the polarity-switching domain towards the surrounding medium. The formulations with different amount of the respective DASA were then coated onto paper substrate, as before, and partially illuminated. Subsequent contact angle analysis revealed, that the addition of di-dodecyl-substituted DASA in fact produced surfaces that would be initially super hydrophobic and would become exceptionally hydrophilic after illumination. Dynamic CA analysis further showed that the switching occurred within 7 seconds after illumination, proving a fast reaction of this system. The now hydrophilic material could subsequently be switched thermally to become hydrophobic again, leading to an orthogonally controllable wetting system. In future work such surface coatings could possibly be utilized in microfluidics or dosing system that are using an *off-on-of* switching sequence.

These first investigations spawned several branches in this work, the first point of interest was, that we noted a strong change in the optical properties of HPC stearic acid ester nano particle coatings when they were heated above T_m. Initially the NP coatings exhibited an exceptional opacity, even coat weights below 1 g/m² were able to cover a black cardboard in a way that made it appearance white, caused by the abundance of scattering centers presented by the particles. After heating above T_m the particulate structure is disintegrated, leading to the formation of a film, that is transparent to visible light. While this was an interesting find on its own, at the time we were not too concerned about this discovery. Someway down the road we were approached by the Papierfabrik August Koehler, a specialty paper manufacturer who is, next to other paper based products, the world leading manufacturer of thermal printing paper. The possibility to create thermal printing paper based around bio-based nano particles and their change in opacity was at this point quiet intriguing to both parties, which is why a cooperation project was started. Unfortunately, initial

investigations swiftly revealed, that the HPC ester based particles were, beyond the proof-of-principle stage, unsuitable for this application due to the comparatively low T_m of 38 °C. Based on this, we screened existing, commercially available, bio based polymers and found the mixed cellulose ester containing acetic and butyric acid (CAB) substituents to be a potential alternative. This material, in the given composition, exhibited a T_m at 141°C, meaning it would for all intents and purposes be stable under normal environmental conditions, even on a dashboard under direct sunlight and during the paper manufacturing process, where temperatures may reach 100 to 120 °C. Furthermore, commercial thermal printers would still be able to trigger the needed phase transition. In consequence we developed a novel precipitation protocol to form nanoparticles from this material in an effort to generate optical properties. The final process used a solution of CAB in THF, which was precipitated into an isopropanol/water mixture containing PVOH to increase colloidal stabilization. This process enabled us to produce roughly 40-50 g CAB nano particles per day using conventional lab equipment. After exchanging the dispersing medium for water, coating color formulations were developed using different pH-values (HCl, NaOH), ion concentrations (NaCl, $CaCl_2$), solid content and binders to improve the film stability. Coatings made from these formulations were analysed using an IR-laser to deposit amounts of energy comparable to a commercial thermal printer, the differences in opacity, i.e. contrast, between the molten and the particular areas were evaluated using a microscope and grey scale analysis, as well as a transparency tester for larger samples. The best coating (highest contrast and mechanical stability) exhibited a change in transparency from below 40 % to over 90 %. In succession to this work a 3-year project was started with the aim to improve the performance further, especially through optimization of the phase transition, but also considering different approaches focused on the generation and thermal destruction of high opacity coatings. This could for instance be achieved through a polymer blend that exhibit reversible phase separation.

Subsequently we investigated another interesting use of HPC stearic acid esters during an international cooperation involving Stefan Spirk (Institute of Paper, Pulp and Fiber Technology, Graz University of Technology, Austria), Christian Teichert (Institute of Physics, University of Leoben, Austria), and Tiina Nypelö (Chalmers University of Technology, Sweden). We discovered, that the combination with trimethyl silyl cellulose and subsequent regeneration led to phase separated film with tunable morphology. This in turn gave control over the friction properties (analyzed via FFM) and the surface roughness. Combination of AFM and AFM Imaging revealed fundamental changes in the surface depending on the material composition, starting with protrusions of HPC ester from a cellulose matrix (3 parts TMSC and 1 part HPC ester) and ending with the inverted picture of cellulose cavities in a HPC ester matrix (1 part TMSC and 3 parts HPC ester). Correlation of the surface roughness with the obtained friction forces demonstrated, that the surfaces with the highest roughness (1 part TMSC and 3 parts HPC ester) exhibited the lowest friction coefficient and vice versa. Finally, the non-specific adsorption of protein (BSA as model) on the different surfaces was investigated via SPR and QCM-D. The low non-specific adsorption of pure cellulose could be increased gradually through the blending with the HPC ester, and we were able to determine that the surface free energy (SFE) was the dominating factor that influenced the adsorption. The correlation between surface free energy and blend-composition was not linearly correlated to the SFE, which is attributed to non-linear phase separation and strong changes in the films morphology depending on the composition. These bio-derived blend materials

could be of use in protein assays (i.e. laminar flow assays) to tune protein retention and absorption for localized increasing of analyte concentrations.

To extend the range of possible uses for HPC derivatives we modified the base polymer further using unsaturated 10-undenoic acid, which left us with a hydrophilic, water absorbing polymer that contained unsaturated side chains. This work was complemented by addition of stearic acid substituents, which in turn yielded a hydrophobic polymer containing unsaturated moieties. We then investigated different approaches to crosslink these compounds utilizing two photo-radical generating species, benzophenone (BP, λ_{ex}: 235 nm or 365 nm) and 4,4′-Bis(diethylamino)benzophenone (DEABP, λ_{ex}:405 nm) that could be excited by different light sources. During these trials we found, that DEABP could very efficiently be excited by a cheap and abundant 405 nm-laser, a device commonly found in blue-ray-players. This enabled the use of a x/y movement system in combination with the aforementioned laser diode and an electronic control unit to generate spatially fine resolved (spotsize $\sim$ 50 μm) polymer-networks trough lithographic means without the need for a stencil or photomask. Furthermore, the illumination time to initiate the crosslinking reaction could be dramatically reduced to 5-30 ms, compared to the illumination trough a conventional UV-lamp, which is needed for BP-based systems, and ranges in in the order of 10 minutes. This reduction is possible because of the very high energy flux, which is provided by the laser beam (100 J/cm²s) compared to the 254 nm UV lamp (0,030 J/cm²s). Analysis of the swelling behavior was carried out using a confocal laser scanning microscope. We facilitated this method through the modification of glass slides with allyl triethoxysilane, in an effort to generate an anchor point for the polymer network. These slides were subsequently dip coated with a solution of the polymer and DEABP to generate a thin film on the surface. In the next step the coated glass slides were illuminated with the laser-system for different amounts of time to generate the network, and finally rinsed with solvent to remove excess polymer. For the actual swelling analysis, the CLSM scans a single row of pixels while moving the sample in z-direction. Through the fast operation of the system it is possible to capture a live video of the cross-section during the swelling process, which revealed, that for low netpoint densities the swelling followed a first order kinetic, which demonstrates, that in this configuration the swelling is controlled by the diffusion of the solvent. High crosslinking densities (i.e. longer illumination times) in turn led to a more complex kinetic, which was the result of hindered diffusion when solvent migrates to the lower areas of the network, necessitation it to pass through the already swollen, highly crosslinked gel. The netpoint density, and thus the swelling behavior could be adjusted through modulation of the laser-illumination time, which led to degrees of swelling between 2 and 6, relative to the dry materials, corresponding to netpoint densities between about 2 μmol/cm³ and 180 μmol/cm³. In a proof-of-principle experiment we generated two microfluidic channels, which each contained one patch of hydrophobic and hydrophilic polymer, respectively. Both channels were then flooded with a solution of pyrene in water and monitored under UV-light to determine the distribution of this model pollutant via grey value analysis of the obtained images. It was revealed that the hydrophilic patch did not affect the pollutant in any way, which was to be expected. The hydrophobic patch on the other hand was able to extract the pyrene, at least partially, which was evident through a reduction of the grey-value between the areas located before and after the patch of 27 %. In the future, it should be investigated if, through tuning of the netpoint density, these polymer gels could be adjusted to selectively bind different analytes, e.g. bio macromolecules or to yield variable spots for live cell adhesion.

As mentioned above, a range of research-paths was spawned by the initial investigations on HPC ester coatings. The earlier trials using DASA-modified HPC ester nanoparticles sparked the interest of the group of Annette Andrieu-Brunsen (Technische Universität Darmstadt, Germany) who is specialized in (porous) silane based surface coatings and membranes. A cooperation project with the goal to incorporate DASA modified silanes in silane based coatings on paper was started, and we began with reference experiments using a plain TEOS dip coating solution and eucalyptus paper made in the laboratory. During this initial test we found that the paper sheets, after the silane was cured at 130 °C to form silica, were becoming hydrophobic on one side while remaining hydrophilic on the other, essentially creating a Janus-type membrane. This was quiet surprising as both components of this system, the paper and the silica coating, are intrinsically hydrophilic. Further investigation into the matter revealed that the hydrophobic side of the paper faced upwards during the curing process and the hydrophilic side faced downwards. To analyze the silica distribution, Rhodamine B was added to the TEOS solution as a fluorescent label and the process was repeated. The labeled sample was embedded in a resin and sliced to yield cross sections which could be analyzed in the CLSM to yield information about the relative silica distribution, which revealed that the hydrophobic top surface exhibited a significant higher amount of silica deposition, indicating that the curing process causes the TEOS to migrate fast to the top, than to the bottom due to faster solvent evaporation. This was confirmed via the complementary curing of another sample set under vacuum, eliminating the differences in evaporation rate, which led to samples that for one were hydrophilic on both surfaces and did not exhibit a significant difference in silica deposition when comparing top and bottom. Furthermore, the TEOS concentration of the dip coating solution was altered in both directions to alter the absolute amount of deposited silica. The coatings with low TEOS concentrations led, without regard for the curing method, to hydrophilic surfaces on all sides, while all surfaces of the trials with high TEOS concentrations were hydrophobic. Now it became clear, that there had to be a threshold amount of coating that has to be exceeded to generate the de-wetting properties. To access this value, we carried out thermo gravimetric analysis to determine the absolute amount of deposited silica, through correlation with the CLSM data of the distribution we were able to calculate that the threshold is located somewhere between 1.85 and 2.05 % silica relative to the fiber mass. In conjunction with the control of the silica distribution even lower absolute silica amounts (as low as 1.6 %) are enough to generate a hydrophobic paper. Given typical paper fiber surface areas (1 to 6 m^2/g) these amounts of silica translate to exceptionally low coating thicknesses somewhere in the range of 10 to 70 nm on the fiber surface. Most intriguingly the Janus-type membrane was able to separate oil and water, which was demonstrated using colored liquids. Materials that are capable of these type of tasks are conventionally creates by laborious multi step processes, involving perfluorinated compounds and polymer membranes. Our process on the other hand results essentially in paper sheets coated with sand and is completed in a single and easy to perform step, which led to a patent application and publication.

In summary this project led to a process that would be easily scalable to industrial application. Further work on this topic will have to focus on detailed investigation of the microstructure on the silica on the fiber surfaces, e.g. via TEM after removal of the cellulose through dissolution. Another point of interest is the effect of partial silica coating on the microfluidic properties of the papers and the possibility to tune adhesion of analytes or tune flow rates via adjustment of the silica amount.

7. Experimental Part

In this section the experimental procedures utilized in the part of the thesis outside of the cumulative part will be presented. For the procedures utilized in the cumulative part, the reader is referred to the respective publications.

7.1. Reagents and Solvents

Acronal®	BASF
Acetic acid	Fisher, 97 %
Bovine serum albumin	Sigma-Aldrich, >95 %)
$CaCl_2$	Grüssing, 99 %
$CDCl_3$	Sigma Aldrich, 99.8 %
Chloroform	Roth, 99 %
Cellulose acetate butyrate	Sigma-Aldrich
Deuterium oxide	Sigma-Aldrich, 99.8 %
Didodecylamine	Fisher, 97 %
Diethylamine	Roth, 99 %
Dihexylamine	Acros Organics, 98 %
Diisopropylethylamine	Fluka, 99 %
4-Dimethylaminopyridine	Sigma-Aldrich, 99 %
Dioctadecylamine	TCI, 99 %
Disodium phosphate heptahydrate	Sigma-Aldrich, >99 %
Glycidyltrimethylammonium chloride	Sigma-Aldrich, >90 %
Hostaphan®-film	Mitsubishi HiTec
Hydrochloric acid	Sigma-Aldrich, 37 %
Hydroxyethyl cellulose 90k	Sigma-Aldrich
Hydroxyethyl cellulose 250k	Sigma-Aldrich
Hydroxyethyl cellulose 720k	Sigma-Aldrich
Hydroxypropylmethyl cellulose	Sigma-Aldrich
Hydroxypropyl cellulose	Alfa Aesar, M_w 100.000 g/mol
Lauric acid chloride	Acros Organics, 98 %
Methanol	Brenntag, technical grade
Methyl cellulose 1600 Cps	Alfa Aesar
Methyl cellulose 8000 Cps	Alfa Aesar
Molecular sieve	Roth, 3 Å
Myristic acid chloride	Aldrich, 97 %
n-Hexane	Brenntag, technical grade
Palmitic acid chloride	Merck, 98 %
2-Propanol	Brenntag, technical grade
Propionic acid chloride	Acros Organics, 98 %
Pyridine	Fisher, 99 %
ROPAQUE™ AF-1570	DOW

Sodium dihydrogen phosphate monohydrate	Sigma-Aldrich, >99 %
Sodium hydroxide	Grüssing, 99 %
Sodium hypochlorite (6-14% active Cl_2)	Merck
Stearic acid	Merck, 97 %
Styronal®	BASF
Tetrahydrofuran	Roth, 98 %)
(2,2,6,6-Tetramethylpiperidin-1-yl)oxyl	Sigma-Aldrich, 98 %
Thionyl chloride	Sigma-Aldrich, 97 %
Toluene	Sigma Aldrich, 99.9 %
Triethylamine	Roth, 99 %
Trimethylsilyl cellulose	Avicel, M_w 185000 g mol^{-1}, M_n 30400 g mol^{-1}

THF (Roth, 98 %) and chloroform (Roth, 99 %) were dried according to standard procedures, stored over molecular sieve 3 Å and under argon atmosphere. All chemicals were, if not explicitly otherwise stated, used as received.

7.2. Paper Modification and Analysis

7.2.1. Preparation of nano particle dispersions from cellulose acetate butyrate

2800 mL isopropanol and 1200 mL distilled water are placed in a 5000 mL beaker. At room temperature, 1000 mL of a 1 wt-% THF-containing cellulose acetate butyrate solution are added from a separating funnel. The precipitation of particles begins with a blue coloration of the solution, which is characteristic for nanoprecipitation. After complete addition, the suspension is stirred for a further to complete solvent exchange. After sedimentation of the particles, the supernatant is decanted and the suspension separated at the centrifuge. The particles are rinsed twice with distilled water and separated again at the centrifuge. The solids content is determined using a dry balance. For observation of the temporal development of the particles after precipitation samples are taken at appropriate intervals (10 to 30 min).

7.2.2. Engineering of coating color formulation using CAB nano particles

To retain comparability all coating color formulations are adjusted to a solid content of 11.75 % and an absolute particle content of 100 mg. The formulations (Table 7-1 through Table 7-26) are evaluated with regards to coating homogeneity, runability and opacity.

7.2.3. Compositions of investigated formulations

Table 7-1: Reference formulation with variation of binder content.

Sample	Ropaque AF 1570 [mg]	Ropaque AF 1570 [µL]	Binder [mg]	Binder [µL]	H_2O [µL]
1	100	558	75	147,4	1525,8
2	100	558	50	98,3	1256,2
3	100	558	25	49,1	986,6
4	100	558	15	29,5	878,7
5	100	558	5	9,8	770,9

Table 7-2: Addition of variable salt (NaCl) content.

Sample	Particle [mg]	NaCl [µL]	H_2O [µL]
6	100	50	825
7	100	125	750
8	100	250	625
9	100	375	500
10	100	0	875

Table 7-3: Addition of variable salt ($CaCl_2$) content.

Sample	Particle [mg]	NaCl [µL]	H_2O [µL]
11	100	25	850
12	100	50	825
13	100	125	750
14	100	250	625
15	100	375	500

Table 7-4: Addition of variable salt (NaCl) and binder (Styronal®) content.

Sample	Particle [mg]	NaCl [µL]	Binder [mg]	Binder [µL]	H_2O [µL]
16	100	50	1	11,8	714,2
17	100	125	2	23,6	640,1
18	100	50	2	23,6	715,1
19	100	125	1	11,8	581,8
20	100	25	1	11,8	681,8
21	100	25	2	23,6	682,8

Table 7-5: Addition of variable salt ($CaCl_2$) and binder (Styronal®) content.

Sample	Particle [mg]	$CaCl_2$ [µL]	Binder [mg]	Binder [µL]	H_2O [µL]
22	100	25	75	147,4	1536,1
23	100	25	50	98,3	1266,5
24	100	25	25	49,1	996,9
25	100	25	15	29,5	889,0
26	100	25	5	10	781,2

Table 7-6: Addition of variable salt (NaCl) and polyelectrolyte (Lupamin 9010®) content.

Sample	Particle [mg]	NaCl [µL]	Lupamin 9010 [mg]	Lupamin 9010 [µL]	H_2O [µL]
27	100	25	75	490,2	1146,9
28	100	50	75	490,2	1121,9
29	100	75	75	490,2	1096,9
30	100	125	75	490,2	1046,9
31	100	25	50	326,8	991,6
32	100	50	50	326,8	966,6
33	100	75	50	326,8	941,6
34	100	125	50	326,8	891,6
35	100	25	25	163,4	836,2
36	100	50	25	163,4	811,2
37	100	75	25	163,4	786,2
38	100	125	25	163,4	736,2

Table 7-7: : Addition of variable salt (NaCl) and polyelectrolyte (Lupamin 4500®) content.

Sample	Particle [mg]	NaCl [µL]	Lupamin 4500 [mg]	Lupamin 4500 [µL]	H_2O [µL]
39	100	25	75	579,2	1234,2
40	100	50	75	579,2	1209,2
41	100	75	75	579,2	1184,2
42	100	125	75	579,2	1134,2
43	100	25	50	386,1	940,4
44	100	50	50	386,1	915,4
45	100	75	50	386,1	890,4
46	100	125	50	386,1	840,4

Table 7-8: Addition of variable salt ($CaCl_2$) and polyelectrolyte (Lupamin 4500®) content.

Sample	Particle [mg]	$CaCl_2$ [µL]	Lupamin 4500 [mg]	Lupamin 4500 [µL]	H_2O [µL]
47	100	25	75	579,2	1234,2
48	100	50	75	579,2	1209,2
49	100	75	75	579,2	1184,2
50	100	125	75	579,2	1134,2
51	100	25	50	386,1	940,4
52	100	50	50	386,1	915,4
53	100	75	50	386,1	890,4
54	100	125	50	386,1	840,4

Table 7-9: Addition of variable salt ($CaCl_2$) and polyelectrolyte (Lupamin 9010®) content.

Sample	Particle [mg]	$CaCl_2$ [µL]	Lupamin 9010 [mg]	Lupamin 9010 [µL]	H_2O [µL]
55	100	25	75	490,2	832,9
56	100	50	75	490,2	807,9
57	100	75	75	490,2	499,7
58	100	125	75	490,2	449,7
59	100	25	50	326,8	557,8
60	100	50	50	326,8	532,8
61	100	75	50	326,8	507,8
62	100	125	50	326,8	457,8
63	100	25	25	163,4	565,8
64	100	50	25	163,4	540,8
65	100	75	25	163,4	515,8
66	100	125	25	163,4	465,8

Table 7-10: Addition of variable polyelectrolyte (Lupamin 4500®) content.

Sample	Particle [mg]	Lupamin 4500 [mg]	Lupamin 4500 [µL]	H_2O [µL]
72	100	75	579,2	941,9
73	100	50	386,1	816,2
74	100	25	193,1	690,5
75	100	15	155,8	640,2
76	100	5	38,6	589,9

Table 7-11: Addition of variable polyelectrolyte (Lupamin 9010®) content.

Sample	Particle [mg]	Lupamin 9010 [mg]	Lupamin 9010 [µL]	H_2O [µL]
67	100	75	490,2	1030,8
68	100	50	326,8	875,5
69	100	25	163,4	720,1
70	100	15	98	658,0
71	100	5	32,7	595,8

Table 7-12: Addition of variable polyelectrolyte (Percol 47®) content..

Sample	Particle [mg]	Percol 47 [mg]	Percol 47 [µL]	H_2O [µL]
77	100	75	490,2	1030,8
78	100	50	326,8	875,5

Table 7-13: Addition of variable polyelectrolyte (Lupamin 9010®) and binder (Styronal®) content.

Sample	Particle [mg]	Lupamin 9010 [mg]	Lupamin 9010 [µL]	Binder [mg]	Binder [µL]	H_2O [µL]
79	100	50	326,8	75	147,4	1994,5
80	100	50	326,8	50	98,3	1724,5
81	100	50	326,8	25	49,1	1145,1
82	100	50	326,8	15	29,5	1037,2
83	100	50	326,8	5	10	929,4

Table 7-14: Addition of variable polyelectrolyte (Lupamin 4500®) and binder (Styronal®) content.

Sample	Particle [mg]	Lupamin 4500 [mg]	Lupamin 4500 [µL]	Binder [mg]	Binder [µL]	H_2O [µL]
84	100	50	386,1	75	147,4	1625
85	100	50	386,1	50	98,3	1355,4
86	100	50	386,1	25	49,1	1273,3
87	100	50	386,1	15	29,5	1165,4
88	100	50	386,1	5	10	1057,6

Table 7-15: Addition of variable polyelectrolyte (Lupamin 4500®) and binder (Styronal®) content at alkaline pH.

Sample	Particle [mg]	Lupamin 4500 [mg]	Lupamin 4500 [µL]	NaOH [µL]	Binder [mg]	Binder [µL]	H_2O [µL]	pH
89	100	50	386,1	25	50	98,3	1517,9	8
90	100	50	386,1	50	50	98,3	1492,9	8
91	100	50	386,1	100	50	98,3	1442,9	8
92	100	50	386,1	150	50	98,3	1392,9	8-9
93	100	50	386,1	200	50	98,3	1353,9	8-9
94	100	50	386,1	300	50	98,3	1253,9	9

Table 7-16: Addition of variable polyelectrolyte (Lupamin 9010®) and binder (Styronal®) content at alkaline pH.

Sample	Particle [mg]	Lupamin 9010 [mg]	Lupamin 9010 [µL]	NaOH [µL]	Binder [mg]	Binder [µL]	H_2O [µL]	pH
95	100	50	326,8	25	50	98,3	1517,9	8
96	100	50	326,8	50	50	98,3	1492,9	8
97	100	50	326,8	100	50	98,3	1442,9	8
98	100	50	326,8	150	50	98,3	1392,9	8-9
99	100	50	326,8	200	50	98,3	1353,9	9
100	100	50	326,8	300	50	98,3	1253,9	9

Table 7-17: Addition of variable polyelectrolyte (Lupamin 4500®) and binder (Styronal®) content at acidic pH.

Sample	Particle [mg]	Lupamin 4500 [mg]	Lupamin 4500 [µL]	HCl [µL]	Binder [mg]	Binder [µL]	H_2O [µL]	pH
101	100	50	386,1	25	50	98,3	1517,9	7-8
102	100	50	386,1	50	50	98,3	1492,9	7-6
103	100	50	386,1	100	50	98,3	1442,9	7-6
104	100	50	386,1	150	50	98,3	1392,9	6
105	100	50	386,1	200	50	98,3	1353,9	6
106	100	50	386,1	300	50	98,3	1253,9	6

Table 7-18: Addition of variable polyelectrolyte (Lupamin 9010®) and binder (Styronal®) content at acidic pH.

Sample	Particle [mg]	Lupamin 9010 [mg]	Lupamin 9010 [µL]	HCl [µL]	Binder [mg]	Binder [µL]	H_2O [µL]	pH
107	100	50	326,8	25	50	98,3	1517,9	7-8
108	100	50	326,8	50	50	98,3	1492,9	7-8
109	100	50	326,8	100	50	98,3	1442,9	7
110	100	50	326,8	150	50	98,3	1392,9	7
111	100	50	326,8	200	50	98,3	1353,9	7-6
112	100	50	326,8	300	50	98,3	1253,9	6

Table 7-19: : Addition of variable polyelectrolyte (Percol 47®), salt ($CaCl_2$), and defoaming agent content.

Sample	Particle [mg]	PEL [mg]	Defoam. [mg]	$CaCl_2$ [µL]	PEL [µL]	Defoam. [PµL]	H_2O [µL]
113	100	25	0,1	50	326,8	3,3	682,2
114	100	25	0,5	50	326,8	16,4	674,1
115	100	25	0,1	75	326,8	3,3	657,2
116	100	25	0,5	75	326,8	16,4	649,1
117	100	25	0,1	125	326,8	3,3	607,2
118	100	25	0,5	125	326,8	16,4	599,1
119	100	50	0,1	25	653,6	3,3	699,1
120	100	50	0,5	25	653,6	16,4	691,1
121	100	50	0,1	50	653,6	3,3	674,1
122	100	50	0,5	50	653,6	16,4	666,1
123	100	50	0,1	125	653,6	3,3	599,1
124	100	50	0,5	125	653,6	16,4	591,1
125	100	75	0,1	50	980,4	3,3	666,1
126	100	75	0,5	50	980,4	16,4	658,0
127	100	75	0,1	125	980,4	3,3	591,1
128	100	75	0,5	125	980,4	16,4	583,0

Table 7-20: Addition of variable polyelectrolyte (Lupamin 9010®), salt (NaCl), and defoaming agent content.

Sample	Partikel	Lupamin 9010 [mg]	Defoam. [mg]	NaCl [µL]	Lupamin 9010 [µL]	Defoam. [µL]	H_2O [µL]
129	100	25	0,1	25	326,8	3,3	707,2
130	100	25	0,5	25	326,8	16,4	699,1

Table 7-21: Addition of variable polyelectrolyte (Lupamin 4500®), salt ($CaCl_2$), and defoaming agent content.

Sample	Particle [mg]	Lupamin 4500 [mg]	Defoam. [mg]	$CaCl_2$ [µL]	Lupamin 4500 [µL]	Defoam. [µL]	H_2O [µL]
131	100	75	0,1	50	579,2	3,3	1067,3
132	100	75	0,5	50	579,2	16,4	1059,3
133	100	75	0,1	125	579,2	3,3	992,3
134	100	75	0,5	125	579,2	16,4	984,3

Table 7-22: Addition of variable polyelectrolyte (Lupamin 9010®), salt ($CaCl_2$) ,and defoaming agent content.

Sample	Particle [mg]	Lupamin 9010 [mg]	Defoam. [mg]	$CaCl_2$ [µL]	Lupamin 9010 [µL]	Defoam. [µL]	H_2O [µL]
135	100	25	1,0	125,0	326,8	32,9	389,2
136	100	25	1,5	125,0	326,8	49,3	379,1
137	100	50	1,0	25,0	653,6	32,9	481,2
138	100	50	1,5	25,0	653,6	49,3	471,1
139	100	50	1,0	50,0	653,6	32,9	456,2
140	100	50	1,5	50,0	653,6	49,3	446,1
141	100	50	1,0	75,0	653,6	32,9	431,2
142	100	50	1,5	75,0	653,6	49,3	421,1
143	100	50	1,0	125,0	653,6	32,9	381,2
144	100	50	1,5	125,0	653,6	49,3	371,1
145	100	75	1,0	50,0	980,4	32,9	448,1
146	100	75	1,5	50,0	980,4	49,3	438,0
147	100	75	1,0	75,0	980,4	32,9	423,1
148	100	75	1,5	75,0	980,4	49,3	413,0
149	100	75	1,0	125,0	980,4	32,9	373,1
150	100	75	1,5	125,0	980,4	49,3	363,0

Table 7-23: Addition of variable polyelectrolyte (Lupamin 4500®), salt ($CaCl_2$), and defoaming agent content.

Sample	Particle [mg]	Lupamin 4500 [mg]	Defoam. [mg]	$CaCl_2$ [µL]	Lupamin 4500 [µL]	Defoam. [µL]	H_2O [µL]
151	100	75	1,0	50,0	579,2	32,9	849,4
152	100	75	1,5	50,0	579,2	49,3	839,3
153	100	75	1,0	125,0	579,2	32,9	670,1
154	100	75	1,5	125,0	579,2	49,3	660,1
155	100	75	1,0	125,0	579,2	32,9	82,5
156	100	75	1,5	125,0	579,2	49,3	72,4

Table 7-24: Addition of variable polyelectrolyte (Lupamin 4500®), and binder (Styronal®) content.

Sample	Particle [mg]	Lupamin 4500 [mg]	Lupamin 4500 [µL]	Binder [mg]	Binder [µL]	H_2O [µL]
157	100	50	386,1	75	147,4	2219,7
158	100	50	386,1	25	49,1	1680,5
159	100	50	386,1	15	29,5	1572,6

Table 7-25: Addition of variable polyvinyl alcohol (85 % hydrolyzed) content. Further addition of PVA to the precipitation solution.

Sample	Particle [mg]	PVA [mg]	PVA [µL]	H_2O [µL]
160	100	5	100	704,3
161	100	10	200	668
162	100	**25**	500	559,3
163	100	50	1000	378
165	100	5	1500	196,8
166	100	10	100	413
167	100	25	200	376,7
168	100	50	500	268

Table 7-26: Addition of variable polyvinyl alcohol (85 % hydrolyzed) content. Further addition of PVA to the precipitation solution. Subsequent variation of coating speed.

Sample	Particle [mg]	PVA [mg]	PVA [µL]	H_2O [µL]
169	100	10	200	376,7
170	100	15	300	340,5
171	100	20	400	304,2
172	100	30	600	231,7
173	100	35	700	195,5
174	100	40	800	159,2
175	100	50	1000	86,7
176	100	10	200	668
177	100	15	300	631,8
178	100	20	400	595,5

7.2.4. Coating and thermal printing of CAB-formulations

Coating was carried out on translucent Hostaphan-membranes as substrate, using an automatic film-applicator by BYK and a blade applicator with a 60 μm gap. Subsequently the samples were parted and one half was dried in a natural convection hot air oven which was preheated to 70 °C for 30 min. Subsequently the thermal printing capabilities were evaluated using an CNC-IR-laser with adjustable power-output (custom built), the parameters used are displayed in Table 7-27.

Table 7-27: Parameters of the employed CNC-Laser-System.

Parameter	Setting
Power(rel.) [%]	10 - 100
Power-Output (max.) [W]	30
Frequency[Hz]	100
Resolution[µm]	40
Speed [mm/s]	2000
Heating time [ms]	3

7.3. Polymer Synthesis

7.3.1. Swern oxidation of HPC

The oxidation of HPC via the Swern-route was carried out by dissolving 1.29 mL oxalyl chloride (15 mmol, 5 eq.) in 3 mL THF and chilling this mixture to -78 °C. Subsequently 2.15 mL (30 mmol, 10 eq.) diluted in 3 mL THF were added dropwise, followed by stirring for 15 minutes. Now 0.49 g HPC (1 mmol, 1 eq.) dissolved in 50 mL THF were added dropwise and the reaction mixture was stirred for 30 minutes. After this period 6.24 mL trimethylamine (45 mmol, 15 eq.) were added and cooling was removed. The reaction mixture was then stirred for 3 h and precipitated in n-hexane. The crude product was purified via dissolution and subsequent precipitation. After drying under reduced pressure the ^{1}H-Analysis of the pure product revealed, that no oxidization has occurred.

7.3.2. TEMPO mediated oxidation of HPC with sodium hypochlorite

The (2,2,6,6-tetramethylpiperidin-1-yl)oxidanyl (TEMPO) mediated oxidation of HPC with sodium hypochlorite as oxidant was carried out according to the following general procedure: hydroxypropyl cellulose was dissolved in water and chilled to 2°C in an ice-bath. To the stirred solution, sodium bromide is added, as well as a solution of TEMPO in chloroform which leads to a biphasic and turbid system. After the addition of the oxidizing agent, sodium hypochlorite, the reaction is left to heat up to 23 °C under continued stirring for 12 h. Afterwards the phases are separated and the aqueous phase is washed 3 times with chloroform. The unified organic phases are dried over $MgSO_4$ and approximately 75 % of the solvent are removed under reduced pressure. The residual solution is precipitated in n-hexane and purified via threefold re-dissolution and re-precipitation. Finally, the product is dried under reduced pressure. The actual formulation used are listed in Table 7-28 to Table 7-35.

Table 7-28: Composition of the reaction mixture used in the TEMPO mediated oxidation of HPC; 1st formulation.

Reagent	n[mmol]	m [mg]	V [mL]
HPC	1	490	
Water			35
TEMPO	1,5	234	
$CHCl_3$			100
NaBr	0,3	30	
NaOCl (6 wt.% solution)	6	0,45	7,5

Table 7-29: Composition of the reaction mixture used in the TEMPO mediated oxidation of HPC; 2nd formulation.

Reagent	n[mmol]	m [mg]	V [mL]
HPC	1	490	
Water			35
TEMPO	1.5	234	
$CHCl_3$			100
NaBr	0.3	30	
NaOCl (6 wt.% solution)	2	150	2.5

Table 7-30: Composition of the reaction mixture used in the TEMPO mediated oxidation of HPC; 3rd formulation.

Reagent	n[mmol]	m [mg]	V [mL]
HPC	50	25	
Water			500
TEMPO	7.5	1170	
$CHCl_3$			100
NaBr	15	1500	
NaOCl (6 wt.% solution)	50	3750	62.5

Table 7-31: Composition of the reaction mixture used in the TEMPO mediated oxidation of HPC; 4th formulation.

Reagent	n[mmol]	m [mg]	V [mL]
HPC	1	500	
Water			50
TEMPO	0.15	23	
$CHCl_3$			10
NaBr	0.3	30	
NaOCl (6 wt.% solution)	6	450	7.5

Table 7-32: Composition of the reaction mixture used in the TEMPO mediated oxidation of HPC; 5th formulation.

Reagent	n[mmol]	m [mg]	V [mL]
HPC	1	500	
Water			50
TEMPO	0.15	23	
$CHCl_3$			10
NaBr	0.3	30	
NaOCl (6 wt.% solution)	6	450	7.5

Table 7-33: Composition of the reaction mixture used in the TEMPO mediated oxidation of HPC; 6th formulation.

Reagent	n[mmol]	m [mg]	V [mL]
HPC	1	500	
Water			10
TEMPO	0.15	23	
$CHCl_3$			100
NaBr	0.3	30	
NaOCl (6 wt.% solution)	6	450	7.5

Table 7-34: Composition of the reaction mixture used in the TEMPO mediated oxidation of HPC; 7th formulation.

Reagent	n[mmol]	m [mg]	V [mL]
HPC	1	500	
Water			50
TEMPO	0.15	23	
$CHCl_3$			100
NaBr	0.3	30	
NaOCl (6 wt.% solution)	6	450	7.5

Table 7-35: Composition of the reaction mixture used in the TEMPO mediated oxidation of HPC; 8th formulation.

Reagent	n[mmol]	m [mg]	V [mL]
HPC	10	5	
Water			250
TEMPO	1.5	230	
CHCl3			500
NaBr	3	300	
NaOCl (6 wt.% solution)	60	4.5	75

7.3.3. Synthesis of HPC-2-hydroxy-*N,N,N*-trimethyl-3-ammonium-propyl-ether

The synthesis of HPC-2-Hydroxy-*N,N,N*-trimethyl-3-ammonium-propyl-ether (GAC-HPC) (Figure 7-1) was carried out using a solution of 5 g HPC (10 mmol, 1 eq.) in 100 mL dry THF. 4.516 g glycidyltrimethylammonium chloride (10 mmol, 1 eq.) and 50 μL concentrated sulfuric acid were added. The reaction mixture was heated to 80 °C for 3 and 6 h, respectively. The reaction mixture war precipitated in cold (5 °C) toluene to afford the crude product. After removal of excess liquid the swollen solid was dissolved using 150 mL of ethanol and reprecipitated in toluene. This process was repeated 3 times to afford the purified products with a DS_{GAC} after 3 h of 0.58 (83 % yield) and DS_{GAC} after 6 h of 1.16 h (86 % yield).

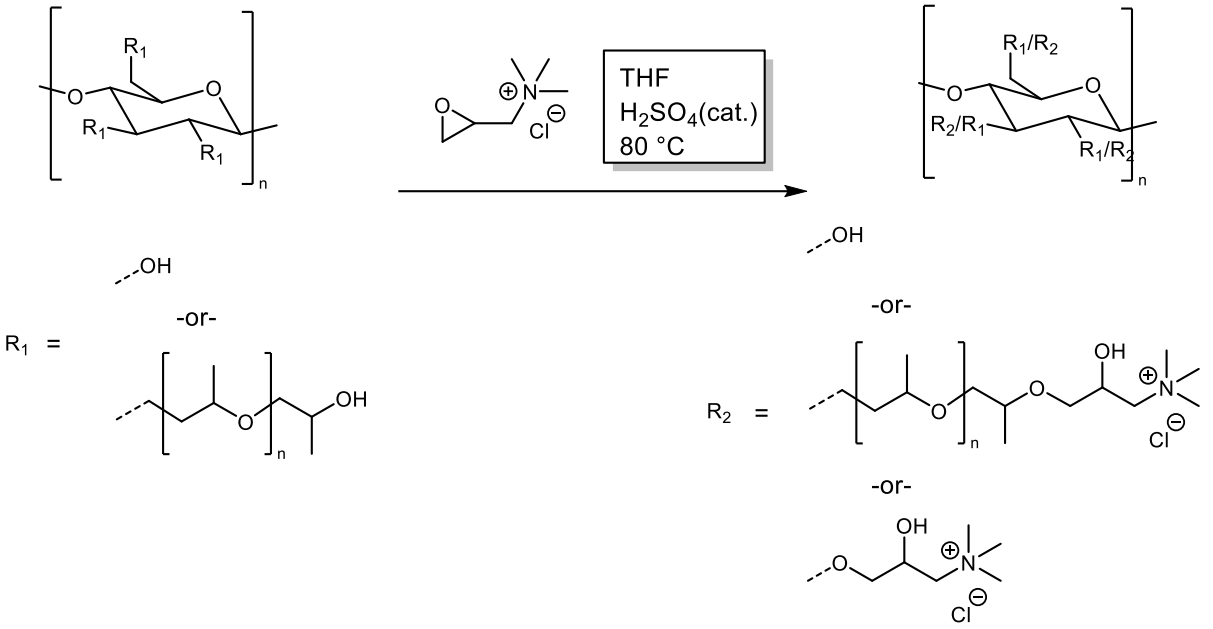

Figure 7-1: Synthesis of GAC-HPC using the sulfuric acid catalyzed etherification. The process led to good yields and gave suitable control over the degree of derivatization which enabled us to create several different GAC-HPC derivatization.

7.4. Wet end paper additives

7.4.1. Analysis of the retention of wet-end additives for paper

To determine the retention a given polymer in the fiber matrix the fiber material was initially hydrated. For this purpose, 48 g of air dried fiber material are soaked in 2.5 liters of water for 24 h and subsequently pulped using an Estanit pulping device (75,000 revolutions over 25 min) The resulting suspension was diluted to 4 L and for each test 166 mL of this suspension were used. The given polymer of interest was added as solution and the whole sample diluted to 250 mL and subsequently filtered to separate the liquid. The liquid phase was evaporated and the residual solids were gravimetrically analyzed to determine the amount of polymer that did not bind to the fiber material. Note, that for this process to yield accurate results, a precise determination of the water-extractables-content has to be carried out in the first place and considered in the calculation.

7.4.2. Photometric determination of the LCST of various cellulose esters

The LCST of the cellulose ethers used during the investigation into beneficial effects of bio-based LCST-polymers were determined using a custom rig consisting of a photometer, a thermostat, and a water bath as shown in Figure 7-2. Initially 15 mL of a solution of the cellulose ether of interest was placed inside the heated vessel. The system was then equipped with a thermal couple and the photometer probe. The photometer was set to monitor transmission at 600 nm.

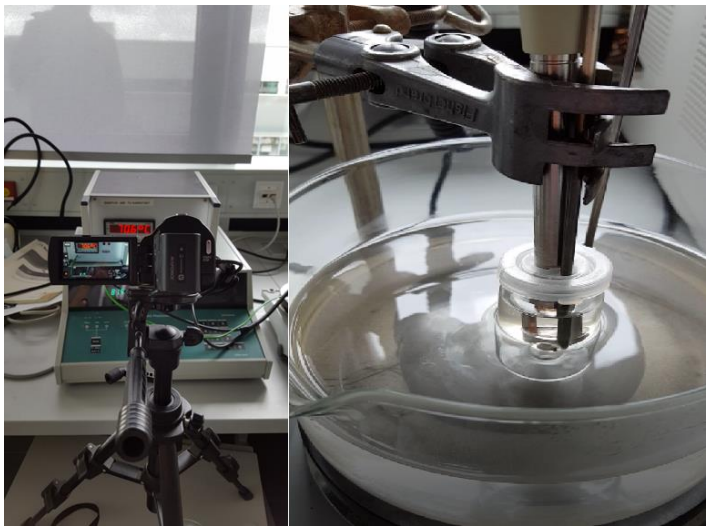

Figure 7-2: Setup utilized for the determination of the LCST of different cellulose ethers.

In the next step the water bath is heated from room temperature up until the transmission has dropped to a constant value, i.e. until the LCST is surpassed. The video is then analyzed to extract correlated data of temperature and transmission and plot them for the determination of the LCST. In Figure 7-3, an example of such data is provided.

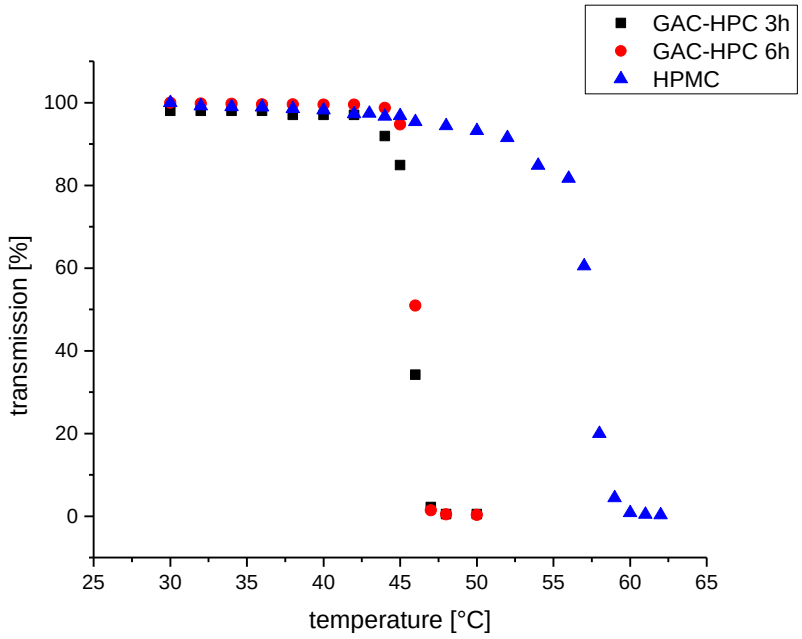

Figure 7-3: Correlation of the data obtained from the photometer with the thermostat. When the LCST is passed, the polymer precipitates from solution, which increases the turbidity of the solution and subsequently decreases the transmission measured by the photometer.

7.4.3. Analysis of the drying rate of paper sheets formed using a lab scale sheet former

This procedure is identical to 7.4.1 up to the point where the polymer solution is added to the fibers. After the Polymer solution is added the fiber suspension is diluted up to a final volume of 0.5 L. this suspension is used in a Räpid-Koethen sheet-former, where the paper sheet is formed according to DIN EN ISO 5269-2. After the sheet formation the samples are dried in the hydrothermal drying unit in 30 second steps and residual moisture is determined for every sample to acquire information on how the additives effect the drying-rate.

8. List of Figures

9. List of Tables

10. References

[1] United Nations, Secretary-General's remarks to the press at COP22, Marrakech, **2016**.
[2] United Nations, 70/1, **2015**.
[3] E. Bioplastics, **2018**, pp. 2-4.
[4] C. Béné, R. Arthur, H. Norbury, E. Allison, M. Beveridge, S. Bush, L. Campling, W. Leschen, D. Little, D. Squires, S. Thilsted, M. Troell, M. Williams, *Contribution of Fisheries and Aquaculture to Food Security and Poverty Reduction: Assessing the Current Evidence, Vol. 79*, **2016**.
[5] S. A. Ashter, *Introduction to Bioplastics Engineering*, 1st ed., Elsevier, **2016**.
[6] Clarivate*, Vol. 2018*, **2018**.
[7] H. J. Park, M. S. Chinnan, *J Food Eng* **1995**, *25*, 497-507.
[8] R. N. Tharanathan, *Trends Food Sci Tech* **2003**, *14*, 71-78.
[9] P. Cazon, G. Velazquez, J. A. Ramirez, M. Vazquez, *Food Hydrocolloid* **2017**, *68*, 136-148.
[10] H. W. Maurer, *Starch and Starch Products in Surface Sizing and Paper Coating Revised Edition*, Technical Association of the Pulp and Paper Industry United States, **2001**.
[11] H. L. Lee, J. Y. Shin, C. H. Koh, H. Ryu, D. J. Lee, C. Sohn, *Tappi J* **2002**, *1*, 34-40.
[12] D. Glittenberg, A. Becker, *Paper Technology* **1998**, *39*, 37-41.
[13] P. Müller, E. Gruber, C. Broßmer, D. Bischoff, *Internationale Papierwirtschaft* **2000**, *T22-T28*.
[14] H. W. Maurer, R. L. Kearney, *Starch - Stärke* **1998**, *50*, 396-402.
[15] E. Psomiadou, *Carbohyd Polym* **1997**, *32*, 329-332.
[16] D. Peressini, B. Bravin, A. Sensidoni, *Ital J Food Sci* **2004**, *16*, 5-16.
[17] F. D. S. Larotonda, K. N. Matsui, P. J. A. Sobral, J. B. Laurindo, *J Food Eng* **2005**, *71*, 394-402.
[18] C. Dury-Brun, P. Chalier, S. Desobry, A. Voilley, *J Food Eng* **2008**, *88*, 114-125.
[19] C. Fringant, M. Rinaudo, N. Gontard, S. Guilbert, H. Derradji, *Starch-Starke* **1998**, *50*, 292-296.
[20] S. Kopacic, A. Walzl, A. Zankel, E. Leitner, W. Bauer, *Coatings* **2018**, *8*.
[21] X. Jiang, G. Chen, Z. Q. Fang, *Advanced Materials Research* **2014**, *893*, 472-477.
[22] F. Ham-Pichavant, G. Sebe, P. Pardon, V. Coma, *Carbohyd Polym* **2005**, *61*, 259-265.
[23] M. Laleg, I. Pikulik Ivan, in *Nord Pulp Pap Res J, Vol. 6*, **1991**, p. 99.
[24] S. H. Wang, Y. Jing, *Bioresources* **2016**, *11*, 1868-1881.
[25] H. Kjellgren, M. Gallstedt, G. Engstrom, L. Jarnstrom, *Carbohyd Polym* **2006**, *65*, 453-460.
[26] N. Bordenave, S. Grelier, F. Pichavant, V. Coma, *J Agr Food Chem* **2007**, *55*, 9479-9488.
[27] N. Bordenave, S. Grelier, V. Coma, *Biomacromolecules* **2010**, *11*, 88-96.
[28] J. Vartiainen, R. Motion, H. Kulonen, M. Ratto, E. Skytta, R. Ahvenainen, *J Appl Polym Sci* **2004**, *94*, 986-993.
[29] Ensymm, www..ensymm.com, **2016**.
[30] F. Renault, B. Sancey, J. Charles, N. Morin-Crini, P. M. Badot, P. Winterton, G. Crini, *Chem Eng J* **2009**, *155*, 775-783.
[31] S. Brown, **2018**.
[32] S. Despond, E. Espuche, N. Cartier, A. Domard, *J Appl Polym Sci* **2005**, *98*, 704-710.
[33] W. W. Zhang, H. N. Xiao, L. Y. Qian, *Carbohyd Polym* **2014**, *101*, 401-406.
[34] B. L. Butler, P. J. Vergano, R. F. Testin, J. M. Bunn, J. L. Wiles, *J Food Sci* **1996**, *61*, 953-&.
[35] J. J. Kester, O. Fennema, *J Food Sci* **1989**, *54*, 1383-1389.
[36] S. Pavlidou, C. D. Papaspyrides, *Prog Polym Sci* **2008**, *33*, 1119-1198.

[37] R. Grewal, W. Sweesy, J. S. Jur, J. Willoughby, in *Functional Materials from Renewable Sources, Vol. 1107*, American Chemical Society, **2012**, pp. 271-296.
[38] A. I. Alateyah, H. N. Dhakal, Z. Y. Zhang, *Adv Polym Tech* **2013**, *32*.
[39] G. Laufer, C. Kirkland, A. A. Cain, J. C. Grunlan, *Carbohyd Polym* **2013**, *95*, 299-302.
[40] T. Wüstenberg, in *Cellulose and Cellulose Derivatives in the Food Industry*, Wiley-VCH Verlag GmbH & Co. KGaA, **2014**, p. 139.
[41] K. J. Edgar, C. M. Buchanan, J. S. Debenham, P. A. Rundquist, B. D. Seiler, M. C. Shelton, D. Tindall, *Prog Polym Sci* **2001**, *26*, 1605-1688.
[42] T. Urbanski, *Vol. I*, Pergamon Press, Oxford, **1965**, pp. 20–21.
[43] T. L. Thomas Heinze, Andreas Koschella, *Esterification of Polysaccharides* Springer, Berlin Heidelberg New York, **2006**.
[44] Klaus Balser, *Ullmann's Encyclopedia of Industrial Chemistry 7th Edition, Vol. 7*, **2011**.
[45] Markets and Markets, Cellulose Esters Market by Type and Region - Global Forecast to 2023, **2018**.
[46] Stratistics Market Research Company, Cellulose Acetate Market Size, Share, Report, Analysis, Trends & Forecast to 2026, **2018**.
[47] Zion Market Research, *Cellulose Acetate Market Poised to Surge from USD 4.82 Billion in 2015 to USD 7.01 Billion, Globally by 2021*, **2017**.
[48] Eastman, Cellulose-based specialty polymers, E 325, **2014**.
[49] T. Iwata, A. Fukushima, K. Okamura, J. Azuma, *J Appl Polym Sci* **1997**, *65*, 1511-1515.
[50] F. Muller, *Papier* **1985**, *39*, 591-600.
[51] C. J. Malm, L. J. Tanghe, H. M. Herzog, M. H. Stewart, *Ind Eng Chem* **1958**, *50*, 1061-1066.
[52] R. Brückner, Springer Spektrum, Berlin Heidelberg, **2004**, pp. 269-279.
[53] X. F. Sun, R. C. Sun, L. Zhao, J. X. Sun, *J Appl Polym Sci* **2004**, *92*, 53-61.
[54] T. Morooka, M. Norimoto, T. Yamada, N. Shiraishi, *J Appl Polym Sci* **1984**, *29*, 3981-3990.
[55] J. A. Heredia-Guerrero, L. Goldoni, J. J. Benitez, A. Davis, L. Ceseracciu, R. Cingolani, I. S. Bayer, T. Heinze, A. Koschella, A. Heredia, A. Athanassiou, *Carbohyd Polym* **2017**, *173*, 312-320.
[56] G. Antova, P. Vasvasova, M. Zlatanov, *Carbohyd Polym* **2004**, *57*, 131-134.
[57] Y. Shimizu, J. Hayashi, *Cell Chem Technol* **1989**, *23*, 661-670.
[58] G. Samaranayake, W. G. Glasser, *Carbohyd Polym* **1993**, *22*, 1-7.
[59] C. J. Malm, D. L. Kendall, G. D. Hiatt, *Ind Eng Chem* **1951**, *43*, 684-688.
[60] C. Vaca-Garcia, G. Gozzelino, W. G. Glasser, M. E. Borredon, *J Polym Sci Pol Phys* **2003**, *41*, 281-288.
[61] A. Geissler, L. Q. Chen, K. Zhang, E. Bonaccurso, M. Biesalski, *Chem Commun* **2013**, *49*, 4962-4964.
[62] A. Grün, F. Wittka, *Angewandte Chemie* **1921**, *34*, 645-648.
[63] A. I. Latetin, L. S. Gal'braikh, Z. A. Rogovin, *Polymer Science U.S.S.R.* **1968**, *10*, 761-766.
[64] C. Smith, J. Tuschhoff, **1961**.
[65] M. Jebrane, N. Terziev, I. Heinmaa, *Biomacromolecules* **2017**, *18*, 498-504.
[66] X. X. Wen, H. H. Wang, Y. Wei, X. Y. Wang, C. F. Liu, *Carbohyd Polym* **2017**, *168*, 247-254.
[67] A. Meller, *Tappi* **1953**, *36*, 264-267.
[68] C. J. Malm, L. J. Tanghe, *Ind Eng Chem* **1955**, *47*, 995-999.
[69] C. J. Malm, K. T. Barkey, J. T. Schmitt, D. C. May, *Ind Eng Chem* **1957**, *49*, 763-767.
[70] T. Heinze, W. G. Glasser, in *Cellulose Derivatives, Vol. 688*, American Chemical Society, **1998**, pp. 2-18.
[71] T. Heinze, A. Koschella, *Polímeros* **2005**, *15*, 84-90.
[72] H. F. Launer, W. K. Wilson, *Anal Chem* **1950**, *22*, 455-458.

[73] A. Ostlund, D. Lundberg, L. Nordstierna, K. Holmberg, M. Nyden, *Biomacromolecules* **2009**, *10*, 2401-2407.
[74] B. Philipp, *J Macromol Sci Pure* **1993**, *A30*, 703-714.
[75] H. Sihtola, E. Kaila, L. Laamanen, *J Polym Sci* **1957**, *23*, 809-824.
[76] T. Miyamoto, Y. Sato, T. Shibata, M. Tanahashi, H. Inagaki, *Journal of Polymer Science: Polymer Chemistry Edition* **1985**, *23*, 1373-1381.
[77] M. a. Markets, **2017**.
[78] T. Heinze, A. Koschella, *Macromol Symp* **2005**, *223*, 13-39.
[79] H. Es-haghi, S. M. Mirabedini, M. Imani, R. R. Farnood, *Colloid Surface A* **2014**, *447*, 71-80.
[80] D. Chemical, **2018**.
[81] T. Wüstenberg, in *Cellulose and Cellulose Derivatives in the Food Industry*, Wiley-VCH Verlag GmbH & Co. KGaA, **2014**, pp. 319-342.
[82] R. G. Bishop, (Ed.: H. Inc), **1964**.
[83] F. Cavani, A. M. Gaffney, in *Sustainable Industrial Chemistry*, **2009**.
[84] J. Caner, Z. J. Liu, Y. Takada, A. Kudo, H. Naka, S. Saito, *Catal Sci Technol* **2014**, *4*, 4093-4098.
[85] J. R. Dethlefsen, D. Lupp, A. Teshome, L. B. Nielsen, P. Fristrup, *Acs Catal* **2015**, *5*, 3638-3647.
[86] Y. Takada, J. Caner, H. Naka, S. Saito, *Pure Appl Chem* **2018**, *90*, 167-174.
[87] G. Bioenergies, **2014**.
[88] F. M. Situ, R. Z. Tan, L. Gong, Z. G. Zha, M. Tu, R. Zeng, H. Wu, J. Q. Zhang, L. H. Zheng, *J Wuhan Univ Technol* **2015**, *30*, 416-422.
[89] H. Steinmeier, P. Zugenmaier, *Carbohyd Res* **1988**, *173*, 75-88.
[90] M. Tu, W. Q. Han, R. Zeng, S. M. Best, R. E. Cameron, *Colloid Surface A* **2012**, *407*, 126-132.
[91] T. A. Yamagishi, F. Guittard, M. H. Godinho, A. F. Martins, A. Cambon, P. Sixou, *Polym Bull* **1994**, *32*, 47-54.
[92] H. Q. Hou, A. Reuning, J. H. Wendorff, A. Greiner, *Macromol Biosci* **2001**, *1*, 45-48.
[93] T. Ishizaki, S. Uenuma, S. Furumi, *Kobunshi Ronbunshu* **2015**, *72*, 737-745.
[94] S. L. Tseng, G. V. Laivins, D. G. Gray, *Macromolecules* **1982**, *15*, 1262-1264.
[95] F. Z. Khan, M. Shiotsuki, F. Sanda, Y. Nishio, T. Masuda, *J Polym Sci Pol Chem* **2008**, *46*, 2326-2334.
[96] B. Huang, J. J. Ge, Y. H. Li, H. Q. Hou, *Polymer* **2007**, *48*, 264-269.
[97] W. W. Chen, W. G. Weng, M. Fu, *J Appl Polym Sci* **2017**, *134*.
[98] J. L. Lee, E. M. Pearce, T. K. Kwei, *Macromolecules* **1997**, *30*, 6877-6883.
[99] V. Sereti, H. Stamatis, C. Pappas, M. Polissiou, F. N. Kolisis, *Biotechnology and Bioengineering* **2001**, *72*, 495-500.
[100] H. Zhao, E. S. Sterner, E. B. Coughlin, P. Theato, *Macromolecules* **2012**, *45*, 1723-1736.
[101] Q. Yan, D. H. Han, Y. Zhao, *Polym Chem-Uk* **2013**, *4*, 5026-5037.
[102] J. Cui, A. del Campo, *Woodhead Publ Mater* **2014**, 93-133.
[103] S. Chatani, C. J. Kloxin, C. N. Bowman, *Polym Chem-Uk* **2014**, *5*, 2187-2201.
[104] O. Bertrand, J. F. Gohy, *Polym Chem-Uk* **2017**, *8*, 52-73.
[105] J. Q. Jiang, X. Tong, Y. Zhao, *Journal of the American Chemical Society* **2005**, *127*, 8290-8291.
[106] J. Q. Jiang, X. Tong, D. Morris, Y. Zhao, *Macromolecules* **2006**, *39*, 4633-4640.
[107] J. Babin, M. Pelletier, M. Lepage, J. F. Allard, D. Morris, Y. Zhao, *Angew Chem Int Edit* **2009**, *48*, 3329-3332.
[108] S. Wiedbrauk, H. Dube, *Tetrahedron Lett* **2015**, *56*, 4266-4274.
[109] A. A. Beharry, G. A. Woolley, *Chemical Society Reviews* **2011**, *40*, 4422-4437.

[110] W. Szymanski, J. M. Beierle, H. A. V. Kistemaker, W. A. Velema, B. L. Feringa, *Chem Rev* **2013**, *113*, 6114-6178.
[111] J. Whelan, D. Abdallah, K. Piskorz, J. T. C. Wojtyk, J. M. Dust, J.-M. Nunzi, S. Hoz, E. Buncel, *Physical Chemistry Chemical Physics* **2012**, *14*, 13684-13691.
[112] R. Klajn, *Chemical Society Reviews* **2014**, *43*, 148-184.
[113] H. Y. Xia, K. Xie, G. Zou, *Molecules* **2017**, *22*.
[114] W. Li, S. Trosien, H. Schenderlein, M. Graf, M. Biesalski, *RSC Advances* **2016**, *6*, 109514-109518.
[115] S. Helmy, F. A. Leibfarth, S. Oh, J. E. Poelma, C. J. Hawker, J. R. de Alaniz, *Journal of the American Chemical Society* **2014**, *136*, 8169-8172.
[116] J. Stenhouse, *Justus Liebigs Annalen der Chemie* **1850**, *74*, 278-297.
[117] J. Stenhouse, *Justus Liebigs Annalen der Chemie* **1870**, *156*, 197-205.
[118] H. Schiff, *Justus Liebigs Annalen der Chemie* **1887**, *239*, 349-385.
[119] T. Zincke, G. Mühlhausen, *Berichte der deutschen chemischen Gesellschaft* **1905**, *38*, 3824-3829.
[120] G. Williams, C. L. Wilson, *Journal of the Chemical Society (Resumed)* **1942**, 506-507.
[121] K. Honda, H. Komizu, M. Kawasaki, *J Chem Soc Chem Comm* **1982**, 253-254.
[122] K. G. Lewis, C. E. Mulquiney, *Tetrahedron* **1977**, *33*, 463-475.
[123] P. Safar, F. Povazanec, N. Pronayova, P. Baran, G. Kickelbick, J. Kozisek, M. Breza, *Collect Czech Chem C* **2000**, *65*, 1911-1938.
[124] S. Helmy, S. Oh, F. A. Leibfarth, C. J. Hawker, J. R. de Alaniz, *Journal of Organic Chemistry* **2014**, *79*, 11316-11329.
[125] J. R. Hemmer, S. O. Poelma, N. Treat, Z. A. Page, N. D. Dolinski, Y. J. Diaz, W. Tomlinson, K. D. Clark, J. P. Hooper, C. Hawker, J. Read de Alaniz, *J Am Chem Soc* **2016**, *138*, 13960-13966.
[126] N. Mallo, P. T. Brown, H. Iranmanesh, T. S. C. MacDonald, M. J. Teusner, J. B. Harper, G. E. Ball, J. E. Beves, *Chem Commun* **2016**, *52*, 13576-13579.
[127] M. M. Lerch, S. J. Wezenberg, W. Szymanski, B. L. Feringa, *J Am Chem Soc* **2016**, *138*, 6344-6347.
[128] A. Balamurugan, H. I. Lee, *Macromolecules* **2016**, *49*, 2568-2574.
[129] S. O. Poelma, S. S. Oh, S. Helmy, A. S. Knight, G. L. Burnett, H. T. Soh, C. J. Hawker, J. R. de Alaniz, *Chem Commun* **2016**, *52*, 10525-10528.
[130] G. Sinawang, B. Wu, J. L. Wang, S. Li, Y. N. He, *Macromol Chem Physic* **2016**, *217*, 2409-2414.
[131] S. Singh, K. Friedel, M. Himmerlich, Y. Lei, G. Schlingloff, A. Schober, *Acs Macro Lett* **2015**, *4*, 1273-1277.
[132] R. Muthyala, X. Lan, in *Chemistry and Applications of Leuco Dyes*, Kluwer Academic Publishers, New York, Boston, Dordrecht, London, Moscow, **2002**.
[133] M. Kondo, K. Yasui, M. Miyake, H. Iwasaki, T. Shiraishi, *Vol. DE2629937* (Ed.: K. P. M. C. Ltd), Kanzaki Paper Manufacturing Co Ltd, Germany, **1975**.
[134] K. Adachi, (Ed.: P. Corp), Panasonic Corp, US, **1972**.
[135] E. C. Agency, European Chemicals Agency, https://echa.europa.eu/-/msc-unanimously-agrees-that-bisphenol-a-is-an-endocrine-disruptor, **2017**.
[136] S. Almeida, A. Raposo, M. Almeida-González, C. Carrascosa, *Comprehensive Reviews in Food Science and Food Safety* **2018**, *17*, 1503-1517.
[137] T. E. Commission, *Official Journal of the European Union* **2016**, *L 337*.
[138] P. A. K. SE, *Vol. 2018*, Papierfabrik August Koehler SE, **2018**.
[139] Y. J. Liu, E. Lotero, J. G. Goodwin, *J Catal* **2006**, *243*, 221-228.
[140] A. Böhm, M. Gattermayer, C. Trieb, S. Schabel, D. Fiedler, F. Miletzky, M. J. C. Biesalski, **2013**, *20*, 467-483.
[141] C. Bunte, O. Prucker, T. König, J. Rühe, *Langmuir* **2010**, *26*, 6019-6027.
[142] S. Hornig, T. Heinze, *Biomacromolecules* **2008**, *9*, 1487-1492.

[143] H. Wondraczek, K. Petzold-Welcke, P. Fardim, T. Heinze, *Cellulose* **2013**, *20*, 751-760.
[144] B. Derjaguin, L. Landau, *Prog Surf Sci* **1993**, *43*, 30-59.
[145] M. M. Lerch, M. Medved, A. Lapini, A. D. Laurent, A. Iagatti, L. Bussotti, W. Szymanski, W. J. Buma, P. Foggi, M. Di Donato, B. Feringa, *J Phys Chem A* **2018**, *122*, 955-964.
[146] W. Kogler, M. Tietz, W. J. Auhorn, in *Ullmann's Encyclopedia of Industrial Chemistry*, **2012**.
[147] R. Sangl, in *Taschenbuch der Papiertechnik* (Ed.: J. Blechschmidt), Carl Hanser Verlag, München, **2012**, pp. 423-478.
[148] J. Husband, A. Hiorns, in *The 6th European Coating Symposium proceeding*, Citeseer, **2015**.
[149] J. Puetz, M. A. Aegerter, in *Sol-Gel Technologies for Glass Producers and Users* (Eds.: M. A. Aegerter, M. Mennig), Springer US, Boston, MA, **2004**, pp. 37-48.
[150] D. Grosso, *Journal of Materials Chemistry* **2011**, *21*, 17033-17038.
[151] T. Young, *Philosophical Transactions of the Royal Society of London* **1805**, *95*, 65-87.
[152] R. N. Wenzel, *Industrial & Engineering Chemistry* **1936**, *28*, 988-994.
[153] A. B. D. Cassie, S. Baxter, *Transactions of the Faraday Society* **1944**, *40*, 546-551.
[154] A. Marmur, *Langmuir* **2003**, *19*, 8343-8348.
[155] C. W. Extrand, Y. Kumagai, *J Colloid Interf Sci* **1995**, *170*, 515-521.
[156] X. F. Yang, *Appl Phys Lett* **1995**, *67*, 2249-2251.
[157] B. Valeur, M. N. Berberan-Santos, *Molecular Fluorescence: Principles and Applications*, Wiley-VCH, **2001**.
[158] M. Heskins, J. E. Guillet, *Journal of Macromolecular Science: Part A - Chemistry* **1968**, *2*, 1441-1455.
[159] C. R. Becer, S. Hahn, M. W. M. Fijten, H. M. L. Thijs, R. Hoogenboom, U. S. Schubert, *J Polym Sci Pol Chem* **2008**, *46*, 7138-7147.
[160] S. Jain, P. S. Sandhu, r. Malvi, B. Gupta, *Cellulose derivatives as thermoresponsive polymer: An overview, Vol. 3*, **2013**.
[161] M. Takahashi, M. Shimazaki, J. Yamamoto, *J Polym Sci Pol Phys* **2001**, *39*, 91-100.

11. Erklärungen

11.1. Erklärung zur Dissertation

Darmstadt,

Erklärung zur Dissertation

Ich erkläre hiermit, dass ich meine Dissertation selbstständig und nur mit den angegebenen Hilfsmitteln angefertigt und noch keinen Promotionsversuch unternommen habe.

_____

(Maximilian Nau)

11.2. Erklärung der Übereinstimmung

Darmstadt,

Erklärung der Übereinstimmung

Ich erkläre hiermit, dass die elektronische Version der Doktorarbeit mit der schriftlichen Version übereinstimmt. Die elektronische Version liegt dem Prüfungssekretariat vor.

_____

(Maximilian Nau)

11.3. Erklärung zur Begutachtung der Veröffentlichungen

Referent: Prof. Dr. Markus Biesalski

Korreferent: Prof. Dr. Annette Andrieu-Brunsen

Darmstadt,

Weder Referent (Prof. Dr. Markus Biesalski) noch Korreferent (Prof. Dr. Annette Andrieu-Brunsen) der vorliegenden kumulativen Doktorarbeit waren an der Begutachtung nachstehender Veröffentlichungen beteiligt:

[1] Maximilian Nau, David Seelinger, Markus Biesalski, “Functional surface coatings from tailor-made long-chain hydroxypropyl cellulose ester nanoparticles”, *Cellulose*, **2018**, 25 (10), 5769-5780

[2] Maximilian Nau, David Seelinger, Markus Biesalski, “Independent Two Way Switching of the Wetting Behavior of Cellulose-Derived Nanoparticle Surface Coatings by Light and by Temperature. ”, *Adv. Mater. Interfaces* **2019**, 6, 1900378

[3] Maximilian Nau, Simon Trosien, David Seelinger, Anna K. Boehm, Markus Biesalski, “Spatially resolved crosslinking of hydroxypropyl cellulose esters for the generation of functional surface-attached organogels”, *Front. Chem*., **2019**, 7, 367

[4] Caterina Czibula, Gundula Teichert, Maximilian Nau, Mathias Hobisch, Chonnipa Palasingh, Markus Biesalski, Stefan Spirk, Christian Teichert and Tiina Nypelö, “Design of friction, morphology, wetting and protein affinity by cellulose blend thin film composition”, *Front. Chem.*, **2019**, 7, 239

[5] Maximilian Nau and Nicole Herzog, Johannes Schmidt, Tobias Meckel, Annette Andrieu-Brunsen and Markus Biesalski, “Janus-Type Hybrid Paper Membranes“ *Adv. Mater. Interfaces* **2019**, 6, 1900892

Referent Korreferent

(Prof. Dr. Markus Biesalski) (Prof. Dr. Annette Andrieu-Brunsen)

11.4. Erklärung zum Eigenanteil an den Veröffentlichungen

Darmstadt,

Im Folgenden ist aufgelistet, mit welchem Anteil ich an den Veröffentlichungen beteiligt war.

Mein Anteil an der folgenden Veröffentlichung beträgt 95 %.

Maximilian Nau, David Seelinger, Markus Biesalski, “Functional surface coatings from tailor-made long-chain hydroxypropyl cellulose ester nanoparticles”, *Cellulose*, **2018**, 25 (10), 5769-5780

Mein Anteil an der folgenden Veröffentlichung beträgt 90 %.

Maximilian Nau, David Seelinger, Markus Biesalski, “Independent Two Way Switching of the Wetting Behavior of Cellulose-Derived Nanoparticle Surface Coatings by Light and by Temperature”, *Adv. Mater. Interfaces* **2019**, 6, 1900378

Mein Anteil an der folgenden Veröffentlichung beträgt 85 %.

Maximilian Nau, Simon Trosien, David Seelinger, Anna K. Boehm, Markus Biesalski, “Spatially resolved crosslinking of hydroxypropyl cellulose esters for the generation of functional surface-attached organogels”, *Front. Chem.*, **2019**, 7, 367

Mein Anteil an der folgenden Veröffentlichung beträgt 30 %.

Caterina Czibula, Gundula Teichert, Maximilian Nau, Mathias Hobisch, Chonnipa Palasingh, Markus Biesalski, Stefan Spirk, Christian Teichert and Tiina Nypelö, “Design of friction, morphology, wetting and protein affinity by cellulose blend thin film composition”, *Front. Chem.*, **2019**, 7, 239

Mein Anteil an der folgenden Veröffentlichung beträgt 50 %.

Maximilian Nau and Nicole Herzog, Johannes Schmidt, Tobias Meckel, Annette Andrieu-Brunsen and Markus Biesalski, “Janus-Type Hybrid Paper Membranes“ *Adv. Mater. Interfaces* **2019**, 6, 1900892

_____

(Maximilian Nau)